Paleoceanographic and climatic teleconnections between the subarctic and subtropical North Atlantic during the last interglacial (MIS 5e)

Dissertation zur Erlangung des Doktorgrades

Dr. rer. nat.

der Mathematisch-Naturwissenschaftlichen Fakultät

der Christian-Albrechts-Universität zu Kiel

vorgelegt von

Anastasia Zhuravleva

Kiel, 2018

1. **Gutachter:** Prof. Dr. Martin Frank
2. **Gutachter:** PD. Dr. Ralf Schiebel

Eingereicht am: 17. Mai 2018
Tag der Disputation: 28. Juni 2018
Zum Druck genehmigt: 28. Juni 2018

Gez. Prof. Dr. Natascha Oppelt, Dekanin

Erklärung

Hiermit erkläre ich an Eides statt, dass ich die vorliegende Abhandlung, abgesehen von der Beratung durch meinen Betreuer, nach Inhalt und Form selbstständig erarbeitet habe und keine anderen, als die von mir aufgeführten Quellen und Hilfsmittel, verwendet wurden.

Diese Arbeit ist unter Einhaltung der Regeln guter wissenschaftlicher Praxis der Deutschen Forschungsgemeinschaft entstanden und wurde weder in Auszügen noch in ganzer Form an einer anderen Stelle im Rahmen eines Prüfungsverfahrens eingereicht.

Teile dieser Arbeit sind bereits in Fachzeitschriften veröffentlicht oder wurden zur Veröffentlichung eingereicht.

Kiel, den 17. Mai 2018

Anastasia Zhuravleva

Table of Contents

Abstract

The last interglacial, MIS (Marine Isotope Stage) 5e, lasting from about ~129 to 116 ka, holds important implications for the projected global warming, as this geological interval is believed to have been significantly warmer-than-preindustrial with smaller ice sheets and a sea level that was higher than today. Existing paleoceanographic reconstructions, however, often provide only a general picture of this critical time period, either assuming that the last interglacial peak was globally synchronous or presenting averaged characteristics over the MIS 5e interval. This thesis refines the current understanding of the last interglacial paleoceanography in the subarctic and subtropical North Atlantic, thereby disentangling forcing mechanisms for temporal changes in the circulation and providing new insights into ice-sheets dynamics, sea level history and cross-latitudinal climatic teleconnections. For this purpose, a multi-proxy dataset comprising stable isotope compositions, foraminiferal assemblages and lithic as well as X-ray fluorescence data was produced using marine sediments from the Nordic Seas and the Bahama region. The investigated core records span the entire last interglacial cycle, including MIS 5e, the penultimate (Saalian) deglaciation and the glacial inception after the peak interglacial conditions.

Several lines of evidence from the Nordic Seas (stable carbon and oxygen isotopes, foraminiferal assemblage data and ice-rafted debris) suggest a strong post-Saalian sea surface freshening that persisted in the region until mid-MIS 5e (~125 ka). In particular, new sediment data from the western Nordic Seas and the eastern Fram Strait reveal continuous deglaciation of the Greenland and Svalbard-Barents Sea Ice Sheets during early MIS 5e. As a result, influence of the Atlantic Water (AW) at the sea surface was reduced during the early phase of MIS 5e, accounting for a weak regional climatic optimum, which developed late within the interglacial when the insolation was already low. Although influence of the AW at the sea surface during the Saalian deglaciation (including early MIS 5e) was notably decreased, its inflow into the Nordic Seas never completely stopped. A thorough inspection of the data (e.g., foraminiferal occurrences) suggests that AW did penetrate polewards during the Saalian deglaciation, likely underneath a low-density halocline layer, which obscured AW-related signals in commonly used foraminiferal data.

Comparison of published data from the Labrador Sea with the new multi-proxy records from the upstream western Nordic Seas (i.e., the East Greenland margin) provides an apparent evidence for a tight freshwater-related coupling between these two basins with implications for regional sea surface evolution and deep-water convection. In particular, a millennial-scale sea surface cooling and reduction in vertical water convection registered in the Labrador Sea during early MIS 5e (at ~126.5 ka) appears to follow a meltwater discharge event documented in the western Nordic Seas and attributed to the Greenland deglaciation. Following few earlier studies, this abrupt climatic reversal could be referred to as a Younger Dryas-like event.

A multiproxy dataset from shallow-water sediments of the Bahama region (geochemical, lithological and stratigraphical data) suggests a late sea level highstand, that is in agreement with a continuing deglaciation reconstructed in the Nordic Seas. In addition, a comparable millennial-scale cooling event as found in the high northern latitudes during early MIS 5e is revealed in the foraminiferal assemblage data from the subtropical North Atlantic, arguing for a potential of this specific event to be used as an important marker allowing for a better chronostratigraphic constraint of the MIS 5e interval. In the Bahamas, the abrupt Younger Dryas-like sea surface cooling is associated with a sudden southward displacement of the Intertropical Convergence Zone. The latter shift is, in turn, related to a temporary reduction in deep-water formation, supporting a high-low latitude teleconnection that influenced the subtropical ocean circulation via ocean-atmospheric forcing. These observations lead to the inference that the persistent high-latitude freshening and unstable deep water overturning in the northern North Atlantic during early MIS 5e accounted for a particularly sensitive climatic regime, resulting in the abrupt cold-warm switches which could be traced across various oceanic basins.

Overall, this thesis supplies valuable data for improving climate models, as the obtained paleoceanographic information helps to constrain forcing mechanisms (insolation, oceanic-atmospheric teleconnections versus freshwater forcing), controlling the North Atlantic climate across the last interglacial cycle.

Kurzfassung

Die letzte Warmzeit, das interglaziale MIS (Marine Isotope Stage) 5e, kann wichtige Rückschlüsse zum Verständnis der gegenwärtigen globalen Erderwärmung zulassen. Es wir allgemein angenommen, dass dieses geologische Intervall (Dauer von ca. ~129 bis 116 ka) durch deutlich höhere Temperaturen gekennzeichnet war als jene in der vorindustriellen Zeit, und es verglichen zu heute damals kleinere Eisschilde und ein höherer Meeresspiegel vorherrschten. Gegenwärtige paläozeanographische Rekonstruktionen dieses Intervalls liefern jedoch oft nur ein allgemeines Bild dieser bedeutenden Zeitperiode, da diese entweder der Annahme unterliegen, dass der letzte interglaziale Höhepunkt weltweit synchron verlief, oder aber nur allgemeine Bedingungen des gesamten MIS 5e präsentieren. Diese vorliegende Arbeit vertieft das aktuelle Verständnis der Paläozeanographie des letzten Interglazials im subarktischen und subtropischen Nordatlantik und beleuchtet damit Mechanismen, welche die zeitlichen Veränderungen der Ozeanzirkulation kontrollierten. Sie liefert damit neue Erkenntnisse zur Eisschilddynamik, der Meeresspiegelgeschichte und zu klimatischen Televerbindungen zwischen verschiedenen Breiten der nördlichen Hemisphäre. Zu diesem Zweck wurde ein Multiproxy-Datensatz bestehend aus stabilen Isotopenzusammensetzungen, Foraminiferen-Zusammensetzungen und Litho- sowie Röntgenfluoreszenzdaten an Sedimenten aus den subarktischen Meeren und der Bahama-Region erhoben. Die untersuchten Kernabschnitte decken den gesamten letzten Interglazialzyklus ab, d.h., einschließlich des MIS 5e, der vorletzten Saale-Kaltzeit und der einsetzenden früheiszeitlichen Phase, die direkt auf das MIS 5e folgte.

Mehrere Parameter, die an Kernen aus den subarktischen Meeren untersucht wurden (einschließlich stabiler Kohlenstoff- und Sauerstoffisotope, Foraminiferen-Zusammensetzungen und eisbergtransportiertes Material) deuten auf eine starke post-saalische Meeresoberflächenaussüßung hin, die in der Region bis zur Mitte des MIS 5e (~125 ka) anhielt. Die neuen Sedimentdaten aus dem westlichen Europäischen Nordmeer und der östlichen Framstraße zeigen insbesondere eine kontinuierliche Enteisung der Grönland- und Svalbard-Barents-Eisschilde während des frühen MIS 5e an. Daher war der Einfluss des atlantischen Wassers an der Meeresoberfläche während der frühen Phase des MIS 5e schwach ausgeprägt, sodass sich das regionale Klimaoptimum erst spät im Interglazial entwickelte, in einer Phase mit abnehmender Sonneneinstrahlung. Obwohl der Einfluss des atlantischen Wassers an der Meeresoberfläche während der Saale-Enteisungsphase (einschließlich des frühen MIS 5e) deutlich verringert war, versiegte die Advektion von Atlantikwasser in die subarktischen Meere nie vollständig. Eine gründliche Auswertung der Daten (z. B. zeitliche Foraminiferen-Verteilungen) legt nahe, dass atlantisches Wasser auch während der Saaleenteisung polwärts transportiert wurde, jedoch vermutlich unterhalb einer Halokline-Schicht geringerer Dichte, sodass die atlantische Signatur nur schwach in den Foraminiferen-Daten ausgeprägt ist.

Ein Vergleich von veröffentlichten Daten aus der Labradorsee mit den neuen Multiproxy-Daten aus den westlichen subarktischen Meeren (d.h. vom ostgrönländischen Kontinentalhang) liefert einen deutlichen Hinweis für eine enge Süßwasser-Kopplung zwischen diesen beiden Becken, was entsprechend Auswirkungen auf die regionale Meeresoberfläche und die Tiefenwasserbildung hatte. Insbesondere eine tausend Jahre anhaltende Abkühlung der Oberflächenwässer und eine Verringerung der vertikalen Wasserkonvektion in der Labradorsee während des frühen MIS 5e (bei ~ 126,5 ka) scheint auf ein Schmelzwasserereignis hinzuweisen, das in den westlichen subarktischen Meeren stattfand und das somit der Enteisung des grönländischen Eisschilds zugeschrieben werden kann. Frühere Studien berücksichtigend könnte diese abrupte Klimaumkehr als eine Art "Jüngere Dryas" (YD) vergleichbares Ereignis bezeichnet werden.

Ein Multiproxy-Datensatz basierend auf Flachwassersedimenten der Bahama-Region (geochemische, lithologische und stratigraphische Daten) deutet auf einen verspäteten Meeresspiegelhochstand hin, der mit einer fortschreitenden Deglaziation in den subarktischen Meeren übereinstimmt. Ein vergleichbares tausendjähriges Abkühlungsereignis wie es in den hohen nördlichen Breiten während des frühen MIS 5e beobachtet wurde ist auch in den Foraminiferen-Verteilungen aus dem subtropischen Nordatlantik erkennbar. Dieses Ereignis könnte somit als wichtiger Marker genutzt werden kann, um eine bessere stratigraphische Eingrenzung des MIS 5e-Intervalls zu ermöglichen. Auf den Bahamas geht die YD-ähnliche Abkühlung einher mit einer südlichen Verlagerung der Intertropischen Konvergenzzone. Die letztgenannte Verschiebung steht wiederum im Zusammenhang mit einer vorübergehenden Verringerung der Tiefenwasserbildung und zeigt die beeinflussende Televerbindung zwischen den hohen und niedrigen Breiten der nördlichen Hemisphäre durch ozeanisch-atmosphärischen Antrieb. Diese Beobachtungen führen zu der Schlussfolgerung, dass die anhaltende Aussüßung und die instabile Tiefenwasserbildung im nördlichen Nordatlantik während des frühen MIS 5e ein besonders sensibles Klimaregime darstellte, die dann zu den überregional beobachteten abrupten Kalt-Warm-Umschlägen führte.

Zusammenfassend liefert diese Arbeit neue Datensätze auch für die Verbesserung von Klimamodellen, da die hier gewonnenen paläozeanographischen Erkenntisse dazu beitragen werden das nordatlantische Klimasystem und dessen kontrollierenden Mechanismen (Sonneneinstrahlung, breitenabhängiger Temperaturgradient, ozeanisch-atmosphärische Wechselwirkungen, nördliche Süßwasserzufuhr und Gletscherschmelze) während des letzten Interglazials besser zu verstehen.

Acknowledgements

First of all, I would like to thank my supervisor Henning Bauch for giving me the opportunity to do this PhD project. Henning, your enthusiasm does motivate and makes me feel excited about the research and about the last interglacial, in particular. Thank you for all the invaluable contributions to my thesis, for the great support, for the criticism, for sharing your ideas, and also for the all coffee-time discussions we had.

Furthermore, I owe many thanks to Martin Frank for the supervision of this work and for his continuous encouragement and support throughout the years. I would also like to thank Ralf Schiebel and Wolfgang Kuhnt for evaluation of my thesis.

My gratitude also goes to Kirsten Fahl and Walter Luttmer for their interest in my research, for introducing me into the biomarker world and for the great time during my short visit at AWI.

I would also like to particularly thank Jörn Thiede for his help and encouragement, and for supplying me with inspiring literature. I am further grateful to Robert Spielhagen for support, for insightful discussions concerning Fram Strait paleoceanography, for keeping the spirit of Christmas more-than-alive and for giving me the opportunity to join in on a fascinating scientific cruise to the northeastern Greenland shelf. My special thanks go to my office mate Zhenya Kandiano for everyday discussions and, notably, for her patience in getting me acquainted with the foraminifera taxonomy; Nicolas Van Nieuwenhove for suggestions and careful proof reading that helped to improve the first manuscript. I am also grateful to Sebastian Fessler and Dirk Nürnberg at GEOMAR for stable isotope analyses in my samples; Samuel Müller for technical assistance during XRF scanning at CAU; Walter Hale for assistance during sampling at the IODP Bremen Core Repository at MARUM; and Daphne and Julia for their help with foraminifera picking.

I wish to thank my colleagues from the Building 4 (Nadja, Christian, Miriam, Stefan, Marc, Quan, Heidi, Karen, Jens, Dorothea, Maciej, Carolyn, Kirstin, Bennet (+Sonja), Benoit, Chistelle) for the good working environment, for a countless number of coffee breaks we shared and for activities outside work; all the wonderful PhD fellows (past and present) from the Building 8 for good times in Kiel; in particular, Kristin and Janett for movie-nights and all the fun; scientific visitors of the legendary “Russian room” in the Building 4: Katya T., Andrei, Vasya, Katya Che., Natascha, Katya O., Jaroslav, Leonid just for being themselves; and, of course, my dear friends Sasha F., Ed, Sasha L., Fernando, Jay, Anechka, Pikulek, Raiskaya, Ksuy, Luba, Katya K., Ira, Ilya for the nice time and for always being there for me.

Lastly, I am grateful to my parents and to the “Nieska-Freiburg-Kiel Gesellschaft” for continuing support, kindness and interest in my studies. And most importantly of all, I owe many thanks to my Georgi. Thank you for making me feel at home and for adding something special to my life.

Chapter 1: Introduction

1.1 Preface

Accelerated Greenland Ice Sheet (GIS) mass loss and intensification of the hydrological cycle, involving increased river runoff and enhanced high-latitude precipitation, have long been recognized as direct consequences of global warming (Curry and Mauritzen, 2005; Wu et al., 2005). As a result of the ongoing freshening in the high-latitude ocean, a global change in the ocean overturning circulation is anticipated with implications for the global climate system (Rahmstorf et al., 2015; Sévellec et al., 2017). While the recent changes are already evidenced by climatic data around the globe (Bryden et al., 2005; Thompson et al., 2010; Smeed et al., 2013; Rahmstorf et al., 2015; Caesar et al., 2018), there is no consensus about the magnitude, abruptness and reversibility of oceanic perturbations in the future (Collins et al., 2013; Liu et al., 2017). In this venue, it is important to know how the Earth's system responded to pre-industrial forcings (e.g., orbital, solar or volcanic), which could be assessed by using appropriate climate data obtained from specific geological archives (Flato et al., 2013).

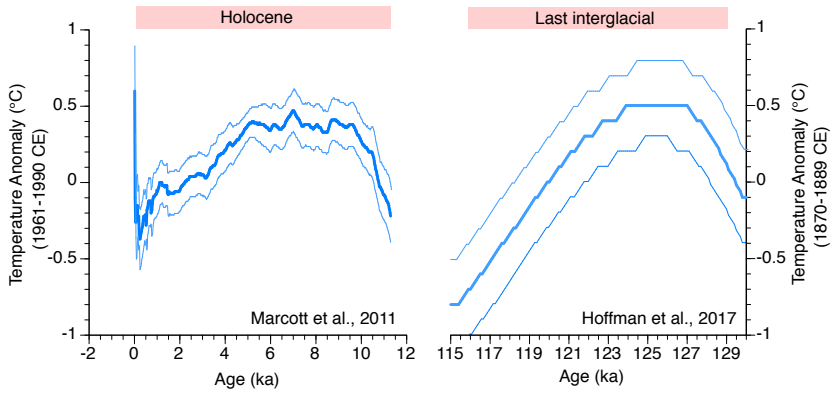

Figure 1.1: **Globally stacked temperature anomalies for the Holocene (Marcott et al., 2011) and the last interglacial (Hoffman et al., 2017) with their 1σ uncertainties**. Note that global temperature anomalies for the Holocene are calculated relative to the 1961-1990 mean and anomalies for MIS 5e are given relative to the HadISST1.1 1870–1889 mean.

The last interglacial, MIS (Marine Isotope Stage) 5e, or the Eemian in terrestrial records, lasting from about ~129 to 116 thousand years before present (hereafter [ka]), holds important implications for the projected global warming, as this geological interval is believed to have been significantly warmer-than-preindustrial and marked by a sea level that was 6 to 9 m above the present levels due to smaller ice sheets (Dutton et al., 2015; Hoffman et al., 2017). While the greenhouse gases concentrations during MIS 5e remained at the preindustrial levels (Lüthi et al., 2008), the main trigger of the warm Eemian climate is thought to be enhanced boreal summer insolation. Unlike the current Holocene interglacial, which has started about 11.7 ka, MIS 5e is a concluded interglacial period, followed by a glacial epoch (Fig. 1.1). It is anticipated, therefore, that the last interglacial can also shed more light on any natural climate responses accompanying the

terminal phase of an interglacial (Govin et al., 2015). The latter is particularly relevant for understanding the climate sensitivity of the current late Holocene time interval, on millennial time scales characterized by orbitally-driven cooling (Kaufman et al., 2009).

Although significant progress in understanding the last interglacial climate evolution has been achieved in the last decades, the existing paleoclimatic reconstructions spanning this crucial interval are still rather sparse to fully assess and disentangle external forcings and internal climatic feedbacks at play. Moreover, earlier studies often provide only averaged characteristics over parts or over the entire interval of MIS 5e (e.g., Turney and Jones, 2010), presenting a very generalized and unrealistic picture of this critical time interval. To facilitate the current understanding of the last interglacial climate progression, a better spatio-temporal representation is urgently needed. New paleoclimate information, in turn, not only enhances theoretical understanding of the climate system, it is also crucial for testing the viability of numerical models. Therefore, climate data of the past help to assess whether or not the current climate change is exceptional and, moreover, may be further utilized to forecast what is to be expected in the future (Masson-Delmotte et al., 2013; Bakker et al., 2014).

1.2 Ocean circulation in the North Atlantic

In the upper limb of the Atlantic Meridional Overturning (AMOC), tropical heat and salt is transferred poleward via the Gulf Stream, contributing to the moderate climate of northern Europe. Cooling and sinking of surface waters occurs in the subarctic Nordic and Labrador seas and is essential for the deep-water southward flow, a crucial component of the AMOC that ventilates the deep ocean and links both hemispheres through the deep cross-equatorial flow (Kuhlbrodt et al., 2007). In contrast to earlier views (e.g., Stommel, 1961), it is suggested now that cooling and sinking of deep waters in the subartic North Atlantic does not drive the ocean overturning, but rather control the strength and shape of the AMOC (Kuhlbrodt et al., 2007; Gelderloos et al., 2012).

The Gulf Stream, a western boundary current of the wind-driven subtropical gyre (STG), is the main conduit of tropical heat to the high northern latitudes (Fig. 1.2). The Gulf Stream originates from the Florida Current after it leaves the Gulf of Mexico through the Straits of Florida and merges with the Antilles Current to the north of the Bahama Banks. The Florida Current and the Antilles Current are fed by the North Equatorial Current, which is pushed westwards by the northeastern trade winds and constitutes the southern limb of the STG. The Florida Current is also fed by the currents from the South Atlantic and is thought to compensate for the southward-directed cross-equatorial flow within the deep branch of the AMOC (Schmitz and Richardson, 1991; Johns et al., 2002).

In the mid-latitude North Atlantic, one branch of the Gulf Stream recirculates southwards, defining the anticyclonic rotation of surface water masses within the STG, while another branch, the North Atlantic Current (NAC), continues northward to the polar regions. The relatively warm and saline NAC splits after it crosses the mid-oceanic ridge between 50-

52°N (Hansen and Østerhus, 2000). Eastern branches pass the Iceland-Scotland Ridge and flow further north into the Nordic Seas (i.e., the Norwegian Sea, the Iceland Sea and the Greenland Sea), as the Norwegian Atlantic Current (NwAC) and the Faroe Current (Hopkins, 1991). A western-flowing branch of the NAC, the Irminger Current, partly circulates around Iceland and enters the Iceland Sea through the Denmark Strait, and partly continues in the subpolar gyre (SPG) towards the Labrador Sea.

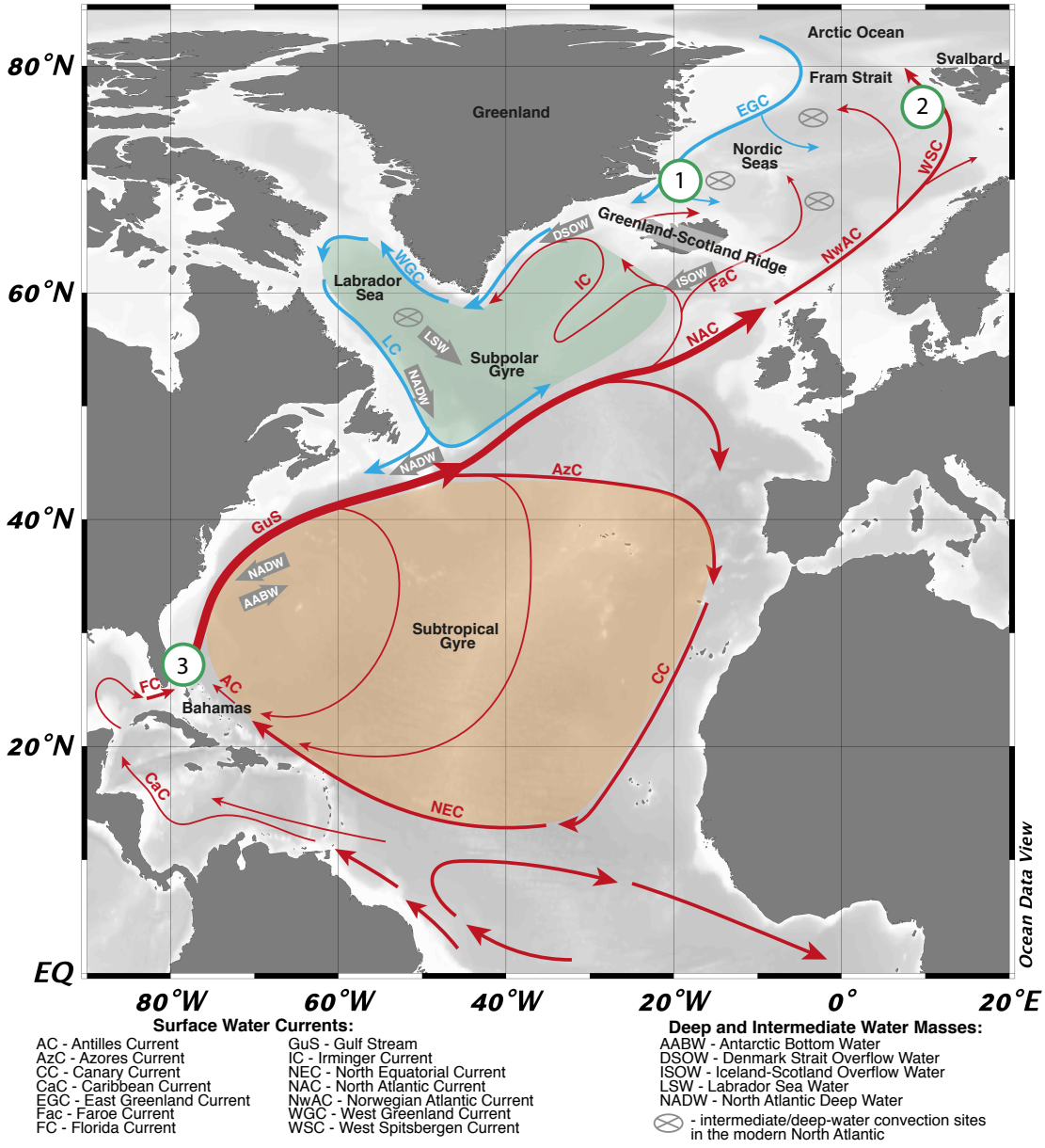

Figure 1.2: Simplified modern hydrography in the North Atlantic and locations of the core sites, investigated in this thesis (green circles). Red/blue arrows indicate major warm/cold surface currents; grey arrows denote the main deep and intermediate water masses (modified after Schott et al., 2004; Rudels et al., 2012; Voelker et al., 2015). The map is created using Ocean Data View (Schlitzer, 2016).

Essentially, warm and saline Atlantic Water (AW) is delivered into the Nordic Seas via the NwAC, which flows towards the Fram Strait as the main component of the West

Spitsbergen Current (WSC) (Mauritzen et al., 2012). Together with the other important inflow through the Barents Sea, the WSC supplies the Arctic Ocean with these Atlantic-sourced waters, which have profound effect on oceanic and sea-ice conditions in the region (Polyakov et al., 2017). Although extent of the sea-ice cover in the Fram Strait and in the Nordic Seas is strongly related to the properties of the Atlantic inflows as well as to atmospheric forcing (Dickson et al., 2000), a perennially ice-free area characterizes the eastern Nordic Seas and the eastern Fram Strait influenced by the WSC.

In the western Nordic Seas, southward-directed outflow of cold and fresh Polar Water from the Arctic Ocean is confined to the East Greenland Current (EGC). Today, the EGC is a well-stratified surface current, transporting not only fresh polar waters and sea ice at the surface, but also entraining water masses of Atlantic origin at intermediate depths, including modified (cooled) AW from the Arctic Ocean, and distinctively warmer AW, which recirculates in the Fram Strait (Rudels et al., 2002, 2012). During southward propagation the EGC adds to the warm subsurface flow from the IC along the southeastern coast of Greenland. As it loops around the southern tip of Greenland, it turns into the West Greenland Current (WGC) and circulates further to the Labrador Sea. The WGC together with the Labrador Current, transporting ice-loaded waters from the Canadian Arctic to the mid-latitudes, constitute the northwestern extension of the SPG (Myers et al., 2007).

Cooling and sinking of AW in the Nordic and Labrador seas constitutes the deep, southward-flowing branch of the AMOC, the North Atlantic Deep Water (NADW). Deep-water overflows from the Nordic Seas have to pass the Greenland-Scotland Ridge and, therefore, are constrained by the sill depths of the two main passages: the Denmark Strait with a sill depth of ~630 m and the Faroe Bank Channel with a sill depth of ~840 m (Jungclaus et al., 2008). These overflow waters, referred to as Denmark Strait Overflow Waters and Iceland-Scotland Overflow Waters, contribute to the lower part of the NADW (~2500-4000 m) and spread around the Labrador Sea and further along the eastern continental margin of North America in a Western Boundary Undercurrent (Stahr and Sanford, 1999). These water masses are overlaid by intermediate-depth (~1500-2500 m) Labrador Sea Water, which is renewed through convective mixing during favorable winter conditions (Yashayaev and Loder, 2008). In the western subtropical North Atlantic, admixture of deep water masses from the southern regions, i.e., the Antarctic Bottom Water, occurs within the deepest components of the NADW, i.e., below ~4000 m (Stahr and Sanford, 1999).

1.3 Atmospheric circulation in the low-latitude North Atlantic

The Atlantic Intertropical Convergence Zone (ITCZ), extending from the South America to the west coast of Africa, is a dynamic low-pressure high-precipitation zone between the southeast and northeast trade winds (Fig. 1.3). The ITCZ and its associated rainfall belt migrates seasonally between 10°N and 5°S, responding to changes in cross-equatorial sea surface temperature (SST) gradient in the tropical Atlantic (Chiang et al., 2002).

Latitudinal migrations of the ITCZ, in turn, strongly affect wind patterns, hydrology and other climatic characteristics on the adjacent land and ocean. In particular, in the subtropical North Atlantic seasonal shifts in the ITCZ are closely related to the northward expansion of the Atlantic Warm Pool of water warmer than 28.5 °C (Fig. 1.3). Thus, during boreal winter, when the ITCZ is its southern position, the Atlantic Pool Water stays largely restricted to the tropics, while the subtropical North Atlantic is dominated by relatively cool, stormy weather with intensified northern winds. During boreal summer season, when the ITCZ is at its northern position, northward expansion of the Atlantic Warm Pool is coupled with increased precipitation and dominance of less intensified trade winds from east and southeast (Wang and Lee, 2007; Stramma and Schott, 1999; World Ocean Atlas, 2013).

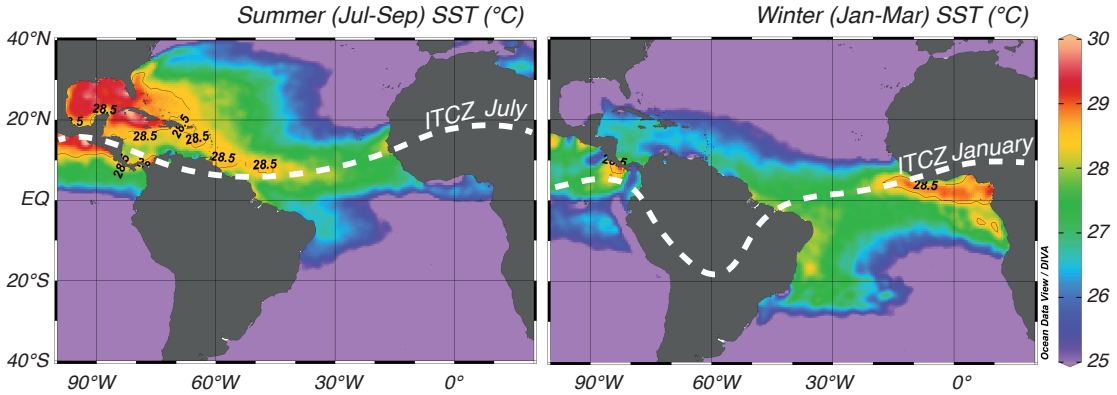

Figure 1.3: Summer and winter sea surface temperatures (SST) in the low-latutide North Atlantic (World Ocean Atlas, 2013) and positions of the Intertropical Convergence Zone (ITCZ) in July and January. The map is created using Ocean Data View (Schlitzer, 2016).

1.4 Background on planktic foraminifera

Planktic foraminiferal assemblages provide valuable information on ancient environments due to their high sensitivity to changing temperature, salinity and chemical composition of ambient seawater, justifying their applicability to reconstruct positions of oceanographic fronts, intensities of marine currents as well as for stratigraphic purposes. Noting that comprehensive reviews of modern planktic foraminifera taxonomy, distribution, evolution, ecology and biology are provided elsewhere (e.g., Schiebel and Hemleben, 2017), in this chapter we briefly address the major issues relevant for interpretation of the produced foraminiferal-based data (for methods see Chapter 2). The investigations were made within two principally different biogeographical settings: the subpolar (Nordic Seas) and the subtropical (Bahama Banks). All distinguished planktic foraminiferal species are listed author-named in Table 1.1.

1.4.1 Nordic Seas

In the Nordic Seas, the planktic foraminiferal assemblage is generally comprised of one polar and six temperate-subpolar species. Polar species *Neogloboquadrina pachyderma* dominates the assemblage, with total relative abundance up to 100 % during cold times. Characterized by very short reproductive season and being adapted to rapid food

consumption, *N. pachyderma* is regarded as one of the most competitive species, explaining its enhanced occurrence not only in polar, but also in upwelling regions (Schiebel et al., 2017). Subpolar symbiont-bearing species *Turborotalita quinqueloba* is the 2nd most frequent species in the study region. The latter two species display a narrow interval of the highest shell production between August and September with maximum abundances at sea-ice margins (Carstens and Wefer, 1992; Simstich et al., 2003). *Neogloboquadrina pachyderma* and *T. quinqueloba* predominantly occur within the upper 100 m, but tend to dwell deeper in ice-free regions (Pados and Spielhagen, 2014). Opposing views exist with regard to their depth habitats in low-salinity or ice-covered regions (Volkmann, 2000; Simstich et al., 2003; Pados and Spielhagen, 2014; Schiebel and Hemleben, 2017).

Turborotalita quinqueloba was shown to prefer normal marine salinities, and, therefore, is particularly useful for tracing AW inflows in the polar regions (e.g., Spielhagen et al., 2011). Traditionally, increased relative abundances of *T. quinqueloba* were interpreted as an indicator of the Arctic Front (Johannessen et al., 1994), which is a dynamic frontal zone between warm and saline AW and cooler and fresher Arctic Water, influenced by polar outflows. Such strict affiliation seems, however, arguable (Zhuravleva et al., 2017a), when consider a wide-spread occurrence of the latter species in the Nordic Seas throughout the early to mid-Holocene (Bauch et al., 1999; Risebrobakken et al., 2011; Van Nieuwenhove et al., 2013). Previous studies further suggest that under polar conditions tests of *T. quinqueloba* predominantly do not grow larger than 150 μm, justifying the need to use smaller size fractions for studying cold-water assemblages (Kandiano and Bauch, 2002, Husum and Hald, 2013). Other important species found in the northern environmental settings include the warm species *Globigerinita glutinata*, *Globigerinita uvula*, *Neogloboquadrina incompta* and *Globigerina bulloides*. These species are, however, rare in the investigated cores.

The rare and patchily distributed subtropical to subpolar species *Beella megastoma* is not found in the high northern latitudes today, but it spread in the Nordic Seas during glacial Terminations 2, 3 and 4, when other faunal proxies suggest polar conditions at the sea surface (Bauch, 1996). Similar oxygen isotopic trends recorded in *N. pachyderma* and *B. megastoma* suggest that the latter species lived and calcified in the Nordic Seas (Bauch et al., 2000). The occurrence of *B. megastoma* may evidence for an unusual vertical column water structure, characterized by invasions of Atlantic-sourced waters underneath a very thick deglacial halocline (Bauch, 2013; Zhuravleva et al., 2017b). However, further studies on environmental preferences of *B. megastoma* are needed to affirm the mechanisms responsible for appearance of this species in the deglacial Nordic Seas sediments.

1.4.2 Subtropical North Atlantic

The vertical water column structure appears to strongly control the low-latitude planktic foraminiferal assemblage (Andreasen and Ravel, 1997; Wolff et al., 1999). In the Bahama

region two distinctly different layers can be distinguished within the upper 500 m of the water column. The uppermost 50-100 meters are occupied by warm and comparatively fresh waters of the mixed layer, which is underlain by a homogeneous pool of cool and salty water, referred to as a thermocline layer (Schmitz and Richardson, 1991). Properties of the mixed layer vary significantly on seasonal timescales and are closely related to the latitudinal migration of the ITCZ.

Table 1.1: Foraminifera species, author-named, identified in the studied core sections

Beella digitata (Brady 1879)
Beella megastoma (Earland 1934)
Candeina nitida (d'Orbigny 1839)
Dentigloborotalia anfracta (Parker 1967)
Globigerina bulloides (d'Orbigny 1826)
Globigerina falconensis (Blow 1959)
Globigerinella calida (Parker 1962)
Globigerinella siphonifera (d'Orbigny 1839)
Globigerinita glutinata (Egger 1893)
Globigerinita uvula (Ehrenberg 1861)
Globigerinoides conglobatus (Brady)
Globigerinoides ruber, white and pink *(*d'Orbigny 1839)
Globigerinoides sacculifer (Brady 1877)
Globigerinoides trilobus (Reuss 1850)
Globorotalia crassaformis (Galloway and Wissler 1927)
Globorotalia hirsuta (d'Orbigny 1839)
Globorotalia inflata (d'Orbigny 1839)
Globorotalia menardii (d'Orbigny in Parker, Jones and Brady 1865)
Globorotalia menardii subsp. neoflexuosa (Srinivasan, Kennett and Bé, 1974)
Globorotalia scitula (Brady 1882)
Globorotalia truncatulinoides, sinistral and dextral (d'Orbigny 1839)
Globorotalia tumida (Brady 1877)
Globoturborotalita rubescens, white and pink (Hofker 1956)
Globoturborotalita tenella (Parker 1958)
Hastigerina pelagica (d'Orbigny 1839)
Neogloboquadrina dutertrei (d'Orbigny 1839)
Neogloboquadrina incompta (Cifelli 1961)
Neogloboquadrina pachyderma (Ehrenberg 1861)
Orbulina universa (d'Orbigny 1839)
Pulleniatina obliquiloculata (Parker and Jones 1865)
Sphaeroidinella dehiscens (Parker and Jones 1865)
Turborotalita humilis (Bardy 1884)
Turborotalita quinqueloba (Natland 1938)

The most frequent mixed-layer species is *Globigerinoides ruber*, exhibiting two phenotypes: white and pink. *Globigerinoides ruber* is a symbiont-bearing species, known to prefer salinities either less than 34.5 or more than 36 (Bé and Tolderlund, 1971). *Globigerinoides ruber* (pink) shows rather coherent abundance maxima in the tropics, while no such affinity is observed for the tropical to subtropical species *G. ruber* (white) (Siccha and Kučera, 2017). Although *G. ruber* (pink) is often considered a "summer species" (Schiebel and Hemleben, 2017), one study reveals a rather even test flux for both varieties of *G. ruber* during the year (Jonkers and Kučera, 2015). The latter authors further note that, as a consequence of annual temperature decrease, the *G. ruber* test flux could become shifted towards warmer months in autumn (Jonkers and Kučera, 2015). A surface-dwelling symbiont-bearing eurohaline species *Globigerinoides sacculifer*,

including a *Globigerinoides trilobus* morphotype, is abundant in the warmer Caribbean Sea and tropical Atlantic (Bé and Tolderlund, 1971; Bijma, 1990) and accounts for less than 10 % within the modern subtropical planktic foraminifera assemblage around Bahamas (Siccha and Kucera, 2017). This species is commonly used as a tracer of tropical waters and geographical shifts of the ITCZ (Poore et al., 2003; Vautravers et al., 2007; Zhuravleva and Bauch, manuscript under review for CP).

Other important constituents of the subtropical foraminiferal assemblage are thermocline-dwelling (average habitat 100-300 m) foraminifera, including *Globorotalia inflata* and right and left varieties of *Globorotalia truncatulinoides*. The life cycle of *G. truncatulinoides* includes winter reproduction in surface waters with a subsequent descend of juveniles to greater depths, where shells continue to grow all year long (Schiebel and Hemleben, 2017). Due to its reproduction cycle with changing habitats, requiring reduced water column stratification to introduce juveniles from shallow to deep water and backward, *G. truncatulinoides* abundance is often used a proxy for vertical water column structure (Lohmann and Schweizer, 1990; Mulitza et al., 1997; Zhuravleva and Bauch, manuscript under review for CP). Transitional to subpolar species *G. inflata* is thought to prefer little seasonal variations in salinity (Hilbrecht, 1996). The latter species together with *Globigerina falconensis* were considered as cold end-member species in the Bahama region (Chabaud, 2016). Tropical to subtropical surface-dwelling species *Globorotalia menardii* together with a subspecies *G. menardii* flexuosa, has proven to be an important stratigraphic marker for delineating Ericson zones (Ericson and Wollin, 1968; Bahr et al., 2011).

1.5 State of the art

1.5.1 Ocean-atmospheric teleconnections between low and high latitudes

Modeling and proxy data suggest that tropical variability of oceanic temperature and salinity directly affects the AMOC functioning and has a profound impact on the global climate on glacial-interglacial timescales, through control of moisture content in the atmosphere (Schmidt et al., 2006a, b; Carlson et al., 2008a; Guihou et al., 2010). Conversely, a high-latitude forcing of the (sub)tropical climate variability is also revealed. In particular, perturbations in the subarctic deep-water formation sites can lead to a reduced convection rate of the AMOC, decreasing the export of tropical heat to the north, thereby warming the (sub)tropical western Atlantic (Rühlemann et al., 1999; Carlson et al., 2008a; Bahr et al., 2013). In addition, intervals of weakened NADW formation are coupled with southward displacements of the ITCZ and its associated rainfall belt (Peterson and Haug, 2006). Accordingly, enhanced sea surface salinities are found in the western (sub)tropical North Atlantic at times of AMOC reductions and southward displacements of the ITCZ (Schmidt et al., 2006a; Carlson et al., 2008a; Bahr et al., 2013). Model simulations and proxy data further suggest that sea-ice extent in the polar North Atlantic can also affect the position of the ITCZ through feedbacks on the thermohaline circulation (e.g., Chiang et al., 2003; Gibson and Peterson, 2014). Climatic

coupling between the high- and low-latitude North Atlantic is well-studied for the last glaciation and Termination I (e.g., Peterson et al., 2000), but has never been investigated for the last interglacial cycle with sufficient resolution.

The last interglacial climatic connectivity between the subpolar and subtropical North Atlantic is discussed in Chapter 5.

1.5.2 The last interglacial cycle: time frames

Dating of geological records spanning the last interglacial cycle appears a critical issue (for overview see Govin et al., 2015), given that this time interval lies beyond the limits of radiocarbon dating. In contrast to earlier findings (Winograd et al., 1988), new U-Th datings from the iconic Devils Hole (Nevada) reconcile the last glacial/interglacial transition with the orbital forcing, showing that the onset of the penultimate deglaciation (Termination 2) follows boreal summer insolation (Moseley et al., 2016). These results support the general accuracy of the astronomically tuned SPECMAP chronology, suggesting an age of 131-130 ka for the mid-point of the MIS 6/5e transition (Martinson et al., 1987). Similar results are provided by the new benthic stack LS16, aligned to radiometrically-dated speleothems (Lisiecki and Stern, 2016). Representing a transition between glacial and full interglacial values, the penultimate (Saalian) deglaciation is associated with a range of climatic changes, related to ice sheets disintegration (Denton et al., 2010). One of the most prominent features of Termination 2 is the massive iceberg discharge event, termed Heinrich Event 11 (~135-129 ka).

Although constrained differently in various studies (e.g., Stein et al., 2017), there is general consensus that, based on age estimates of the sea level highstand, the last interglacial lasted between 129 and 116 ka (Masson-Delmotte et al., 2013; Capron et al., 2017; Hoffman et al., 2017). This age is in agreement with the so called last interglacial "plateau" of low benthic stable oxygen isotopes values and coral-based chronology (Stirling et al., 1998; Shackleton et al., 2003). It should be, however, noted that controversy still exists regarding the initiation and duration of the sea level highstand as well as about any sea level variability within that time period (Hearty et al., 2007; Kopp et al., 2009; Grant et al., 2012; Masson-Delmotte et al., 2013). Also, recognition of the last interglacial onset, essential for construction of accurate age model and robust core-to-core correlations, appears challenging for high latitude sediment records, because of deglacial overprints during early MIS 5e (Bauch et al., 1996; Van Nieuvenhove et al., 2011; Govin et al., 2012; Capron et al., 2014). At the end of MIS 5e, the last interglacial "plateau" terminates and a changeover towards colder conditions after ~116.7 ka signifies the onset of the Weichselian glacial inception, i.e., the last interglacial/glacial (MIS 5d) transition (NGRIP community members, 2004).

The age model construction for MIS 5e is thoroughly discussed in Chapter 3. Insights into sea level history of the last interglacial are given in Chapter 5.

1.5.3 Peak warmth of the last interglacial

In contrast to earlier views (e.g., Turney and Jones, 2010), it is established now that the warmest phase of MIS 5e was not globally synchronous (Capron et al., 2014). Thus, the peak temperatures in the Southern Ocean and over Antarctica were reached several millennia earlier than in the northern high latitudes (Masson-Delmotte et al., 2011). In the low-latitude North Atlantic, an early peak warming, between 129 and 125 ka, is revealed by a recent compilation of MIS 5e SST records (Hoffman et al., 2017). The highest temperatures in the mid-latitude North Atlantic, over Europe and in the Labrador Sea established rapidly at the end of Heinrich Event 11 (~129 ka), phasing maximum boreal summer insolation values (Cortijo et al., 1999, Oppo et al., 2006, Bauch and Knadiano, 2007; Bauch et al., 2012, Sanchez-Goñi et al., 2012; Irvali et al., 2012). In contrast, in the Nordic Seas a rather late and weak climatic optimum is found (Bauch et al., 1999, 2011; Van Nieuwenhove et al., 2011; Govin et al., 2012). A reason for this is suggested to be enormous meltwater discharge from the Saalian terrestrial ice that could have hindered propagation of warm surface waters polewards during the glacial termination and, notably, early MIS 5e (Bauch, 2013; Thiebodeau et al., 2017). The recognition of the "transitional" phase during early MIS 5e is not new, but only several authors have pointed out its importance for understanding the last interglacial climatic evolution beyond the subpolar regions (e.g., Schwab et al., 2013; Kandiano et al., 2014).

For the Arctic region, it appears difficult to robustly constrain the MIS 5e peak, due to low-resolution of available sedimentary records. Nevertheless, the last interglacial for this region is often described as an interval characterized by strongly reduced sea-ice cover with summer temperatures 5 °C warmer than present over circum-Arctic land (Brigham-Grette and CAPE-Last Interglacial Project Members, 2006; Nørgaard-Pedersen et al., 2007a, 2007b; Adler et al., 2009; Polyak et al., 2010). Yet, a recent biomarker study reveals that sea ice was present in the central Arctic Ocean throughout the year (Stein et al., 2017). Importance of the AW heat flux for sea surface properties in the polar North is well documented (Spielhagen et al., 2011; Polyakov et al., 2017). However, opposing views on the strength and extent of the AW inflows into the polar region exist for the last interglacial. Thus, while some authors suggest an enhanced poleward advection of the AW when compared to the Holocene (Funder et al., 2002; Grøsfjeld et al., 2006), others determine a reduced presence of AW at the sea surface in the northern and eastern Nordic Seas (Bauch et al., 1999; Van Nieuvenhove et al., 2008).

Causes of the late and weak interglacial optimum in the Nordic Seas are provided in Chapters 3 and 4. Impacts of the "transitional" climatic regime of early MIS 5e on climates beyond the subpolar North Atlantic are addressed in Chapter 5. The role of the Atlantic-derived inflows for polar sea surface evolution during MIS 5e and Holocene is examined in Chapter 4.

1.5.4 Instability of the last interglacial climate

Recent studies from the North Atlantic demonstrate that the climate of the last interglacial was rather unstable, involving one or several cooling events (Maslin et al., 1998; Fronval and Jansen, 1997; Lehman et al., 2002; Bauch et al., 2011, 2012). These climatic shifts were shown to be strongly related to changes in deep-water circulation (Adkins et al., 1997). It is well established that deep overflows from the Nordic Seas, constituting nowadays the lower NADW, strengthened (deepened) only during the second phase of MIS 5e (Hodell et al., 2009; Barker et al., 2015), after the meltwater input into the region ceased (Bauch and Erlenkeuser, 2008; Van Nieuwenhove et al., 2011). It is further suggested that suppressed AMOC mode during early MIS 5e resulted in the asymmetrical temperature signal across the Atlantic Ocean, perhaps facilitated through the interhemispheric seesaw mechanism, which is thought to have reduced oceanic heat transport towards the northern North Atlantic (Hoffman et al., 2017).

Although the full resumption of the AMOC from a shallow or weak mode during the deglacial termination occurred only by ~124 ka, recent studies show that the AMOC abruptly recovered at ~ 129 ka, presumably due to a deepened winter convection in the Northwestern Atlantic (Galaasen et al., 2014; Deaney et al., 2017). The early MIS 5e deepening of the NADW and strengthening of the AMOC was interrupted around 127-126 ka (Galaasen et al., 2014; Deaney et al., 2017) likely due to a brief increase in freshwater input into the subpolar North Atlantic region that was accompanied by a sea surface cooling (Irvali et al., 2012; Zhuravleva et al., 2017b). Several studies refer to this millennial-scale climatic reversal as to a Younger Dryas-like event (Bauch et al., 2012; Jiménez-Amat and Zahn, 2015).

Causes and consequences of the last interglacial climate instability are discussed in Chapters 3, 4, and 5.

1.6 Rationale, objectives and contributions to the chapters

A better knowledge of warmer-than-today interglacial climates can help to draw conclusions about future climate development and justifies the importance of paleoclimatic reconstructions from MIS 5e. To acquire a realistic picture of the last interglacial climate progression, a better spatio-temporal representation is urgently needed. Accordingly, the overall goal of this study is to investigate climate development of the entire last warm cycle (MIS 6/5e/5d) by reconstructing sea surface properties (i.e., trends in temperatures, salinities) at several key sites in the North Atlantic. More specifically, the study aims at understanding ocean and atmospheric circulation patterns as well as climatic mechanisms (insolation versus oceanic forcing), including high-low latitude teleconnections. The new time-series, spanning the entire last interglacial cycle, supply dependable data for improving climate models.

Two sediment cores from the Nordic Seas and one sediment core from the Bahama region were investigated to achieve the objectives of the thesis (for Material and methods see

Chapter 2). Results of the study are presented in **Chapters 3-5**, consisting of two manuscripts that have been published and one being submitted to a scientific journal. Rationale for selected cores, specific research questions and my contributions to each chapter are stated below.

Chapter 3 has been published in the journal *Quaternary Science Reviews*, authored by Anastasia Zhuravleva, Henning A. Bauch and Nicolas Van Nieuwenhove under the title: **Last Interglacial (MIS5e) hydrographic shifts linked to meltwater discharges from the East Greenland margin** (doi:10.1016/j.quascirev.2017.03.026). In the context of very limited Eemian data from Greenland, this study aims at providing first high-resolution marine records documenting GIS variability during the penultimate glacial/interglacial transition and MIS 5e. In addition, the poorly investigated East Greenland margin is influenced by the EGC, which plays a key role in transporting low-density Polar Water and sea ice to the convectional sites of the subpolar North Atlantic. In this venue, the main research questions are:

- What information could be deduced from marine sediments in terms of GIS variability during Eemian times?
- How is GIS melt coupled with the documented AMOC shifts during the last interglacial?
- Are there any changes in the properties of the EGC during the last interglacial cycle and what are the consequences for deep-water formation in the Nordic and Labrador seas?

My contributions to this chapter comprised core sampling and preparation of samples for carbonate microfossil analysis (e.g., sieving procedures), counting planktic foraminifera in the size fractions >150 μm and 100-150 μm, counting lithic grains, collecting of foraminiferal tests for stable isotope measurements, data interpretation and writing of the manuscript. My co-authors H. A. Bauch and N. Van Nieuwenhove contributed with valuable discussions and helped to improve the text of the manuscript. H. A. Bauch in addition provided unpublished stable isotope data for cores PS1247 and M23485 (MIS 5e).

Chapter 4 has been published in the journal *Global and Planetary Change,* authored by Anastasia Zhuravleva, Henning A. Bauch and Robert F. Spielhagen under the title: **The Atlantic Water heat transfer through the Arctic Gateway (Fram Strait) during the Last Interglacial** (doi:10.1016/j.gloplacha.2017.09.00). In this chapter, the existing views on the strength of the poleward-directed AW inflows during MIS 5e are reevaluated through the use of high-resolution records from the only deep Arctic Gateway, the Fram Strait. Briefly, the chapter focuses on the following questions:

- Are there any changes in strength and properties of the poleward-directed AW inflows across the last interglacial and what are the consequences for the polar regions?

- What are the mechanisms controlling poleward-directed AW heat transfer during MIS 5e and how do they differ from the Holocene situation?
- What information about fluctuations of the Svalbard-Barents Sea Ice Sheet could be obtained from our sediment data?

My contributions to this chapter include sampling of the core at the IODP Bremen Core Repository, preparing the samples for microfossil analysis, performing countings of planktic foraminifera in the size fractions >150 μm and 100-150 μm, countings of benthic foraminifera (*Cibicidoides wuellerstorfi* only) in the size fraction >250 μm, countings of fragmented tests, ice-rafted debris grains and coal fragments, picking of foraminiferal tests for stable isotope measurements, interpreting the data and writing the manuscript. My co-authors H. A. Bauch and R. F. Spielhagen contributed to the discussions and improved the text of the manuscript. H. A. Bauch in addition provided unpublished census faunal data from core M23071 (Holocene).

Chapter 5 is currently under review in the journal *Climate of the Past,* authored by Anastasia Zhuravleva and Henning A. Bauch under the title: **The last interglacial (MIS 5e) cycle at Little Bahama Bank: A history of climate and sea level changes** (doi:10.5194/cp-2018-38). This chapter focuses on the sensitivity of the subtropical North Atlantic region to past climatic and sea level changes. Shallow-water sediments from the slope of the Little Bahama Bank are ideally suitable to reconstruct past ITCZ movements, given that today the area lies at the northern edge of the influence of the Atlantic Warm Pool, expansion of which is closely related to the seasonal shifts of the ITCZ. Thus, the chapter seeks to address the following questions:

- What are the mechanisms (insolation versus oceanic and/or atmospheric forcing) regulating subtropical climate across the last interglacial?
- Is there a climatic coupling between the AMOC strength and ITCZ during the last interglacial cycle (i.e., subpolar forcing on the low-latitude climate)?
- Can the sea level history of the last interglacial be refined by using a multiproxy dataset from shallow-water periplatform sediments (geochemical, lithological and stratigraphical data)?

I contributed to this manuscript by counting planktic foraminifera in the size fractions 150-250 μm and >250 μm, performing X-ray fluorescence analysis, interpreting the data and writing the manuscript. My co-author H. A. Bauch contributed with the discussions and suggestions to improve the manuscript. Picking of foraminiferal tests for stable isotope measurements was made by a student assistant instructed and supervised by me.

Chapter 2: Material and methods

Three major sediment cores from the critical sites in the North Atlantic have been selected in this thesis to produce a suite of new multiproxy-proxy records, spanning the last interglacial cycle, i.e., MIS 6/5e/5d (Fig. 2.1). Some unpublished data from several cores in the Nordic Seas have also been used in Chapters 3 and 4, but these cores are not discussed in this chapter. Core M23351 (GIK23351-1) was recovered in 1988 from the lower slope of the eastern Greenland continental margin during a Meteor cruise (campaign M7/5) by a Kasten corer (Voelker, 1999). The Site 986 (SVAL-1) was drilled at the lower slope of the western Svalbard continental margin during the Ocean Drilling Project (ODP) Leg 162 in 1995 (Jansen et al., 1996). Core MD99-2202 was taken from the northern slope of the Little Bahama Bank in 1999 by the Calypso Giant Piston Coring System onboard a research vessel Marion Dufresne (Lantzsch et al., 2007). The overview of the sediment cores and produced proxy-records are shown in Table 2.1.

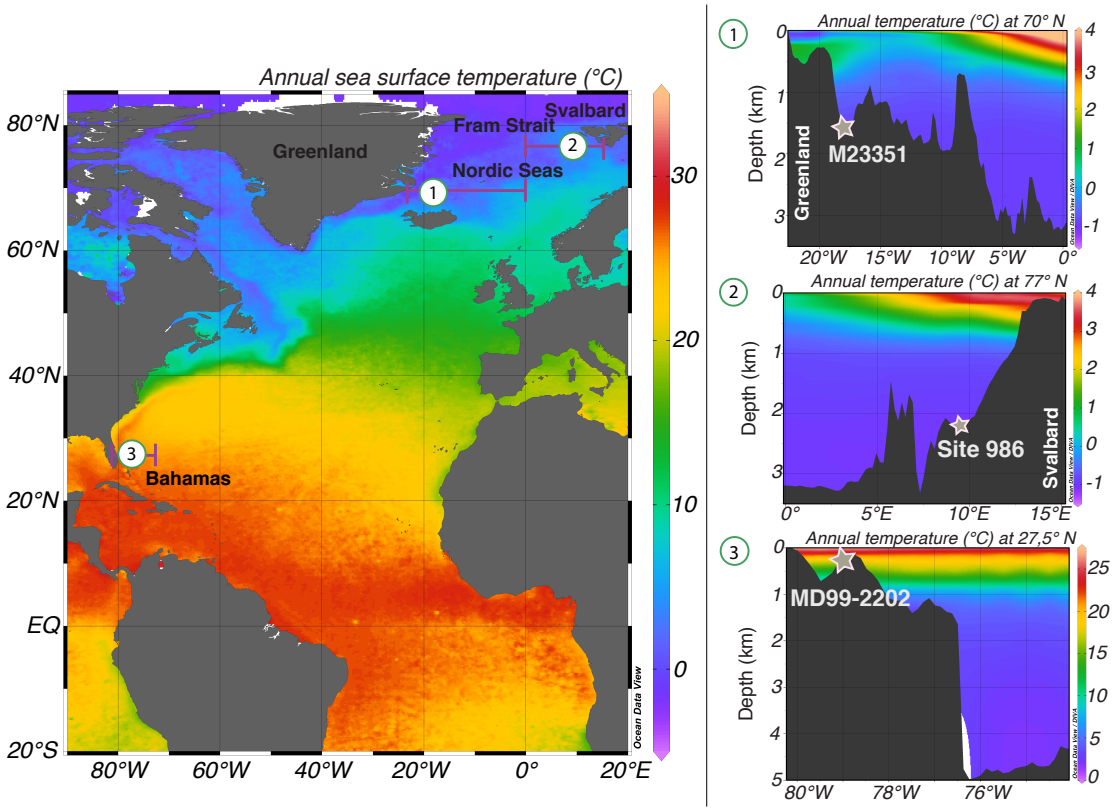

Figure 2.1: Locations of the major investigated cores, used in this thesis. Violet lines indicate the transects along c. 70°N, 77°N, 27.5°N shown, respectively, in the insets 1, 2 and 3 and discussed in Chapters 3, 4, 5. Temperature and bathymetry profiles are based on data from the World Ocean Atlas 2013 (Levitus et al., 2013) and created by using Ocean Data View (Schlitzer, 2016).

2.1 Sample preparation

Core M23351 was sampled as 1 cm thick slabs every 1 cm; sediments from Site 986 were similarly sampled at 1 cm resolution, besides the (de)glacial parts, which were sampled every 3 cm. The samples were then freeze-dried, weighed, wet-sieved using a 63 µm mesh

size, and dry-sieved into 63-100 µm, 100-150 µm and >150 µm mesh sizes. Sieved samples from core MD99-2202 were already available at GEOMAR storage facilities from previous studies (Lantzsch et al., 2007).

Table 2.1: Investigated sediment cores and obtained proxy data.

Core	Latitude	Longitude	Water Depth (m)	Study area	Section (cm)	Obtained proxy*	Chapter
M23351	70°21´N	18°13´W	1673	East Greenland margin	460-570	SI (Be, Pl), foram assembl., IRD	3
Site 986	77°20´N	09°04´E	2052	Fram Strait	1350-1920	SI (Be, Pl), foram. assembl., fragmentation, IRD (+clastic), coal, CW	4
MD99-2202	27°35´N	78°58´W	460	Bahama Bank	150-509	SI (Be, Pl), foram assembl., XRF	5

* SI – stable isotope data, Be – benthic, Pl – planktic foraminifera, foram. assembl. – planktic foraminiferal assemblage countings, IRD – ice-rafted debris counts, clastic – clastic ice-rafted debris counts, coal – coal fragments, CW – number of *C. wuellerstorfi* per gram sediment, XRF – X-ray fluorescence analysis

2.2 Stable isotopes

Continuous stable oxygen ($\delta^{18}O$) and stable carbon ($\delta^{13}C$) isotope records represent an essential tool for paleoclimatic reconstructions. Stable isotope analyses on planktic foraminifera were performed on ~25-30 tests of left-coiled *Neogloboquadrina pachyderma* and on ~10-30 tests of right-coiling (dextral) *Globorotalia truncatulinoides* and *Globorotalia inflata*; crushed tests of similar morphotype and size (150-250 µm) were used. Also, about ~3-10 tests of epibenthic species *Cibicidoides wuellerstorfi* (Schwager) and ~5-20 specimens of shallow-endobenthic species *Oridorsalis umbonatus* (Reuss) were used to produce benthic foraminiferal isotope data. To splice records and to account for species-dependent departures from isotopic equilibrium, $\delta^{18}O$ values were corrected by +0.64 ‰ and +0.36 ‰ for *C. wuellerstorfi* and *O. umbonatus*, respectively (Duplessy et al., 1988). Analyses were performed using a Finnigan MAT 253 mass spectrometer at the GEOMAR Stable Isotope Laboratory. Calibration to the Vienna Pee Dee Belemnite (V-PDB) reference scale was made via the NBS-19 and an internal laboratory standard. The analytical precision of in-house standards was reported to be better than 0.08 ‰ for $\delta^{18}O$ and 0.04 ‰ for $\delta^{13}C$.

2.3 Foraminiferal census counts

Planktic foraminiferal assemblages were counted following a conventional procedure. After samples were reduced by means of micro-splitter, at least 300 foraminiferal tests were counted on the counting tray with the help of binocular microscope. In accordance

with the latest taxonomic status (Darling et al., 2006; Kučera, 2007), the left-coiling (sinistral) specimens of *N. pachyderma* are referred to as *N. pachyderma*, whereas right-coiling (dextral) specimens are referred to as *N. incompta*, in the case that the sample contained at least 3 % dextral specimens. If a sample contains less than 3 % right-coiling specimens, they can be considered as genotypically identical to left-coiling specimens (Bauch et al., 2003) and calculated together with *N. pachyderma*. According to a standard practice, *G. menardii* and *G. tumida* as well as *G. sacculifer* and *G. trilobus* were grouped together, and referred to as *G. menardii* and *G. sacculifer*, respectively (Poore et al., 2003; Kandiano et al., 2012; Chabaud, 2016).

For the subpolar cores M23351 and Site 986 planktic foraminiferal assemblages were obtained from representative splits in the size fractions >150 μm and 100-150 μm. The census data from the two size fractions were subsequently added up and recalculated into planktic foraminiferal assemblage composition for the fraction >100 μm. For the subtropical core MD99-2202 relative abundances of planktic foraminifera were counted in the fractions 150-250 μm and >250 μm and subsequently recalculated in faunal census data in the fraction >150 μm. To achieve a high statistical robustness, counts on rare species (e.g., *B. megastoma* in M23351) were performed in a second run, and separately from the method described above. For this procedure the number of splits was reduced, to count as much rare species as possible.

2.4 Foraminiferal fragmentation index

In the high latitudes, dissolution and preservation of fossil planktic foraminifera was shown to be an important proxy for studying paleoceanographic shifts (Zamelczyk et al., 2013). To evaluate preservation changes of marine calcium carbonate at Site 986, we established a foraminiferal tests fragmentation index, by calculating the percentage of fragmented planktic foraminiferal tests relative to the total number of planktic foraminifera and fragments in the sample. The degree of fragmentation (%) was determined in the fraction 100-150 μm using the following equation (after Pfuhl and Shackleton, 2004):

$$\text{Fragmentation (\%)} = \#\text{Fragments/g}/(\#\text{Fragments/g}/3+\#\text{Test/g})$$

2.5 Ice-rafted debris and coal fragments

Ice-rafted debris (IRD), usually defined as the coarse sediment fraction (>63 μm or coarser fractions), is commonly used as an indicator of deposition from ice, which can include both iceberg and sea-ice rafting (Lisitzin, 2012). IRD were counted in the size fraction >150 μm in the subpolar sediment cores, following the procedure described in 2.3. The number of counted IRD grains was projected for the entire sample, by multiplying the result by a corresponding split factor, and the final result is reported as IRD grains per gram of dry bulk sediment. Additionally, at Site 986 clastic sedimentary rocks, often represented as darkish-grey siltstones, were distinguished from the other IRD. Previous studies have pointed to the Barents Sea shelf area as a principal source

area of such organic-rich clastic grains (e.g., Elverhøi et al., 1995; Bischof et al., 1997; Hebbeln and Wefer, 1997; Bauch et al., 2001). Marked increases in clastic IRD inputs could thus be related to fluctuations of the Svalbard-Barents Sea Ice Sheet.

Proportions of coal fragments relative to the number of IRD grains in the size fraction >250 µm were counted for Termination 2 at Site 986. Occurrences of coal fragments can indicate the source area of icebergs.

2.6 X-ray fluorescence

X-ray fluorescence (XRF) spectroscopy is widely used for rapid non-destructive and nearly continuous assessment of elemental composition in unprocessed marine sediments. Bulk-sediment elemental data are essential in sedimentological and paleoclimatic studies, for stratigraphic correlations and sea level reconstructions (e.g., Haug et al., 2001; Tjallingii et al., 2008; Chabaud et al., 2016). The XRF core scanner measures intensities of major elements in total counts (cnts) or counts per second (cps) directly at the surface of split sediment cores, making the process of samples preparation very straightforward (Jansen et al., 1998). However, individual element intensities derived from XRF core scanning can be influenced by physical properties of sediment cores and depend on hardware settings (e.g., Röhl and Abrams, 2000; Tjallingi et al., 2007; Chabaud et al., 2016).

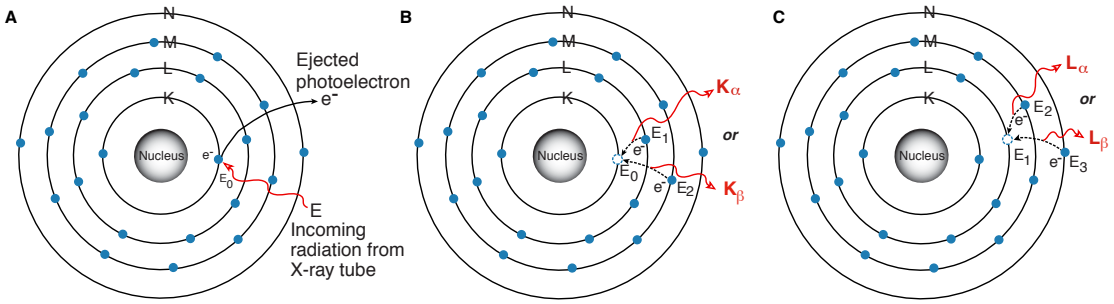

Figure 2.2: The X-ray fluorescence process in a Titanium atom (Ti, atomic number 22). (**A**) An electron in the K-shell is ejected by the incoming radiation from the X-ray tube, creating unstable conditions of an atom and ejecting a K-shell electron. (**B**) An electron from the outer (L or M) shells fills the vacancy in the K-shell, emitting the element characteristic radiation (K_α by a L-shell electron and K_β by a M-shell electron). (**C**) An electron from a M-shell or a N-shell fills the vacancy in the L-shell, emitting, respectively, the element characteristic L_α or L_β radiation (modified after: http://www.amptek.com/pdf/xrf.pdf).

The XRF spectroscopy uses a radioactive source that generates the primary X-rays, which strike a sample, ejecting electrons from an inner shell (K-shell) of an atom (Fig. 2.2). Thus, an unstable condition of an atom is created. Subsequently, the vacancies of an inner electron shell are filled by an electron from the outer (L or M) shells. During this process, the outer shell electron emits the characteristic surplus energy as X-ray fluorescence photons. This X-ray energy is specific for every atom, it is characterized by a particular frequency and wavelength and corresponds to the energy difference between the two shells of the electron (Jansen et al., 1998). According to the Moseley´s Law, the emitted fluorescence radiation of an element increases with the square atomic number (Moseley,

1914). Thus, lighter elements emit lower fluorescence energies, which are more susceptible for adsorption within the sample material. In addition, elements with lower atomic numbers respond to X-ray ionization at smaller sample depths (the critical depth for Al and Si - a few μm, for Ca - several tens of μm, for Fe - a few hundreds of μm; Jenkins and De Vries, 1970; Jansen et al., 1998). Due to the small response depth of lighter elements and, therefore, a smaller analyzed sample volume, assessment of light elements intensities is particularly sensitive to sample heterogeneity and water content (Tjallingii, 2006; Tjallingi et al., 2007; Hennekam and de Lange, 2012).

X-ray analyses was performed using Aavatech XRF Core Scanner at Christian-Albrecht University of Kiel (for technical details see Richter et al., 2006). To obtain intensities of elements with lower atomic weight (e.g., Ca, Cl), the XRF scanning measurements were carried out with a X-ray tube voltage of 10 kv, a tube current of 750 μA and a counting time of 10 seconds. To analyze heavy elements (e.g., Fe, Sr), the X-ray generator settings of 30 kv and 2000 μA and the counting time of 20 seconds were used. A palladium thick filter was placed in the X-ray tube to reduce the high background radiation generated by the higher source energies. The XRF Core Scanner data were collected directly from the split core sediment surface, that had been flattened and covered with a 4 μm-thick ULTRALENE SPEXCerti Prep film to prevent contamination of the measurement unit and desiccation of the sediment (Richter et al., 2006; Tjallingii et al., 2007). The XRF scanning analysis (at 1 to 3 mm steps) was made for the Bahama sediment core (MD99-2202), made up of typical periplatform oozes with strong dominance of calcium and strontium (Chapter 5). To account for potential biases related to physical properties of the sediment core, the XRF intensities (raw counts) of a given element were normalized.

Chapter 3

Last Interglacial (MIS5e) hydrographic shifts linked to meltwater discharges from the East Greenland margin

Anastasia Zhuravleva[1], Henning A. Bauch[2] and Nicolas Van Nieuwenhove[3,4]

[1]Academy of Sciences, Humanities and Literature | Mainz c/o GEOMAR Helmholtz Centre for Ocean Research, Wischhofstr. 1-3, 24148 Kiel, Germany
[2]Alfred Wegener Institute Helmholtz Centre for Polar and Marine Research c/o GEOMAR Helmholtz Centre for Ocean Research, Wischhofstr. 1-3, 24148 Kiel, Germany
[3]Department of Geoscience, Aarhus University, Høegh-Guldbergs Gade 2, DK 8000 Aarhus C, Denmark
[4]Department of Glaciology and Climate, Geological Survey of Denmark and Greenland, Øster Voldgade 10, 1350 Copenhagen, Denmark

Published in Quaternary Science Reviews

Abstract. Proximal evidence of the surface ocean response to the size reduction of the Greenland Ice Sheet (GIS) during the Last Interglacial (MIS5e) and preceding glacial termination (T2) remains largely elusive. Using a new sediment record from the western Iceland Sea, the behavior of the northeastern GIS and its relation to the subpolar North Atlantic surface hydrography is examined. Extremely light oxygen isotopic ($\delta^{18}O$) values are found off central East Greenland during early MIS5e and point to enhanced meltwater release, potentially from the northeastern sector of the GIS. Data from downstream the cold East Greenland Current (EGC) and its eastward branches suggest a far-reaching effect of this meltwater not only in the Nordic Seas but also in the SE Labrador Sea. In particular, whereas an early MIS5e warming (at ~128.5-126.5 ka) in the two regions coincided with the relative reduction of meltwater input into the EGC, the subsequent cooling noted at ~126.5 ka followed a renewed major freshwater event off central East Greenland. Our data further indicate persistent freshwater influence from the East Greenland margin over the entire MIS5e interval and, in addition, also reveal a late MIS5e meltwater event. The latter event occurred just prior to the last glacial inception and emphasizes the importance of Greenland meltwater as forcing factor on Interglacial climates.

3.1 Introduction

Present day mass loss of the Greenland Ice Sheet (GIS) and the retreat of Arctic sea ice lead to accumulation of low-density water in the convection areas of the Nordic Seas and the Labrador Sea (Masson-Delmotte et al., 2013; Böning et al., 2016). Significant changes of winter convection in the Labrador Sea linked to upper ocean freshening are known from historical observations as “great salinity anomalies” (e.g., Belkin, 2004 and references therein). Such surface processes may not only affect deep convection locally but also impact the Atlantic Meridional Overturning Circulation (AMOC), and thus the global climate (Rahmstorf et al. 2015). Freshwater additions into the subpolar regions also modulate the strength of the North Atlantic subpolar gyre (SPG) (Born and Stocker,

2014), eventually also affecting the northward heat and salt transfer into the deep convection sites of the Nordic Seas (Hátún et al., 2005, 2009).

To assess the effects of freshwater forcing on the AMOC, numerous studies have focused on late Pleistocene intervals. The Last Interglacial, i.e., the Eemian or Marine Isotope Stage (MIS) 5e, is a particularly suitable period for testing future oceanic responses as this interval is believed to have been globally at least 2 °C warmer than the present (Masson-Delmotte et al., 2013), with a sea level 4-6 meters higher than today (Hearty et al., 2007; Kopp et al., 2009). Because of limited direct field evidence from Greenland (Funder et al., 1998, 2011; Vasskog et al., 2015) including the absence of stratigraphically well-preserved Eemian ice (e.g., NEEM community members, 2013) – the response of the GIS to a warmer climate is largely based on numerical modeling efforts. Yet ice sheet simulations generate considerably different model outputs in terms of the size and timing of the changes of the GIS, depending on the methodology and boundary conditions used (Masson-Delmotte et al., 2013 and references therein).

Marine sediments can provide valuable insight into past GIS dynamics and oceanic responses, dating back to the Eemian and older geological intervals (e.g., Alley et al., 2010). For instance, sedimentary evidence from the Labrador Sea is in line with previous assumptions of a reduced southern GIS extent during the Eemian (Otto-Bliesner et al., 2006; de Vernal and Hillaire-Marcel, 2008; Carlson et al., 2008b; Colville et al., 2011). However, interpretations of the surface water evolution in this area are complicated by the Laurentide Ice Sheet dynamics as well as sea-ice/freshwater export from the Arctic region (Hillaire-Marcel et al., 2001; Cottet-Puinel et al., 2004; Born et al., 2010; Nicholl et al., 2012). Sizeable meltwater discharges during the Saalian deglaciation (Termination 2) were also documented in the Nordic Seas (Van Nieuwenhove et al., 2011; Bauch, 2013; Thibodeau et al., 2016). Yet the role of the GIS in the formation of a thick, freshened surface layer, which significantly delayed peak MIS5e sea surface temperatures (SSTs) (Bauch et al., 1999; Hodell at al., 2009; Govin et al., 2012), remains unclear.

Unlike the well-known areas to the south of the GIS and in the eastern Nordic Seas, the East Greenland margin and the adjacent surface current the East Greenland Current (EGC) are still poorly investigated due to the scarcity of available archives and the low resolution of existing records (Nam et al., 1995; Stein et al., 1996; Fronval and Jansen, 1996, 1997; Funder et al., 1998). However, the EGC plays a crucial climate-regulating role, given that it transports polar water to the convection sites of the Nordic Seas and the Labrador Sea (Dickson et al., 1988, 2007; Aksenov et al., 2010; Rudels et al., 2012; Luo et al., 2016) and potentially changes the properties and dynamics of the SPG (Born and Stocker, 2014).

The purpose of this study is twofold. First, we focus on the southwestern Nordic Seas (i.e., the Iceland Sea) and examine how the GIS instabilities interacted with the properties of the EGC and the Atlantic water inflows across the entire last interglacial cycle. In a second step, we compare the MIS5e sea surface evolution off the East Greenland margin

with climate development further downstream, i.e., the area still within the influence of polar waters confined to the EGC, to assess hydrographic connections between the Nordic Seas and the SE Labrador Sea.

3.2 Oceanographic settings and core sites

As part of the upper cell of the AMOC, warm and saline surface currents transport heat from the tropics northwards into the SPG and across the Iceland-Scotland Ridge into the polar gyres of the Nordic Seas (Fig. 3.1; Hansen and Østerhus, 2000). Opposed to that is the outflow of the EGC carrying low-salinity polar waters and sea ice from the Arctic Ocean southward along the Greenland continental margin (Aagaard and Coachman, 1968; Hopkins, 1991). Today, the EGC is a well-stratified surface current, transporting not only fresh polar waters at the surface, but also entraining water masses of Atlantic origin at intermediate depths, including modified (cooled) Atlantic waters from the Arctic Ocean, and distinctively warmer Atlantic water, which re-circulates in the Fram Strait (Rudels et al., 2002, 2012). In the southwestern Nordic Seas, an eastward branch of the EGC combines with the warm Irminger Current forming the relatively cold East Iceland Current (EIC), which continues eastward along the northern Icelandic shelf. After having passed the Denmark Strait, the polar waters of the EGC either loop around the southern tip of Greenland and continue further into the Labrador Sea or turn southwards into the interior of the SPG (Holliday et al., 2007). The convective sinking of Atlantic waters in the Nordic Seas and the Labrador Sea forms the deep, southward-flowing branch of the North Atlantic Deep Water, constituting the lower limb of the AMOC (Eldevik et al., 2009).

It has been shown that the properties of the Atlantic water flowing into the Nordic Seas and, therefore, the rate and intensity of the AMOC, are modulated by the strength and shape of the SPG (e.g., Hátún et al., 2009). In particular, a weaker, north-south oriented SPG results in enhanced injections of Atlantic salt and heat into the Nordic Seas, whereas a stronger, east-west oriented SPG contributes more freshwater into the poleward Atlantic flow (Häkkinen and Rhines, 2004; Hátún et al., 2005, 2009). The SPG strength is controlled by wind stress (e.g., Lohmann et al., 2009a, 2009b; Chaudhuri et al., 2011) but also by buoyancy forcing (e.g., Levermann and Born, 2007). Simplified, addition of freshwater into the Labrador Sea hampers water convection and, therefore, reduces the baroclinic contrasts between the center and the rim of the gyre, eventually leading to a weak mode of SPG circulation (e.g., Born and Stocker, 2014).

Marine sediment records were selected from key oceanographic sites in the (subpolar) North Atlantic (Table 3.1, Fig. 3.1): new paleoceanographic records were produced from a site off mid-eastern Greenland (M23351) and from two sites in the Iceland Sea (PS1247, M23485). These records were then complemented with published core data from the central Nordic Seas (M23352, PS1243), the mid-latitude Northeastern (NE) Atlantic (M23414 and Ocean Drilling Program (ODP) Site 980 of Leg 162), and the Greenland Rise (Eirik Drift) in the SE Labrador Sea (HU90-013-013 and MD03-2664).

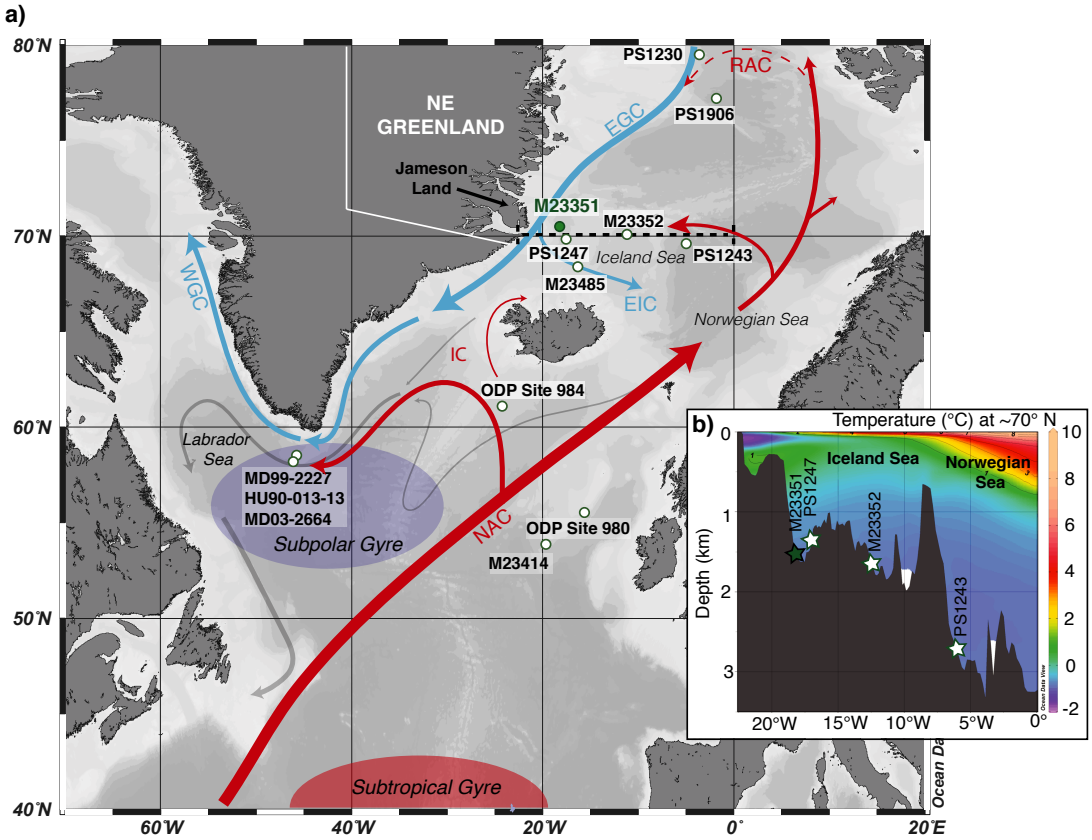

Figure 3.1: Simplified modern hydrography in the subpolar North Atlantic and locations of core sites with the inset representing temperature and bathymetry profile across the southwestern Nordic Seas. **(a)** Red/blue arrows indicate major warm/cold surface currents; dashed arrow indicates a subsurface current and grey arrows denote the main deep-water pathways (modified after Schott et al., 2004 and Rudels et al., 2012). The green dot marks the location of the investigated core M23351 (70°21´N, 18°13´W, 1673 m water depth); white dots indicate the locations of other cores discussed in the text (see Table 3.1). White lines drawn across Greenland delimit the northeastern sector of GIS. Black dashed line indicates the transect along ~70°N shown in **(b)**. EGC – East Greenland Current, EIC – East Iceland Current, WGC – West Greenland Current, NAC – North Atlantic Current, IC – Irminger Current, RAC – Return Atlantic Current. **(b)** Temperature and bathymetry profile across the Iceland Sea and the western Norwegian Sea from World Ocean Atlas 2013 (Levitus et al., 2013) together with the locations of investigated cores. The figures are created using Ocean Data View (Schlitzer, 2016).

3.3 Methods

3.3.1 Sample Preparation

The last interglacial interval in core M23351 (460-570 cm) was continuously sampled as 1 cm thick sediment slabs. The samples were then freeze-dried, weighed, wet-sieved using a 63 µm mesh size, and dry-sieved at 150 µm and 100 µm mesh sizes.

3.3.2 Foraminiferal assemblages and iceberg-rafted debris

Given that the subpolar Atlantic-water indicative species *Turborotalita quinqueloba* (Natland) rarely grows larger than 150 µm in polar conditions (Bauch, 1994; Kandiano and Bauch, 2002), planktic foraminiferal counts were performed in the size fraction

>100 µm. Following the conventional procedure, each sample was reduced by means of a microsplitter and, when possible, a minimum total of 300 foraminifera was counted. Samples containing less than 100 specimens were not considered for foraminiferal relative abundances calculations, but test concentrations (number of specimens per gram sediment) were calculated for all samples. In all of the samples foraminifera were well preserved without significant signs of corrosion.

Table 3.1: List of cores considered in this study.

Core	Latitude	Longitude	Water Depth (m)	Reference
M23351	70°21´N	18°13´W	1673	Voelker, 1999 *this study*
M23352	70°00´N	12°26´W	1819	Bauch et al., 2000 Van Nieuwenhove et al., 2013
PS1247	69°30´N	17°07´W	1388	Bauch et al., 1999 *this study*
M23485	67°55´N	17°52´W	1120	*this study*
PS1243	69°22´N	06°32´W	2710	Bauch et al., 2012
PS1230	78°52´N	4°50´W	1248	Thiede et al., 2011
PS1906	76°51´N	2°09´W	2901	Bauch, 2013
ODP Site 980	55°29´N	14°43´W	2179	Oppo et al., 2006
M23414	53°32´N	20°17´W	2199	Bauch and Kandiano, 2007 Bauch et al., 2012
HU90-013-013	58°13´N	48°22´W	3380	Hillaire-Marcel et al., 1994, 2001 Stoner et al., 1995 Seidenkrantz et al., 1995
MD03-2664	57°26´N	48°36´W	3440	Irvali et al., 2012, 2016 Galaasen et al., 2014
MD99-2227	58°12´N	48°22´W	3460	Carlson et al., 2008b Winsor et al., 2012
ODP Site 984	61°15´N	24°02´W	1648	Mokeddem et al., 2014

In accordance with the latest taxonomic status (Darling et al., 2006; Kucera, 2007), the left-coiling (sinistral) specimens of *Neogloboquadrina pachyderma* (Ehrenberg) are referred to as *N. pachyderma*, whereas right-coiling (dextral) specimens are referred to as *N. incompta,* in case that sample contained at least 3 % dextral specimens. If the sample contained less than 3 % right-coiling specimens, they were considered as genotypically identical to left-coiling specimens (Bauch et al., 2003) and calculated together with *N. pachyderma*.

Occurrences of the rare, but stratigraphically important species *Beella megastoma* (Earland) were investigated separately from the general counting procedure and on the entire unsplit sample in the fraction >150 µm (Bauch, 1996). Not much is known about the environmental preferences of this subtropical species, but it has been found at greater depths (down to 1000 m) in the low latitude North Atlantic and Mediterranean Sea (Hemleben et al., 1989; Bauch et al., 2000; Bauch, 2013).

Iceberg-rafted debris (IRD) counts were performed in the fraction >150 µm at a 1-cm interval. The results are expressed as IRD grains per gram of dry bulk sediment. While

executing the IRD counts, each sample was also checked for a potential presence of tephra grains.

3.3.3 Stable isotope analyses

Oxygen ($\delta^{18}O$) and carbon ($\delta^{13}C$) stable isotope ratios were measured on both planktic and benthic foraminifera. For the planktic foraminifera about 25-30 tests of *N. pachyderma* of similar morphology and size (150-250 μm) were picked when possible, crushed and homogenized. In some deglacial samples, where presumably high sedimentation rates diluted the number of available specimens, replicate runs were performed (when possible) on available tests (5-10). Benthic foraminiferal isotope data were produced using 5-10 specimens of the epibenthic species *Cibicidoides wuellerstorfi* (Schwager) and 5-20 specimens of the shallow-endobenthic species *Oridorsalis umbonatus* (Reuss) (e.g., Rathburn and Corliss, 1994). Both of these records were then spliced together. To account for species-dependent departures from isotopic equilibrium, $\delta^{18}O$ values were corrected by +0.64 ‰ and +0.36 ‰ for *C. wuellerstorfi* and *O. umbonatus,* respectively (Duplessy et al., 1988).

Stable isotope analyses were carried out on a Finnigan MAT 253 mass spectrometer at the GEOMAR Stable Isotope Laboratory. Results were calibrated to the Vienna Pee Dee Belemnite (VPDB) isotope scale via the NBS-19 and an internal laboratory standard. Analytical precision (1σ) of in-house standards is better than 0.04 ‰ for $\delta^{13}C$ and 0.08 ‰ for $\delta^{18}O$ (N=69).

3.4 Results from core M23351

Proxy records from core M23351 (Fig. 3.2) show that the early deglacial transition at ~565-555 cm is characterized by a 0.3-0.7 ‰ decrease in planktic $\delta^{18}O$ values and a 1.3-1.6 ‰ negative change in benthic $\delta^{18}O$ values. Further up within T2, two spikes of extremely depleted *N. pachyderma* $\delta^{18}O$ values (<1.8 ‰) occur, centered at ~545 and ~515 cm. These two events are separated by a reversal, associated with increased planktic $\delta^{13}C$ (0.4 ‰) and intermediate $\delta^{18}O$ (up to 4 ‰) values; note that the sediment section at ~545-530 cm did not contain any *O. umbonatus* specimens. A first occurrence of the subtropical species *B. megastoma* as well as of the epibenthic species *C. wuellerstorfi* is noted around the second peak of depleted $\delta^{18}O$, near the end of T2 (at ~515 cm). Although oxygen isotopic offsets between *O. umbonatus* and *C. wuellerstorfi* disappear soon thereafter, a small, but noticeable difference (0.3 ‰) is observed around 500 cm.

The MIS5e peak (marine interglacial optimum) stands out by lowest proportions of the polar species *N. pachyderma*, whereas relative abundances of its subpolar counterpart *T. quinqueloba* are highest. The subpolar species *Globigerinita uvula* (Ehrenberg) also constitutes up to 0.5 % of the assemblage during the MIS5e peak (data not shown). Planktic and benthic $\delta^{18}O$ show relatively constant values until about 490 cm, however, rapid negative excursions of $\delta^{18}O$ values in *N. pachyderma*, *C. wuellerstorfi* and *O. umbonatus* are observed at the end of MIS5e (at 492 cm). This is followed by an

increase in IRD input and *N. pachyderma* proportions, indicating the glacial inception after the warmest interval. Planktic foraminifera abundance (specimens/g), consisting thereafter exclusively of *N. pachyderma*, increases after the demise of interglacial warmth, and remains high until about 475 cm. No apparent ash layers were recognized within the entire record.

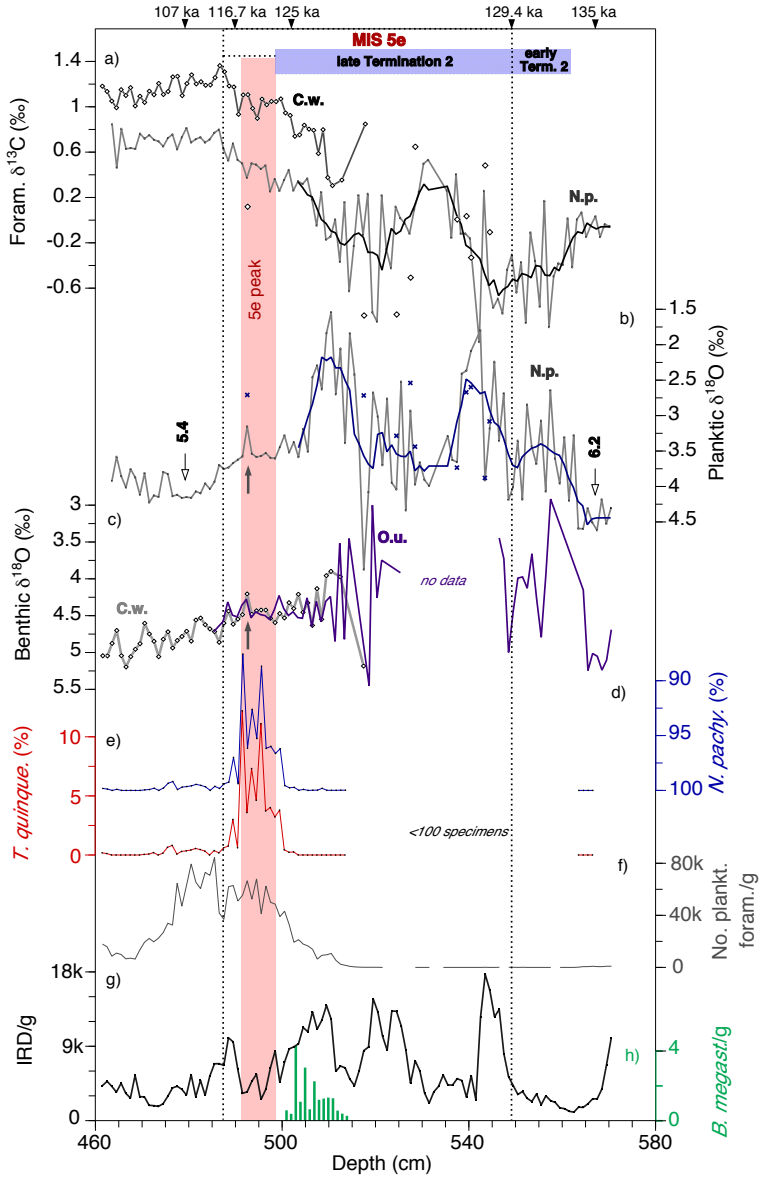

Figure 3.2: **Proxy data of core M23351 (off the East Greenland margin) over the last interglacial cycle versus depth**: **(a)** $\delta^{13}C$ values of *C. wuellerstorfi* and *N. pachyderma*, **(b)** $\delta^{18}O$ (smoothed and original) of *N. pachyderma*, **(c)** benthic (*C. wuellerstorfi* and *O. umbonatus*) $\delta^{18}O$ data, **(d** and **e)** proportions of *N. pachyderma* and *T. quinqueloba*, respectively, **(f)** number of planktic foraminifera per gram dry sediment, **(g)** iceberg-rafted debris (IRD), grains per gram dry sediment, **(h)** number of *B. megastoma* per gram dry sediment. Second-run measurements on stable isotopes O/C are marked respectively with crosses/diamonds. The interval of MIS5e peak warmth is highlighted in red. The upward grey arrows at 492 cm mark the light $\delta^{18}O$ values of *N. pachyderma, C. wuellerstorfi* and *O. umbonatus* representing a meltwater event. Also indicated are isotopic events 6.2 and 5.4 (Martinson et al., 1987). Black triangles with age indicate the age control points (see Fig. 3.3). C.w. – *C. wuellerstorfi;* N.p. – *N. pachyderma*; O.u. – *O. umbonatus.*

3.5 Core correlations and time scales

The framework of our marine age model is built on the recent AICC2012 ice core chronology, which incorporates ice records from Antarctica and Greenland (Bazin et al., 2013; Veres et al., 2013) and is expressed as thousand of calendar years before present (i.e., 1950) or "ka". The construction of the age model thus implies a stepwise transfer of age tie points from the ice cores to the cores studied here (Table S3.1), following alignment of marker events (Govin et al., 2015) using AnalySeries 2.0.8 (Paillard et al., 1996).

In a first step, the stratigraphic markers, tying the ice core records (NorthGRIP community members, 2004; Loulergue et al., 2008) to ODP Site 980 as identified by Capron et al. (2014), were adopted and applied to nearby core M23414 in the NE Atlantic, whose age model was further improved (Fig. S3.1). The same approach was then also used to transfer the Labrador Sea cores (MD03-2664 and HU90-03-013) and core PS1243 from the Nordic Seas onto the AICC2012 chronology (Figs. S3.2 and S3.3). The reader is referred to the appendix for a more elaborate discussion on the rationale of each tie point.

Because of a more complex depositional regime, constructing a common stratigraphy for sediment cores recovered in proximity to the GIS margin (M23352 and most notably M23351) is challenging, particularly in the deglacial intervals. For instance, correlating deep-sea benthic $\delta^{18}O$ records – generally regarded to reflect global ice volume – can be hampered due to offsets in $\delta^{18}O$ signatures between the ocean basins (Dokken and Jansen, 1999; Shackleton, 2000; Lisiecki and Raymo, 2009) and other deglacial overprints in ice-sheet-proximal environments (e.g., Bauch et al., 2000). Climatic alignments on the base of SST records and faunal data that appear justified for the North Atlantic (e.g., this study; Govin et al., 2012) have limited applicability in the circum-Arctic regions, particularly at the onset of MIS5e due to the belated progression of interglacial warmth towards the polar North Atlantic (Cortijo et al., 1999; Rasmussen et al., 2003b; Van Nieuwenhove et al., 2011). In addition, the abrupt global methane increase (dated at ~128.7±0.5 ka in Antarctic ice cores; Loulergue et al., 2008) coherent with post-Saalian warming in the North Atlantic (Carlson et al., 2008b; Waelbroeck et al., 2008; Govin et al., 2012; Capron et al., 2014), remains difficult to trace in the high northern latitudes by using faunal–based proxies (Govin et al., 2012; Capron et al., 2014).

We selected core PS1243 as stratigraphical reference base for cores M23352 and M23351 because of its relatively even sedimentation rates over the last interglacial cycle (see appendix). The last interglacial cycle in cores M23352 and M23351 can easily be discerned from the readily identifiable peaks of heavy planktic $\delta^{18}O$ values at 135 ka and 107 ka in PS1243, here associated with the isotopic events 6.2 and 5.4 (Figs. 3.3 and S3.4; Martinson et al., 1987). The changeover from the MIS5e "plateau" of low stable planktic and benthic $\delta^{18}O$ values to markedly heavier values in both records reflects the glacial

inception (early Weichselian) and seemingly corresponds to a cooling identified in the NorthGRIP ice core at ~116.7 ka (NorthGRIP community members, 2004).

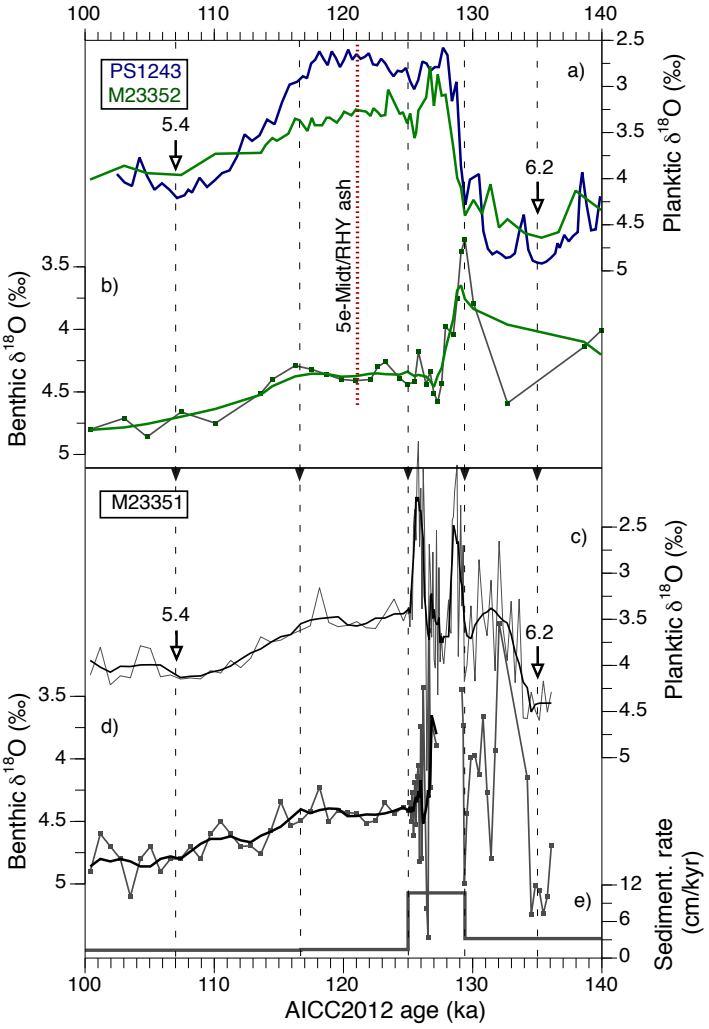

Figure 3.3: Age model for core M23351. Vertical dashed lines show correlations to the reference cores PS1243 (upper panel, in blue; Bauch et al., 2012) and M23352 (upper panel, in green; Bauch et al., 2000). Black triangles denote the applied tie points (see Table S3.1 in the appendix). All correlations were made by aligning planktic $\delta^{18}O$ records (**(a)** and **(c)**), with the exception of one tie point at ~125 ka, where smoothed benthic $\delta^{18}O$ records (**(b)** and **(d)**) were employed. Sedimentation rates in core M23351 are shown in **(e)**. The dashed red line indicates the position of the 5e-Midt/RHY tephra in cores PS1243 and M23352. Also marked are isotopic events 6.2 and 5.4 (Martinson et al., 1987).

The age model of core M23352 was further constrained for T2 by specifying two additional tie points based on the striking resemblance with the *N. pachyderma* $\delta^{18}O$ record in core PS1243 (Fig. S3.4): (1) the mid-point of the deglacial transition following the "first step" of decreasing $\delta^{18}O$ values at 129.4 ka; (2) the prominent return to higher $\delta^{18}O$ values at 125.5 ka, indicating the end of T2 (e.g., Bauch et al., 2000). Additionally, a rhyolitic tephra layer in core M23352, was aligned to the 5e-Midt/RHY ash layer found in PS1243 at ~121 ka (e.g., Fronval and Jansen, 1996).

For core M23351 two additional tie points were used to better constrain the age model around the MIS6/5e transition (Fig. 3.3): (1) a less obvious end of the deglacial "first step" (129.4 ka) was set around 549 cm, just before a drastic increase in IRD (Fig. 3.2g), roughly corresponding to the mid-point of the steep decrease in planktic $\delta^{18}O$ values across the MIS6/5e transition; (2) for the second tie point, at 125 ka, the (smoothed) benthic rather than the planktic oxygen isotope records were used, given that the planktic signatures could have been biased by meltwater overprints close to the active GIS. Based

on the proximity and similar water depth of cores M23352 and M23351, it was assumed that both sites were influenced by the same deepwater mass. Thus, the onsets of the benthic $\delta^{18}O$ "plateaus" at 125 ka were aligned and their timing additionally crosschecked with faunal, IRD and planktic isotopic (O/C) data.

Despite the arguments provided above (and in the appendix), the construction of the stratigraphic framework applied here, may still carry some uncertainties, for instance, due to the diachronous nature and/or spatially-restricted influence of meltwater events. However, it should be noted that relative uncertainties can be assumed to be minimal due to incorporation of several independent age markers in a suite of benthic and planktic records. Thus, any remaining uncertainties would seem marginal in the context of the assessment of millennial-scale events across the studied regions.

3.6 Discussion

3.6.1 Saalian deglaciation in the Nordic Seas: influence from northeastern Greenland

The overall course of the Saalian deglaciation (T2) in the Nordic Seas was shaped by large meltwater release from the collapsing continental ice sheets and fringing ice shelves, especially on the Eurasian side (e.g., Hebbeln et al., 1998; Knies and Vogt, 2003; Spielhagen et al., 2004; Knies et al., 2007; Bauch, 2013). It therefore seems difficult to trace meltwater pulses back to their provenances in general (Spielhagen and Bauch, 2015).

In the western Iceland Sea (core M23351) the extremely light planktic $\delta^{18}O$ values documented during early MIS5e (late T2) are significantly lower than deglacial values anywhere else in the central Nordic Seas, where *N. pachyderma* $\delta^{18}O$ recorded both a post-glacial SST increase and surface freshening (Fig. 3.4c and f). These values, therefore, clearly reflect a deglacial meltwater overprint along the East Greenland margin. Although identification of freshwater origin is complicated by the variety of potential sources, likely candidates for these early MIS5e meltwater events are the circum-Arctic region as well as the GIS.

To better evaluate the Arctic Ocean's role in the observed abrupt and large decreases in planktic $\delta^{18}O$ values, we compared core M23351 with available isotopic data from the upstream region, i.e., the western Fram Strait and the Greenland Sea (Fig. 3.4). There, the Saalian deglacial meltwater pulses, easily identifiable in IRD and planktic $\delta^{18}O$ records, do not show equally high-amplitude isotopic excursions as during the last deglaciation (Fig. 3.4a and b; Köhler and Spielhagen, 1990; Stein et al., 1996; Antonow et al., 1997; Bauch et al., 1999, 2001; Spielhagen et al., 2004; Knies et al., 2007; Thiede et al., 2011; Telesiński et al., 2014, 2015). These post-Saalian values farther north are much higher than the time-coeval values downstream in the western Iceland Sea, excluding the circum-Arctic region as a principal source for the early MIS5e isotopic excursions in core M23351.

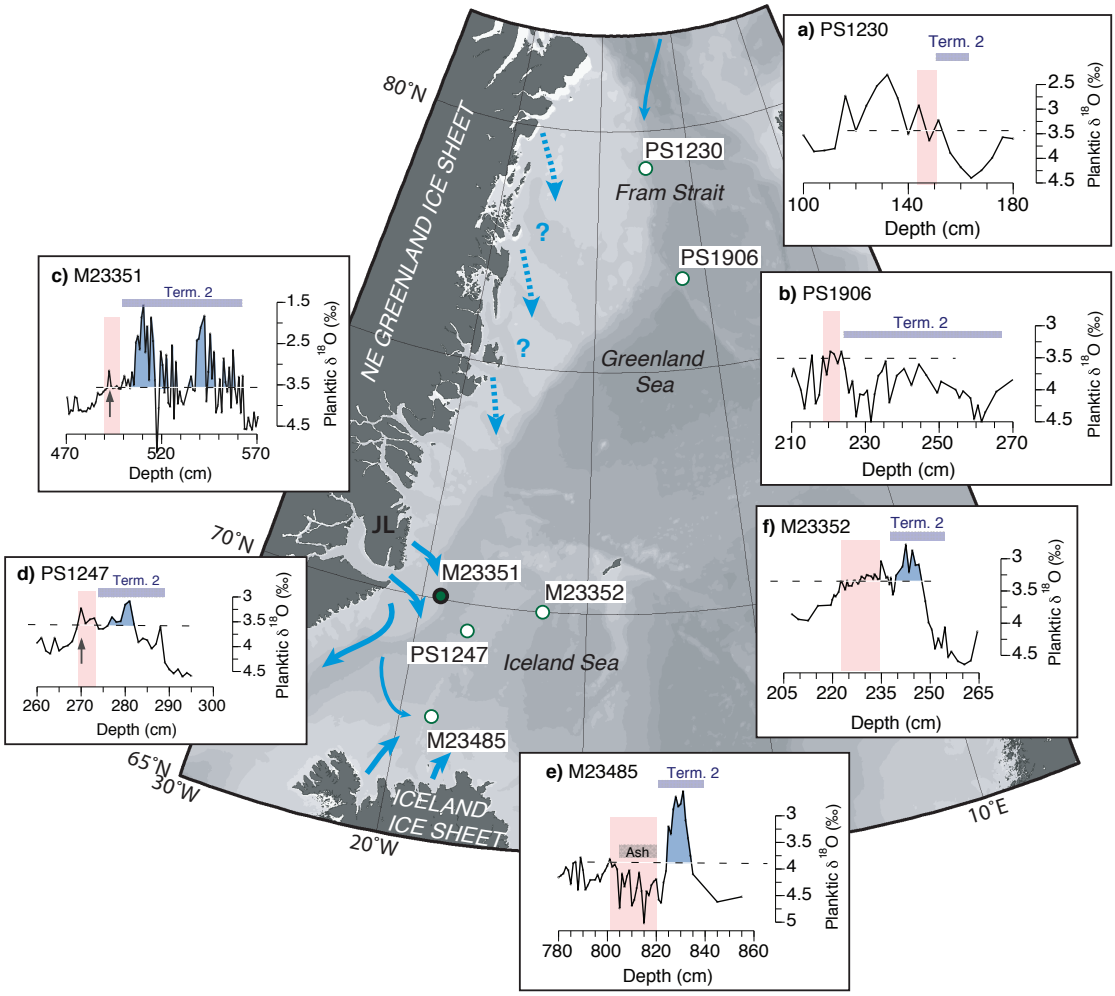

Figure 3.4: Comparison of $\delta^{18}O$ values of *N. pachyderma* during the Saalian deglaciation across (a) the western Fram Strait (core PS1230, Thiede et al., 2011), **(b)** the Greenland Sea (PS1906, Bauch, 2013), **(c-f)** and the Iceland Sea (from west to east: cores M23351, M23485, PS1247, M23352 (Bauch et al., 2000)). The interval of MIS5e peak warmth is highlighted in pink. Intervals within the glacial termination with $\delta^{18}O$ values lower than the interglacial average (indicated by horizontal dashed lines) are colored in blue. In core M23485 **(e)** interpretation of peak interglacial $\delta^{18}O$ values is hampered by low sedimentation rates and a relatively thick basaltic ash layer (at 805-820 cm). The upward arrows in **(c)** and **(d)** indicate the late MIS5e meltwater event. Blue arrows on the map mark the pathways of post-Saalian meltwater based on data discussed in the text. The bathymetry map is created using Ocean Data View (Schlitzer, 2016). JL – Jameson Land peninsula.

Since freshwater contributions from the Arctic region are thus regarded to have been of secondary importance, meltwater from the GIS is, therefore, considered here as the most likely cause for the very low planktic $\delta^{18}O$ values found in the western Iceland Sea during late T2. In the absence of marine records from the northeastern Greenland shelf, recent simulations reveal a complete Eemian GIS collapse north of ~79°N (e.g., Born and Nisancioglu, 2012; Stone et al., 2013). However, sediment cores retrieved off North Greenland, i.e., in the vicinity of an important route for GIS meltwater propagation (Gillard et al., 2016), do not provide evidence for significant freshwater runoff from the high-latitude GIS during this time (Nørgaard-Pedersen et al., 2007). Collapse of the mid-

eastern GIS during T2 can be deduced from the terrestrial data from Jameson Land to the northwest of site M23351 (Fig. 3.1). This area was extensively glaciated during the Saalian, but has remained more or less ice-free since Eemian times (Funder et al., 1998, 2011; Håkansson et al., 2009). Taking into account the variety of potential GIS sources, it is suggested here that the entire northeastern sector of the GIS, including the glacier outlets between ~70° and 83°N (Fig. 3.1), could have played a role in the sea surface freshening revealed at site M23351.

The related freshwater release during early MIS5e appears to be traceable eastward of M23351, at site PS1247 – there, the low sedimentation rates in combination with bioturbation likely biased *N. pachyderma* $\delta^{18}O$ towards higher values (Fig. 3.4d) – and to the site of core M23485, north of Iceland (Fig. 3.4e). The comparatively low $\delta^{18}O$ values found at the latter site may suggest additional freshwater contributions from other sources, i.e., from a decaying Icelandic ice sheet.

3.6.2 Early MIS5e meltwater events (129-125 ka)

As shown in Fig. 3.5, the deglacial record from the East Greenland margin (core M23351) clearly documents the stepwise nature of the deglaciation (e.g., Seidenkrantz et al., 1996; Rasmussen et al., 2003a, 2003b; Risebrobakken et al., 2006; Bauch and Erlenkeuser, 2008; Van Nieuwenhove et al., 2011). Within the second step, which reaches into early MIS5e at these latitudes, at least two prominent meltwater events can be identified based on the paired low planktic $\delta^{18}O$-$\delta^{13}C$ values and the IRD record (Fig. 3.5). The two events are separated by a millennial-scale reversal (~128.5-126.5 ka) evident from a pronounced increase of planktic $\delta^{18}O$ values (up to 4 ‰) and a significant abrupt decrease of IRD at ~128.5 ka in core M23351.

According to our age model, the first major meltwater event within early MIS5e occurred around 129 ka and followed shortly after the first deglacial step, when global sea level rise caused increased ice sheet instability and enhanced glacier calving (Funder et al., 1998). The ablation and calving from the GIS was probably reinforced by the increasing boreal insolation and, particularly, by positive late spring-early summer solar insolation anomalies (Otto-Bliesner et al., 2006).

During phases of significant meltwater input, low planktic $\delta^{13}C$ values are generally attributed to the input of glacial meltwater, which typically has very low $\delta^{13}C$ values (Bauch and Weinelt, 1997; Bhatia et al., 2013; Xiao et al., 2014), and a deeper, less-ventilated habitat for *N. pachyderma* with an increased supply of C^{13}-depleted metabolic CO_2 from bacterial respiration (Spielhagen and Erlenkeuser, 1994; Xiao et al., 2014; Spielhagen and Bauch, 2015). The pronounced shift to much higher planktic $\delta^{13}C$ at ~128.5 ka in core M23351, therefore, suggests a marked change in the environment, and together with heavier planktic $\delta^{18}O$ values and reduced IRD points to a significant reduction in meltwater input, arguing for an interruption of deglacial processes between ~128.5 and 128 ka (Fig. 3.5). The following interval until ~126.5 ka is characterized by

elevated IRD deposition but generally high $\delta^{18}O$ values of *N. pachyderma*. It therefore seems to reflect a time of relatively reduced meltwater input into the EGC.

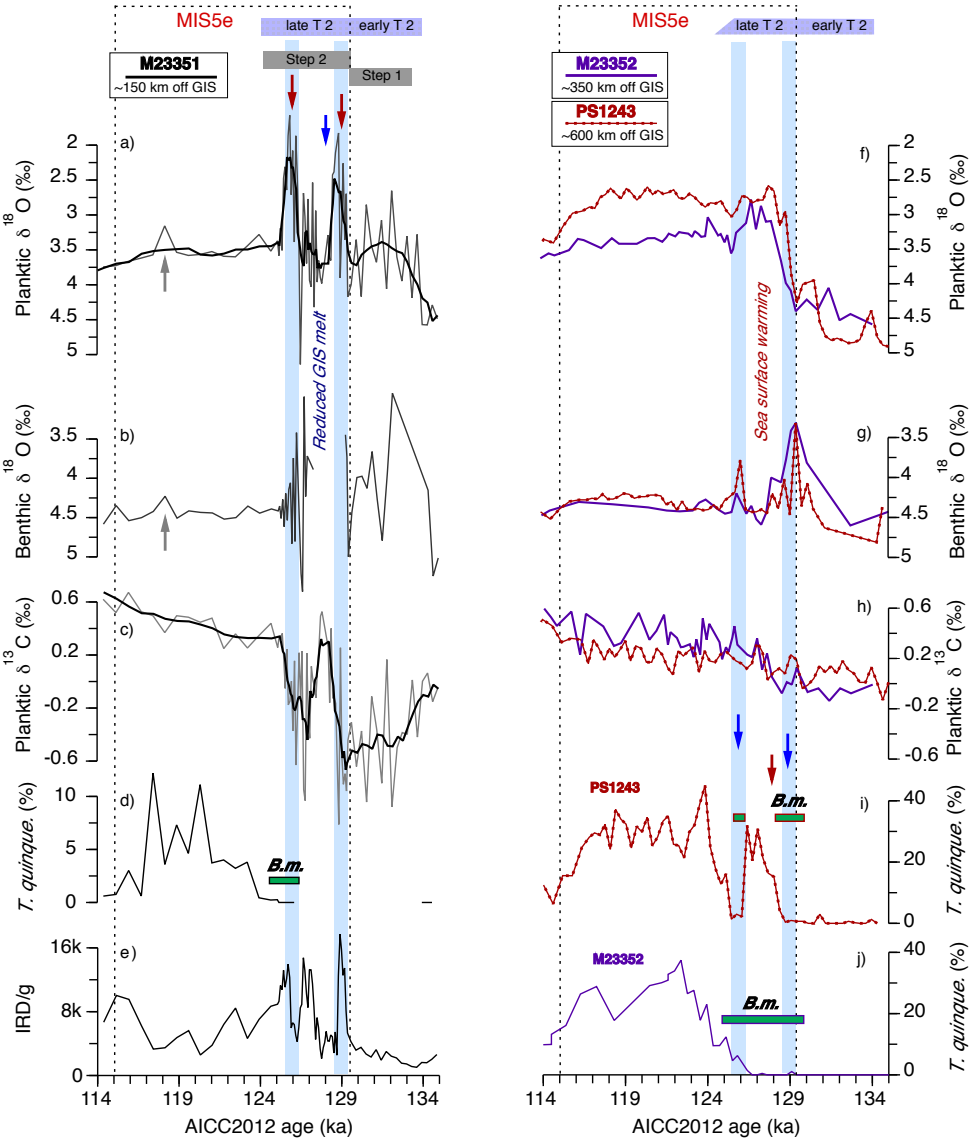

Figure 3.5: Proxy records from cores M23351, M23352 (Bauch et al., 2000) and PS1243 (Bauch et al., 2012) for the period 135-114 ka. Left panel (core M23351): **(a)** $\delta^{18}O$ of *N. pachyderma*, **(b)** $\delta^{18}O$ of spliced *C. wuellerstorfi* and *O. umbonatus*, **(c)** $\delta^{13}C$ of *N. pachyderma*, **(d)** proportion of *T. quinqueloba* and **(e)** IRD grains per gram dry sediment. Right panel (cores M23352 (violet line) and PS1243 (dashed red line)): **(f)** $\delta^{18}O$ of *N. pachyderma*, **(g)** $\delta^{18}O$ of *C. wuellerstorfi*, **(h)** $\delta^{13}C$ of *N. pachyderma*, **(i** and **j)** proportions of *T. quinqueloba* respectively in cores PS1243 and M23352. The horizontal bars in **(d)**, **(i)** and **(j)** mark occurrences of *B. megastoma* (*B.m.*) in cores M23351, PS1243 and M23352, respectively. Note a longer-lasting Termination 2 at the site more proximal to the GIS (M23351) compared to the central Nordic Seas (PS1243 and M23352; of which T2 was longer for M23352). Early MIS5e meltwater events off the East Greenland margin are highlighted with blue bars. Opposite sequences of warm and cool episodes within the stepwise Termination 2 are marked with downward arrows (red/blue) for cores M23351 and PS1243. Upward-pointing grey arrows at ~118 ka in core M23351 denote the late MIS5e meltwater event.

Throughout early MIS5e (~129-127 ka), including both phases of increased (~129 ka) and decreased (~128 ka) melting of the GIS, the sedimentary record at site M23351 is

almost barren of fossils, including *N. pachyderma* and *O. umbonatu*s (Fig. 3.2c and d). The latter shallow-endobenthic species is capable to tolerate environments with low fluxes of organic matter (Mackensen et al., 1985; Rathburn and Corliss, 1994). Such reduced numbers of planktic and benthic foraminifera likely indicate low bioproductivity due to cold surface conditions, limited food abundance and/or enhanced sea-ice cover (Nam et al., 1997; Bauch et al., 2001; Perner et al., 2015).

The second (younger) prominent IRD-enriched freshwater episode, centered around 126 ka in M23351, reflects a continuation of the northeastern GIS deglaciation but with less severe conditions than during the first event (Fig. 3.5). This is deduced from increased planktic foraminiferal abundances and the appearance of *C. wuellerstorfi*, suggesting increased sea surface productivity and seasonally open waters (Fig. 3.2c and f; Wollenburg et al., 2001). As an epibenthic-living suspension feeder, *C. wuellerstorfi* is typically abundant during interglacial times when reinforced bottom currents assure high food supply (Mackensen et al., 1985; Lutze and Thiel, 1989).

Analogies to the stepwise deglaciation as revealed by our marine record can be found in sedimentary successions on Jameson Land (Fig. 3.1) that apparently reflect Eemian sea level changes (Lysa and Landvik, 1994; Funder et al., 1998). Here, an initial eustatic sea level rise ("deglacial flooding") was succeeded by a regressive phase, which likely resulted from isostatic rebound. That phase was then followed by a second transgression due to resumed melting of Saalian ice elsewhere but on Jameson Land (Lysa and Landvik, 1994; Funder et al., 1998). It seems relevant to link the terrestrial sequence of events to the step-wise deglaciation found at site M23351. And yet, such a correlation between the onshore and offshore records remains largely tentative and speculative, also because it cannot be excluded that site M23351 was affected by several simultaneous meltwater discharge events that originated from potentially different sources.

3.6.3 Implications of climatic oscillations during early MIS5e

3.6.3.1 Nordic Seas

In contrast to the more proximal site M23352, core PS1243 further away from the GIS in the western Norwegian Sea documents a pronounced post-glacial surface warming as early as ~128 ka (Fig. 3.5). This relatively early MIS5e warming is linked to the intrusion of Atlantic water at the sea surface, as seen by the rapid increase of the subpolar, symbiont-bearing species *T. quinqueloba* around 128 ka (Fig. 3.5i). Such high proportions of this species indicate at least seasonally open waters and a rather restricted influence of deglacial meltwater for this area at that time. Enhanced presence of Altantic-sourced waters at the sea surface corresponds with the initiation of vertical convection in the central Nordic Seas at ~128 ka, as inferred from benthic $\delta^{13}C$ (Fig. 3.6a-c). That warm phase was, however, interrupted by an abrupt short-term surface cooling at ~126.5 ka, coherent with a temporal reduction of deep water ventilation. According to our age model, the early climatic amelioration in core PS1243 appears to coincide with the phase of decreased melting of the northeastern GIS (~128.5-126.5 ka), whereas the subsequent

cooling followed upon a renewed GIS freshwater release at ~126.5 ka. Admixture of this low-density water would inhibit the vertical convention, however, noting that the GIS should only be considered as one of several possible sources.

The intensified melting from the northeastern GIS around ~129 ka and ~126 ka corresponds in time (within the age uncertainties) with the first and the last intrusions of subtropical species *B. megastoma* into the southern Nordic Seas (Fig. 3.5), revealing a possible link between subsurface heat advection and ice sheet melting (e.g., Marcott et al., 2011). In the Nordic Seas, the occurrence of *B. megastoma* coincides with abrupt depletions in benthic $\delta^{18}O$ values, including the freshwater event around 126 ka found off the East Greenland margin (Fig. 3.5). The onset of the so-called *B. megastoma* event (at ~126 ka) there was obviously delayed in comparison to the more central regions of the Nordic Seas (Bauch, 1996). There, the species occurred as early as the latest phase of Heinrich Event 11, providing evidence for an existing, although variable, subtropical-to-polar "teleconnection" at subsurface water depths during T2 (Bauch et al., 2012; Bauch, 2013).

At times of overall suppressed ocean overturning due to freshwater forcing (e.g., Oppo et al., 1997; Bauch and Erlenkeuser, 2008; Hodell et al., 2009; Sánchez Goñi et al., 2012; Govin et al., 2012), the *B. megastoma* events suggest that warmer and denser Atlantic-sourced water masses propagated into the Nordic Seas at the subsurface, very much like it is seen in the Arctic Ocean today (e.g., Rudels, 2015). Considering that during early MIS5e the northward flow of subsurface Atlantic waters in the eastern Nordic Seas was likely hindered by a rather thick deglacial meltwater lid, its main flow could have been deflected westward into the Iceland Sea (Bauch et al., 1999). There, the re-circulated Atlantic-sourced waters were either entrained beneath the cold polar waters of the EGC or transported further west across the Greenland shelf break, eventually affecting the GIS mass balance through submarine ice melting. Accordingly, modern observations reveal a pivotal role of such topographically-dependant warm intrusions in melting of marine-terminating glaciers and ice streams (Hellmer et al., 2012; Straneo et al., 2012; Wilson and Straneo, 2015).

When compared with the time interval of increased vertical convection in the central Nordic Seas at ~128-126.5 ka, during the *B. megastoma* events density changes of the Atlantic water flowing across the Nordic Seas are inferred to have been minimal, thereby arguing for an enhanced Atlantic heat transfer towards the east Greenland shelf at that time (Fig 3.7a and c). Accordingly, a relatively stronger (colder) EGC could be inferred for the time interval of enhanced water column ventilation at ~128-126.5 ka, which coincided with reduced/moderate melting of the northeastern GIS (Fig. 3.7b). This lasted until another significant reduction in deep water ventilation happened at ~126 ka, coincidently with another *B. megastoma* event (Fig. 3.7c).

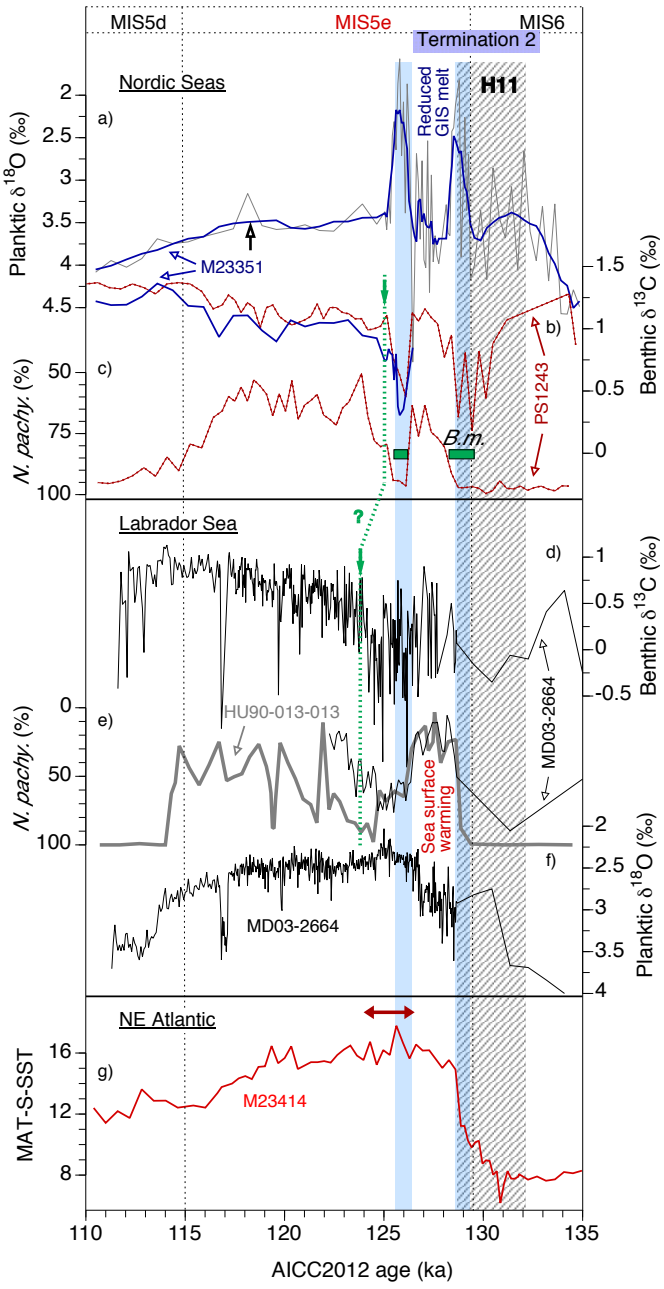

Figure 3.6: Comparison of proxy records from the Nordic Seas cores M23351 and PS1243 (Bauch et al., 2012), the Labrador Sea cores MD03-2664 (Irvali et al., 2012; Galaasen et al., 2014) and HU90-013-013 (Seidenkrantz et al., 1995) and the NE Atlantic core M23414 (Bauch et al., 2012) for the period 135-110 ka. **(a)** $\delta^{18}O$ values of *N. pachyderma* in core M23351, **(b)** $\delta^{13}C$ values of *C. wuellerstorfi* in cores M23351 and PS1243, **(c)** *N. pachyderma* proportions in PS1243; horizontal green bars mark occurrences of *B. megastoma (B.m.)* in core PS1243, **(d)** $\delta^{13}C$ values of *C. wuellerstorfi* in MD03-2664, **(e)** *N. pachyderma* proportions in HU90-013-013 and MD03-2664, **(f)** $\delta^{18}O$ values of *N. pachyderma* in MD03-2664, **(g)** Modern Analogue Technique (MAT) summer sea surface temperature (S-SST) in M23414. Early MIS5e meltwater events off the East Greenland margin are shown with blue bands. Horizontal double-ended red arrow in **(g)** shows an interval of peak SSTs as revealed in Bauch and Kandiano (2007). Upward black arrow in core M23351 **(a)** at ~118 ka indicates the late MIS5e meltwater event. Note that the duration of Termination 2 varied depending on the region and is shown here for core M23351. The dotted green line indicates a tentative correlation of events in the Nordic and Labrador Seas, as discussed in the text. Heinrich Event 11 (H11) is allocated based on core M23414 data (see Fig. S3.1).

During the *B. megastoma* events the associated relatively dense subsurface inflow probably promoted the initiation of a deeper convection in the central Nordic Seas. A comparable process is suggested for the last deglaciation when a surplus of Atlantic salt and heat transported from the mid-latitudes into the Nordic Seas at subsurface depths facilitated an AMOC resumption (Thornalley et al., 2010; Repschläger et al., 2015). Heat released from the subsurface waters caused thermobaric instability of the water column and led to a diminished stratification (Thiagarajan et al., 2014). As an additional trigger for reduced stratification at that time, a possible release of the glacial heat stored in the deep Nordic Seas can be invoked. Considering that low deglacial benthic $\delta^{18}O$ values in the Nordic Seas could be partly related to geothermal heating of isolated bottom water masses (Adkins et al., 2005; Thiagarajan et al., 2014; Thornalley et al., 2015), the deep-ocean heat release may be supported by the increasing trends in benthic $\delta^{18}O$ records in cores M23352 and PS1243 between 129.5 and 128 ka (Fig. 3.5g). However, the lack of a clear understanding of the nature behind such isotopic depletions in deep-sea benthic foraminifera (e.g., Lehmann et al., 1993; Rasmussen et al., 2003b; Dokken and Jansen, 1999; Bauch and Bauch, 2001; Stanford et al., 2011) precludes any further affirmation of such a mechanism at this time.

3.6.3.2 Labrador Sea and North Atlantic

Throughout T2 and up to mid-MIS5e the Labrador Sea was strongly influenced by elevated freshwater supply from the GIS and the Laurentide Ice Sheet (de Vernal and Hillaire-Marcel, 2008; Carlson et al., 2008b; Colville et al., 2011). Although foraminiferal data and SSTs indicate warming during early MIS5e (~128.5-126.5 ka) at the Eirik Drift sites MD03-2664 and HU90-013-013 (Fig. 3.6e), data from nearby core MD99-2227 (Fig. 3.1) lack a similar early climatic amelioration (Carlson et al., 2008b; Winsor et al., 2012). Accordingly, higher planktic $\delta^{18}O$ values at the other two Eirik Drift sites (Fig. 3.6f) evidence the influence of a warmer surface current (e.g., Irvali et al., 2012), whereas at MD99-2227 site lowered $\delta^{18}O$ values in *N. pachyderma* from ~128 ka onwards would rather suggest continuous influence of a cold and fresh EGC, implying a strong hydrographic gradient at the sea surface (Winsor et al., 2012). And yet, such comparisons may remain tentative (Carlson et al., 2008b; Winsor et al., 2012), if one considers different age model concepts used for core MD99-2227 (Evans et al., 2007; Channell et al., 2009; Sánchez Goñi et al., 2012) and cores MD03-2664 and HU90-013-013 (this study; Hillaire-Marcel et al., 2001; Irvali et al., 2012; Galaasen et al., 2014). Instead, striking resemblance of overall $CaCO_3$ records of cores HU90-013-013 (Stoner et al., 1995) and MD99-2227 (Carlson et al., 2008b) as well as correlations of red detrital layers deposited after the final collapse of the Laurentide Ice Sheet (Nicholl et al., 2012; Galaasen et al., 2014) could be considered a firmer basis for correlating between cores (Fig. S3.2).

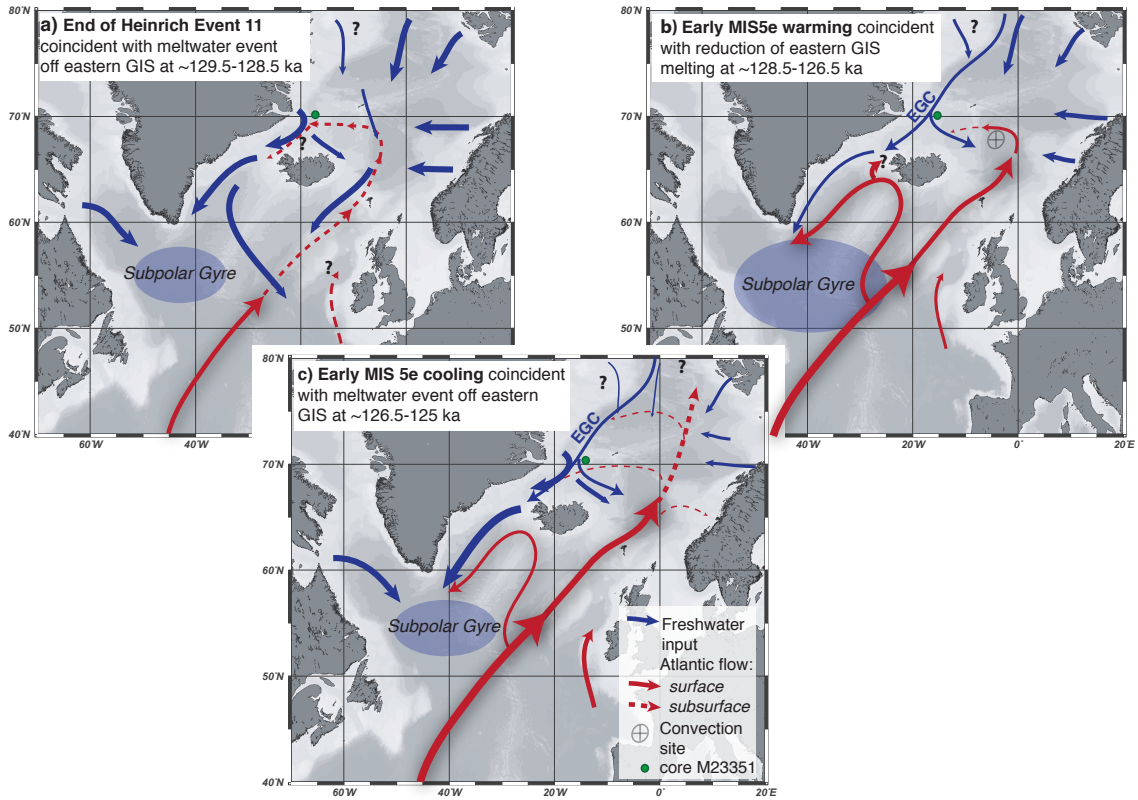

Figure 3.7: Schematic representation of surface and subsurface circulation during three different time slices within the early MIS5e (~129.5–125 ka), based on data discussed in the text. Subsurface flows are based on occurrences of *B. megastoma*. **(a)** End of Heinrich Event 11 (~129.5–128.5 ka). A meltwater event off eastern GIS corresponds in time with the subsurface Atlantic inflow into the Nordic Seas and a weak SPG; **(b)** Early MIS5e warming (~128.5–126.5 ka) in the NE Atlantic, the SE Labrador Sea and the Nordic Seas caused by the influence of Atlantic water at the sea surface. The warm phase coincides with a reduction of meltwater input from the East Greenland margin, initiation of vertical convection in the central Nordic Seas and a strong SPG; **(c)** Surface cooling in the SE Labrador Sea and the Nordic Seas (~126.5–125 ka) coincides with a renewed meltwater event off the East Greenland margin. The subsurface Atlantic inflow into the Nordic Seas appears to have been far-reaching but short-lasting (~126.5–125 ka). EGC – East Greenland Current.

The influence of a warmer surface current during early MIS5e in the SE Labrador Sea is also recognized on the opposite side of the SPG, in the NE Atlantic (Fig. 3.6g; Cortijo et al., 1994; Oppo et al., 2006; Bauch and Kandiano, 2007; Bauch et al., 2012). In spite of initial climate ameliorations noticeable in the central Nordic Seas at ~128 ka (Fig. 3.6c), ongoing significant meltwater input from the disintegrating ice sheets limited the propagation of Atlantic surface heat through the eastern Nordic Seas and into the Arctic Ocean (e.g., Van Nieuwenhove et al., 2011). That situation accounted for excess heat storage in the mid-latitudes (Bauch and Kandiano, 2007; Bauch et al., 2012; Sánchez Goñi et al., 2012) with positive climatic feedbacks on the Labrador Sea (Figs. 3.6f and 7b; Irvali et al., 2012; Galaasen et al., 2014) and the area off southern Iceland (ODP Site 984, Fig. 3.1; Mokkedem et al., 2014).

Rapid increases of *N. pachyderma* proportions in the SE Labrador Sea and in the central Nordic Seas starting at ~126.5 ka indicate a significant cooling that punctuated the early

MIS5e warming in these regions (Fig. 3.6c and e; Seidenkrantz et al., 1995, 1996; Fronval and Jansen, 1996; Irvali et al., 2012; Bauch et al., 2012; Galaasen et al., 2014). Superimposed on the continuous ablation of the southern GIS at that time (Carlson et al., 2008b), a large meltwater discharge at ~126.5 ka as evidenced by the planktic $\delta^{18}O$ record in core M23351 can be invoked as additional trigger for the cooling observed at the Eirik Drift (Fig. 3.6). The meltwater released during this discharge was likely carried eastwards and southwards (towards the Eirik Drift area) by the EIC and EGC respectively. It is further conceivable that the southward transport of freshwater together with sea ice caused a weakening and contraction of the SPG (Fig. 3.7c; Hátún et al., 2005, 2009; Thornalley et al., 2009; Born et al., 2010; Born and Stocker, 2014). Coincident with cold surface conditions at the western SPG periphery, records from the NE Atlantic show peak SSTs at ~126.5–123 ka (Fig. 3.6g; Bauch and Kandiano, 2007). The associated high abundance of subtropical foraminifera there would indicate a smaller east-west expansion of the SPG, which enabled more tropical waters to be advected into the NE Atlantic (Hátún et al., 2009; Thornalley et al., 2009) at times when the northward surface flow was still blocked by the presence of a thick meltwater lid (Fig. 3.7c). That Atlantic water did nonetheless flow further into the Nordic Seas at that time, presumably as a subsurface current, is documented by the rare but omnipresent occurrence of subtropical *B. megastoma* (Fig. 3.6; Bauch et al., 2000, 2012).

At the Eirik Drift, colder conditions also started to develop at ~126.5 ka but persisted about 2-3 kyr longer than in the central Nordic Seas, i.e., until ~123 ka (Fig. 3.6e), perhaps amplified by a non-linear response of the SPG to surface freshening and atmospheric forcing (Lohmann et al., 2009a; Born et al., 2010). The continuing melting of the southern GIS across the early and mid-MIS5e (de Vernal and Hillaire-Marcel, 2008; Carlson et al., 2008b; Colville et al., 2011) together with a surge event from the Laurentide Ice Sheet (Nicholl et al., 2012) may have contributed to this longer-lasting, regional cooling. In addition, the increased freshwater presence might have added to the reduction of Labrador Sea Water formation at that time (Hillaire-Marcel et al., 2001; Cottet-Puinel et al., 2004; Born et al., 2010).

The cold surface conditions at the Eirik Drift after ~126.5 ka (core MD03-2664) are characterized by very low *C. wuellerstorfi* $\delta^{13}C$ values (Fig. 3.6d; Galaasen et al., 2014). Also in the Nordic Seas at shallow depth in M23351 and at greater depth in PS1243 depleted benthic $\delta^{13}C$ values are seen for this time period and coincide with the freshwater release from the northeastern GIS (Fig. 3.6a and b). In the Labrador Sea, these depletions associated with rapid reductions of deep water formation were suggested by Galaasen et al. (2014) to occur during the peak interval of MIS5e. We, however, interpret the aforementioned $\delta^{13}C$ depletions in MD03-2664 to belong stratigraphically and climatically still to the main deglaciation, very much like in other records from the Nordic Seas (e.g., Van Nieuwenhove et al., 2011). Thus, also the earlier MIS5e warm episodes documented in the central Nordic Seas (Bauch et al., 2012) and at the Eirik Drift (Irvali et al., 2012, 2016) between ~128.5 – 126.5 ka (Fig. 3.6c and e) are suggested here to be

part of the main deglaciation. Accordingly, because of the different physical constraints inherent to the Saalian deglaciation, these climatic events present quite different environmental circumstances when compared to proper, peak interglacial conditions with high global sea level and insignificant meltwater influence (Bauch et al., 2012). In addition, given that stratigraphical markers across MIS5e are scarce and could be biased because of deglacial processes, particularly in proximity to ice sheet margins (Govin et al., 2015), it cannot be ruled out that the entire cold, $\delta^{13}C$-depleted event which started in MD03-2664 at ~126.5 ka might in fact be time-equivalent to the cold event recognized in PS1243 between ~126.5 and 125 ka (Fig. 3.6b-e).

3.6.4 Peak MIS5e and a meltwater event preceding the glacial inception

According to our new age model, the main deglaciation came to an end in the central Nordic Seas around 125.5 ka, whereas in the western Nordic Seas substantial amounts of IRD together with lowered planktic $\delta^{18}O$ values (surface meltwater) persisted for another 2-3 kyr (Fig. 3.5). A freshened sea surface at this time is also seen in phytoplankton-based reconstructions from core M23352 (Van Nieuwenhove et al., 2013). Together with the continued IRD input at the Greenland margin, the $\delta^{18}O$ offset between *O. umbonatus* and *C. wuellerstorfi* (Fig. 3.2c) is a further indication for ongoing ice sheet melting and a deep water environment which had not approached a stable climate mode typical for an interglacial (Bauch and Erlenkeuser, 2003).

Over the peak of MIS5e, defined here by highest proportions of *T. quinqueloba*, the deposition of IRD along the East Greenland margin never completely ceased and some notable variability in IRD input occurred in phase with polar foraminiferal increases (Fig. 3.5d and e), something not mirrored in the isotope data (in contrast to the early MIS5e). The reason for this may have been stable summer temperatures at the base of the seasonal mixed layer, and much less freshwater influence during the foraminiferal reproduction period (Jonkers et al., 2010; Pados and Spielhagen, 2014). A recent multi-proxy study from core M23352 revealed an early optimum and a cooling trend, which started already after 120 ka (Van Nieuwenhove et al., 2013). According to our revised age model for this core, which also considers the 5e-Midt/RHY ash layer, the cooling trend is observed in this record even earlier within the MIS5e, already after ~122 ka (Fig. 3.5j). In contrast, core M23351 would rather indicate a late MIS5e foraminiferal optimum, very comparable to what is reported from the eastern Nordic Seas (Bauch and Erlenkeuser, 2003). While keeping in mind the low resolution across the peak of MIS5e in this core, we cannot discount the possibility that the elevated proportions of *T. quinqueloba* and, by inference, the lower shares of *N. pachyderma* during late MIS5e may not exactly capture the actual peak of SSTs (Fig. 3.5d). Foraminiferal census data can also reflect specific changes at the species habitat depths, incorporating different forcing mechanisms (e.g., food and light availability, predation) with regard to their respective seasonal occurrence (e.g., Simstich et al., 2003; Jonkers et al., 2010).

The end of the last interglacial warmth off the East Greenland margin (core M23351) is marked by a pronounced short-term depletion in both planktic and benthic $\delta^{18}O$ values around 118 ka, associated here with a freshwater pulse (Figs. 3.5a, b and 3.6a). A similar rapid negative planktic $\delta^{18}O$ excursion is observed in nearby core PS1247 (Fig. 3.4d) and further downstream in core MD99-2227 (Winsor et al., 2012). In the M23351 record, a decrease in subpolar foraminifera proportions as well as a significant increase in IRD indicate that regional ice sheet growth and the onset of glacial inception followed upon that event (Fig. 3.5d and e). Because of the low temporal resolution of core M23351, one can only speculate whether the meltwater pulse was also related to one of the SST-cooling events described from the North Atlantic (McManus et al., 1994; Oppo et al., 2006; Irvali et al., 2016).

Intensification of the AMOC during late MIS5e as a result of enhanced injections of tropical heat and salt into the Nordic Seas due to a weak and contracted SPG has been proposed on the basis of paleoclimatic data and modeling studies (e.g., McManus et al., 2002; Risebrobakken et al., 2007; Born et al., 2000, 2011; Mokkedem et al., 2014). It is thought that the elevated moisture transport from the North Atlantic superimposed on the orbital forcing initiated glacier growth in the high latitudes (McManus et al., 2002; Risebrobakken et al., 2005, 2007; Bauch and Kandiano, 2007). If the scenario of a weakened SPG is valid, the meltwater pulse off the eastern GIS at ~118 ka could have played a role in the Labrador Sea freshening and, consequently, the spatial shrinking of the SPG (Mokkedem et al., 2014). However, given that the SPG properties, besides the freshwater forcing (e.g., Levermann and Born, 2007; Mengel et al., 2012; Born and Stocker, 2014), are controlled by atmospheric circulation patterns (e.g., Lohmann et al., 2009a, 2009b; Chaudhuri et al., 2011), further investigations of the complex and non-linear interactions between the SPG properties, wind stress and the AMOC are needed to understand the past and present climatic teleconnections.

3.7 Conclusions

New sedimentary data from the western Iceland Sea encompassing the last interglacial cycle (late MIS6/T2/MIS5e/early MIS5d) document the temporal dynamics of the water masses in response to GIS variability. During early MIS5e (~129.5-125 ka) extremely light $\delta^{18}O$ values registered along the East Greenland margin point to pronounced retreat of the northeastern GIS, and our data argue for a potentially far-reaching influence of this meltwater downstream the EGC and its eastward branches. In agreement with other reconstructions from high northern latitudes, a step-like and long-lasting Saalian deglaciation postponed the establishment of optimum marine conditions in the Iceland Sea until ~123 ka, i.e., out of phase with peak summer insolation. The planktic isotope data also reveal a short but pronounced meltwater event off the East Greenland margin at ~118 ka, immediately following the warmest phase of MIS5e and just prior to the last glacial inception.

The data further demonstrate a strong climatic decoupling between the central/western Nordic Seas, the SE Labrador Sea and the NE Atlantic over MIS5e, related to GIS instabilities and associated changes of the EGC properties. In particular, comparison of combined proxy data indicates that the early MIS5e warming (~128.5-126.5 ka) in the central Nordic Seas and SE Labrador Sea coincided with a temporary but pronounced reduction of deglacial processes of the northeastern GIS region. Subsequently, the termination of warm surface conditions occurred simultaneously in both regions at ~126.5 ka and appears to have coincided with a prominent meltwater event off the East Greenland margin. Downstream propagation of this low-density (and sea-ice-laden) water masses may have affected the convection sites in the Iceland Sea and the Labrador Sea and likely played a significant role in changing the properties of the SPG at that time.

Deciphering the relation between hydrographic shifts observed in different areas of the subpolar North Atlantic requires a careful core-to-core correlation and the construction of a robust chronology. Especially for the early and mid-MIS5e, this study adds to a growing body of evidence showing comparable sequences of millennial-scale climatic events and trends across the various regions of the North Atlantic. These observations not only illustrate the sensitivity of the subpolar ocean to freshwater forcing, they also reveal the potential of specific events as important markers that can be traced across various oceanic basins, eventually allowing for a better (chrono)stratigraphic constraint of the actual MIS5e interval.

Acknowledgements

We are grateful to N. Irvali (University of Bergen, Norway) for providing the data for core MD03-2664. M.-S. Seidenkrantz (Aarhus University, Denmark) is thanked for sharing the faunal data on core HU90-013-013. We are also thankful to S. Fessler (GEOMAR) for performing measurements on stable isotopes. The manuscript benefited from the constructive comments and suggestions made by 3 anonymous reviewers. A. Z. acknowledges the German Federal Ministry of Education and Research (BMBF) for supporting the project "Laptev-Sea: TRANSDRIFT" (BMBF grant 03G0833C). Additional financial support to A. Z. was provided by the German Research Foundation (DFG grant BA1367/12-1), to N. V. N. and H. A. B. by DFG project NI1248/1.

Supplementary information

Last Interglacial (MIS5e) hydrographic shifts linked to meltwater discharges from the East Greenland margin

S3.1 Core correlations and time scales

Correlation scheme

The construction of a common time scale was based on a stepwise correlation of climatic/isotopic signals in ice cores, NE Atlantic records (ODP Site 980 and core M23414), SE Labrador Sea records (cores MD03-2664 and HU90-013-013) and the Nordic Seas records (cores PS1243, M23352 and M23351). Note, that the development of the age model for cores M23351 and M23352 as well as other issues associated with the intra-Nordic Seas chronology are discussed in the main text (Chapter 3). All ages are expressed on the AICC2012 ice core chronology (Bazin et al., 2013; Veres et al., 2013) as thousand of calendar years before present (refers to 1950) and denoted here as "ka". All tie points used for the age models are shown in Table S3.1 from the appendix. The NEEM ice core was transferred from the EDML1 age scale onto the AICC2012 chronology by Emilie Capron, using correspondence between the EDC3 age and the AICC2012 age for every depth level and taking into account that the EDML1 age scale is coherent with EDC3 by construction (Capron et al., 2014; Govin et al., 2015; Capron, pers. comm., 2016).

North Atlantic

For the NE Atlantic cores, ODP Site 980 (Oppo et al., 2006) and core M23414 (Bauch et al., 2012), we generally adopted stratigraphic age markers from Capron et al. (2014). These authors, following the approach of Govin et al. (2012), aligned the warming indicated in SST proxy records at the beginning of MIS5e to a sharp methane increase at 128.7±0.5 ka in the EPICA Dome C (EDC) ice core (Loulergue et al., 2008). That assumption is based on the coeval timing of warm phases over Greenland and rapid global methane emissions as recorded in Antarctic ice cores during well-dated Termination 1 (Chappellaz et al., 1993; Huber et al., 2006; Loulergue et al., 2008; Baumgartner et al., 2014). Further tie points for ODP Site 980 and core M23414 were based on alignment of faunal-based SSTs to ice cores. One of the age markers – used as an age control point for all age models in the current study – represents a conspicuous changeover in a suite of proxies indicating the glacial inception at the end of the MIS5e. This crucial age marker was linked to a corresponding cooling in the NorthGRIP ice core at ca. 116.7 ka (NorthGRIP community members, 2004) and referred to as the North Atlantic C26 cold event (Oppo et al., 2006; Bauch and Kandiano, 2007).

The only age marker in M23414, which differed from what is suggested in Capron et al. (2014), tied the heavy excursion in planktic $\delta^{18}O$ values with a similar feature in ODP

Site 980 around 135 ka, referred to as isotopic event 6.2 (Martinson et al., 1987). By using this tie point we attained a better coherence between the benthic $\delta^{13}C$ trends seen at ODP Site 980 and M23414 (Fig. S3.1).

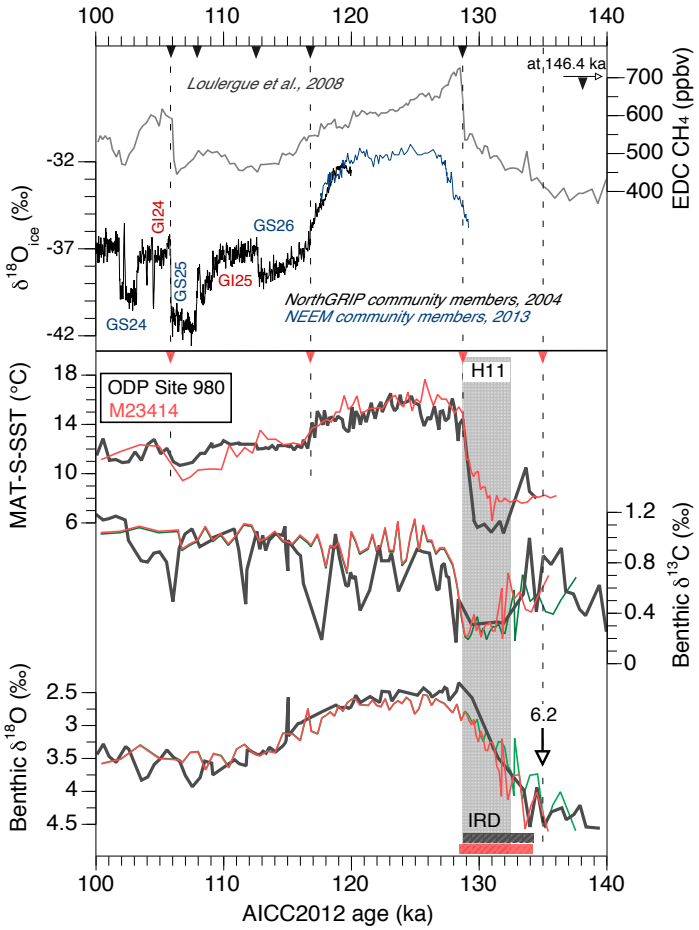

Figure S3.1: Age models for ODP Site 980 (Oppo et al., 2006) and core M23414 (Bauch et al., 2012). Black triangles show tie points used to correlate ODP Site 980 to ice cores (upper panel). The age model for ODP Site 980 was taken from Capron et al. (2014). Vertical dashed lines and red triangles show age control points for core M23414 (see Table S3.1 in the appendix). Green lines show M23414 records using an alternative age model from Capron et al. (2014), which was slightly modified here (see above). Also indicated is isotopic event 6.2 (Martinson et al., 1987). GS – Greenland Stadial, GI – Greenland Interstadial (NorthGRIP members, 2004); H11 – Heinrich Event 11.

Labrador Sea

To transfer cores MD03-2664 (Irvali et al., 2012; Galaasen et al., 2014) and HU90-013-013 (Hillaire-Marcel et al., 2001; Seidenkrantz et al., 1995) onto the AICC2012 chronology we aligned the early MIS5e sea surface warming to the steep methane increase in Antarctica (as suggested in Govin et al. (2012) and Capron et al. (2014)) and defined the turn to the glacial inception on the basis of faunal and isotopic data (Fig. S3.2). Taking into account the good coherence between isotopic records of HU90-013-013 and MD03-2664, the glacial inception in HU90-013-013 was determined at 1280 cm. Highest planktic $\delta^{18}O$ values in both cores were aligned to similar features at ODP Site 980 and identified as isotopic event 6.2 (135 ka). Finally, we tied the first pronounced planktic and benthic $\delta^{18}O$ increase at the glacial onset to Greenland Stadial 26 (GS 26, 112.7 ka, NorthGRIP members, 2004). Note that within "the MIS5e plateau" (128-116.1 ka in Shackleton et al., 2002, 2003) our age model for MD03-2664 remains relatively consistent with previously published age models for this core (Irvali et al., 2012, 2016; Galaasen et al., 2014; Capron et al., 2014).

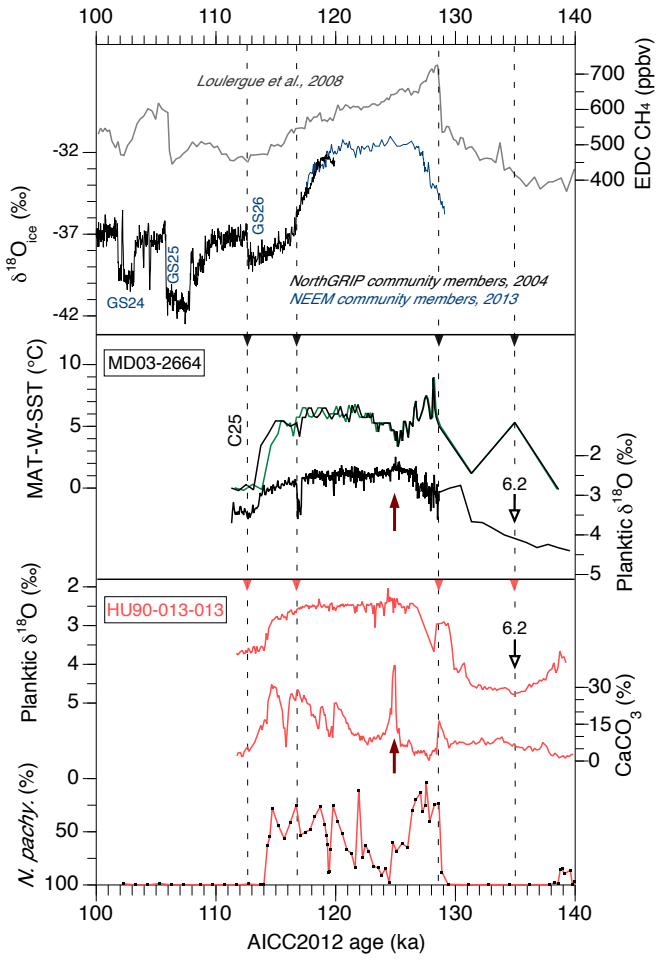

Figure S3.2: Age models for the SE Labrador Sea cores MD03-2664 (Irvali et al., 2012; Galaasen et al., 2014) and HU90-013-013 (Seidenkrantz et al., 1995; Hillaire-Marcel et al., 2001). Vertical dashed lines along with black and red triangles show age control points (see Table S3.1). Age models are based on correlation to ice cores (upper panel) as well as to ODP Site 980 (Fig. S3.1; Oppo et al., 2006). For comparison, the green solid line shows the MD03-2664 winter foraminifera-derived SSTs (MAT-W-SST) transferred onto a common age scale by using the Capron et al. (2014) model. Upward arrows indicate the position of red detrital sediment layers after the Laurentide outburst flooding event (Nicholl et al., 2012; see chapter 3.6.3.2 in the main text). Also indicated is isotopic event 6.2 (Martinson et al., 1987). GS – Greenland Stadial (NorthGRIP community members, 2004); C25 – the North Atlantic sea surface cooling event (McManus et al., 1994).

Central Nordic Seas

Here, several indicative features in core PS1243 were used and correlated to the NorthGRIP ice core and ODP Site 980 – both records themselves turned onto the AICC2012 age scale (Fig. S3.1) – to develop the chronology of core PS1243 (Fig. S3.3). We identified 4 age markers (see Table S3.1): (1) In accordance with previous studies (e.g., Bauch et al., 2012), the heaviest planktic $\delta^{18}O$ values during MIS6 (corresponding to isotopic event 6.2, Martinson et al., 1987) in PS1243 (270 cm) were aligned to a similar feature in the core from ODP Site 980 (at 135 ka). (2) A dramatic increase in benthic $\delta^{13}C$ at ODP Site 980 (and also in M23414) at ~127.7 ka, which followed the end of Heinrich Event 11 – as identified in the North Atlantic by McManus et al. (1994) – was aligned to a corresponding $\delta^{13}C$ increase in PS1243 (249 cm). This correlation is based on an assumption of a simultaneous establishment of deep water ventilation on either side of the Iceland-Scotland Ridge and intensification (deepening) of the Iceland-Scotland Overflow Water (Rasmussen et al., 2003b; Hodell et al., 2009). The tie point is also further supported by a concurrent initial decrease in *N. pachyderma* proportions at both ODP Site 980 and PS1243 roughly corresponding to an abrupt global methane increase at ~128.7 ka (Loulergue et al., 2008). (3) A prominent trend switch (214.5 cm) subsequent to the low interglacial planktic $\delta^{18}O$ values was correlated to the glacial inception

(116.7 ka) and is corroborated by the coeval termination of the benthic $\delta^{18}O$ plateau, recurrence of IRD and pronounced increase in *N. pachyderma* proportions. (4) Finally, the ensuing peak of heavy planktic $\delta^{18}O$ in PS1243 at ~198 cm was aligned to a similar isotopic peak at ODP Site 980 (107 ka) and associated with the isotopic event 5.4 (Martinson et al., 1987).

We also note here that the tie points used for construction of the PS1243 chronology in Capron et al. (2014) appear to result in an earlier establishment of warm surface conditions in the central Nordic Seas, when compared to lower-latitude sites of the North Atlantic as ODP Site 980 and M23414 (Fig. S3.3). The latter disagrees with the belated progression of interglacial warmth towards the northern North Atlantic (Cortijo et al., 1999; Rasmussen et al., 2003b; Van Nieuwenhove et al., 2011).

Western Nordic Seas

Development of time frames for cores M23352 (Bauch et al., 2000) and M23351 (by alignment to core PS1243) is discussed in the main text (Chapter 3.5).

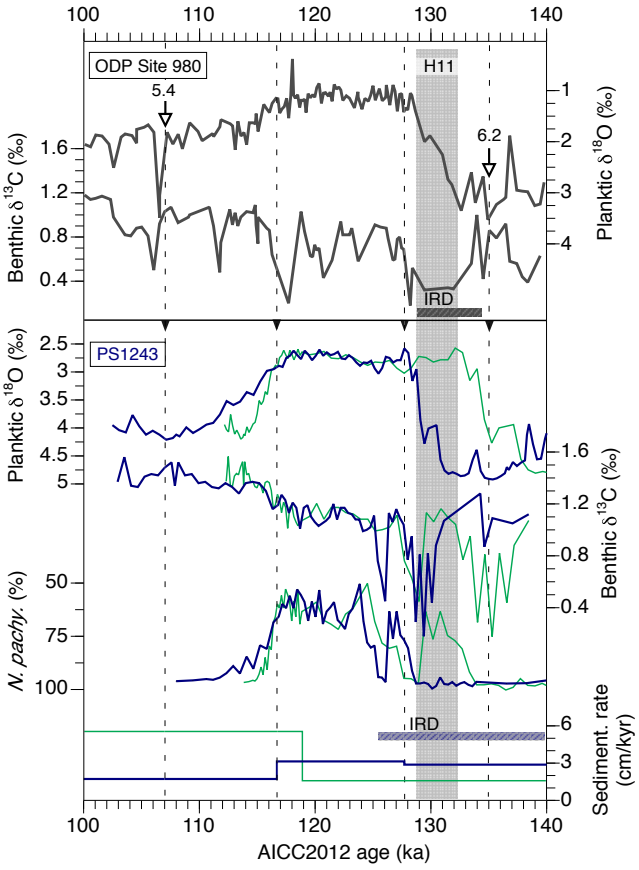

Figure S3.3: Age model for core PS1243 (Bauch et al., 2012), based on alignment to ODP Site 980 (Oppo et al., 2006). Vertical dashed lines and black triangles reflect age control points (see Table S3.1). The green lines show the PS1243 records using the alternative age model from Capron et al. (2014). Also indicated are isotopic events 6.2 and 5.4 (Martinson et al., 1987). H11 – Heinrich Event 11.

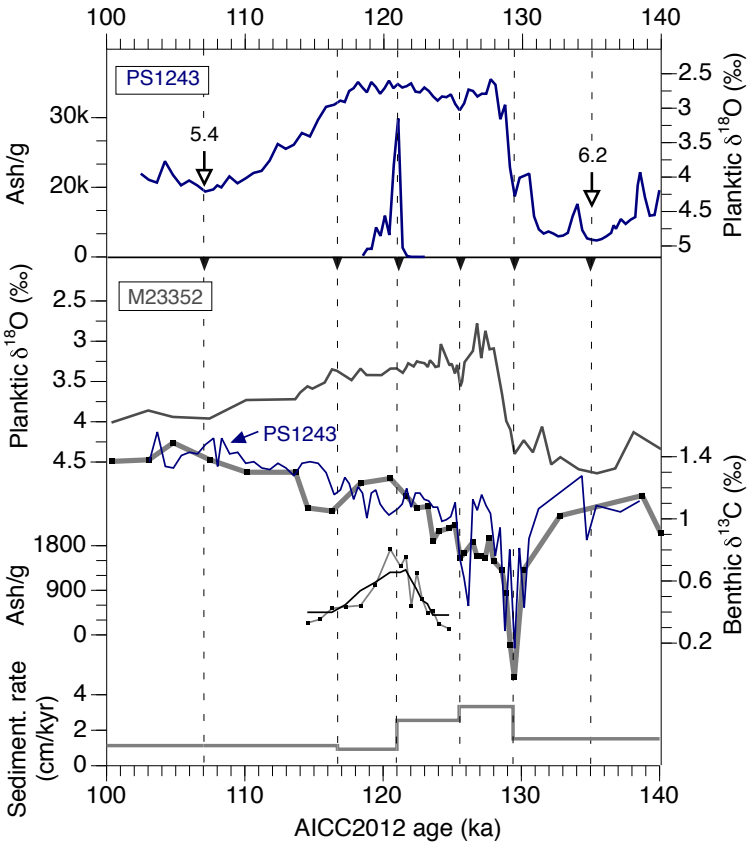

Figure S3.4: Age model for the Iceland Sea core M23352 (Bauch et al., 2000). Vertical dashed lines and black triangles show age control points (see Table S3.1). The age model is based on alignment to the planktic $\delta^{18}O$ record of core PS1243 (Bauch et al., 2012) and correlation of the 5e-Midt/RHY ash layers (at ~121 ka). Also indicated are isotopic events 6.2 and 5.4 (Martinson et al., 1987).

Table S3.1: Tie points used to transfer records onto AICC2012 age scale.

Abbreviations

GI: Greenland Interstadial
GS: Greenland Stadial
NP: *Neogloboquadrina pachyderma*
CW: *Cibicidoides wuellerstorfi*
SST: Sea surface temperature
IE: Isotopic event

Core Site	Depth [cm]	AICC2012 age [ka]	Sedimentation rates [cm/kyr]	Rationale and tie point reference
ODP Site 980 (Fig. S3.1)	1389.5	105.8	10.0	SST and NorthGRIP ice $\delta^{18}O$ (start of GI 24)[a)]
	1410.6	107.9	5.6	SST and NorthGRIP ice $\delta^{18}O$ (end of GI 25)[a)]
	1436.7	112.6	15.2	SST and NorthGRIP ice $\delta^{18}O$ (start of GI 25)[a)]
	1499.0	116.7	20.0	SST and NorthGRIP ice $\delta^{18}O$ (glacial inception)[a)]
	1738.5	128.7	7.4	Final warming and EDC CH_4 increase[)]
	1869.4	146.4	7.4	NP percentage and EDC CH_4[a)]
M23414 (Fig. S3.1)	357.9	105.8	1.7	SST and NorthGRIP ice $\delta^{18}O$ decrease; coherence with ODP Site 980 SST[a)]
	376.1	116.8	3.0	SST and NorthGRIP ice $\delta^{18}O$ decrease; coherence with ODP Site 980 SST[a)]
	412.4	128.8	5.6	Final warming and EDC CH_4 increase[)]
	446.7	135	5.6	Coherence with ODP Site 980 NP $\delta^{18}O$ (IE 6.2)[b)]
MD03-2664 (Fig. S3.2)	2368.1	112.7	13.0	NP $\delta^{18}O$ and NorthGRIP ice $\delta^{18}O$ (GS 26)[b)]
	2420.0	116.7	32.8	Coherence with ODP Site 980 NP $\delta^{18}O$, SST and NorthGRIP ice $\delta^{18}O$ (glacial inception)[b)]
	2813.1	128.7	1.1	Final warming and EDC CH_4 increase[a)]
	2820.0	135	1.1	Coherence with ODP Site 980 NP $\delta^{18}O$ (IE 6.2)[b)]
HU90-013-013 (Fig. S3.2)	1240	112.7	10	Coherence with MD03-2664 NP $\delta^{18}O$ and NorthGRIP ice $\delta^{18}O$ (GS 26)[b)]
	1280	116.7	13.0	Coherence with MD03-2664 NP $\delta^{18}O$ and NorthGRIP ice $\delta^{18}O$ (glacial inception)[b)]
	1433	128.7	5.9	Final warming and CH_4 increase[)]
	1473	135	5.9	Coherence with ODP Site 980 NP $\delta^{18}O$ (IE 6.2)[b)]
PS1243 (Fig. S3.3)	197.8	107	1.8	NP $\delta^{18}O$ and NorthGRIP ice $\delta^{18}O$ (GS 25, IE 5.4)[b)]

	214.5	116.7	3.1	Coherence with ODP Site 980 *N. incompta* $\delta^{18}O$ and NorthGRIP ice $\delta^{18}O$ (glacial inception)[b)]
	249.0	127.7	2.9	Coherence with ODP Site 980 CW $\delta^{13}C$[b)]
	270.0	135	2.9	Coherence with ODP Site 980 *N. incompta* $\delta^{18}O$ (IE 6.2)[b)]
M23352 (Fig. S3.4)	212	107	1.1	NP $\delta^{18}O$ and NorthGRIP ice $\delta^{18}O$ (GS 25, IE 5.4)[b)]
	223	116.7	0.9	NP $\delta^{18}O$ and NorthGRIP ice $\delta^{18}O$ (glacial inception)[b)]
	227	121	2.6	Midt/RHY ash layer (coherence with PS1243)[b)]
	238.5	125.5	3.3	Coherence with PS1243 NP $\delta^{18}O$ (end of deglacial termination)[b)]
	251.5	129.4	1.5	Coherence with PS1243 CW $\delta^{13}C$ (MIS6/5e boundary)[b)]
	260.0	135	1.5	Coherence with PS1243 NP $\delta^{18}O$ (IE 6.2)[b)]
M23351 (Fig. 3.3)	478.0	107	1.3	NP $\delta^{18}O$ and NorthGRIP ice $\delta^{18}O$ (GS 25, IE 5.4)[b)]
	490.5	116.7	1.4	NP $\delta^{18}O$ and NorthGRIP ice $\delta^{18}O$ (glacial inception)[b)]
	502	125	10.7	Coherence with M23352 CW $\delta^{18}O$, $\delta^{13}C$, NP $\delta^{18}O$, IRD[b)]
	549.0	129.4	3.2	Coherence with PS1243 NP $\delta^{18}O$ (MIS6/5e boundary)[b)]
	567.0	135	3.2	Coherence with PS1243 NP $\delta^{18}O$ (IE 6.2)[b)]

a) Capron, E., Govin, A., Stone, E.J., Masson-Delmotte, V., Mulitza, S., Otto-Bliesner, B., Rasmussen, T.L., Sime, L.C., Waelbroeck, C., Wolff, E.W., 2014. Temporal and spatial structure of multi-millennial temperature changes at high latitudes during the Last Interglacial. Quat. Sci. Rev. 103, 116–133. doi:10.1016/j.quascirev.2014.08.018.

b) this study

Chapter 4

The Atlantic Water heat transfer through the Arctic Gateway (Fram Strait) during the Last Interglacial

Anastasia Zhuravleva[1], Henning A. Bauch[2] and Robert F. Spielhagen[3]

[1]Academy of Sciences, Humanities and Literature | Mainz c/o GEOMAR Helmholtz Centre for Ocean Research, Wischhofstr. 1-3, 24148 Kiel, Germany
[2]Alfred Wegener Institute Helmholtz Centre for Polar and Marine Research c/o GEOMAR Helmholtz Centre for Ocean Research, Wischhofstr. 1-3, 24148 Kiel, Germany
[3]GEOMAR Helmholtz Centre for Ocean Research, Wischhofstr. 1-3, 24148 Kiel, Germany

Published in Global and Planetary Change

Abstract. The Last Interglacial in the Arctic region is often described as a time with warmer conditions and significantly less summer sea ice than today. The role of Atlantic Water (AW) as the main oceanic heat flux agent into the Arctic Ocean remains, however, unclear. Using high-resolution stable isotopes and faunal records from the only deep Arctic Gateway, the Fram Strait, we note for the upper water column a diminished influence of AW and generally colder-than-Holocene surface ocean conditions. After the main Saalian deglaciation had terminated, a first intensification of northward-advected AW happened (~124 ka). However, an intermittent sea surface cooling, triggered by meltwater release at ~122 ka, caused a regional delay in the further development towards peak interglacial conditions. Maximum AW heat advection occurred during late MIS 5e (118.5-116 ka) and interrupted a longer-term cooling trend at the sea surface that started from about 120 ka on. Such a late occurrence of the major AW-derived near-surface warming in the Fram Strait – this is in stark contrast to an early warm peak in the Holocene – compares well in time with upstream records from the Norwegian Sea, altogether implying a coherent development of south-to-north ocean heat transfer through the eastern Nordic Seas and into the high Arctic during the Last Interglacial.

4.1 Introduction

In the Fram Strait, the northward transport of warm and saline AW is confined to the topographically guided two branches of the West Spitsbergen Current (WSC). The western WSC branch largely re-circulates in the Fram Strait and then returns into the Nordic Seas at the subsurface, whereas the eastern WSC branch enters the Arctic Ocean and continues as a boundary current at intermediate depth (Beszczynska-Möller et al., 2012). In contrast to the Arctic Ocean, where the possible link between observed warming of the AW inflows and shrinking of the sea-ice cover is highly debated (cf. Spielhagen et al., 2011; Polyakov et al., 2017), importance of AW heat flux for oceanic and sea-ice conditions in the Fram Strait is well documented (Walczowski and Piechura, 2011). Various climatic records prove this relation also for present interglacial, the Holocene. During its early phase an intensified poleward AW advection appears to coincide with a peak in sea surface warmth and a sea-ice minimum in the Fram Strait (e.g., Salvigsen et al., 1992; Müller et al., 2009; Risebrobakken et al., 2011; Werner et al., 2016).

Despite the apparent climatic sensitivity of the Fram Strait, marine sediment core data never revealed warmer-than-Holocene surface conditions for the Last Interglacial, or Marine Isotope Stage (MIS) 5e (Köhler and Spielhagen, 1990; Hebbeln and Wefer, 1997; Hebbeln et al., 1998; Bauch et al., 1999; Risebrobakken et al., 2005, 2007). This lack of evidence may indicate a reduced transfer of AW heat and salt through the Arctic Gateway (e.g., Van Nieuwenhove et al., 2011). However, opposing views on the strength of the northward-directed AW flow during MIS 5e also exist (Knies et al., 1998; Matthiessen et al., 2001; Wollenburg et al., 2001; Grøsfjeld et al., 2006). It is worth noting that in the Fram Strait and along the northern Eurasian continental margin marine fossil records are sparse, and/or often biased by enhanced dissolution of biogenic carbonate during interglacial peaks (e.g., Wollenburg et al., 2001; Spielhagen et al., 2004). In the context of warm Eemian climate and mild ice conditions inferred for the Arctic region (Funder et al., 2002; CAPE-Last Interglacial Project Members, 2006; Grøsfjeld et al., 2006; Otto-Bliesner et al., 2006; Nørgaard-Pedersen et al., 2007; Polyak et al., 2010), it seems particularly important to reevaluate the existing views on the AW influence in the Arctic Gateway during MIS 5e.

To provide a refined picture of MIS 5e climatic developments in the polar North, we compiled a new multi-proxy record from the eastern Fram Strait (ODP Site 986). To allow a better documentation of the AW heat advection, the high-resolution foraminiferal assemblage study was performed in the relevant small-size fraction (Kandiano and Bauch, 2002; Husum and Hald, 2012). In an attempt to add to understanding of the mechanisms regulating the northward-directed AW heat transfer, our MIS 5e data were compared to some new and published Holocene records from the eastern Nordic Sea.

4.2 Regional Setting

At present, warm and saline AW is delivered to the southeastern Nordic Seas, i.e., the Norwegian Sea, via the topographically guided Norwegian Atlantic Current (NwAC). Together with another important extension of the NwAC in the Barents Sea, the WSC in the eastern Fram Strait feeds the Arctic Ocean with AW and defines the perennially ice-free Atlantic Domain (Fig. 4.1; Walczowski, 2013). In the central Fram Strait mixing of AW and Arctic-sourced Polar Water, confined to the East Greenland Current, results in cooler, fresher and seasonally ice-covered Arctic Water (ArW) of the Arctic Domain (Hansen and Østerhus, 2000). ArW, together with sea ice, is also transported across the western Svalbard shelf within the East Spitsbergen Current (Saloranta and Svendsen, 2001). The Atlantic Domain is separated from ArW by the Arctic Front (Swift, 1986). In the eastern Fram Strait such dynamic frontal zones may be found just to the west of the offshore WSC branch and just to the east of the inner WSC branch, i.e., at the Svalbard shelf break (Saloranta and Svendsen, 2001; Walczowski, 2013).

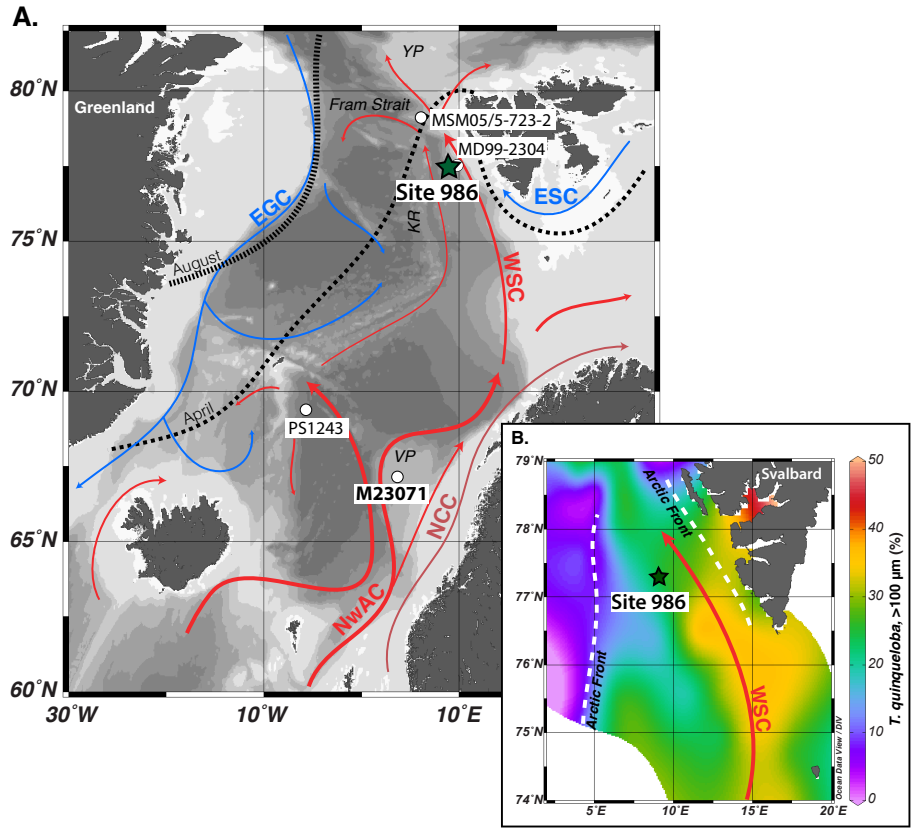

Figure 4.1: Maps of the study area showing location of the investigated Site 986 (asterisk) and other sediment cores mentioned in the text (see Table 4.1). **(A)** Red and blue arrows schematically represent surface circulation, i.e., Atlantic Water inflows and Polar Water outflows, respectively. Major surface currents are after Hansen and Østerhus (2000). Black dashed lines show median sea-ice limits (1981-2010) for August and April (National Snow and Ice Data Center; http://nsidc.org/data/seaice/). EGC – East Greenland Current, NwAC – Norwegian Atlantic Current, NCC – Norwegian Coastal Current, WSC – West Spitsbergen Current, ESC – East Spitsbergen Current, YP – Yermak Plateau, VP – Vøring Plateau, KR – Knipovich Ridge. **(B)** Modern distribution of *T. quinqueloba* (sediment surface) in the fraction >100 µm. Data from Husum and Hald (2012) and Pados and Spielhagen (2014). Arctic Front position is after Saloranta and Svendsen (2001) and Walczowski (2013). All maps were created using Ocean Data View (Schlitzer, 2016).

4.3 Material and methods

New sedimentological data were produced from Site 986, drilled at the lower slope of the western Svalbard continental margin (77°20´N, 9°04´E, 2051 m water depth) during Ocean Drilling Project (ODP) Leg 162 (Jansen et al., 1996). Also, some new data are shown from core M23071 (67°05´N, 2°55´E, 1308 m water depth) from the Vøring Plateau (see Table 4.1).

4.3.1 Site 986

Using unpublished low-resolution planktic $\delta^{18}O$ and $\delta^{13}C$ records (T. Snow and A. Shevenell, pers. comm. 2013), we identified MIS 5e and then re-sampled the entire sediment core section spanning from late MIS 6 into late MIS 5. The interval corresponding to the peak interglacial phase of MIS 5e (between 15.30 and 15.89 mcd) -

termed here as MIS 5e *sensu stricto* (*ss)* following Bauch et al. (1996) - was sampled continuously every 1 cm, whereas the remaining parts of the core were sampled as 1 cm thick slabs every 3 cm.

Table 4.1: List of investigated cores.

Core	Latitude	Longitude	Water Depth (m)	Time interval	Reference
Site 986	77°20´N	9°04´E	2052	MIS 5e	*this study*
M23071	67°05´N	2°55´E	1308	Holocene	*this study* Voelker, 1999
				MIS 5e	Bauch and Erlenkeuser, 2008 Van Nieuwenhove et al., 2008
PS1243	69°22´N	6°32´W	2710	Holocene and MIS 5e	Bauch et al., 2012
MD99-2304	77°37´N	9°57´E	1315	MIS 5e	Risebrobakken et al., 2005, 2007
MSM05/5-723-2	79°09´N	5°20´E	1350	Holocene	Werner et al., 2016

Stable isotopes analyses ($\delta^{18}O$ and $\delta^{13}C$) were performed on ~25-30 specimens of left-coiled *Neogloboquadrina pachyderma* (Ehrenberg) and ~3-10 tests of epibenthic species *Cibicidoides wuellerstorfi* (Schwager), using a Finnigan MAT 253 mass spectrometer at the GEOMAR Stable Isotope Laboratory. The analytical accuracy of in-house standards was better than 0.03 ‰ for $\delta^{13}C$ and 0.08 ‰ for $\delta^{18}O$. Results were calibrated to the Vienna Pee Dee Belemnite (VPDB) isotope scale via the NBS-19 and an internal laboratory standard.

Abundance of planktic foraminifera was counted in the size fraction >150 µm for all samples. Initially, planktic foraminiferal assemblages were obtained for MIS 5e-*ss* from representative splits with a minimum of 300 foraminiferal tests in the size fraction >150 µm. In a second step, samples taken from MIS 5e-*ss* were also counted in the size fraction 100-150 µm. The census data from the two size fractions were subsequently added up and recalculated into planktic foraminiferal assemblage composition for the fraction >100 µm. Small-sized *Globigerinita glutinata* (Egger) and *Globigerinita uvula* (Ehrenberg) were added up and shown here as *Globigerinita* spp.

The fraction 100-150 µm was also used to calculate the percentage of fragmented planktic foraminiferal tests relative to the total number of planktic foraminifera and fragments in the sample. The degree of fragmentation (%) was determined using the following equation (after Pfuhl and Shackleton, 2004):

$$\text{Fragmentation (\%)} = \#\text{Fragments/g}/(\#\text{Fragments/g}/3+\#\text{Test/g})$$

Counts of the total number of ice-rafted detritus (IRD) were made in the fraction >150 µm and are reported as IRD grains per gram of dry bulk sediment. Additionally, clastic

sedimentary rocks, often represented in our record as darkish-grey siltstones, were distinguished from the other IRD. Previous studies have pointed to the Barents Sea shelf area as a principal source area of such organic-rich clastic grains (e.g., Elverhøi et al., 1995; Bischof et al., 1997; Hebbeln and Wefer, 1997; Bauch et al., 2001). Marked increases in clastic IRD inputs could thus be related to fluctuations of the Svalbard-Barents Sea ice sheet. In addition, proportion of coal fragments relative to the number of IRD grains in the fraction >250 μm was counted for Termination 2 (T2). Since the appearance of *C. wuellerstorfi* has been recognized as a reliable indicator of increased bottom water ventilation after a deglaciation (Struck, 1997), numbers of this benthic species were also noted from the fraction >250 μm.

4.3.2 Core M23071

Planktic foraminiferal census data and IRD countings for the Holocene were made in the fraction >150 μm. This new data set complements the already existing stable oxygen and carbon isotope records for the Holocene section (Voelker, 1999). For MIS 5e, some published sedimentological evidence (e.g., Bauch and Erlenkeuser, 2008; Van Nieuwenhove et al., 2008) is also shown, however, a slightly different chronology is suggested and explained below.

4.4 Age framework

To place the MIS 5e records from Site 986 and M23071 on the common AICC2012 ice core chronology (Bazin et al., 2013; Veres et al., 2013) we used core PS1243 from the central Nordic Seas (Fig. 4.2; see also Table S4.1 for age tie points), which has relatively constant sedimentation rates over the entire MIS 5e interglacial (see Zhuravleva et al., 2017b for a detailed discussion on the age model construction). Based upon *N. pachyderma* $\delta^{18}O$ records we tied the readily identifiable isotopic events 5.4 and 6.2 (Martinson et al., 1987) at 107 and 135 ka, respectively. Accordingly, we transferred the age of 129.5 ka to the midpoints of the deglacial transition. The changeovers from the MIS 5e plateau of low stable benthic and planktic $\delta^{18}O$ values towards notably higher values are considered as the onset of the glacial inception (116.7 ka, NorthGRIP Community Members, 2004). To better frame the peak interglacial phase of MIS 5e in core M23071, we tied the prominent return to higher $\delta^{18}O$ values, signifying the end of the main deglaciation, with a similar feature at 125.5 ka in PS1243. Finally, the onset of MIS 5e-*ss* at Site 986, inferred from combined faunal and isotopic evidence, was aligned to a similar climatic amelioration observed in core M23071 at ~124.7 ka. The Holocene age model for core M23071 (short trigger box core) was taken from Voelker (1999).

We are aware that changes in environmental conditions may have occurred in a time-transgressive manner along the pathway of AW from the Norwegian Sea to the Fram Strait during a glacial termination – as indicated by Hald et al. (2007) for the earliest Holocene. However, more recent high-resolution Holocene data show that the time-offset in the change of dominant planktic foraminifera species is hardly detectable (Werner et

al., 2016; see also discussion further below). Accordingly, we assume such offsets for late T2 to have been small in the context of the millennial-centennial scale climatic variations discussed here.

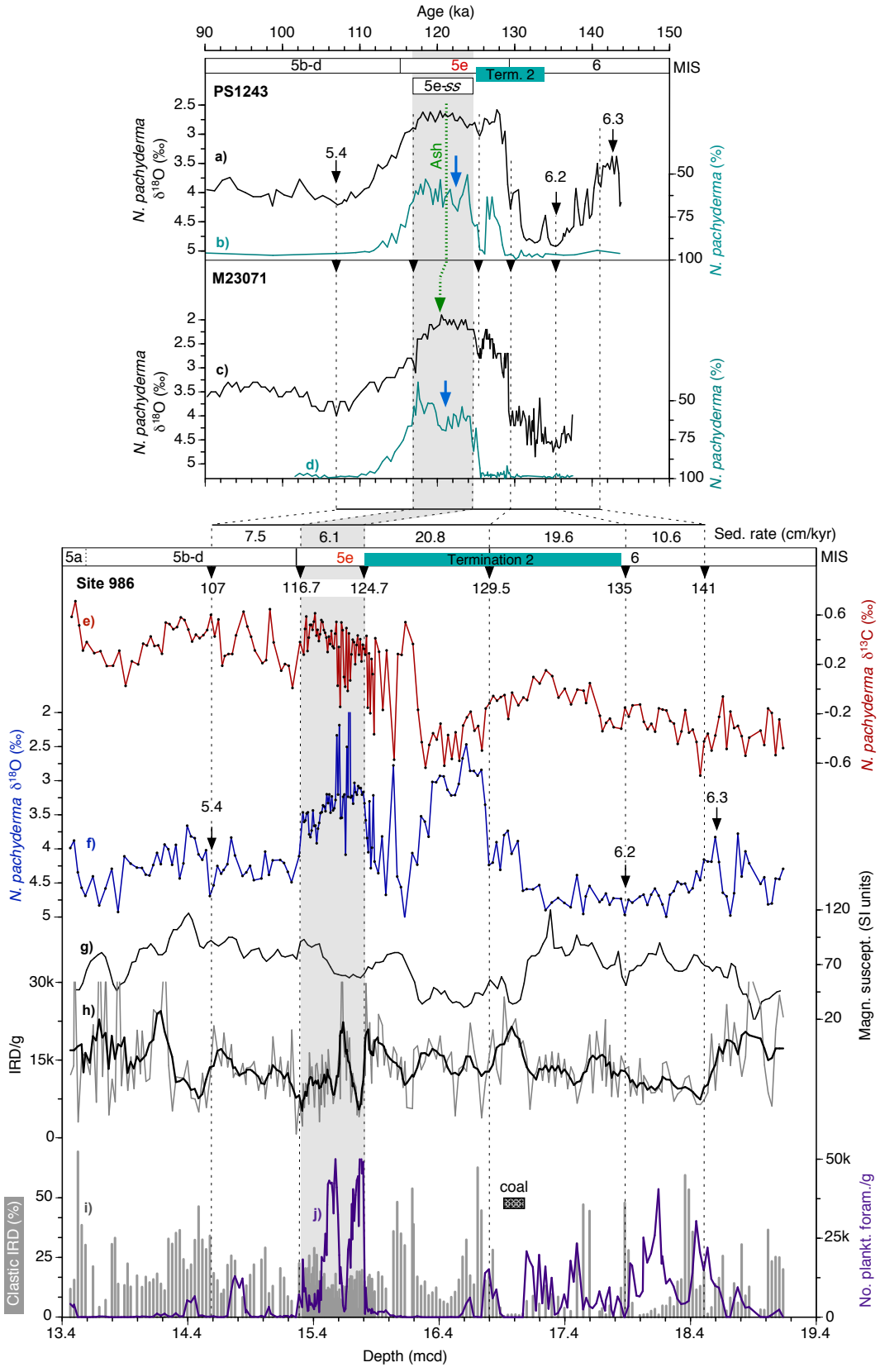

Figure 4.2: Age models for core M23071 (upper panel) (Bauch and Erlenkeuser, 2008) and Site 986 (lower panel). Vertical dashed lines show correlations to reference core PS1243 **(a-b)** (Bauch et al., 2012). Black triangles denote the applied tie points (see Table S4.1 in the Supplementary information). Isotopic events are indicated after Martinson et al. (1987). The grey bar marks the peak interglacial conditions (MIS 5e-*ss*). The dashed green line in **(a-b)** indicates the position of the 5e-Midt/RHY tephra in core PS1243 and the dashed green arrow in **(c-d)** marks the inferred stratigraphic position of this ash layer in core M23071, deduced from correlation with a core from the southeastern Norwegian Sea (Brendryen et al., 2010). Blue arrows denote the mid-MIS 5e cooling event (see text for discussion). Proxy records of Site 986 include **(e-f)** $\delta^{13}C$ and $\delta^{18}O$ values in *N. pachyderma*, **(g)** magnetic susceptibility from the Janus Web Database (http://www-odp.tamu.edu/database/), **(h)** IRD, grains per gram of dry sediment, **(i)** numbers of planktic foraminifera per gram of dry sediment and **(j)** relative abundances of clastic sedimentary rocks in the total amount of IRD grains.

4.5 Results

4.5.1 Site 986

Sediments comprising the late Saalian (MIS 6, between 144 and 132 ka) are characterized by high IRD amounts and variable, but generally elevated planktic foraminiferal abundances with highest numbers corresponding to reductions in clastic IRD (Fig. 4.3). At 132 ka negative trends in magnetic susceptibility and planktic $\delta^{13}C$ values commence. An abrupt increase in IRD and the virtual disappearance of planktic foraminifera at ca. 131 ka go along with a rapid decrease in planktic $\delta^{18}O$ values and could be ascribed to the onset of the main Saalian deglaciation (131-125 ka). Around 129.5 ka a short-term return to elevated planktic foraminiferal abundances and magnetic susceptibility coupled with slightly higher $\delta^{18}O$ values in *N. pachyderma* is noted.

The onset of peak last interglacial conditions (MIS 5e-*ss*, between 125 and 116.7 ka) corresponds in the eastern Fram Strait to an abrupt increase in numbers of planktic foraminifera coupled with a drop in IRD (Fig. 4.4). Following the taxonomic classification of Darling et al. (2006), small percentages of right-coiling tests of *N. pachyderma* (*<3 %)* calculated for MIS 5e-*ss* were regarded insignificant for paleoenvironmental reconstructions and added together with left-coiling specimens of *N. pachyderma.* Although *N. pachyderma* strongly dominates the foraminiferal assemblage across entire MIS 5e-*ss*, reduced proportions of this polar species are noted around 124 and 117 ka. This corresponds to increased relative and absolute abundances of subpolar planktic foraminifera *T. quinqueloba* and *Globigerinita* spp., as well as to elevated numbers of benthic *C. wuellerstorfi.*

Considering various sedimentological features, we distinguish between an early (125-120 ka) and a late (120-116 ka) phase within the MIS 5e-*ss* (Fig. 4.4). The early phase is characterized by enhanced shell fragmentation and high numbers of planktic foraminifera. A reduction in foraminiferal abundance noted around 122 ka is associated with an IRD increase, highly unstable planktic $\delta^{18}O$ values (between 0 and 4 ‰) and strong shell fragmentation. Following the beginning of the late phase of MIS 5e-*ss* at 120 ka, a rapid decrease in planktic foraminiferal abundance and an increase in planktic

and benthic $\delta^{18}O$ values together with a change towards higher fragmentation are observed. IRD amounts are generally higher than during the first phase of MIS5e-*ss*, however, the increase occurred already prior to 120 ka. After a coherent increase between 120 and 118.5 ka, a trend towards lighter oxygen isotopic values is noted in both benthic and planktic foraminifera. The second phase of MIS 5e-*ss* is concluded by a rapid increase in $CaCO_3$ preservation (low fragmentation) at 117 ka and lowered planktic and benthic $\delta^{18}O$ values.

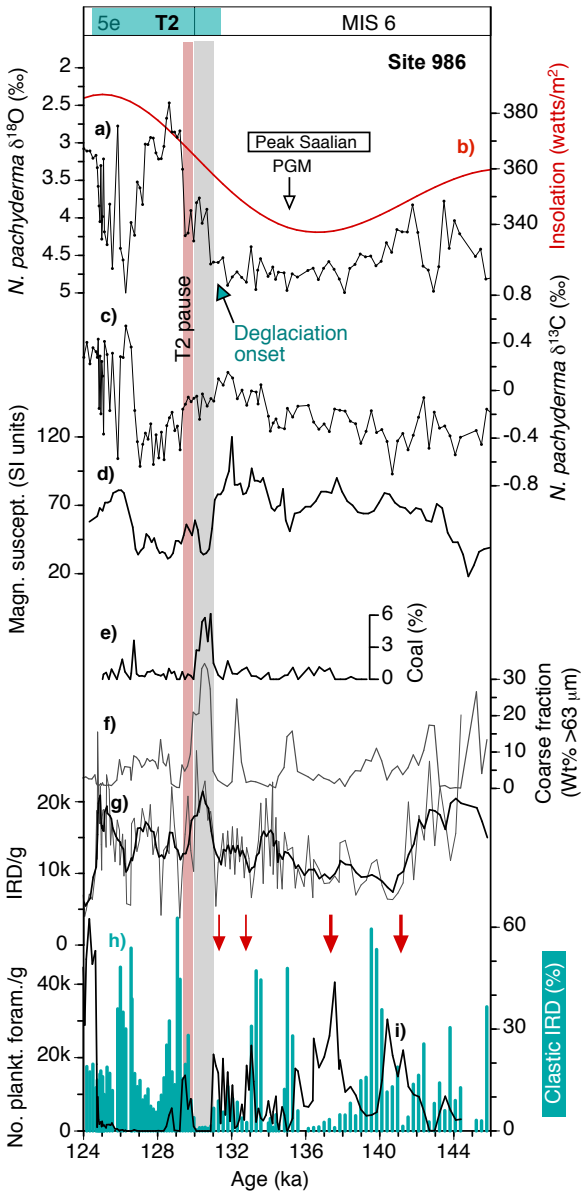

Figure 4.3: Proxy records from Site 986 for the late Saalian and Termination 2 (T2). (a and **c)** $\delta^{13}C$ and $\delta^{18}O$ values in *N. pachyderma,* **(d)** magnetic susceptibility from the Janus Web Database (http://www-odp.tamu.edu/database/), **(e)** proportion of coal fragments relative to the number of IRD grains, **(f)** >63µm fraction content, **(g)** IRD, grains per gram of dry sediment, **(h)** relative abundances of clastic sedimentary rocks in the total amount of IRD grains, **(i)** number of planktic foraminifera per gram of dry sediment. Also shown is **(b)** mean summer insolation at 75°N (computed with AnalySeries 2.0.8 (Paillard et al., 1996) using the Laskar et al. (2004) data). The red arrows mark Atlantic Water influence inferred for the late Saalian. The grey band indicates the first step of the Saalian deglaciation. The pink bar denotes the pause in the deglaciation. PGM – Penultimate Glacial Maximum.

4.6 Discussion

4.6.1 Late Saalian and Termination 2 in the eastern Fram Strait

During the late Saalian, including the penultimate glacial maximum at ~135 ka, inflows of warm AW facilitated seasonally open conditions and high planktic foraminiferal productivity along the western Svalbard margin (Fig. 4.3; Hebbeln and Wefer, 1997; Spielhagen et al., 2004). Despite the generally cold surface conditions reconstructed

farther upstream and to the north of the Greenland-Scotland Ridge (e.g., Bauch et al., 2012), such a strong AW impact on the eastern Fram Strait could have been amplified by several factors in a similar manner as was suggested for the Last Glacial Maximum (Nørgaard-Pedersen et al., 2003). Among them are a shallowing of the AW layer as a result of reduced halocline thickness, a relative strengthening of the Fram Strait branch at the expense of the blocked Barents Sea branch and/or the formation of open waters (polynyas) along the Svalbard-Barents Sea ice sheet margin (Nørgaard-Pedersen et al., 2003). It is further evident from our records that the peaks in clastic IRD deposition, largely indicating fluctuations of the proximal Svalbard-Barents Sea ice sheet, correspond with the low numbers of planktic foraminifera (Fig. 4.3), pointing to a rather local freshwater-related cause (i.e., near-surface salinities close to the tolerance limit of foraminifera) for some of the observed foraminiferal variability (e.g., around 140 and 135.5 ka).

An abrupt decrease of AW influence in the Fram Strait after the onset of the main Saalian deglaciation around 131 ka is deduced from the rapid disappearance of planktic foraminifera and a strong decrease in magnetic susceptibility (Fig. 4.3). The latter proved to be a reliable proxy for the strength of the meridional overturning as far north as the eastern Fram Strait, given that the transport of magnetic material from the nearby Knipovich Ridge is enhanced/reduced at times of intensified/suppressed northwardly propagating surface and deep water currents (Risebrobakken et al., 2006). In spite of strong post-Saalian insolation forcing, our planktic foraminiferal abundance record thus argues for a relatively warm "glacial world" when compared to the ensuing T2, which in the northern North Atlantic continued well into MIS 5e (e.g., Van Nieuwenhove et al., 2011).

During its first step, from 131 to 130 ka, T2 is indicated by a rapid lowering in planktic $\delta^{18}O$ values and an increased input of the non-clastic IRD (Fig. 4.3). This relatively well-sorted, medium to fine-grained sand layer also contains coal fragments, which may point to both the westernmost Siberian shelf region and the northwestern European ice sheet margin as potential source areas for the icebergs (Bischof et al., 1990; Wagner and Henrich, 1994; Henrich et al., 1995). In contrast, the major meltwater event that followed at ~129 ka more likely involved disintegration of the Svalbard-Barents Sea ice sheet, as can be deduced from the high proportions of clastic IRD.

4.6.2 MIS 5e-ss (~125-116 ka) in the eastern Fram Strait

Studies from the Fram Strait have shown that increased abundances of planktic foraminifera occur at marginal ice zones where sea-ice melt fosters primary production in a stratified water column (Wadhams, 1986; Hebbeln and Wefer, 1991; Carstens et al., 1997; Pados and Spielhagen, 2014). Accordingly, the rather high absolute abundances of cold-water adapted *N. pachyderma* during early MIS 5e-*ss* (125-120 ka) may be associated with increased food availability close to the sea-ice edge (Fig. 4.4). The notably lower $\delta^{13}C$ values of *N. pachyderma* recorded at nearby site MD99-2304, which

may have experienced a stronger influence of the WSC (Fig. 4.1; Risebrobakken et al., 2005, 2007), similarly suggest that a highly productive and thus ^{12}C-depleted ArW-like water mass may have prevailed at Site 986.

The relatively high proportions of subpolar planktic species – *T. quinqueloba* and *Globigerinita* spp. – in conjunction with elevated numbers of benthic *C. wuellerstorfi* around 124 ka may reflect the influence of warm and saline waters of Atlantic origin, high primary productivity, and at least seasonally open water conditions in the eastern Fram Strait (Wollenburg et al., 2001). Importantly, the increase in proportion of subpolar planktic foraminifera appears to lag slightly behind the climatic amelioration which is deduced at Site 986 from the rapid increase of foraminiferal abundance and the IRD decrease already at ~125 ka (Fig. 4.4). Likewise, the foraminifera-rich but IRD-poor layer centered at 121 ka lacks a clear response in the subpolar assemblage. Strong foraminiferal fragmentation and selective dissolution of less calcified subpolar species may partly explain such a weak and sporadic response in our faunal proxies.

The significant return to cold conditions around ~122 ka with low planktic foraminiferal abundance and no subpolar species but high amounts of IRD is framed by large-amplitude fluctuations in planktic $\delta^{18}O$ and $\delta^{13}C$ (Fig. 4.4). While the depletions in planktic $\delta^{18}O$ and $\delta^{13}C$ suggest at least two pronounced meltwater events, the strong cooling in-between seems corroborated by the positive excursion in $\delta^{18}O$ values of *C. wuellerstorfi* and *N. pachyderma.* Although we cannot point to the actual source area of meltwater before and after this significant climatic episode, our data clearly demonstrate a freshwater-induced cooling, probably as a result of enhanced regional iceberg activity.

The mid-MIS 5e cold event in the eastern Fram Strait does not appear to be of local nature. On a more regional level a very pronounced mid-MIS 5e cooling was noted for the eastern Norwegian Sea (Bauch et al., 2011) and in Scandinavia (Helmens et al., 2015; Plikk et al., 2016). At site PS1243, in the central Nordic Seas, a cold event, interpreted as an eastward expansion of Polar Water (Thibodeau et al., 2017), occurred ~1 ka prior to deposition of the 5e-Midt/RHY ash layer (~121 ka on the AICC2012 age scale). This finding has important implications, when constraining stratigraphic position of the mid-MIS 5e cooling event in other high-latitude records containing tephra deposits (Fig. 4.2a-d; e.g., Cortijo et al., 1994; Fronval and Jansen, 1997; Fronval et al., 1998).

From about 120 ka onwards our proxy records suggest decreasing sea surface temperatures (SSTs) in the eastern Fram Strait, more or less in phase with insolation decrease and cooling over Greenland (Fig. 4.4). This cooling trend may be termed MIS 5e-Neoglaciation (in analogy to the late Holocene cooling, see e.g., Werner et al., 2016) and is inferred from a significant increase in $\delta^{18}O$ values of *N. pachyderma*, elevated amounts of IRD and a strongly diminished presence of subpolar foraminifera. The cooling trend probably led to regional advances of polar ice caps (Fronval and Jansen, 1997), and it was likely contemporaneous to a SST drop found in the western Iceland Sea (Van Nieuwenhove et al., 2013) and off southern Greenland (Irvali et al., 2016), altogether

pointing to a climatic link between regions strongly affected by the polar waters of the East Greenland Current (e.g., Born et al., 2010).

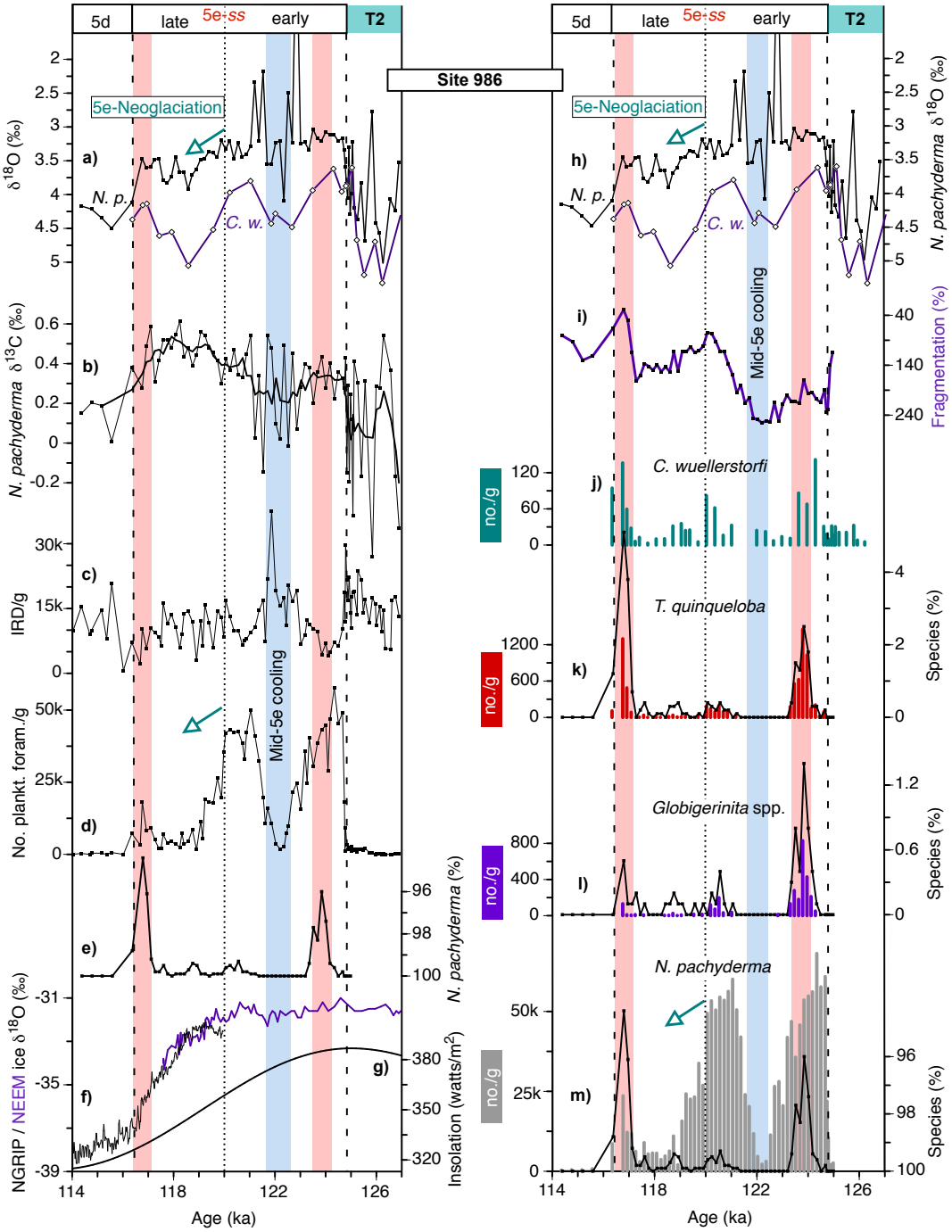

Figure 4.4: Proxy records from Site 986 for MIS 5e-ss: (a and **h)** $\delta^{18}O$ values of *N. pachyderma* (*N. p.*) and *C. wuellerstorfi* (*C. w.*), **(b)** $\delta^{13}C$ values of *N. pachyderma*, **(c)** IRD, grains per gram of dry sediment, **(d)** number of planktic foraminifera per gram of dry sediment, **(e)** percentage of *N. pachyderma*, **(i)** degree of fragmentation of planktic foraminiferal tests, **(j)** number of *C. wuellerstorfi* per gram of dry sediment, **(k-m)** percentage and number per gram of dry sediment of *T. quinqueloba*, *Globigerinita* spp. and *N. pachyderma*, respectively. Also shown are **(f)** Greenland ice core data (NorthGRIP Community Members, 2004; NEEM Community Members, 2013) and **(g)** mean summer insolation at 75°N (Laskar et al., 2004). Pink bars indicate the intervals of enhanced surface oceanic heat transfer at 124 and 117 ka. Blue bars mark the mid-5e cooling event. Also indicated is the surface cooling trend during late MIS 5e (5e-Neoglaciation).

An interesting feature which interrupted the late MIS 5e sea surface cooling trend is the intermittent increase of *T. quinqueloba* proportion at ~117 ka, time-coeval with a significant improvement in $CaCO_3$ preservation, low IRD, and decreased $\delta^{18}O$ values of *N. pachyderma* (Fig. 4.4). In agreement with other studies (Risebrobakken et al., 2005, 2007), we interpret these data to reflect an intensified northward AW advection just prior to the last glacial inception.

It seems evident that local oceanic processes (e.g., brines) could have affected our benthic $\delta^{18}O$ record, also within the MIS 5e period of low global ice volume (128-116.1 ka; Shackleton et al., 2002). Whatever the mechanisms, the coherent behavior of the planktic and benthic $\delta^{18}O$ records during late MIS 5e-*ss* is interesting (Fig. 4.4a). The positive planktic and benthic $\delta^{18}O$ trends from about 120 ka (and following the onset of the 5e-Neoglaciation) reverse after 118.5 ka. The change towards lighter planktic isotopic values may represent a climatic amelioration at a subsurface depth, linked to a strengthening of AW advection. The aforementioned rapid increase in relative abundances of subpolar species *T. quinqueloba* at 117 ka occurs simultaneously with a strong reduction of foraminiferal shell fragmentation and clearly after the $\delta^{18}O$ values in *N. pachyderma* had lowered. It could therefore be speculated that, while the AW advection at the subsurface depths intensified from 118.5 ka on, it was only at 117 ka when a rapid hydrographic change allowed for a better preservation of *T. quinqueloba*. The intensification of the northward-directed subsurface and deep water currents during late MIS 5e may be further supported by the increased magnetic susceptibility values noted for this time interval in our core record (Fig. 4.2g; Risebrobakken et al., 2006).

Several studies have revealed that the strongest AW influence in the polar North occurred towards the late phase of MIS 5e (Bauch et al., 1999; Hald et al., 2001; Risebrobakken et al., 2005, 2007; Van Nieuwenhove et al., 2011). In addition to these earlier studies, our new high-resolution data emphasize that in the Arctic Gateway this late intensification of near-surface AW advection was superimposed on a longer-term cooling trend at the sea surface (5e-Neoglaciation) that started from about 120 ka on (Fig. 4.4).

4.6.3 Expansion of Atlantic Water during MIS 5e: from the Norwegian Sea to the Fram Strait

Although interpretation of proxy records from the Fram Strait is complicated by the complex regional hydrography and variable calcite corrosion, our new record clearly corroborates the two-phase picture of enhanced dominance of AW during MIS 5e-*ss* (Fig. 4.4; see also Risebrobakken et al., 2005, 2007). Moreover, this assumption is in agreement with the circulation pattern reconstructed from farther south, on the Vøring Plateau (e.g., Bauch and Erlenkeuser, 2008; Bauch et al., 2011), implying a rather coherent AW heat transfer through the eastern Nordic Seas and into the high Arctic.

On the basis of different climatic proxies, it was revealed for the Norwegian Sea that the full marine optimum (in terms of both diminished sea surface freshening and maximum presence of AW) was reached only at the end of the Last Interglacial, between ~118.5 and

116 ka, when insolation was already quite low (Fig. 4.5; Van Nieuwenhove et al., 2008; Bauch and Erlenkeuser, 2008; Van Nieuwenhove and Bauch, 2008; Bauch et al., 2011). In spite of some possible uncertainties in age models, this late MIS 5e-*ss* intensification of the poleward heat flux corresponds well in time with the late AW pulse found in the Fram Strait (Fig. 4.6).

In core M23071, the full marine optimum between ~118.5 and 116 ka coincides with the highest shares of *T. quinqueloba*, whereas the proportions of *N. incompta* remain relatively low (Fig. 4.5; Van Nieuwenhove et al. 2008). A comparable antiphase behavior of *T. quinqueloba* and *N. incompta* is also noted for the early Holocene. Considering that the modern maximum abundance of *N. incompta* in sediment surface samples is along the southern Norwegian margin (Pflaumann et al., 1996), its decreasing shares during late MIS 5e could be attributed to a diminishing influence of the freshwater-enriched Norwegian Coastal Current (Van Nieuwenhove et al. 2008). Further, we interpret the increasing numbers of *T. quinqueloba* in core M23071 after 118.5 ka in terms of an eastward expansion of ArW, in agreement with previous studies (Johannessen et al., 1994; Risebrobakken et al., 2005, 2007; Van Nieuwenhove et al. 2008).

Regarding interpretations of *T. quinqueloba* occurrence, however, we refrain from strictly interpreting this species as an indicator of the Arctic Front (cf. Johannessen et al., 1994), since it is evident that *T. quinqueloba* was widespread almost everywhere in the Nordic Seas throughout the early to mid-Holocene (Bauch et al., 1999; Risebrobakken et al., 2011; Van Nieuwenhove et al., 2013). The strong affinity of this species to the Arctic Front appears particularly problematic in the narrow Fram Strait with its complex surface hydrography. There, enhanced proportions of *T. quinqueloba* (core tops) are usually associated with AW inflows rather than with frontal systems as found to the west and to the east of the Atlantic Domain (Fig. 4.1B; Husum and Hald, 2012; Pados and Spielhagen, 2014).

A potential cause that facilitated the presence of more warm and salty AW in the Fram Strait during the terminal phase of MIS 5e was a spatial shrinkage of the subpolar gyre in the North Atlantic, leading to a relative increase of subtropical inflows into the Nordic Seas (Born et al., 2010, 2011; Mokeddem et al., 2014). A shift towards a more positive North Atlantic Oscillation (NAO) mode was also suggested (Bauch and Kandiano, 2007; Risebrobakken et al., 2007), and in a similar manner the same was inferred for the AW strengthening during the early Holocene (Rimbu et al., 2003). Such an increase in heat transport is in line with modern observations from the Norwegian Sea revealing, for times of positive NAO, a reduced heat loss from the NwAC as a result of a restricted current width (Blindheim et al., 2000; Blindheim and Østerhus, 2005).

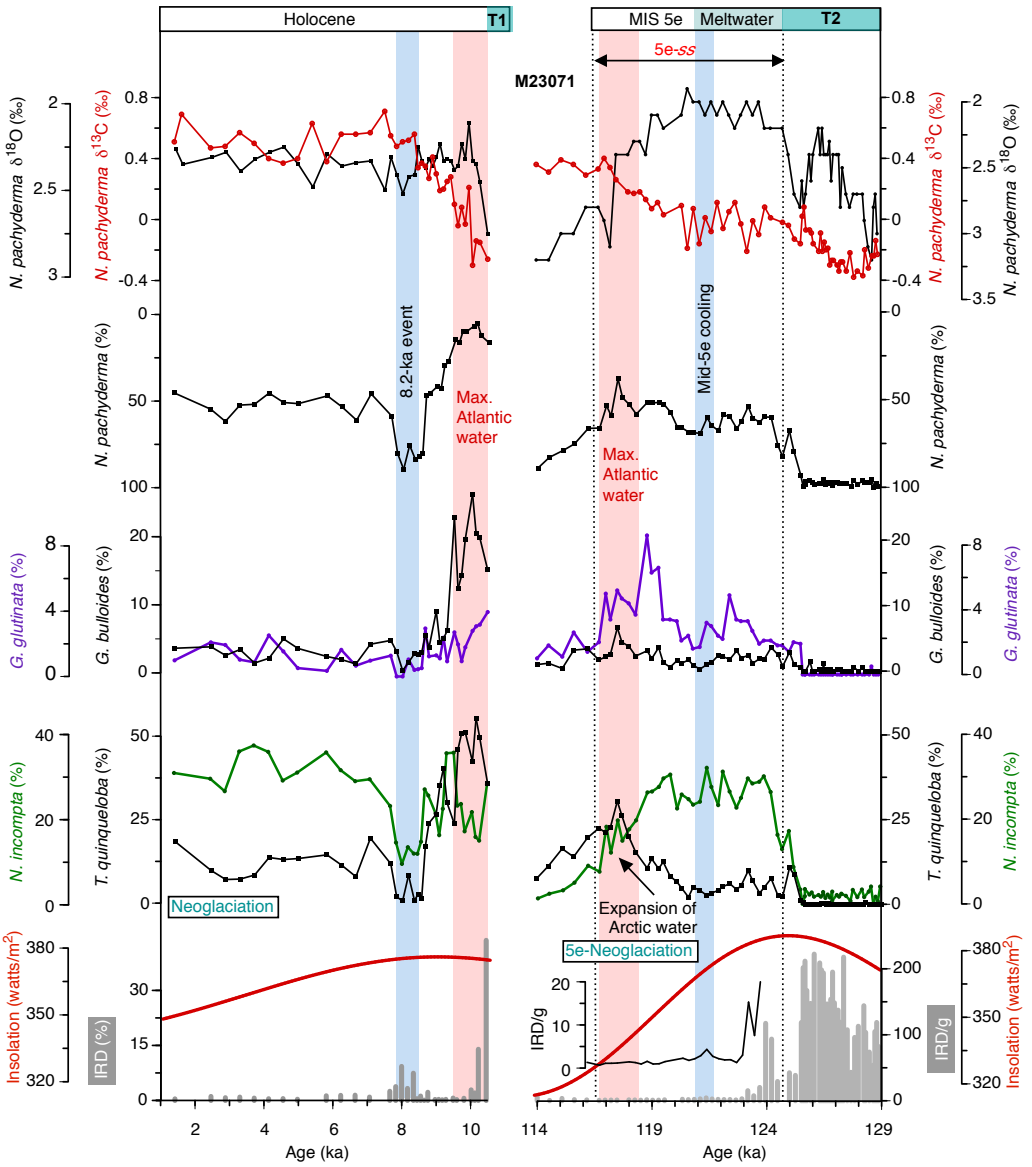

Figure 4.5: Comparison of climatic records for the Holocene (this study, Voelker, 1999) and MIS 5e from core M23071 (Bauch and Erlenkeuser, 2008; Van Nieuwenhove et al., 2008). Proxy data include (from top to bottom) $\delta^{13}C$ and $\delta^{18}O$ values of *N. pachyderma*, percentage of *N. pachyderma*, *G. glutinata*, *G. bulloides*, *N. incompta* and *T. quinqueloba* and IRD proxies (for Holocene - proportion of IRD grains relative to the number of planktic foraminifera, for MIS 5e - number of IRD grains per gram of dry sediment). Also shown is mean summer insolation at 75°N (Laskar et al., 2004). Pink bars denote intervals of inferred maximum northward Atlantic Water advection. Blue bars mark the 8.2-ka cold event during the Holocene and the mid-MIS 5e cooling event. Also indicated are the Neoglacial cooling trends during late Holocene (e.g. Werner et al., 2016) and late MIS 5e.

4.6.4 Comparing Atlantic Water heat fluxes during the last two interglacials

Most foraminifera-based Holocene records from along the Barents Sea-Svalbard margin prove maximum poleward advection of warm and salty AW during the early phase, between ~11 and 9 ka (Sarnthein et al., 2003; Hald et al., 2007; Risebrobakken et al., 2011; Werner et al., 2016). The early Holocene AW intensification was associated with occurrences of near-surface dwelling species *G. bulloides* - today restricted to the Atlantic

Domain of the southern Nordic Seas (Pflaumann et al., 1996) - as far north as the NW Svalbard margin (Aagaard-Sørensen et al., 2014; Werner et al., 2016). Although existing foraminifera-based (transfer function) SSTs do not reconstruct a comparable early Holocene peak near the mid-Norwegian continental margin (Risebrobakken et al., 2003; Andersson et al., 2010), our census data from the flowpath center of the NwAC, site M23071 on the southern Vøring Plateau (Fig. 4.1), now clearly demonstrate the same early Holocene AW strengthening (Fig. 4.5). This finding implies a rather coherent propagation of oceanic heat from the southern Nordic Seas through the eastern Fram Strait and into the high Arctic.

Significantly higher-than-Holocene proportions of polar species *N. pachyderma* found during MIS 5e in the northern Nordic Seas have previously been interpreted as indications of reduced flux of AW heat into the northern Nordic Seas during the Last Interglacial (Fig. 4.6; Bauch et al., 1999). On the contrary, it was stated that carbonate dissolution during MIS 5e could have biased the foraminifera-based reconstructions towards colder oceanic conditions (e.g., Knies et al., 1998; Matthiessen et al., 2001). Notwithstanding the specific mechanism behind foraminiferal shell corrosion at our site (Fig. 4.4i), we argue that the enhanced fragmentation could generally be attributed to marginal ice zone conditions and sea-ice related processes coupled with a reduced influence of AW at our site during MIS 5e. Associated with marginal ice zones, enhanced primary productivity and increased flux of organic matter could lead to increased acidity at the sea bottom, causing enhanced calcite dissolution (Berger et al., 1982; Huber et al., 2000). An influence of more productive ArW-like water masses at our site may be discerned from high $\delta^{13}C$ values in *N. pachyderma*. In contrast, good calcite preservation was reported from nearby site MD99-2304 which may have been influenced by less productive AW-like water masses, as evidenced by remarkably lower planktic $\delta^{13}C$ values (Risebrobakken et al., 2005, 2007). On the other hand, lateral transportation of foraminifera across the narrow domain between the two discussed cores should not be neglected, as it would likely level out such sharp sea surface gradients during the sedimentation process (von Gyldenfeldt et al., 2000). Considering the close vicinity to shelf areas with potential brine formation (Rasmussen and Thompsen, 2009), the observed strong shell fragmentation at Site 986 may also be related to the influence of corrosive brine waters, enriched in organic carbon and respiratory CO_2 (Steinsund and Hald, 1994; Giannelli et al., 2001), and therefore probably indicating enhanced sea-ice production in the Fram Strait during MIS 5e. Finally, it has been shown for the Fram Strait that good carbonate preservation characterized the early Holocene when AW advection was at a maximum (Fig. 4.6; Rasmussen et al., 2007; Zamelczyk et al., 2014; Werner et al., 2016). Analogously, the significantly improved preservation of foraminiferal shells notable at our site during late MIS 5e (~117 ka) could perhaps reflect the phase with the strongest AW influence in the eastern Fram Strait.

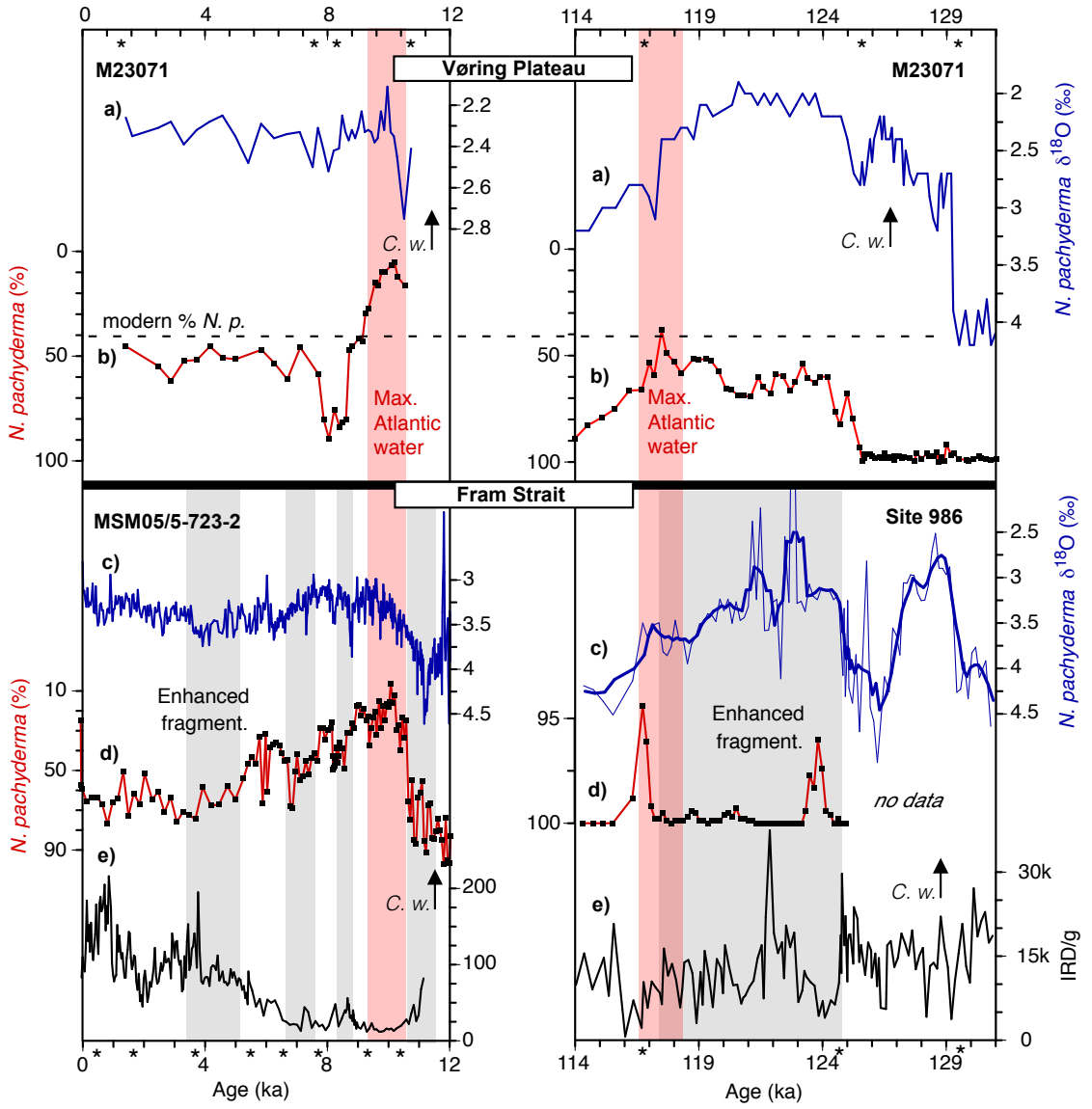

Figure 4.6: Correlation of Holocene and MIS 5e climatic events between the Vøring Plateau core M23071 (this study, Voelker, 1999; Bauch and Erlenkeuser, 2008; Van Nieuwenhove et al., 2008) and Fram Strait cores MSM05/5-723-2 (Werner et al., 2016) and Site 986 (this study). Proxy records in core M23071 for the Holocene and MIS 5e intervals include **(a)** $\delta^{18}O$ values of *N. pachyderma* and **(b)** percentage of *N. pachyderma*. Proxy records from core MSM05/5-723-2 and Site 986 include **(c)** $\delta^{18}O$ values in *N. pachyderma,* **(d)** percentage of *N. pachyderma* and **(e)** IRD, grains per gram of dry sediment. Modern proportion of *N. pachyderma (N. p.)* in the Norwegian Sea is from Pflaumann et al (1996). Pink bands denote intervals of inferred maximum northward Atlantic water advection. Periods of enhanced planktic foraminiferal shell fragmentation are highlighted in grey. First major occurrences of *C. wuellerstorfi (C. w.)* are indicated by arrows (data after Sarnthein et al., 2003; Bauch et al., 2011; Werner et al., 2016). Age control points (Holocene in M23071 from Voelker (1999) and in MSM05/5-723-2 from Werner et al. (2016); MIS 5e in M23071 and Site 986 from this study) are marked by asterisks.

The reason why less near-surface heat was carried by AW northward to the eastern Fram Strait during MIS 5e compared to the early Holocene may be explained by a greater water depth of the AW flow within the Nordic Seas due to the existence of a thicker, colder and more freshened surface layer in the course of a rather long Saalian deglaciation (e.g., Bauch, 2013; Thibodeau et al., 2017). Such a layer could have changed not only the

oceanic conditions, but also inhibited the environmental preferences (e.g., food and light availability) of shallow-dwelling subpolar foraminifera in the eastern Fram Strait. Superimposed on strong carbonate dissolution, this has made it more difficult to trace the propagation of AW heat flux towards the polar North during entire MIS 5e, when compared to the early Holocene.

It has been suggested for MIS 5e that the very warm waters passed the western Svalbard continental margin during MIS 5e, entered the Arctic Ocean and spread across the Yermak Plateau as well as the northern Eurasian shelves (Nowaczyk et al., 1994; Matthiessen et al., 2001; Spielhagen et al., 2004). Our new data, however, underscore a significantly reduced flux of oceanic heat from the Atlantic through the eastern part of the Arctic Gateway. This should be taken in account when reconstructing the last interglacial conditions in the Eurasian sector of the Arctic Ocean.

Although maximum AW influence in the eastern Fram Strait was attained only late in the Last Interglacial, it should be noted that AW penetrated northward across the Greenland-Scotland Ridge already during the early Saalian deglaciation. A presence of AW during T2 is evident during the "pause" in the deglacial trend at about 130 ka, reflected by elevated numbers of planktic foraminifera and increased magnetic susceptibility values at Site 986 (Fig. 4.3; Risebrobakken et al., 2006). Further evidence of subsurface poleward flow of AW during T2 comes from the ubiquitous finds of subtropical species *B. megastoma* in the Nordic Seas (Bauch, 1996) and benthic foraminifera of the "Atlantic group" on either side of the Iceland-Scotland Ridge (Rasmussen et al., 2003b).

High-resolution records from underneath the main flowpath of AW suggest a roughly simultaneous post-Saalian appearance of the suspension-feeding epibenthic species *C. wuellerstorfi* (Struck, 1997; Wollenburg et al., 2001) during the second major meltwater event at about ~128-127 ka (Fig. 4.6). A solid age estimation of 11.5-11.3 ka was deduced for the first major occurrence of this species during the Holocene (Sarnthein et al., 2003; Werner et al., 2016). At face value, such occurrences of *C. wuellerstorfi* may imply a comparable "early interglacial" timing of bottom current activation linked to first AW intrusions during both Holocene and MIS 5e. However, the continuing Saalian deglaciation of the northern Eurasian continental margin with its longer-than-T1 duration of meltwater discharge likely obscured an AW-related early warming in the eastern Nordic Seas comparable to that in the early Holocene. By contrast, coring sites in the central Nordic Seas, i.e., away from the collapsing European and Greenland ice sheets, were less affected by deglacial freshwater influence and do indeed reveal the AW-driven SST increase during early MIS 5e/late T2, at ~128 ka (Fig. 4.2b; Bauch et al., 2012; Bauch, 2013; Zhuravleva et al., 2017b). This supports the view that a very thick halocline, a result of sizeable post-Saalian meltwater input from the surrounding continents, rather than a strongly reduced or absent AW inflow was likely responsible for the low faunal signal along the Norway-Svalbard continental margin.

4.7 Conclusions

A new multi-proxy record from the eastern Fram Strait allows to reconstruct the AW heat transport at the Arctic Gateway from the late Saalian (144-130 ka) through the Last Interglacial (130-116 ka) in unprecedented resolution. During the penultimate glacial maximum, rather strong impact of AW facilitated high planktic foraminferal productivity and seasonally ice–free conditions off western Svalbard. Although the influence of AW during the Saalian deglaciation was notably decreased, the inflows of Atlantic-derived waters into the Nordic Seas never completely stopped. For MIS 5e our study confirms earlier conclusions on a generally reduced influence of AW in the high-northern latitudes. When compared to the early Holocene, a less pronounced signal of the AW flow into the Arctic region during the Last Interglacial could be explained by:

1) a thicker post-Saalian halocline and a greater water depth flow of AW;

2) a longer-lasting Saalian deglaciation which delayed the surface warming relative to solar radiation;

3) a reduced strength of AW inflows related to the oceanic-atmospheric system, i.e., wind patterns, oceanographic fronts and gyre intensities;

4) some bias due to a variable preservation of biogenic carbonate.

Our data further reveal the mid-MIS 5e cooling off Svalbard triggered by an iceberg/meltwater event. We conclude that the AW influence on the upper water hydrography in the Fram Strait was strongest during the late phase of MIS 5e-*ss*, corresponding in time with a period of diminished sea surface stratification and peak surface ocean heat transfer to the Norwegian Sea. We finally emphasize that the recognition of a generally weaker-than-Holocene AW influence in the polar North during MIS 5e needs to be taken into account for more plausible interpretations of circum-Arctic fossil records from the last interglacial period.

Acknowledgments

This study used samples and data provided by the Ocean Drilling Program. We thank T. Snow and A. Shevenell for providing insight into some core material and unpublished isotopic data from ODP Site 986. W. Hale is thanked for his help during sampling at the IODP Bremen Core Repository, S. Fessler and C. Not for performing measurements on stable isotopes. We also thank two anonymous referees for their constructive comments, which helped us to improve the manuscript. This work was supported by the German Federal Ministry of Education and Research (BMBF), project "Laptev-Sea: TRANSDRIFT" (BMBF grant 03G0833C) and the German Research Foundation (DFG grant BA1367/12-1).

Supplementary information

The Atlantic Water heat transfer through the Arctic Gateway (Fram Strait) during the Last Interglacial

Table S4.1: Tie points used to transfer records onto AICC2012 age scale.

Abbreviations

IE: Isotopic event
NP: *Neogloboquadrina pachyderma*

Core	Depth [cm]	Depth [m]	Age [ka BP]	Sedimentation Rate [cm/kyr]	Rationale
M23071	610	6.1	107	1.9	IE 5.4
	628	6.28	116.7	3.9	Coherence with PS1243[a)] NP $\delta^{18}O$ (glacial inception)
	662	6.62	125.5	12.5	Coherence with PS1243 NP $\delta^{18}O$ (end of deglacial termination)
	712	7.12	129.5	11.6	Coherence with PS1243 NP $\delta^{18}O$ (MIS 6/5e boundary)
	776	7.76	135	11.6	IE 6.2
Site 986	1458	14.58	107	7.5	IE 5.4
	1531.1	15.311	116.7	6.1	Coherence with M23071 NP $\delta^{18}O$ (glacial inception)
	1579.7	15.797	124.7	20.8	Coherence with M23071 NP $\delta^{18}O$ (onset of MIS 5e-*ss*)
	1679.5	16.795	129.5	19.6	Coherence with M23071 NP $\delta^{18}O$ (MIS 6/5e boundary)
	1787.4	17.874	135	10.6	IE 6.2
	1850.9	18.509	141	10.6	Coherence with PS1243 NP $\delta^{18}O$ (end of IE 6.3)

a) Age model for core PS1243 is from Zhuravleva et al. (2017b)

Chapter 5

The last interglacial (MIS 5e) cycle at Little Bahama Bank: A history of climate and sea-level changes

Anastasia Zhuravleva[1] and Henning A. Bauch[2]

[1]Academy of Sciences, Humanities and Literature | Mainz c/o GEOMAR Helmholtz Centre for Ocean Research, Wischhofstr. 1-3, 24148 Kiel, Germany
[2]Alfred Wegener Institute Helmholtz Centre for Polar and Marine Research c/o GEOMAR Helmholtz Centre for Ocean Research, Wischhofstr. 1-3, 24148 Kiel, Germany

Under review in Climate of the Past

Abstract. Shallow-water sediments of the Bahama region containing the last interglacial (MIS 5e) are ideal to investigate the region's sensitivity to past climatic and sea level changes. Here we present new faunal, isotopic and XRF-sediment core data from the northern slope of the Little Bahama Bank. The results suggest that the bank top remained flooded across the last interglacial "plateau", ~129-117 ka, arguing for a relative sea level above -6 m for this time period. In addition, climatic variability, which today is closely coupled with movements of the Intertropical Convergence Zone (ITCZ), is interpreted based on stable isotopes and foraminiferal assemblage records. During early MIS 5e, the mean annual ITCZ position moved northward in line with increased solar forcing and a recovered Atlantic Meridional Overturning Circulation (AMOC). The early MIS 5e warmth peak was intersected, however, by a millennial-scale cooling event, consistent with a southward shift in the mean annual ITCZ position. This tropical shift is ascribed to the transitional climatic regime of early MIS 5e, characterized by persistent high-latitude freshening and, thereby, unstable AMOC mode. Our records from the Bahama region demonstrate that not only was there a tight relation between local sedimentation regimes and last interglacial sea level history, via the atmospheric forcing we could further infer an intra-interglacial connectivity between the polar and subtropical latitudes that left its imprint also on the ocean circulation.

5.1 Introduction

The last interglacial (MIS 5e) has attracted a lot of attention as a possible analog for future climatic development as well as a critical target for validation of climatic models. This globally warmer-than-preindustrial interval is associated with significantly reduced ice sheets and a sea level rise up to 6-9 meters above the present levels (Dutton et al., 2015; Hoffman et al., 2017). However, controversy still exists regarding the initiation and duration of the sea level highstand as well as about any sea level variability within that time period (Hearty et al., 2007; Kopp et al., 2009; Grant et al., 2012; Masson-Delmotte et al., 2013). Also, the spatial coverage of the existing sea surface temperature (SST) reconstructions is insufficient to allow for a robust understanding of the climatic forcings at play during the last interglacial.

At the western boundary of the wind-driven subtropical gyre (STG), sediments from the

shallow-water carbonate platforms of the Bahama archipelago can serve as an important climatic link between the tropical and subpolar North Atlantic. Given its critical location near the origin of the Gulf Stream, sediment records from the Bahama Bank region have been investigated in terms of climatic variability, ocean circulation, sea level change and sediment diagenesis (Slowey and Curry, 1995; Henderson et al., 2000; Slowey et al., 2002; Roth and Reijmer, 2004; 2005; Chabaud, 2016). For the last interglacial, earlier studies were focused on absolute dating of corals and sediments (Neumann and Moore, 1975; Slowey et al., 1996; Henderson and Slowey, 2000) as well as on coastal geomorphology and changes in sediment properties in relation to sea level fluctuations (Hearty and Neumann, 2001; Lantzsch et al., 2007; Chabaud et al., 2016). However, a thorough study of the last interglacial climate evolution underpinned by a critical stratigraphical insight deduced from periplatform oozes is lacking so far, as previous authors mainly worked on timescales covering several interglacials (Lantzsch et al., 2007; Chabaud et al., 2016). Here, we attempt to close this gap, by using core MD99-2202 from the upper northern slope of the Little Bahama Bank (LBB), which is the northernmost shallow-water carbonate platform of the Bahamian archipelago.

5.2 Regional Setting

Core MD99-2202 (27°34.5´N, 78°57.9´W, 460 m water depth) was taken from the northern slope of the LBB in the vicinity to the western boundary current of the North Atlantic STG, the Gulf Stream (Fig. 5.1A). The Gulf Stream supplies both heat and salt to the high northern latitudes and thereby constituting the upper cell of the Atlantic Meridional Overturning Circulation (AMOC). It originates from the Florida Current after it leaves the Gulf of Mexico through the Straits of Florida and merges with the Antilles Current to the north of the LBB.

In the western subtropical North Atlantic two distinctly different layers can be distinguished within the upper 500 m of the water column. The uppermost mixed layer (upper 50-100 m) is occupied by warm and comparatively fresh waters (T>24 °C, S<36.4 psu), predominantly coming from the equatorial Atlantic (Schmitz and McCartney, 1993; Johns et al., 2002). Properties of this water mass vary significantly on seasonal timescales and are closely related to the latitudinal migration of the Intertropical Convergence Zone (ITCZ) (Fig. 5.1B-C). During boreal winter (December-April), when the ITCZ is at its southernmost position, the Bahama region is dominated by relatively cool, stormy weather with prevailing northern and northeastern trade winds and is affected by cold western fronts, that increase evaporation and vertical convective mixing (e.g., Wilson and Roberts, 1995). During May to November, as the ITCZ moves northward, the LBB is influenced by relatively weakened trade winds from the east and southeast, by increased precipitation and very warm waters of Atlantic Warm Pool (T>28.5 °C), which expand into the Bahama region from the Caribbean Sea and the equatorial Atlantic (Stramma and Schott, 1999; Wang and Lee, 2007; Levitus et al., 2013). Today the LBB region lies at the northern edge of the influence of the Atlanitc Warm Pool, making our site particularly sensitive to monitor past shifts of the ITCZ. The

mixed layer is underlain by a thermocline layer, which is comprised of a homogeneous pool of comparatively cool and salty (12<T<24 °C, S>36.4 psu) water (Schmitz and Richardson, 1991). These "mode" waters are formed in the North Atlantic STG through wintertime subduction of surface waters driven by wind-driven Ekman downwelling and buoyancy flux (Slowey and Curry, 1995).

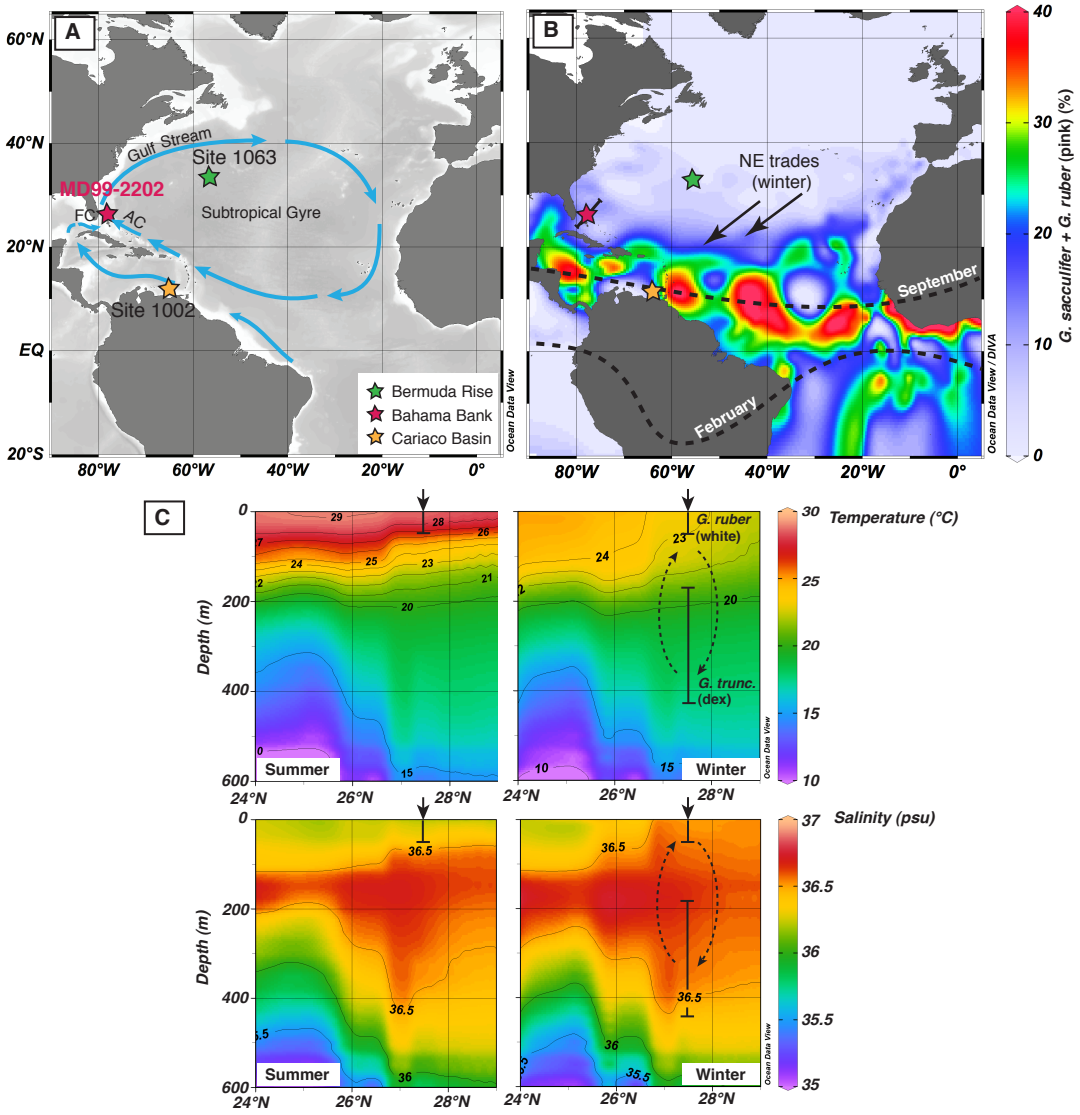

Figure 5.1: Maps showing positions of investigated core records and atmospheric/oceanic circulation. (**A**) Simplified surface water circulation in the (sub)tropical North Atlantic and positions of investigated sediment records: MD99-2202 (27°34.5´N, 78°57.9´W, 460 m water depth; *this study*), Ocean Drilling Program (ODP) Site 1002 (10°42.7´N, 65°10.2´W, 893 m water depth; Gibson and Peterson, 2014) and ODP Site 1063 (33°41.4´N, 57°37.2´W, 4584 m water depth; Deaney et al., 2017). **(B)** Relative abundances of tropical foraminifera *G. sacculifer* and *G. ruber* (pink) (Siccha and Kučera, 2017) and positions of the Intertropical Convergence Zone (ITCZ) during boreal winter and summer. **(C)** Summer and winter hydrographic sections (black line in **B)**, showing temperature and salinity obtained from World Ocean Atlas (Levitus et al., 2013). Vertical bars denote calcification depths of *G. ruber* (white) and *G. truncatulinoides* (dex), respectively. Note, that today *G. truncatulinoides* (dex) reproduce in winter time (Jonkers and Kučera, 2015) and due to its life cycle with changing habitats (as shown with arrows) accumulate signals from different water depths. AC – Antilles Current, FC – Florida Current, STG – subtropical gyre. Maps are created using Ocean Data View (Schlitzer, 2016).

5.3 Methods

5.3.1 Foraminiferal counts and stable isotopes analyses

Planktic foraminiferal assemblages were counted on representative splits of the 150-250 µm fraction containing at least 300 individual specimens. Counts were also performed in the >250 µm fraction. The census data from the two size fractions were added up and recalculated into relative abundance of planktic foraminifera in the fraction >150 µm. Faunal data were obtained at each 2 cm for the core section between 508.5 and 244.5 cm and at each 10 cm between 240.5 and 150.5 cm. According to a standard practice, *Globorotalia menardii* and *Globorotalia tumida* as well as *Globigerinoides sacculifer* and *Globigerinoides trilobus* were grouped together, and referred to as *G. menardii* and *G. sacculifer*, respectively (Poore et al., 2003; Kandiano et al., 2012; Chabaud, 2016).

New oxygen isotope data were produced at 2 cm steps using ~10-30 tests of *Globorotalia truncatulinoides* (dex) and ~5-20 tests of *Globorotalia inflata* for depths 508.5-244.5 cm and 508.5-420.5 cm, respectively. Analyses were performed using a Finnigan MAT 253 mass spectrometer at the GEOMAR Stable Isotope Laboratory. Calibration to the Vienna Pee Dee Belemnite (V-PDB) isotope scale was made via the NBS-19 and an internal laboratory standard. The analytical precision of in-house standards was better than 0.07 ‰ (1σ) for $\delta^{18}O$. Deep-dwelling foraminifera *G. truncatulinoides* and *G. inflata* are found in greatest abundances at the base of the seasonal thermocline (100-200 m), under environmental stress, e.g., temperatures warmer than 16 °C, however, the species can migrate to greater depths (Cléroux et al., 2007). As calcification of their tests starting in the mixed layer continues in the main thermocline, the abovementioned species are thought to accumulate hydrographic signals from different water depths (Groeneveld and Chiessi, 2011; Mulitza et al., 1997).

5.3.2 XRF scanning

X-ray fluorescence (XRF) analysis was performed in two different runs using the Aavatech XRF Core Scanner at Christian-Albrecht University of Kiel (for technical details see Richter et al., 2006). To obtain intensities of elements with lower atomic weight (e.g., calcium (Ca), chlorine (Cl)), XRF scanning measurements were carried out with the X-ray tube voltage of 10 kv, the tube current of 750 µA and the counting time of 10 seconds. To analyze heavy elements (e.g., iron (Fe), Sr), the X-ray generator setting of 30 kv and 2000 µA and the counting time of 20 seconds were used; a palladium thick filter was placed in the X-ray tube to reduce the high background radiation generated by the higher source energies. XRF Core Scanner data were collected directly from the split core sediment surface, that had been flattened and covered with a 4 µm-thick ULTRALENE SPEXCerti Prep film to prevent contamination of the measurement unit and desiccation of the sediment (Richter et al., 2006; Tjallingii et al., 2007). The core section between 150 and 465 cm was scanned at 3 mm step size, whereas the coarser-

grained interval between 465 and 600 cm was analyzed at 10 mm resolution.

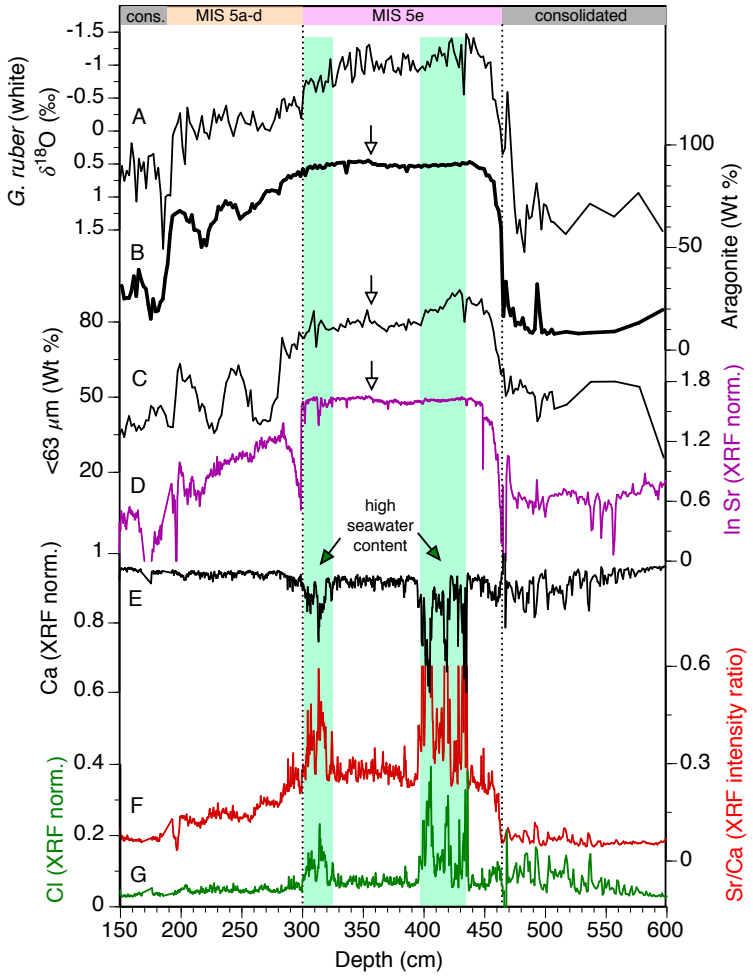

Figure 5.2: XRF-scan results and sedimentological data from core MD99-2202. (**A**) $\delta^{18}O$ values in *G. ruber* (white); (**B**) aragonite content; (**C**) fraction with grain size <63 µm; (**A-C**) is from Lantzsch et al. (2007). Normalized elemental intensities of (**D**) ln Sr, (**E**) Ca and (**G**) Cl and (**F**) Sr/Ca intensity ratio (truncated at value 0.6). Green bars denote the core intervals with biased elemental intensities due to inferred high seawater content (see main text). The white arrows mark a coherent change in sedimentological proxies at 350 cm (**B-D**).

To account for potential biases related to physical properties of the sediment core, XRF intensities of Sr were normalized to Ca (Fig. 5.2), the raw total counts of Fe and Sr were normalized to the total counts of the 30kv-run; counts of Ca and Cl were normalized to the total counts of 10kv-run, excluding Rh intensity, because this element intensities are biased by the signal generation (Bahr et al., 2014).

All data will be made available in the online database PANGAEA (www.pangaea.de).

5.4 Age model

By using our foraminiferal assemblage data, we were able to refine the previously published age model of core MD99-2202 (Lantzsch et al., 2007). To correctly frame MIS 5e, stratigraphic subdivision of the unconsolidated aragonite-rich sediment package between 190 and 464 cm is essential (Fig. 5.3). In agreement with Lantzsch et al. (2007) we interpret this core section to comprise MIS 5, which is supported by key biostratigraphic markers used to identify the well-established faunal zones of late Quaternary (Ericson and Wollin, 1968). Thus, the last occurrences of *G. menardii* and *G.*

menardii flexuosa at the end of the aragonite-rich sediment package are in agreement with the estimated late MIS 5 age (ca. 80-90 ka; Boli and Saunders, 1985; Slowey et al., 2002; Bahr et al., 2011; Chabaud, 2016). The coherent variability observed between aragonite content and relative abundances of warm surface-dwelling foraminifera of *Globigerinoides* genus (*G. ruber,* white and pink varieties, *G. conglobatus* and *G. sacculifer*) between ~200-300 cm, points to simultaneous climate and sea level-related changes and likely reflects the warm/cold substages of MIS 5. The detected substages were then correlated with the global isotope benthic stack LS16 (Lisiecki and Stern, 2016) using AnalySeries 2.0.8 (Paillard et al., 1996). Further, boundaries between MIS 6/5e and 5e/5d as well as the penultimate glaciation (MIS 6) peak, defined from $\delta^{18}O$ record of *G. ruber* (white), were aligned to the global benthic stack (Lisiecki and Stern, 2016).

Given that sedimentation rates at the glacial/interglacial transition could have changed drastically due to increased production of Sr-rich aragonite material above the initially flooded carbonate platform top (Roth and Reijmer, 2004; Chabaud et al., 2016), we applied an additional age marker to better frame the onset of the MIS 5e "plateau" and to allow for a better core-to-core comparison. Thus, we tied the increased relative abundances of warm surface-dwelling foraminifera of *Globigerinoides* genus, which coincides with the rapid decrease in foraminiferal $\delta^{18}O$ record at 456 cm, with the onset of MIS 5e "plateau" at ~129 ka (Masson-Delmotte et al., 2013). This age is in good agreement with many marine and speleothem records, dating a rapid post-stadial warming and monsoon intensification to 129-128.7 ka (Galaasen et al., 2014; Govin et al., 2015; Jiménez-Amat and Zahn, 2015) coincident with the sharp methane increase in the EPICA Dome C ice core (Loulergue et al., 2008; Govin et al., 2012). Although we do not apply a specific age marker to frame the decline of the MIS 5e "plateau", the resulting decrease in the percentage of warm surface-dwelling foraminifera of *Globigerinoides* genus as well as the initial increase in the planktic $\delta^{18}O$ values dates back to ~117 ka (Fig. 5.4), which broadly coincides with the cooling over Greenland (NGRIP community members, 2004). A similar subtropical-polar climatic coupling was proposed in earlier studies from the western North Atlantic STG (e.g., Vautravers et al., 2004; Schmidt et al., 2006a; Bahr et al., 2013; Deaney et al., 2017).

5.5 Results

5.5.1 XRF data in the lithological context

In Fig. 5.2 XRF-derived elemental data are plotted against lithological and physical sediment properties. Beyond the intervals with low Ca counts corresponding to high Cl intensities (at 300-325 cm and 395-440 cm), Ca intensities do not vary significantly, which is in line with a stable carbonate content of about 94 % Wt (Lantzsch et al., 2007). Our Sr record closely follows the aragonite curve and the grain size data, demonstrating that the interglacial minerology is dominated by aragonite. Beyond the intervals containing reduced Ca intensities, a good coherence between Sr/Ca and aragonite content is observed. The rapid increase in Sr/Ca and aragonite is found at the end of the

penultimate deglaciation (Termination 2, T2), coeval with the elevated absolute abundances of *G. menardii* per sample (Fig. 5.4). The gradual step-like Sr/Ca and aragonite decrease characterizes both the glacial inception and the later MIS 5 phase. Intensities of Fe abruptly decrease at the beginning of the last interglacial, but gradually increase during the glacial inception (Fig. 5.5D). At ~120 ka (355 cm), a minor but clear increase in Sr intensities goes along with the change in aragonite and grain-size (Figs. 5.2 and 5.4), arguing that this feature is not a signal artefact but represents a significant sedimentological shift. Between ~112 and 114.5 ka, the actual XRF measurements were affected by a low sediment level in the core tube.

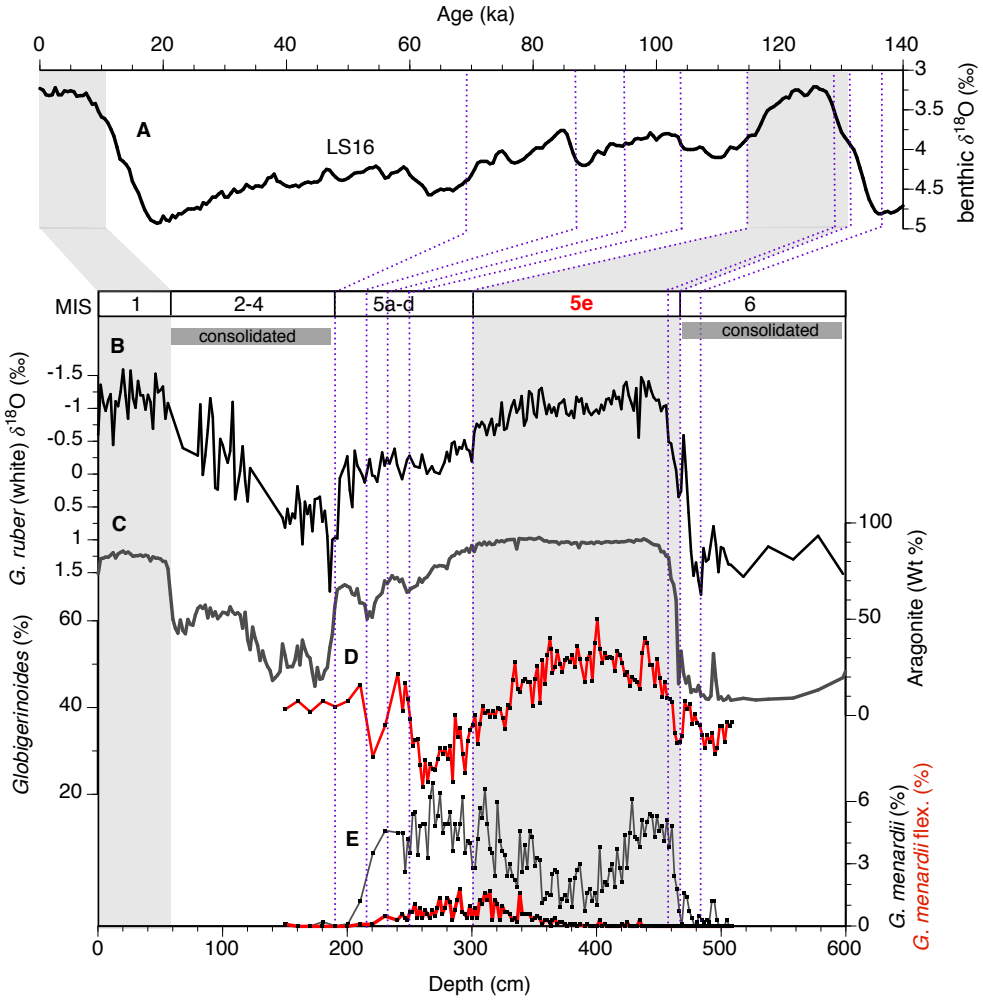

Figure 5.3: Chronology of core MD99-2202. Age model is based on alignment of (**D**) relative abundance record of *Globigerinoides* species and (**B**) planktic $\delta^{18}O$ values (Lantzsch et al., 2007) with (**A**) global benthic isotope stack LS16 (Lisiecki and Stern, 2016). (**C**) Aragonite content (Lantzsch et al., 2007) and (**E**) relative abundances of *G. menardii* and *G. menardii* flexuosa are shown to support the stratigraphic subdivision of MIS 5.

5.2 Climate-related proxies

During the major deglacial transition, ~135-129 ka, low isotopic gradients between *G. ruber* (white), *G. truncatulinoides* (dex) and *G. inflata* are consistent with high relative abundances of *G. truncatulinoides* (dex) and *G. inflata* (Fig. 5.5). Across MIS 5e species

of *Globigerinoides* genus dominate the total assemblage, however, significant changes in the proportions of three main *Globigerinoides* species are observed: *G. sacculifer* and *G. ruber* (pink) essentially dominate the assemblage during early MIS 5e (129-124 ka), whereas *G. ruber* (white) proportions are at their maximum during late MIS 5e (124-117 ka). At the onset of MIS 5e, *G. ruber* (pink) and *G. sacculifer* relative abundances rise in a successive manner, with a rapid increase in *G. sacculifer* occurring c. 2 ka later than the rise in *G. ruber* (pink) proportions. At around 127 ka, all $\delta^{18}O$ records show abrupt increase, *G. falconensis* and *G. inflata* reappear, while relative abundances of *G. ruber* (pink) and *G. sacculifer* become reduced (Figs. 5.5-5.6). After 120 ka, $\delta^{18}O$ values in *G. ruber* (white) and *G. truncatulinoides* (dex) become unstable (Fig. 5.5A-B). This instability coincides with an abrupt drop in *G. sacculifer* relative abundances (Fig. 5.6B).

5.6 Discussion

5.6.1 Platform sedimentology and sea level change

In shallow-water records from the Bahamas, downcore variations in Sr/Ca intensity ratio can be applied as a good proxy for relative sea level (RSL) change (Chabaud et al., 2016). However, given that the measured intensities of Ca account for more than 70 % of all elements signal intensities, Sr/Ca values are strongly dependent on the quality of the Ca signal. While our Sr record likely represents a non-affected signal because of good coherence with the aragonite curve, some of the Ca intensity values are reduced due increased seawater content, as evidenced by simultaneously measured elevated Cl intensities (Fig. 5.2). Because enhanced seawater content in the sediment appears to reduce only Ca intensities, leaving measures of elements with higher atomic numbers (e.g., Fe, Sr) less affected (Tjallingii et al., 2007; Hennekam and de Lange, 2012), normalization of Sr counts to Ca results in very high Sr/Ca intensity ratios across the Cl-rich intervals. The general consistency of the measured Sr intensities argues against an early marine diagenesis that would strongly reduce and homogenize the Sr/Ca intensity ratio, altering isotopic signatures and often causing a change in sediment color (Chabaud, 2016) that is not observed in our sediment core. Consequently, the spikes in Sr/Ca within the last interglacial could be related to a change in physical properties of the sediment, such as elevated sediment porosity linked to increased sand size fraction, that would facilitate enhanced pore-water content in these intervals (Henderson et al., 2000; Tucker and Bathurst, 2009; Chabaud, 2016). Indeed, the late MIS 5e Sr/Ca spike falls within the interval of strongly decreased sediment density and increased porosity (Labeyrie and Reijmer, 2005). However, on the basis of these data alone it is not possible to assess whether the observed sedimentological and geochemical shifts represent a syn- or postdepositional change. Yet, comparing all the records it seems conceivable that the pronounced Sr/Ca and Cl spikes may contain clues about interglacial sedimentary regime changes on the upper slope of the LBB at these times.

Beyond these problematic intervals described above, XRF-derived Sr/Ca values agree well with the aragonite curve and, thus, can be interpreted in terms of RSL variability (Fig. 5.4). Around 129 ka, Sr/Ca as well as aragonite content rapidly reach maximum values, indicating the onset of the LBB flooding interval. Absolute abundance of *G. menardii* per sample supports the inferred onset of the flooding interval (Fig. 5.4D), since amounts of planktic foraminifera in the sample can be used to assess the relative accumulation of platform-derived vs. pelagic sediment particles (Slowey et al., 2002). After *G. menardii* repopulated the tropical waters at the end of the penultimate glaciation (Bahr et al., 2011; Chabaud, 2016), its increased absolute abundances are found between ~131-129 ka. That feature could be attributed to a reduced input of fine-grained aragonite at times of partly flooded platform. Consequently, as the platform top became completely submerged, established aragonite shedding gained over pelagic input, thereby reducing the number of *G. menardii* per given sample.

Despite some possible isostatic subsidence (1-2 m per hundred thousand years), the LBB is generally regarded as tectonically stable (Carew and Mylroie, 1995; Hearty and Neumann, 2001). Considering that the modern water depth of the platform is between 6-10 m, a RSL above -6 m of its present position is required to completely flood the platform top and allow for a drastic increase in aragonite production (Carew and Mylroie, 1997; Chabaud et al., 2016). In that context, the onset of the major flooding interval with RSL above -6 m could be assumed from c.129 ka on (Fig. 5.4). Since the last interglacial sea level highstand is estimated to have been 6-9 meters above the modern (Dutton et al., 2015), an additional sea level rise of 12-15 m must have been reached some time later within MIS 5e. A late peak is indeed in agreement with a continuing deglaciation observed in the northern hemisphere (e.g., Bauch et al., 2012; Deaney et al., 2017); a sea–level contribution from the Antarctic Ice Sheets have also been suggested (Hearty and Neumann, 2001; O´Leary et al., 2013).

Our data do not allow to make assumptions about the exact timing of the last interglacial sea level peak, which is controversially placed by different studies into either early (Grant et al., 2012; Lisiecki and Stern, 2016), mid or late MIS 5e (Hearty and Neumann, 2001; Hearty et al., 2007; Kopp et al., 2009; O´Leary et al., 2013; Spratt and Lisiecki, 2016). And yet, our proxy records suggest that the aragonite production on top of the platform was abundant until late MIS 5e (unequivocally delimited by foraminiferal $\delta^{18}O$ and faunal data), arguing for a longer-lasting flooding interval of the LBB across MIS 5e (~12 ka with the RSL above -6 m), when compared to previous sea level reconstructions (Fig. 5.4H). The drop in RSL below -6 m only during the terminal phase of MIS 5e (~117 ka on our timescale) is corroborated by a coincident changeover in the aragonite content and the increase in absolute abundance of *G. menardii*, further supporting the hypothesis that aragonite shedding was suppressed at that time, causing relative enrichment in foraminiferal abundances (per sample).

As mentioned above, the inferred LBB flooding time period differs from the actual minimal ice volume interval, but it appears to correspond roughly with the well-known

last interglacial "plateau" of low benthic $\delta^{18}O$ values between ~129 and 116-118 ka (Adkins et al., 1997; Cortijo et al., 1999; Masson-Delmotte et al., 2013). Given that the intra-interglacial sea level change is plausible, this observation underscores the importance of critical consideration of deep-sea $\delta^{18}O$ records, accumulating both ice volume and ocean temperature/salinity signals.

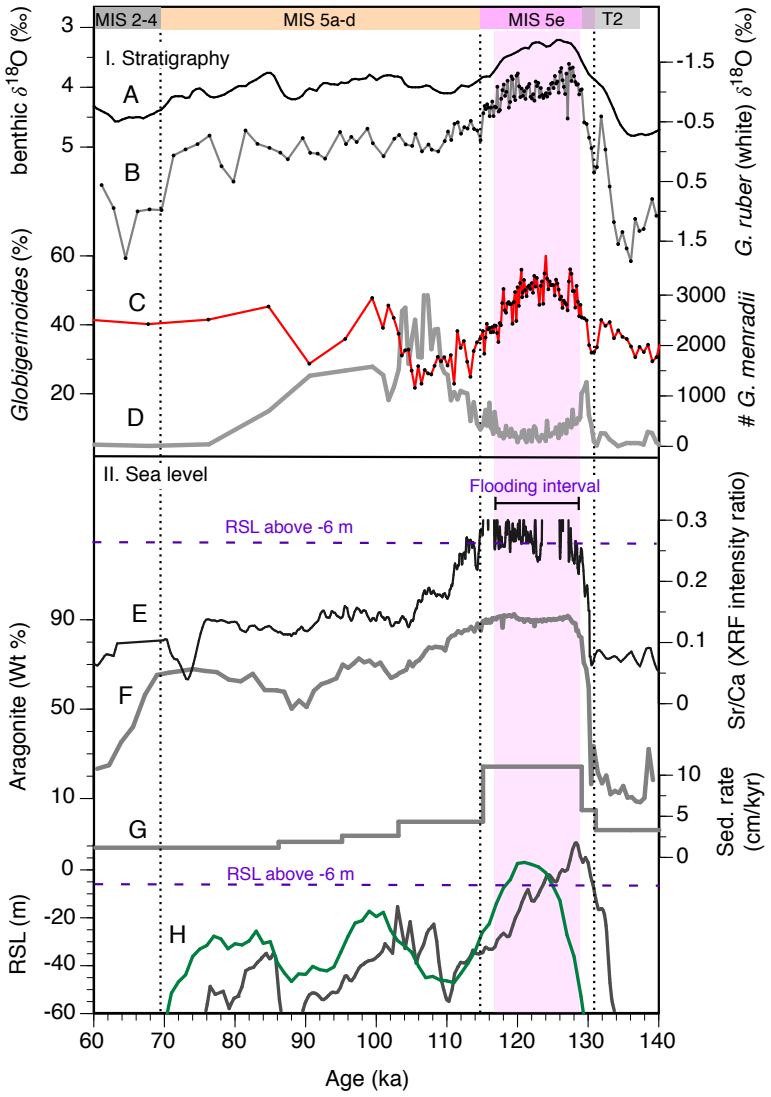

Figure 5.4: Sedimentological and foraminiferal data from core MD99-2202. Proxy records are compared to (**A**) global benthic isotope stack LS16 (Lisiecki and Stern, 2016) and (**H**) relative sea level (RSL) estimates (grey is from Grant et al. (2012); green is from Spratt and Lisiecki (2016)). (**B**) $\delta^{18}O$ values in *G. ruber* (white) (Lantzsch et al., 2007), (**C**) relative abundances of *Globigerinoides* species, (**D**) absolute abundances of *G. menardii* per sample, (**E**) Sr/Ca intensity ratio, (**F**) aragonite content (Lantzsch et al., 2007), (**G**) computed sedimentation rates. Inferred platform flooding interval (lilac bar) is consistent with the enhanced production of Sr-rich aragonite needles and a RSL above -6 m (Chabaud et al., 2016). T2 – refers to the position of the penultimate deglaciation (Termination 2).

5.6.2 Termination 2

Prior to the MIS 5e "plateau", the elevated occurrences of transitional to subpolar species *G. inflata* indicate generally cold-water conditions off the LBB (Fig. 5.5). Isotopic

gradients between $\delta^{18}O$ values in surface- and thermocline-dwelling foraminifera during T2 are strongly reduced, arguing for decreased water column stratification. At times of suppressed overturning during T2 (Deaney et al., 2017), the inferred decreased stratification could have resulted from sea surface cooling/salinification and/or subsurface warming (e.g., Zhang, 2007). Nevertheless, direct surface/subsurface temperature estimations across T2 and early MIS 5e so far reveal warm/cold conditions for the subtropical western North Atlantic (Bahr et al., 2013). It is known, however, that species-specific temperature signals should be considered with caution, as they could be complicated due to adaptation strategies of foraminifera, such as seasonal shifts in the peak foraminiferal tests flux and/or habitat changes (Schmidt et al., 2006a, b; Bahr et al., 2013; Jonkers and Kučera, 2015). Alternatively, reduced water column stratification could have led to a situation when calcification of the thermocline-dwelling foraminifera could have commenced in shallower and, therefore, relatively warmer waters, causing a lower isotopic gradient between shallow- and deep-dwelling foraminifera (Mulitza et al., 1997).

High abundances of *G. truncatulinoides* (Fig. 5.5E) further support the hypothesis involving reduced stratification and deep vertical mixing, given that today this species requires reduced upper water column stratification to be able to complete its reproduction cycle with changing habitats, from c. 400-600 m to near-surface depths (Lohmann and Schweizer, 1990; Hilbrecht, 1996; Mulitza et al., 1997). For instance, in the modern tropical Caribbean, reproduction of *G. truncatulinoides* is inhibited by strong thermocline in well-stratified waters (Schmuker and Schiebel, 2000). This is in contrast to the subtropical North Atlantic where winter sea surface cooling (T<23 °C) and deep mixing occur alongside with increase of *G. truncatulinoides* up to 15 % (Levitus et al., 2013; Siccha and Kučera, 2017). It could, therefore, be proposed that the overall abundance of *G. truncatulinoides* in our subtropical settings was at least partly controlled by oceanic conditions occurring nearer to the sea surface (Mulitza et al., 1997; Jonkers and Kučera, 2016).

Sea surface water properties as well as vertical convective mixing in the Bahama region are closely related to the strength of the atmospheric circulation as defined by the position of the ITCZ (e.g., Slowey and Curry, 1995; Wolff et al., 1999). Today, intensified trade winds coupled with cold meteorological fronts enhance upper water column mixing in the region through evaporative cooling during boreal winter, when the ITCZ is at the southernmost position (e.g., Wilson and Roberts, 1995). Previous studies from the western subtropical North Atlantic have shown that time periods with reduced AMOC strength are consistent with southward displacements of the ITCZ and its associated rainfall belt, causing sea surface salinification (Schmidt et al., 2006a; Carlson et al., 2008a; Bahr et al., 2013). Acknowledging the fact that our study region lies too far north to be influenced by changes in the winter position of the ITCZ (Ziegler et al., 2008) – this would be of primary importance for modern-like winter-spring reproduction timing of *G. truncatulinoides* (Jonkers and Kučera, 2015) - we suggest that a southward displacement

of the mean annual position of the ITCZ during T2 (Wang et al., 2004) could have promoted favorable conditions for *G. truncatulinoides* through generally strong sea surface cooling/salinification amplified by intensified atmospheric circulation.

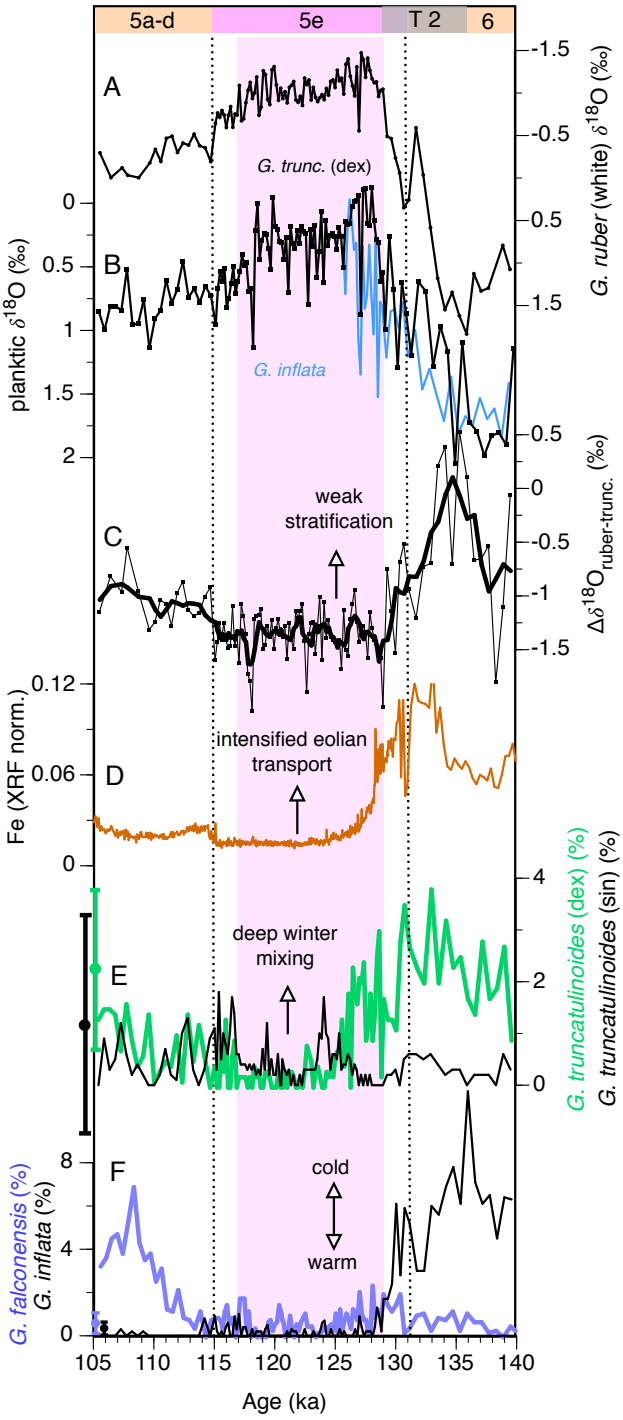

Figure 5.5: Proxy records from core MD99-2202 over the last interglacial cycle. (**A**) $\delta^{18}O$ values in *G. ruber* (white) (Lantzsch et al., 2007), (**B**) $\delta^{18}O$ values in *G. truncatulinoides* (dex) and *G. inflata,* (**C**) gradient $\Delta\delta^{18}O$ between $\delta^{18}O$ values in *G. ruber* (white) and *G. truncatulinoides* (dex), (**D**) normalized Fe intensities, (**E**) relative abundances of *G. truncatulinoides* (dex) (green) and *G. truncatulinoides* (sin) (black), (**F**) relative abundances of *G. falconensis* (violet) and *G. inflata* (black). Also shown in (**E**) and (**F**) are modern relative foraminiferal abundances (average value ±1σ) around Bahama Bank, computed using 7 nearest samples from Siccha and Kučera (2017) database. Shaded in lilac is the platform flooding interval (as defined in Fig. 5.4). T2 – Termination 2.

In the Bahamas, siliclastic inputs by other processes than wind transport is very limited, therefore, increased Fe content in the sediments could be attributed to enhanced trade winds strength which is coupled with a southern shift of the ITCZ (Roth and Reijmer, 2004). Accordingly, the elevated XRF-derived Fe counts in our record during T2 (Fig. 5.5D) may support intensification of trade winds and increased transport of Saharan dust

at times of enhanced aridity over North Africa, i.e., during colder periods (Helmke et al., 2008; Tjallingii et al., 2008). Finally, increased velocities of the wind-driven Antilles Current in the southwestern limb of the STG during glacial interval and T2 are thought to enhance winnowing of fine-grained material on the northern slopes of LBB, which, together with the limited supply of aragonite needles, promoted enhanced sediment consolidation (Chabaud et al., 2016).

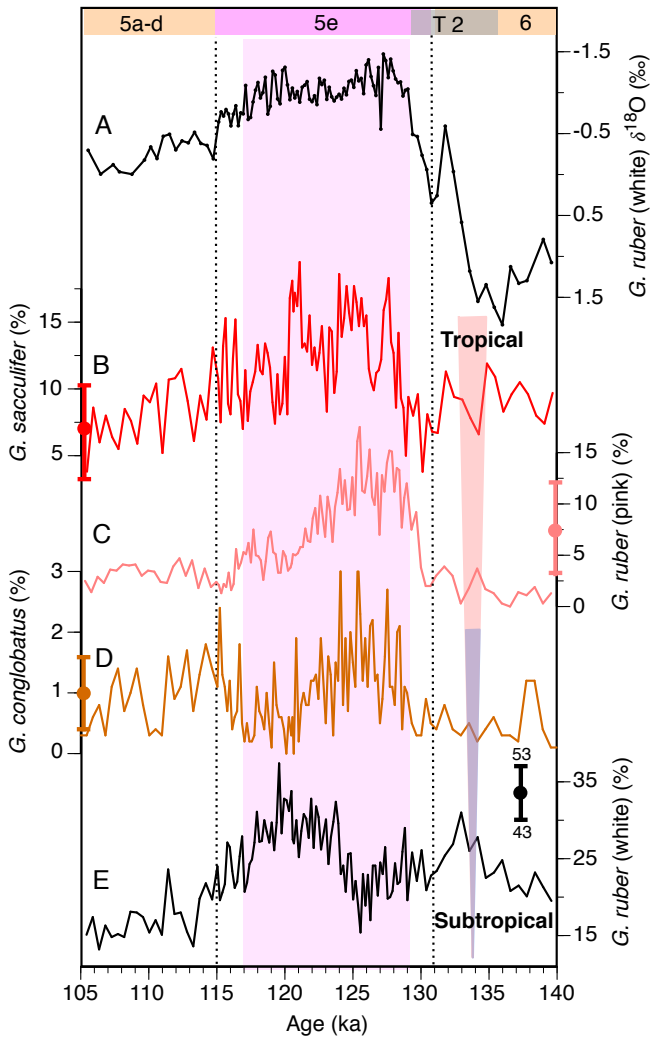

Figure 5.6: Relative abundances of main *Globigerinoides* species in core MD99-2202. (**A**) $\delta^{18}O$ values in *G. ruber* (white) (Lantzsch et al., 2007), relative abundances of (**B**) *G. sacculifer*, (**C**) *G. ruber* (pink), (**D**) *G. conglobatus*, (**E**) *G. ruber* (white). Also shown in (**B-E**) are modern relative foraminiferal abundances (average value ±1σ) around Bahama Bank, computed using 7 nearest samples from Siccha and Kučera (2017) database. Shaded in lilac is the platform flooding interval (as defined in Fig. 5.4). T2 – Termination 2.

5.6.3 Early MIS 5e

Various environmental properties (temperature, salinity, nutrients) can account for the proportional change in different *Globigerinoides* species (Fig. 5.6). *G. sacculifer* – it makes up less than 10 % of the planktic foraminiferal assemblage around the LBB today (Siccha and Kučera, 2017) – is abundant in the Caribbean Sea and tropical Atlantic and commonly used as a tracer of tropical waters and geographical shifts of the ITCZ (Poore et al., 2003; Vautravers et al., 2007). Also, *G. ruber* (pink) shows rather coherent abundance maxima in the tropics (between 20°N and 20°S), while no such affinity is observed for *G. ruber* (white) and *G. conglobatus* (Siccha and Kučera, 2017; Schiebel

and Hemleben, 2017). Therefore, fluctuations in relative abundances of *G. sacculifer* and *G. ruber* (pink) are referred here as to represent a warm tropical end-member (Fig. 5.1B).

As shown in Fig. 5.7B, relative abundances of the tropical species (here and further in the text *G. ruber* (pink) and *G. sacculifer* calculated together) increased before the onset of the last interglacial "plateau" at ~129 ka. This transition was possibly coupled with the intensification of the Gulf Stream at MIS 6/5e boundary (Bahr et al., 2011). In addition, a gradual rise in accumulation of redox-sensitive element molybdenum (Mo) in sediment data from Cariaco Basin is observed across the penultimate deglaciation (Fig. 5.7D). At that latter location, high Mo content is found in sediments deposited under anoxic conditions, occurring only during warm interstadial periods associated with a northerly shifted ITCZ (Gibson and Peterson, 2014). Accordingly, a gradual northward migration of the mean annual position of the ITCZ at the onset of MIS 5e could be implied. In line with increasing low latitude summer insolation (Fig. 5.7C), this ITCZ displacement would also promote a northward expansion of the Atlantic Warm Pool (Ziegler et al., 2008). Because core MD99-2202 is located at the northern edge of the ITCZ influence, the rapid shift in foraminiferal proportions at ~130 ka could, in fact, represent the onset of the Atlantic Warm Pool influence, which resulted from a gradual northward-directed ITCZ movement. Similarly, the pronounced increase in the tropical species relative abundances at 129-128 ka, a result of the rapid rise in *G. sacculifer* proportions (Figs. 5.6-5.7), may then reflect a continuing northward expansion of the Atlantic Warm Pool. Abrupt sea surface warming at the onset of the interglacial "plateau" is likewise found in some proxy records from the western subtropical North Atlantic (Fig. 5.7E; Cortijo et al., 1999; Deaney et al., 2017). Within some age uncertainties such a switch to warmer conditions could, however, correspond to the rapid rise in accumulation of Mo in sediments from the Cariaco Basin (Fig. 5.7D).

Further, our data reveal a millennial-scale cooling/salinification event at ~127 ka, characterized by decreased proportions of tropical foraminifera and elevated planktic $\delta^{18}O$ values (Figs. 5.5-5.7). That the abrupt cooling across the entire upper water column occurred at the onset of the event is indicated by the re-occurrence of cold-water species *G. falconensis* and *G. inflata* coincident with brief positive excursions in $\delta^{18}O$ of shallow and deep-dwelling foraminifera. A coherent cooling event, dated by U-Th to be centered around 127 ka, is also evident in an isotopic record from the southwestern slope of the LBB (Slowey et al., 1996; Henderson et al., 2000), suggesting at least a regional expression of the event. Simultaneously, the XRF record from the Cariaco sediments reveals a stadial-like Mo-depleted (ITCZ southward) interval (Fig. 5.7D). The close similarity between the tropical-species record from the Bahamas and the XRF data from Cariaco Basin supports the hypothesis that the annual displacements of the ITCZ are also documented in our faunal counts. Moreover, because the aforementioned abrupt climatic shift at ~127 ka cannot be reconciled with the insolation changes, additional forcings at play during early MIS 5e should be considered.

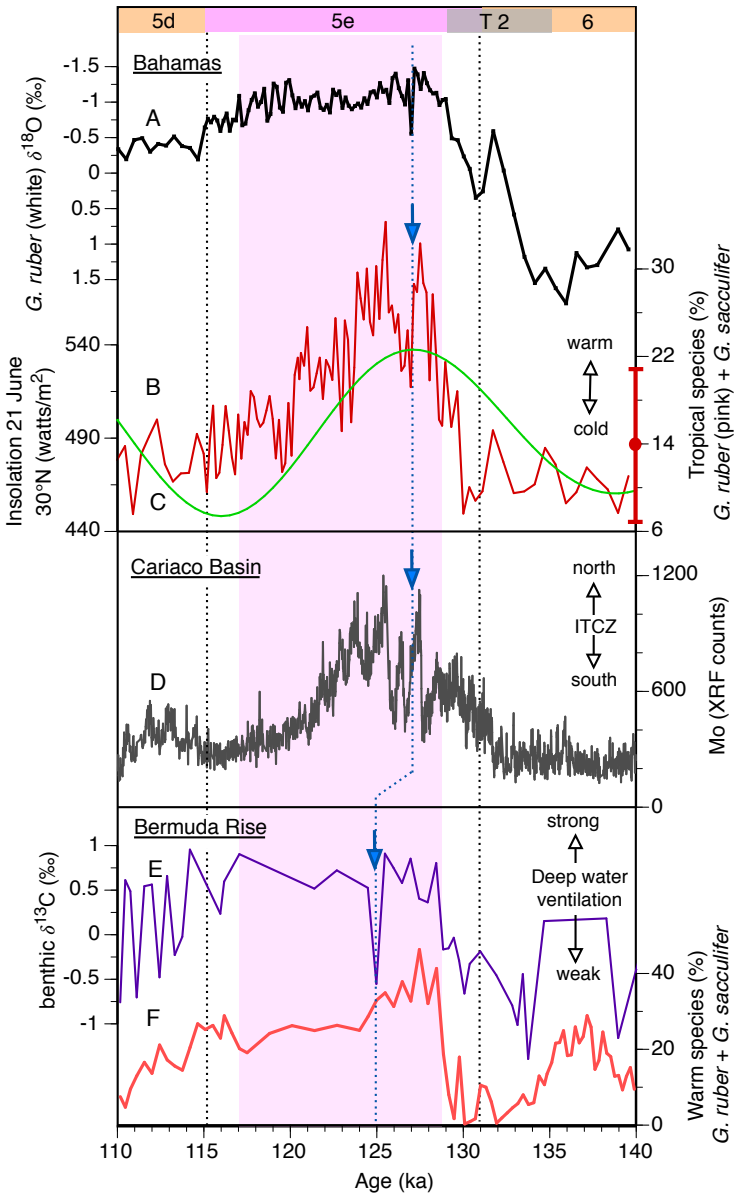

Figure 5.7: Comparison of proxy records from (sub)tropical North Atlantic. (**A**) $\delta^{18}O$ values in *G. ruber* (white) in core MD99-2202 (Lantzsch et al., 2007), (**B**) relative abundances of tropical species *G. sacculifer* and *G. ruber* (pink) in core MD99-2202, (**C**) boreal summer insolation (21 June, 30°N), computed with AnalySeries 2.0.8 (Paillard et al., 1996) using Laskar et al. (2004) data, (**D**) molybdenum (Mo) record from ODP Site 1002 (Gibson and Peterson, 2014), (**E-F**) $\delta^{13}C$ values measured in benthic foraminifera and relative abundances of *G. ruber* (total) and *G. sacculifer* from ODP Site 1063 (Deaney et al., 2017). Also shown in (**B**) are modern relative abundances of *G. sacculifer* and *G. ruber* (pink) (average value ±1σ) around Bahama Bank, computed using 7 nearest samples from Siccha and Kučera (2017) database. The blue arrows and the dashed line suggest correlation of abrupt event events (so-called Younger Dryas-like cooling) in the subtropical and tropical North Atlantic (see text). Shaded in lilac is the platform flooding interval (as defined in Fig. 5.4). ITCZ -Intertropical Convergence Zone. T2 – Termination 2.

Although the full resumption of the AMOC from a shallow or weak mode during T2 occurred only by ~124 ka, several studies show that the AMOC abruptly recovered at the beginning of MIS 5e, apparently due to a deepened winter convection in the Labrador Sea (Adkins et al., 1997; Galaasen et al., 2014; Deaney et al., 2017). In accordance with

previous studies from the tropical North Atlantic suggesting a coupling between ITCZ position and ocean overturning (Rühlemann et al., 1999; Schmidt et al., 2006a; Carlson et al., 2008a), it could be argued that the northward ITCZ shift coeval with the rise in tropical foraminifera proportions at our site at ~129-128 ka was consistent with the deepening of NADW and resumption of the AMOC (Fig. 5.7E). In turn, the millennial-scale climatic reversal between 127 and 126 ka could have been related to the known reductions of deep water ventilation during early MIS 5e (Galaasen et al, 2014; Deaney et al., 2017). A corresponding cooling and freshening event – referred elsewhere as to a Younger Dryas-like event - is captured in some high- and mid-latitude North Atlantic records (Bauch et al., 2012; Irvali et al., 2012; Schwab et al., 2013; Govin et al., 2014; Jiménez-Amat and Zahn, 2015; Zhuravleva et al., 2017b). Coherently with the Younger Dryas-like cooling and the reduction/shallowing in the NADW, an increase in the Antarctic Bottom Water formation is revealed in the Southern Ocean core data, arguing for existence of an "interglacial" bipolar seesaw (Hayes et al., 2014). The out-of-phase climatic relationship between high northern and high southern latitudes, typical for the last glacial termination (Barker et al., 2009), could be attributed to a strong sensitivity of the transitional climatic regime of early MIS 5e due to persistent high-latitude freshening (continuing deglaciation) and suppressed overturning in the Nordic Seas. This is important because it helps to explain such a late occurrence of the Younger Dryas-like event during T2, when compared to the actual Younger Dryas in the last deglaciation.

5.6.4 Late MIS 5e

Relative abundances of tropical foraminifera in our core suggest an early SST maximum (between 128 and 124 ka) in the low-latitude North Atlantic, which agrees in time with the recent compilation of global MIS 5e SST (Hoffman et al., 2017). As the insolation forcing decreased during late MIS 5e and the ITCZ gradually moved southward (Fig. 5.7C-D), the white variety of *G. ruber* started to dominate the assemblage (Fig. 5.6), arguing for generally colder sea surface conditions. The inferred broad salinity tolerance of this species, also to neritic conditions (Bé and Tolderlund, 1971; Schmuker and Schiebel, 2002), was used in some studies to link high proportions of *G. ruber* (pink and white varieties) with low surface salinities (Vautravers et al., 2007; Kandiano et al., 2012). The plots of the global distribution pattern of *G. ruber* (white) and *G. ruber* (pink), however, suggest that when relative abundances of these two species are approaching maximum values (40 % and 10 %, respectively), the sea surface salinities would be higher for specimens of the white variety of *G. ruber* (Hilbrecht, 1996). Therefore, the strongly dominating white vs. pink *G. ruber* variety observed in our records during late MIS 5e could be linked not only to decreasing SST, but also to increasing sea surface salinity.

In their study from the western STG, Bahr et al. (2013) also reconstruct sea surface salinification during late MIS 5e in response to enhanced wind stress at times of deteriorating high-latitude climate and increasing meridional gradients. Accordingly, our isotopic and faunal data (note the abrupt decrease in *G. sacculifer* proportion at 120 ka; Fig. 5.6B) suggest a pronounced climatic shift that could be attributed to a so-called

"neoglaciation", consistent with the sea surface cooling in the western Nordic Seas and the Labrador Sea (Van Nieuwenhove et al., 2013; Irvali et al., 2016) as well as with a renewed growth of terrestrial ice (Fronval and Jansen, 1997; Zhuravleva et al., 2017b).

Notably, a small but coherent increase in the aragonite content and Sr counts is evident at 120 ka and coincides with the change towards finer-grained sediments, altogether arguing for a change in sedimentary regime before the end of the major flooding interval at ~117 ka (Figs. 5.2 and 5.4). Further interpretations of the aragonite changes based on the available data appear rather speculative, given that the aragonite precipitation on the platform top at times of sea level highstand is controlled by level of aragonite supersaturation, which, in turn, depends on a number of climate-related parameters, such as CO_2 amounts, temperature, salinity, water depth above the bank top as well as residence time of the water mass above the platform (Morse and MacKenzie, 1990; Morse and He, 1993; Schlager et al., 1994; Roth and Reijmer, 2004; 2005). Nevertheless, the coherent shift in the carbonate minerology revealed after 120 ka may support major oceanographic and atmospheric changes during the late phase of MIS 5e possibly coupled with a significant sea level change.

5.7 Conclusions

New isotopic, faunal and XRF evidence combined with published sedimentological data from a sediment core obtained from the slope of the LBB were studied for changes in water masses, sedimentary regimes, and RSL change across the last interglacial. By using new data, we were able to better constrain the last interglacial cycle in the investigated core section (cf. Lantzsch et al., 2007). Elemental analyses, aragonite content and foraminiferal abundance records suggest that the LBB became rapidly flooded at ~129 ka. The carbonate platform remained submerged until late MIS 5e, c. 117 ka, implying a prolonged interval with a RSL above -6 m. Although our data do not allow us to reconstruct the exact timing of the last interglacial sea level peak, our sedimentological proxies point to changing sedimentary regimes on the slope of the LBB, possibly as a result of intra-interglacial sea level and/or climatic fluctuations.

The overall climatic evolution of the last interglacial cycle in the Bahama region was closely coupled with the ITCZ movements, which, in turn, were the result of insolation and the AMOC forcing:

1. Termination 2: Strongly reduced $\delta^{18}O$ gradients between mixed-layer and thermocline-dwelling foraminifera suggest decreased water column stratification. High proportions of *G. truncatulinoides* could be attributed to a deep vertical mixing as a result of sea surface cooling/salinification and intensified trade winds strength at times of ITCZ being shifted far to the south.
2. Early MIS 5e: Computed together, relative abundances of tropical foraminifera *G. sacculifer* and *G. ruber* (pink) agree well with the published ITCZ-related Cariaco record (Gibson and Peterson, 2014), suggesting climatic coupling between the regions.

Based on these data, a northward displacement of the mean annual ITCZ position, in line with strong insolation forcing, could be inferred for early MIS 5e. However, an abrupt climatic shift intersected the early MIS 5e warmth. This so-called Younger Dryas-like cooling event likely involved AMOC-related forcing that influenced (sub)tropical climate. The relatively late occurrence of Younger Dryas-like cooling event, when compared to the actual Younger Dryas in the last deglaciation, is attributed to the transitional climatic regime of early MIS 5e, characterized by persistent high-latitude freshening and unstable deep-water overturning in the North Atlantic.

3. Late MIS 5e: Overall sea surface cooling and possibly salinification is reconstructed for the Bahama region, in accordance with insolation decrease and a gradual southward displacement of the mean annual ITCZ. A coherent change is observed in faunal, isotopic and sedimentological proxies, arguing for coupled oceanic and northern hemisphere cryospheric reorganizations before the end of the major flooding period.

Acknowledgments

We wish to thank H. Lantzsch and J. J. G. Reijmer for providing us with the sediment core and data from core MD99-2202, S. Fessler for performing measurements on stable isotopes, S. Müller and D. Garbe-Schönberg for technical assistance during XRF scanning, J. Lübbers for her help with sample preparation, and E. Kandiano for introduction into tropical foraminiferal assemblages. A. Z. acknowledges funding from German Research Foundation (DFG grant BA1367/12-1).

Chapter 6: Conclusions and outlook

6.1 Conclusions

Motivated by the growing threat of global warming, this thesis focuses on the warmer-than-present last interglacial interval (MIS 5e, Eemian, ~129-116 ka) including the penultimate (Saalian) deglaciation and the glacial inception after the peak interglacial conditions. A suite of benthic and planktic stable isotope records, faunal census data, IRD as well as XRF data were obtained and evaluated to provide new and valuable information on ice-sheets fluctuations, sea level variability and sea surface evolution across the North Atlantic, linking the subarctic and subtropical regions.

New reconstructions from the high northern latitudes (**Chapters 3 and 4**), based on stable oxygen and carbon isotopes, foraminiferal assemblage and IRD data suggest a strong post-Saalian meltwater influence that persisted in the Nordic Seas during early MIS 5e (~129-125 ka). This "transitional" phase of the last interglacial is interpreted to be part of the main deglaciation and has implications for the climate development beyond the subpolar North Atlantic (see further below). New lines of evidence including stable isotope records and IRD content reveal major freshwater additions from the disintegrating Svalbard-Barents Sea Ice Sheet (SBIS) and the northeastern GIS until ~125 ka. The data also indicate that a thick deglacial meltwater lid – SBIS and GIS should only be considered as two out of several possible sources – hindered a northward propagation of warm and saline AW at the sea surface during early MIS 5e. As a result, full resumption of the AMOC with modern-like deep-water overflows from the Nordic Seas established only in mid-MIS 5e when the freshwater influence in the region lowered. Although the influence of the AW at the sea surface during the Saalian deglaciation, including early MIS 5e, was notably decreased, its inflow into the Nordic Seas never completely ceased. Indeed, a thorough inspection of the data (e.g., occurrences of *B. megastoma*, magnetic susceptibility) suggests that the AW penetrated polewards during the Saalian deglaciation, likely underneath the low-density halocline layer, which obscured AW-related signals in widely used foraminiferal data. This revised view is crucial for understanding variations in the vertical water mass structure in the Nordic Seas, which influences deep-water formation and overflow into the North Atlantic.

Comparison of published data from the Labrador Sea with the new multiproxy records from the Nordic Seas (**Chapter 3**) suggests a tight freshwater-related coupling between these two basins with apparent feedbacks for regional sea surface evolution and deep-water convection. In particular, sea surface warming and resumption of vertical convection (~128.5-126.5 ka) documented in the central Nordic Seas and in the southern Labrador Seas coincided with a temporary but pronounced reduction of freshwater addition from the northeastern GIS. Subsequently, following a new meltwater event documented off East Greenland margin at ~126.5 ka, an abrupt sea surface cooling and reduction in vertical water convection occurred in the Nordic and Labrador seas. Following few earlier studies, this millennial-scale climatic reversal could be referred to

as a Younger Dryas-like event. Indications for links between the vertical water mass structure in the Nordic Seas (meltwater versus the AW) and melting of the ice sheets during the deglacial termination were found but need to be further investigated by dedicated future studies.

In the Nordic Seas, the thick post-Saalian halocline and deeper flow of the AW during the early phase of MIS 5e accounted for a delayed regional sea surface warming, which developed only during late MIS 5e and out of phase with the maximum summer insolation. A critical Holocene-Eemian comparison (**Chapter 4**) provides an unequivocal evidence, based on foraminiferal assemblage and carbonate dissolution data, for an enhanced influence of the AW circulating in the Fram Srait during late MIS 5e. The latter observation is in strong contrast to an early and much stronger interglacial optimum in the Holocene. Intensified near-surface advection of the AW occurred just prior to the last glacial inception and compares well in time with the published upstream records from the Norwegian Sea, altogether implying a coherent development of south-to-north ocean heat transfer through the eastern Nordic Seas and into the high Arctic.

Elemental analyses and foraminiferal abundance records from shallow-water sediments of the Bahama region (**Chapter 5**), underpinned by oxygen isotope chronology, suggest a rather late sea level highstand after ~129 ka, that is in agreement with a continuing deglaciation reconstructed for the high northern latitudes. In addition, a comparable millennial-scale Younger Dryas-like cooling event, as revealed in the subpolar North Atlantic, is also found in the planktic foraminiferal assemblage data from the Bahama region during early MIS 5e. Given that today the investigated area lies at the northern edge of the influence of the Atlantic Warm Pool, expansion of which is closely related to the seasonal shifts of the ITCZ, the aforementioned cooling could be linked to a sudden southward shift of the ITCZ. Because this abrupt climate change cannot be reconciled with the insolation curve, the Younger Dryas-like event apparently involved a short-term reduction in the AMOC strength that left an imprint on the ITCZ position via ocean-atmospheric teleconnections. As such, the coupling between the ITCZ and AMOC, as revealed for the last deglaciation, is considered as an additional forcing mechanism for the low-latitude climate during early MIS 5e. These results help to disentangle the roles of different mechanisms controlling subtropical climate across MIS 5e (insolation versus oceanic, atmospheric and freshwater forcings). Chapter 5, in particular, denotes the strong sensitivity of the low-latitude climate to the subarctic forcing during early MIS 5e. This leads to the conclusion that the persistent high-latitude freshening and unstable deep-water overturning during early MIS 5e accounted for a “transitional” and, therefore, particularly vulnerable climatic regime during this time period, causing the cold-warm switches akin to those observed during the last glacial termination.

Overall, this thesis refines the current understanding of the last interglacial cycle in the subarctic North Atlantic, with special attention given to the influence of the AW. The sensitivity of the subtropical Bahama region to past climatic and sea level changes is also investigated. Finally, a comparable sequence of millennial-scale climatic events is found

across various oceanic basins, arguing for a potential of these specific events to be used as important markers allowing for a better chronostratigraphic constraint of the MIS 5e interval.

6.2 Outlook

6.2.1 SST reconstructions - towards improved proxy interpretation and better spatial coverage

It is well-established that SST reconstructions could be complicated by undesirable environmental signals incorporated within proxy data. In particular, seasonal shifts in the peak flux of foraminifera appear important for species-dependent reconstructions, such as Mg/Ca-derived SST. In their study from the Blake Outer Ridge (31°41´N, 75°25´W; western rim of the STG), Bahr et al. (2013) reveal peak in the Mg/Ca-derived SSTs as early as the late deglaciation of MIS 6 (Fig. 6.1). This temperature peak leads by several millennia the warmest surface conditions inferred from the faunal proxy data presented in this thesis (core MD99-2202, 27°35´N, 78°58´W), but closely follows the low-latitude summer insolation curve. Discrepancies between the faunal and geochemical proxy data were also observed in the record from the Blake Outer Ridge during Greenland Stadials of MIS 3, with Mg/Ca SSTs to be as much as 5 °C warmer than faunal-based SSTs (Vautravers et al., 2004; Schmidt et al., 2006a). Although *G. ruber* (white) shows a rather even test flux during the year, it was revealed that under stressful conditions (SST<26 °C) the species flux shifts towards warmer summer-autumn months (Jonkers and Kučera, 2015). Thus, the inconsistency between Mg/Ca- and assemblage-based SST proxy records could be attributed to a warm-season bias incorporated into Mg/Ca ratios of *G. ruber* (white), while faunal census data would rather record annual mean conditions (Schmidt et al., 2006a, b; Bahr et al., 2013). In this context, it is important to note that due to particularly strong seasonality, past distortions of the ITCZ coherent with reductions in the ocean overturning strength could have been restricted to winter months only, and, therefore, would not be captured in summer proxy records (Ziegler et al., 2008). It is further worth to mention that seasonality may also leave an imprint on interglacial proxy records (Leduc et al., 2010), owing to orbitally-forced changes in seasonal insolation, that were particularly strong during MIS 5e (Bakker et al., 2014; Brocas et al., 2016).

Considering the above, future studies should deepen the present understanding of the SST signals recorded in proxy records with regard to adaptation strategies of planktic organisms used to obtain paleodata. A critical issue is paleo-seasonality and its impact on seasonal temperature trends that appear difficult to constrain by using only common proxy records. Multiproxy SST reconstructions, based on Mg/Ca, alkenone and faunal data, would help to distinguish between different influencing mechanisms, ultimately improving understanding of SST proxies. In the absence of the well-established independent proxy for sea surface salinity, this would, in turn, increase reconstruction accuracy for this crucial parameter.

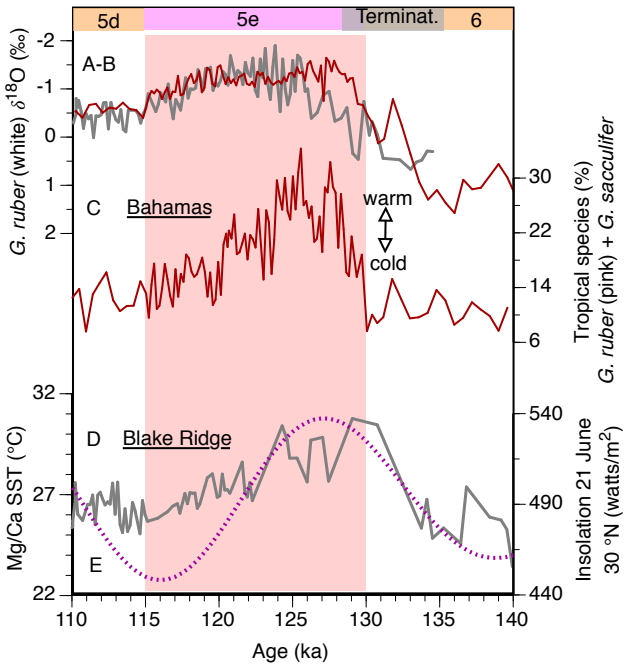

Figure 6.1: Comparison of the proxy records from the Little Bahama Bank and the Blake Outer Ridge covering the last interglacial cycle. (**A-B**) $\delta^{18}O$ values in *G. ruber* (white) in core MD99-2202 (red) (Lantzsch et al., 2007) and at Site 1058 (grey) (Bahr et al., 2013), (**C**) relative abundances of tropical species *G. sacculifer* and *G. ruber* (pink) in core MD99-2202 (Zhuravleva and Bauch, manuscript under review for CP), (**D**) SSTs at Site 1058, based on Mg/Ca ratios in *G. ruber* (white) (Bahr et al., 2013), (**E**) boreal summer insolation (21 June, 30°N), computed with AnalySeries 2.0.8 (Paillard et al., 1996) using Laskar et al. (2004) data. Shaded in lilac is MIS 5e. Terminat. – Deglacial termination.

Particularly for the last interglacial cycle, there is a lack of information on upper water characteristics in the mid-latitude North Atlantic. However, given a pronounced climatic variability revealed in this thesis for the SPG region, there must have been changes in the STG properties (temperature, salinity, gyre strength) through time. The latter assumption is based on earlier studies, revealing expansion and warming of the STG (i.e., low-latitude buildup of heat) in response to high-latitude freshening, reduction in ocean overturning and SPG weakening (Carlson et al., 2008a; Naafs et al., 2013). In turn, changes in the STG heat storage have important implications for intermediate and deep-water formation as well as for stabilization of the high-latitude climate (Repschläger et al., 2017), a linkage that has never been investigated for the last interglacial cycle. Thus, accurate representation of surface and subsurface temperatures in the STG region would be required to understand the mechanisms regulating the cross-latitudinal heat transport and its role for the deep-water formation in the Nordic and Labrador seas. Finally, robust understanding of the last interglacial meridional SST gradients across the Atlantic Ocean would help to draw conclusions on the interhemispheric seesaw patterns during this time interval.

6.2.2 Intermediate and deep ocean paleoceanography in the North Atlantic during the last interglacial cycle

Recent proxy reconstructions from the Bermuda Rise based on dissolved radiogenic Nd isotope (expressed in ε_{Nd}; a proxy for water mass provenance) and stable carbon isotope ($\delta^{13}C$) compositions in benthic foraminifera (a proxy for bottom water chemistry) suggest that the ocean overturning abruptly recovered at the onset of MIS 5e, due to drastic deepening of convection in the Northwestern Atlantic (Deaney et al., 2017). On contrary, deep-water overflows from the Nordic Seas remained weak or shallow until mid-MIS 5e (Hodell et al., 2011; Barker et al., 2015). This is intriguing with regard to the models and

historical observations, suggesting that deep-water convection in the Labrador Sea is more sensitive to sea surface dilution than convection in the Nordic Seas (Dickson et al., 1988; Wood et al., 1999). Accordingly, Holocene proxy data infer an earlier strengthening of the Nordic Seas overflows when compared to the onset of intermediate water formation in the Labrador Sea (Hillaire-Marcel et al., 2001; Thornalley et al., 2013). If this was the case, a principally different density structure of the water column in the North Atlantic during the last interglacial could be hypothesized, resulting in an altered propagation depth of the overflow waters, when compared to the Holocene situation.

In contrast to the Holocene, only limited data based on $\delta^{13}C$ and sediment grain size (a proxy for intermediate/deep water flow speed) are available to draw conclusions on deep water circulation changes across the last interglacial. Further investigations based on combined use of $\delta^{13}C$, sediment grain size, ε_{Nd} and Pa/Th data (a proxy for overturning strength) extracted from high-resolution sediment cores obtained from intermediate and deep water sites in the North Atlantic would be necessary to reconcile the large-scale overturning variability during the last interglacial cycle, including the penultimate deglaciation and Heinrich Event 11. Notably, the apparent lack of detrital carbonate in sediments dated to Heinrich Event 11 implies absence of a major deglacial Laurentide Ice Sheet surging during this time (Obrochta et al., 2014), which points to a more important freshening role of the European and/or Greenland Ice Sheets. In addition, the apparent lack of a Younger Dryas-like reduction in deep-water overturning during MIS 5e in ε_{Nd} and Pa/Th data (Böhm et al., 2015; Deaney et al., 2017) should be reconciled with the contrasting evidence for a shoaling/reinvigoration of deep waters of northern/southern origin as revealed by benthic $\delta^{13}C$ records (Galaasen et al., 2014; Hayes et al., 2014).

Finally, further research is required to improve the current understanding of glacial-interglacial intermediate and deep-water paleoceanography of the Nordic Seas. The new studies should, in particular, focus on regional vertical water column structure and propagation depth of the AW, but also on brine formation, possible deep water warming, bottom water ventilation and implications for the overflow waters (Bauch, 2013; Thornalley et al., 2015).

List of Abbreviations

AABW	Antarctic Bottom Water
AC	Antilles Current
AICC2012	Antarctic Ice Core Chronology 2012
AMOC	Atlantic Meridional Overturning Circulation
ArW	Arctic Water
AW	Atlantic Water
AzC	Azores Current
B.m.	*Beella megastoma*
C.w. / CW	*Cibicidoides wuellerstorfi*
CaC	Caribbean Current
CC	Canary Current
CP	Climate of the Past
DSOW	Denmark Strait Overflow Water
EDC	EPICA Dome C
EGC	East Greenland Current
EIC	East Iceland Current
EPICA	European Project for Ice Coring in Antarctica
FC	Florida Current
FaC	Faroe Current
GI	Greenland Interstadial
GIS	Greenland Ice Sheet
GuS	Gulf Stream
GS	Greenland Stadial
H11	Heinrich Event 11
IC	Irminger Current
IE	Isotopic event
IODP	International Ocean Discovery Programm
IRD	Ice-rafted debris
ISOW	Iceland-Scotland Overflow Water
ITCZ	Intertropical Convergence Zone
ka	thousand years before present (1950)
KR	Knipovich Ridge
LBB	Little Bahama Bank
LSW	Labrador Sea Water
MAT	Mass Spectrometer
MIS	Marine Isotope Stage
N.p. / NP	*Neogloboquadrina pachyderma*
NAC	North Atlantic Current
NEC	North Equatorial Current
NEEM	North Greenland Eemian Ice Drilling
NorthGRIP/NGRIP	North Greenland Ice Core Project
NwAC	Norwegian Atlantic Current
ODP	Ocean Drilling Project
O. u.	*Oridorsalis umbonatus*
PGM	Penultimate Glacial Maximum
RAC	Return Atlantic Current
RSL	Relative Sea Level
SBIS	Svalbard-Barents Sea Ice Sheet
SPECMAP	Mapping Spectral Variability in Global Climate Project
SPG	Subpolar Gyre
SST	Sea surface temperature
STG	Subtropical Gyre
T2	Termination 2
V-PDB	Vienna Pee Dee Belemnite
VP	Vøring Plateau
WGC	West Greenland Current
WSC	West Spitsbergen Current
XRF	X-ray fluorescence spectroscopy
YP	Yermak Plateau

References

Aagaard, K., Coachman, L. K., 1968. The East Greenland current north of Denmark Strait: part i., Arctic, pp. 181–200.

Aagaard-Sørensen, S., Husum, K., Hald, M., Knies, J., 2010. Paleoceanographic development in the SW Barents Sea during the Late Weichselian–Early Holocene transition. Quat. Sci. Rev. 29, 3442–3456. https://doi.org/10.1016/j.quascirev.2010.08.014.

Aagaard-Sørensen, S., Husum, K., Werner, K., Spielhagen, R. F., Hald, M., Marchitto, T. M., 2014. A Late Glacial–Early Holocene multiproxy record from the eastern Fram Strait, Polar North Atlantic. Mar. Geol. 355, 15–26. https://doi.org/10.1016/j.margeo.2014.05.009.

Adkins, J. F., Boyle, E. A., Keigwin, L., Cortijo, E., 1997. Variability of the North Atlantic thermohaline circulation during the last interglacial period. Nature 390, 154. https://doi.org/doi:10.1038/36540.

Adkins, J. F., Ingersoll, A. P., Pasquero, C., 2005. Rapid climate change and conditional instability of the glacial deep ocean from the thermobaric effect and geothermal heating. Quat. Sci. Rev. 24, 581–594. https://doi.org/10.1016/j.quascirev.2004.11.005.

Adler, R. E., Polyak, L., Ortiz, J. D., Kaufman, D. S., Channell, J. E. T., Xuan, C., Grottoli, A. G., Sellén, E., Crawford, K. A., 2009. Sediment record from the western Arctic Ocean with an improved Late Quaternary age resolution: HOTRAX core HLY0503-8JPC, Mendeleev Ridge. Glob. Planet. Change 68, 18–29. https://doi.org/10.1016/j.gloplacha.2009.03.026.

Aksenov, Y., Bacon, S., Coward, A. C., Holliday, N. P., 2010. Polar outflow from the Arctic Ocean: A high resolution model study. Journal of Marine Systems 83, 14–37. https://doi.org/10.1016/j.jmarsys.2010.06.007.

Alley, R. B., Andrews, J. T., Brigham-Grette, J., Clarke, G. K. C., Cuffey, K. M., Fitzpatrick, J. J., Funder, S., Marshall, S. J., Miller, G. H., Mitrovica, J. X., Muhs, D. R., Otto-Bliesner, B. L., Polyak, L., White, J. W. C., 2010. History of the Greenland Ice Sheet: paleoclimatic insights. Quat. Sci Rev. 29, 1728–1756. https://doi.org/10.1016/j.quascirev.2004.11.005.

Andersen, C., Koç, N., Jennings, A., Andrews, J. T., 2004. Nonuniform response of the major surface currents in the Nordic Seas to insolation forcing: Implications for the Holocene climate variability. Paleoceanography 19, 2155–2166. https://doi.org/10.1029/2002PA000873.

Andersson, C., Pausata, F. S., Jansen, E., Risebrobakken, B., Telford, R. J., 2010. Holocene trends in the foraminifer record from the Norwegian Sea and the North Atlantic Ocean. Clim. Past. 179–193. https://doi.org/10.5194/cp-6-179-2010.

Andreasen, D. J., Ravelo, A. C., 2010. Tropical Pacific Ocean thermocline depth reconstructions for the Last Glacial Maximum. Paleoceanography 12, 395–413. https://doi.org/10.1029/97PA00822.

Antonow, M., Goldschmidt, P. M., Erlenkeuser, H., 1997. The climate-sensitive Vesterisbanken area (central Greenland Sea): Depositional environment and paleoceanography during the past 250,000 years. Contributions to Micropaleontology and Paleoceanography of the North Atlantic, Grzybowski Foundation Special Publication, Krakow, pp. 101–118.

Bahr, A., Nürnberg, D., Schönfeld, J., Garbe-Schönberg, D., 2011. Hydrological variability in Florida Straits during Marine Isotope Stage 5 cold events. Paleoceanography 26. https://doi.org/10.1029/2010PA002015.

Bahr, A., Nürnberg, D., Karas, C., Grützner, J., 2013. Millennial-scale versus long-term dynamics in the surface and subsurface of the western North Atlantic Subtropical Gyre during Marine Isotope Stage 5. Glob. Planet. Change 111, 77–87. https://doi.org/10.1016/j.gloplacha.2013.08.013.

Bahr, A., Jiménez-Espejo, F. J., Kolasinac, N., Grunert, P., Hernández-Molina F. J, Röhl U., Voelker, A. H. L., Escutia, C., Stow, D. A. V., Hodell, D., Alvarez-Zarikian, C. A., 2014. Deciphering bottom current velocity and paleoclimate signals from contourite deposits in the Gulf of Cádiz during the last 140 kyr: An inorganic geochemical approach. Geochem. Geophys. Geosyst. 15, 3145–3160. https://doi.org/10.1002/2014GC005356.

Bakker, P., Masson-Delmotte, V., Martrat, B., Charbit, S., Renssen, H., Gröger, M., Krebs-Kanzow, U., Lohmann, G., Lunt, D. J., Pfeiffer, M., Phipps, S. J., Prange, M., Ritz, S. P., Schulz, M., Stenni, B., Stone, E. J., Varma, V., 2014. Temperature trends during the Present and Last Interglacial periods – a multi-model-data comparison. Quat. Sci. Rev. 99, 224–243. https://doi.org/10.1016/j.quascirev.2014.06.031.

Barker, S., Diz, P., Vautravers, M. J., Pike, J., Knorr, G., Hall, I. R., Broecker, W. S., 2009. Interhemispheric Atlantic seesaw response during the last deglaciation. Nature 457, 1097. https://doi.org/doi:10.1038/nature07770.

Barker, S., Chen, J., Gong, X., Jonkers, L., Knorr, G., Thornalley, D., 2015. Icebergs not the trigger for North Atlantic cold events. Nature 520, 333. http://dx.doi.org/10.1038/nature14330.

Bauch, D., Bauch, H. A., 2001. Last glacial benthic foraminiferal $\delta^{18}O$ anomalies in the polar North Atlantic: A modern analogue evaluation. J. Geophys. Res.: Oceans 106, 9135–9143. https://doi.org/10.1029/1999JC000164.

Bauch, D., Darling, K., Simstich, J., Bauch, H. A., Erlenkeuser, H., Kroon, D., 2003. Palaeoceanographic implications of genetic variation in living North Atlantic *Neogloboquadrina pachyderma*. Nature 424, 299–302. https://doi.org/10.1038/nature01778.

Bauch, H. A., 1994. Significance of variability in *Turborotalita quinqueloba* (Natland) test size and abundance for paleoceanographic interpretations in the Norwegian-Greenland Sea. Mar. Geol. 121, 129–141. https://doi.org/10.1016/0025-3227(94)90162-7.

Bauch, H. A., 1996. Monitoring Termination II at high latitude: anomalies in the planktic foraminiferal record. Mar. Geol. 131, 89–102. https://doi.org/10.1016/0025-3227(95)00147-6.

Bauch, H. A., 2013. Interglacial climates and the Atlantic meridional overturning circulation: is there an Arctic controversy? Quat. Sci. Rev. 63, 1–22. https://doi.org/10.1016/j.quascirev.2012.11.023.

Bauch, H. A., Erlenkeuser, H., 2003. Interpreting glacial-interglacial changes in ice volume and climate from subarctic deep water foraminiferal $\delta^{18}O$, in: Earth's Climate and Orbital Eccentricity: The Marine Isotope Stage 11 Question. American Geophysical Union, pp. 87–102.

Bauch, H. A., Erlenkeuser, H., 2008. A “critical” climatic evaluation of last interglacial (MIS 5e) records from the Norwegian Sea. Pol. Res. 27, 135–151. https://doi.org/10.1111/j.1751-8369.2008.00059.x.

Bauch, H. A., Kandiano, E. S., 2007. Evidence for early warming and cooling in North Atlantic surface waters during the last interglacial. Paleoceanography 22, PA1201. https://doi.org/10.1029/2005PA001252.

Bauch, H. A., Weinelt, M. S., 1997. Surface water changes in the norwegian sea during last deglacial and holocene times. Quat. Sci. Rev. 16, 1115–1124. https://doi.org/10.1016/S0277-3791(96)00075-3.

Bauch, H. A., Erlenkeuser, H., Grootes, P. M., Jouzel, J., 1996. Implications of Stratigraphic and Paleoclimatic Records of the Last Interglaciation from the Nordic Seas. Quat. Res. 46, 260–269. https://doi.org/10.1006/qres.1996.0065.

Bauch, H. A., Erlenkeuser, H., Fahl, K., Spielhagen, R. F., Weinelt, M. S., Andruleit, H., Henrich, R., 1999. Evidence for a steeper Eemian than Holocene sea surface temperature gradient between Arctic and sub-Arctic regions. Palaeogeogr. Palaeoclimatol. Palaeoecol. 145, 95–117. https://doi.org/10.1016/S0031-0182(98)00104-7.

Bauch, H. A., Erlenkeuser, H., Jung, S. J. A., Thiede, J., 2000. Surface and deep water changes in the subpolar North Atlantic during Termination II and the Last Interglaciation. Paleoceanography 15, 76–84. https://doi.org/10.1029/1998PA000343.

Bauch, H. A., Erlenkeuser, H., Spielhagen, R. F., Struck, U., Matthiessen, J., Thiede, J., Heinemeier, J., 2001. A multiproxy reconstruction of the evolution of deep and surface waters in the subarctic Nordic seas over the last 30,000 yr. Quat. Sci. Rev. 20, 659–678. https://doi.org/10.1016/S0277-3791(00)00098-6.

Bauch, H. A., Kandiano, E. S., Helmke, J., Andersen, N., Rosell-Mele, A., Erlenkeuser, H., 2011. Climatic bisection of the last interglacial warm period in the Polar North Atlantic. Quat. Sci. Rev. 30, 1813–1818. https://doi.org/10.1016/j.quascirev.2011.05.012.

Bauch, H. A., Kandiano, E. S., Helmke, J. P., 2012. Contrasting ocean changes between the subpolar and polar North Atlantic during the past 135 ka. Geophys. Res. Lett. 39. https://doi.org/10.1029/2012GL051800.

Baumann, K.-H., Lackschewitz, K. S., Mangerud, J., Spielhagen, R. F., Wolf-Welling, T. C. W., Henrich, R., Kassens, H., 1995. Reflection of Scandinavian Ice Sheet Fluctuations in Norwegian Sea Sediments during the Past 150,000 Years. Quat. Res. 43, 185–197. https://doi.org/10.1006/qres.1995.1019.

Baumgartner, M., Kindler, P., Eicher, O., Floch, G., Schilt, A., Schwander, J., Spahni, R., Capron, E., Chappellaz, J., Leuenberger, M., Fischer, H., Stocker, T. F., 2014. NGRIP CH_4 concentration from 120 to 10 kyr before present and its relation to a $\delta^{15}N$ temperature reconstruction from the same ice core. Clim. Past 10, 903–920. https://doi.org/10.5194/cp-10-903-2014.

Bazin, L., Landais, A., Lemieux-Dudon, B., Toyé Mahamadou Kele, H., Veres, D., Parrenin, F., Martinerie, P., Ritz, C., Capron, E., Lipenkov, V., Loutre, M.-F., Raynaud, D., Vinther, B., Svensson, A., Rasmussen, S. O., Severi, M., Blunier, T., Leuenberger, M., Fischer, H., Masson-Delmotte, V., Chappellaz, J., Wolff, E., 2013. An optimized multi-proxy, multi-site Antarctic ice and gas orbital

chronology (AICC2012): 120–800 ka. Clim. Past 9, 1715–1731. https://doi.org/10.5194/cp-9-1715-2013.

Bé, A. W. H., Tolderlund, D. S., 1971. Distribution and ecology of living planktonic foraminifera in surface waters of the Atlantic and Indian Oceans, in: Funnel, B. and Riedel, W.R. (Eds.) The Micropalaeontology of Oceans. Cambridge University Press, Cambridge, pp. 105–149.

Belkin, I. M., 2004. Propagation of the "Great Salinity Anomaly" of the 1990s around the northern North Atlantic. Geophys. Res. Lett. 31, L08306. https://doi.org/10.1029/2003GL019334.

Beszczynska-Möller, A., Fahrbach, E., Schauer, U., Hansen, E., 2012. Variability in Atlantic water temperature and transport at the entrance to the Arctic Ocean, 1997–2010. ICES J. Mar. Sci. 852–863. https://doi.org/10.1093/icesjms/fss056.

Bhatia, M. P., Das, S. B., Xu, L., Charette, M. A., Wadham, J. L., Kujawinski, E. B., 2013. Organic carbon export from the Greenland ice sheet. Geochim. Cosmochim. Acta 109, 329–344. https://doi.org/10.1016/j.gca.2013.02.006.

Bijma, J., Faber, W. W., Hemleben, C., 1990. Temperature and salinity limits for growth and survival of some planktonic foraminifers in laboratory cultures. J. Foraminiferal Res. 20, 95. https://doi.org/10.2113/gsjfr.20.2.95.

Bintanja, R., van Oldenborgh, G. J., Drijfhout, S. S., Wouters, B., Katsman, C. A., 2013. Important role for ocean warming and increased ice-shelf melt in Antarctic sea-ice expansion. Nature Geosci. 6, 376–379. https://doi.org/10.1038/ngeo1767.

Birgel, D., Stein, R., Hefter, J., 2004. Aliphatic lipids in recent sediments of the Fram Strait/Yermak Plateau (Arctic Ocean): composition, sources and transport processes. Mar. Chem. 88, 127–160. https://doi.org/10.1016/j.marchem.2004.03.006.

Bischof, J., Koch, J., Kubisch, M., Spielhagen, R. F., Thiede, J., 1990. Nordic Seas surface ice drift reconstructions: evidence from ice rafted coal fragments during oxygen isotope stage 6. Geological Society, London, Special Publications 53, 235–251. https://doi.org/10.1144/GSL.SP.1990.053.01.13.

Bischof, J., Lund, J. J., Ecke, H.-H., 1997. Palynomorphs of ice rafted clastic sedimentary rocks in Late Quaternary glacial marine sediments of the Norwegian Sea as provenance indicators. Palaeogeogr. Palaeoclimatol. Palaeoecol. 129, 329–360. https://doi.org/10.1016/S0031-0182(97)88176-X.

Blindheim, J., Østerhus, S., 2005. The Nordic Seas, main oceanographic features, in: The Nordic Seas: An Integrated Perspective. pp. 11–37.

Blindheim, J., Borovkov, V., Hansen, B., Malmberg, S.-A., Turrell, W. R., Østerhus, S., 2000. Upper layer cooling and freshening in the Norwegian Sea in relation to atmospheric forcing. Deep Sea Res. Part I: Oceanogr. Res. Pap. 47, 655–680. https://doi.org/10.1016/S0967-0637(99)00070-9.

Böhm, E., Lippold, J., Gutjahr, M., Frank, M., Blaser, P., Antz, B., Fohlmeister, J., Frank, N., Andersen, M. B., Deininger, M., 2014. Strong and deep Atlantic meridional overturning circulation during the last glacial cycle. Nature 517, 73. http://dx.doi.org/10.1038/nature14059.

Boli, H. M., Saunders, J. B., 1985. Oligocene to Holocene low latitude planktic foraminifera., in: In: Bolli, H.M., Saunders, J.B., Perch-Nielsen, K. (Eds.), Plankton Stratigraphy. Cambridge University Press, New York, pp. 155–262.

Böning, C. W., Behrens, E., Biastoch, A., Getzlaff, K., Bamber, J.L., 2016. Emerging impact of Greenland meltwater on deepwater formation in the North Atlantic Ocean. Nature Geosci. 9, 523–527. http://dx.doi.org/10.1038/ngeo2740.

Born, A., Stocker, T. F., 2014. Two Stable Equilibria of the Atlantic Subpolar Gyre. J. Phys. Oceanogr. 44, 246–264. https://doi.org/10.1175/JPO-D-13-073.1.

Born, A., Nisancioglu, K. H., Braconnot, P., 2010. Sea ice induced changes in ocean circulation during the Eemian. Clim. Dyn. 35, 1361–1371. https://doi.org/10.1007/s00382-009-0709-2.

Born, A., Nisancioglu, K. H., Risebrobakken, B., 2011. Late Eemian warming in the Nordic Seas as seen in proxy data and climate models. Paleoceanography 26, PA2207. https://doi.org/10.1029/2010PA002027.

Brendryen, J., Haflidason, H., Sejrup, H. P., 2010. Norwegian Sea tephrostratigraphy of marine isotope stages 4 and 5: Prospects and problems for tephrochronology in the North Atlantic region. Quat. Sci. Rev. 29, 847–864. https://doi.org/10.1016/j.quascirev.2009.12.004.

Brigham-Grette, J., Hopkins, D. M., 1995. Emergent Marine Record and Paleoclimate of the Last Interglaciation along the Northwest Alaskan Coast. Quat. Res. 43, 159–173. https://doi.org/10.1006/qres.1995.1017.

Brocas, W. M., Felis, T., Obert, J. C., Gierz, P., Lohmann, G., Scholz, D., Kölling, M., Scheffers, S. R., 2016. Last interglacial temperature seasonality reconstructed from tropical Atlantic corals. Earth Planet. Sci. Lett. 449, 418–429. https://doi.org/10.1016/j.epsl.2016.06.005.

Bryden, H. L., Longworth, H. R., Cunningham, S.A., 2005. Slowing of the Atlantic meridional overturning circulation at 25° N. Nature 438, 655. https://doi.org/10.1038/nature04385.

Caesar, L., Rahmstorf, S., Robinson, A., Feulner, G., Saba, V., 2018. Observed fingerprint of a weakening Atlantic Ocean overturning circulation. Nature 556, 191–196. https://doi.org/10.1038/s41586-018-0006-5.

CAPE-Last Interglacial Project Members, 2006. Last Interglacial Arctic warmth confirms polar amplification of climate change. Quat. Sci. Rev. 25, 1383–1400. https://doi.org/10.1016/j.quascirev.2006.01.033.

Capron, E., Govin, A., Stone, E. J., Masson-Delmotte, V., Mulitza, S., Otto-Bliesner, B., Rasmussen, T. L., Sime, L. C., Waelbroeck, C., Wolff, E. W., 2014. Temporal and spatial structure of multi-millennial temperature changes at high latitudes during the Last Interglacial. Quat. Sci. Rev. 103, 116–133. https://doi.org/10.1016/j.quascirev.2014.08.018.

Capron, E., Govin, A., Feng, R., Otto-Bliesner, B. L., Wolff, E. W., 2017. Critical evaluation of climate syntheses to benchmark CMIP6/PMIP4 127 ka Last Interglacial simulations in the high-latitude regions. Quat. Sci. Rev. 168, 137–150. https://doi.org/10.1016/j.quascirev.2017.04.019.

Carew, J. L., Mylroie, J. E., 1995. Quaternary tectonic stability of the Bahamian archipelago: evidence from fossil coral reefs and flank margin caves. Quat. Sci. Rev. 14, 145–153. https://doi.org/10.1016/0277-3791(94)00108-N.

Carew, J. L., Mylroie, J. E., 1997. Geology of the Bahamas, in: Geology and Hydrogeology of Carbonate Islands. Developments in Sedimentology 54. Elsevier Science, pp. 91–139.

Carlson, A. E., Oppo, D. W., Came, R. E., LeGrande, A. N., Keigwin, L. D., Curry, W. B., 2008a. Subtropical Atlantic salinity variability and Atlantic meridional circulation during the last deglaciation. Geology 36, 991–994. https://doi.org/doi.org/10.1130/G25080A.

Carlson, A. E., Stoner, J. S., Donnelly, J. P., Hillaire-Marcel, C., 2008b. Response of the southern Greenland Ice Sheet during the last two deglaciations. Geology 36, 359–362. https://doi.org/10.1130/G24519A.1.

Carstens, J., Wefer, G., 1992. Recent distribution of planktonic foraminifera in the Nansen Basin, Arctic Ocean. Deep Sea Res. Part I: Oceanogr. Res. Pap. 39, S507–S524. https://doi.org/10.1016/S0198-0149(06)80018-X.

Carstens, J., Hebbeln, D., Wefer, G., 1997. Distribution of planktic foraminifera at the ice margin in the Arctic (Fram Strait). Mar. Micropal. 29, 257–269. https://doi.org/10.1016/S0377-8398(96)00014-X.

Chabaud, L.: Modèle stratigraphique et processus sédimentaires au Quaternaire sur deux pentes carbonatées des Bahamas (leeward et windward), Doctoral dissertation, Université de Bordeaux, Francais, 2016.

Chabaud, L., Ducassou, E., Tournadour, E., Mulder, T., Reijmer, J. J. G., Conesa, G., Giraudeau, J., Hanquiez, V., Borgomano, J., Ross, L., 2016. Sedimentary processes determining the modern carbonate periplatform drift of Little Bahama Bank. Mar. Geol. 378, 213–229. https://doi.org/10.1016/j.margeo.2015.11.006.

Channell, J. E. T., Xuan, C., Hodell, D. A., 2009. Stacking paleointensity and oxygen isotope data for the last 1.5 Myr (PISO-1500). Earth Planet. Sci. Lett. 283, 14–23. https://doi.org/10.1016/j.epsl.2009.03.012.

Chappellaz, J., Bluniert, T., Raynaud, D., Barnola, J. M., Schwander, J., Stauffert, B., 1993. Synchronous changes in atmospheric CH_4 and Greenland climate between 40 and 8 kyr BP. Nature 366, 443–445. https://doi.org/10.1038/366443a0.

Chiang, J. C., Kushnir, Y. and Giannini, A., 2002. Deconstructing Atlantic Intertropical Convergence Zone variability: Influence of the local cross-equatorial sea surface temperature gradient and remote forcing from the eastern equatorial Pacific. J. Geophys. Res.: Atmosph., 107(D1). https://doi.org/10.1029/2000JD000307.

Chiang, J. C. H., Biasutti, M., Battisti, D. S., 2003. Sensitivity of the Atlantic Intertropical Convergence Zone to Last Glacial Maximum boundary conditions. Paleoceanography 18. https://doi.org/10.1029/2003PA000916.

Cléroux, C., Cortijo, E., Duplessy, J., Zahn, R., 2007. Deep-dwelling foraminifera as thermocline temperature recorders. Geochem. Geophys. Geosyst. 8. https://doi.org/10.1029/2006GC001474.

Collins, M., Knutti, R., Arblaster, J., Dufresne, J.-L., Fichefet, P., Gao, X., Gutowski, W. J., 2013. Long-term climate change: Projections, commitments and irreversibility. In: Stocker, T.F., Qin, D., Plattner, G.-K., Tignor, M., Allen, S. K., Boschung, J., Nauels, A., Xia, Y., Bex, V., Midgley, P. M. (Eds.), Climate Change 2013: The Physical Science Basis. Contribution of Working Group I to the Fifth Assessment Report of the Intergovernmental Panel on Climate Change, Cambridge: Cambridge University Press, pp. 1029-1136.

Colville, E. J., Carlson, A. E., Beard, B. L., Hatfield, R. G., Stoner, J. S., Reyes, A. V., Ullman, D. J., 2011. Sr-Nd-Pb Isotope Evidence for Ice-Sheet Presence on Southern Greenland During the Last Interglacial. Science 333, 620. https://doi.org/10.1126/science.1204673.

Cortijo, E., Duplessy, J., Labeyrie, L., Leclaire, H., Duprat, J., Van Wearing, T., 1994. Eemian cooling in the Norwegian Sea and North Atlantic ocean preceding continental ice-sheet growth. Nature 372, 446–449.

Cortijo, E., Lehman, S., Keigwin, L., Chapman, M., Paillard, D., Labeyrie, L., 1999. Changes in Meridional Temperature and Salinity Gradients in the North Atlantic Ocean (30°–72°N) during the Last Interglacial Period. Paleoceanography 14, 23–33. https://doi.org/10.1029/1998PA900004.

Cottet-Puinel, M., Weaver, A. J., Hillaire-Marcel, C., de Vernal, A., Clark, P.U., Eby, M., 2004. Variation of Labrador Sea Water formation over the Last Glacial cycle in a climate model of intermediate complexity. Quat. Sci. Rev. 23, 449–465. https://doi.org/10.1016/S0277-3791(03)00123-9.

Cronin, T. M., Gemery, L., Briggs Jr., W. M., Jakobsson, M., Polyak, L., Brouwers, E. M., 2010. Quaternary Sea-ice history in the Arctic Ocean based on a new Ostracode sea-ice proxy. Quat. Sci. Rev. 29, 3415–3429. https://doi.org/10.1016/j.quascirev.2010.05.024.

Curry, R., Mauritzen, C., 2005. Dilution of the Northern North Atlantic Ocean in Recent Decades. Science 308, 1772. https://doi.org/10.1126/science.1109477.

Darling, K. F., Kucera, M., Kroon, D., Wade, C. M., 2006. A resolution for the coiling direction paradox in Neogloboquadrina pachyderma. Paleoceanography 21, PA2011. https://doi.org/10.1029/2005PA001189.

de Vernal, A., Hillaire-Marcel, C., 2008. Natural Variability of Greenland Climate, Vegetation, and Ice Volume During the Past Million Years. Science 320, 1622. https://doi.org/10.1126/science.1153929.

Deaney, E. L., Barker, S., van de Flierdt, T., 2017. Timing and nature of AMOC recovery across Termination 2 and magnitude of deglacial CO_2 change. Nat. Commun. 8, 14595. https://doi.org/doi:10.1038/ncomms14595.

Denton, G. H., Anderson, R. F., Toggweiler, J. R., Edwards, R. L., Schaefer, J. M., Putnam, A. E., 2010. The Last Glacial Termination. Science 328, 1652. https://doi.org/10.1126/science.1184119.

Dickson, R. R., Meincke, J., Malmberg, S.-A., Lee, A. J., 1988. The “great salinity anomaly” in the Northern North Atlantic 1968–1982. Prog. Oceanogr. 20, 103–151. https://doi.org/10.1016/0079-6611(88)90049-3.

Dickson, R. R., Osborn, T. J., Hurrell, J. W., Meincke, J., Blindheim, J., Adlandsvik, B., Vinje, T., Alekseev, G., Maslowski, W., 2000. The Arctic Ocean Response to the North Atlantic Oscillation. J. Climate 13, 2671–2696. https://doi.org/10.1175/1520-0442(2000)013<2671:TAORTT>2.0.CO;2.

Dickson, R. R., Rudels, B., Dye, S., Karcher, M., Meincke, J., Yashayaev, I., 2007. Current estimates of freshwater flux through Arctic and subarctic seas. Progr. Oceanogr. 73, 210–230. https://doi.org/10.1016/j.pocean.2006.12.003.

Dokken, T. M., Jansen, E., 1999. Rapid changes in the mechanism of ocean convection during the last glacial period. Nature 401, 458–461. https://doi.org/10.1038/46753.

Duplessy, J. C., Shackleton, N. J., Fairbanks, R. G., Labeyrie, L., Oppo, D., Kallel, N., 1988. Deepwater source variations during the last climatic cycle and their impact on the global deepwater circulation. Paleoceanography 3, 343–360.

Dutton, A., Carlson, A. E., Long, A. J., Milne, G. A., Clark, P. U., DeConto, R., Horton, B. P., Rahmstorf, S., Raymo, M. E., 2015. Sea-level rise due to polar ice-sheet mass loss during past warm periods. Science 349, 6244. https://doi.org/10.1126/science.aaa4019.

Ebbesen, H., Hald, M., Eplet, T.H., 2007. Lateglacial and early Holocene climatic oscillations on the western Svalbard margin, European Arctic. Quat. Sci. Rev. 26, 1999–2011. https://doi.org/10.1016/j.quascirev.2006.07.020.

Eldevik, T., Nilsen, J. E. O., Iovino, D., Anders Olsson, K., Sando, A. B., Drange, H., 2009. Observed sources and variability of Nordic seas overflow. Nature Geosci. 2, 406–410. https://doi.org/10.1038/ngeo518.

Elverhøi, A., Andersen, E. S., Dokken, T., Hebbeln, D., Spielhagen, R., Svendsen, J. I., Sørflaten, M., Rørnes, A., Hald, M., Forsberg, C.F., 1995. The Growth and Decay of the Late Weichselian Ice Sheet in Western Svalbard and Adjacent Areas Based on Provenance Studies of Marine Sediments. Quat. Res. 44, 303–316. https://doi.org/10.1006/qres.1995.1076.

Ericson, D. B., Wollin, G., 1968. Pleistocene climates and chronology in deep-sea sediments. Science 162(3859), 1227–1234. https://doi.org/doi:10.1126/science.162.3859.1227.

Evans, H. F., Channell, J. E. T., Stoner, J. S., Hillaire-Marcel, C., Wright, J. D., Neitzke, L. C., Mountain, G. S., 2007. Paleointensity-assisted chronostratigraphy of detrital layers on the Eirik Drift (North Atlantic) since marine isotope stage 11. Geochem. Geophys. Geosyst. 8, Q11007. https://doi.org/10.1029/2007GC001720.

Flato, G., Marotzke, J., Abiodun, B., Braconnot, P., Chou, S. C., Collins, W. J., Cox, P., Driouech, F., Emori, S., Eyring, V., Forest, C., Gleckler, P., Guilyardi, E., Jakob, C., Kattsov, V., Reason, C., Rummukaines, M., 2013. Evaluation of Climate Models. In: Stocker, T.F., Qin, D., Plattner, G.-K., Tignor, M., Allen, S. K., Boschung, J., Nauels, A., Xia, Y., Bex, V., Midgley, P. M. (Eds.), Climate Change 2013: The Physical Science Basis. Contribution of Working Group I to the Fifth Assessment Report of the Intergovernmental Panel on Climate Change, Cambridge University Press, pp. 741–866.

Fronval, T., Jansen, E., 1996. Rapid changes in ocean circulation and heat flux in the Nordic seas during the last interglacial period. Nature 383, 806–810. https://doi.org/10.1038/383806a0.

Fronval, T., Jansen, E., 1997. Eemian and Early Weichselian (140–60 ka) Paleoceanography and paleoclimate in the Nordic Seas with comparisons to Holocene conditions. Paleoceanography 12, 443–462. https://doi.org/10.1029/97PA00322.

Fronval, T., Jansen, E., Haflidason, H., Sejrup, H. P., 1998. Variability in surface and deep water conditions in the nordic seas during the last interglacial period. Quat. Sci. Rev. 17, 963–985. https://doi.org/10.1016/S0277-3791(98)00038-9.

Funder, S., Hjort, C., Landvik, J. Y., Nam, S.-I., Reeh, N., Stein, R., 1998. History of a stable ice margin—East Greenland during middle and upper Pleistocene. Quat. Sci. Rev. 17, 77–123. https://doi.org/10.1016/S0277-3791(97)00082-6.

Funder, S., Demidov, I., Yelovicheva, Y., 2002. Hydrography and mollusc faunas of the Baltic and the White Sea–North Sea seaway in the Eemian. Palaeogeogr.

Palaeoclimatol. Palaeoecol. 184, 275–304. https://doi.org/10.1016/S0031-0182(02)00256-0.

Funder, S., Kjeldsen, K. K., Kjær, K. H., Cofaigh, C., 2011. The Greenland Ice Sheet during the past 300,000 years: A review, in: Developments in Quaternary Science. pp. 699–713.

Galaasen, E. V., Ninnemann, U. S., Irvalı, N., Kleiven, H. (Kikki) F., Rosenthal, Y., Kissel, C., Hodell, D.A., 2014. Rapid Reductions in North Atlantic Deep Water During the Peak of the Last Interglacial Period. Science 343, 1129. https://doi.org/10.1126/science.1248667.

Gelderloos, R., Straneo, F., Katsman, C. A., 2012. Mechanisms behind the Temporary Shutdown of Deep Convection in the Labrador Sea: Lessons from the Great Salinity Anomaly Years 1968–71. J. Climate 25, 6743–6755. https://doi.org/10.1175/JCLI-D-11-00549.1.

Gibson, K. A., Peterson, L. C., 2014. A 0.6 million year record of millennial-scale climate variability in the tropics. Geophys. Res. Lett. 41, 969–975. https://doi.org/10.1002/2013GL058846.

Govin, A., Braconnot, P., Capron, E., Cortijo, E., Duplessy, J.-C., Jansen, E., Labeyrie, L., Landais, A., Marti, O., Michel, E., Mosquet, E., Risebrobakken, B., Swingedouw, D., Waelbroeck, C., 2012. Persistent influence of ice sheet melting on high northern latitude climate during the early Last Interglacial. Clim. Past 8, 483–507. https://doi.org/10.5194/cp-8-483-2012.

Govin, A., Varma, V., Prange, M., 2014. Astronomically forced variations in western African rainfall (21°N–20°S) during the Last Interglacial period. Geophys. Res. Lett. 41, 2117–2125. https://doi.org/10.1002/2013GL058999.

Govin, A., Capron, E., Tzedakis, P. C., Verheyden, S., Ghaleb, B., Hillaire-Marcel, C., St-Onge, G., Stoner, J. S., Bassinot, F., Bazin, L., Blunier, T., Combourieu-Nebout, N., El Ouahabi, A., Genty, D., Gersonde, R., Jimenez-Amat, P., Landais, A., Martrat, B., Masson-Delmotte, V., Parrenin, F., Seidenkrantz, M.-S., Veres, D., Waelbroeck, C., Zahn, R., 2015. Sequence of events from the onset to the demise of the Last Interglacial: Evaluating strengths and limitations of chronologies used in climatic archives. Quat. Sci. Rev. 129, 1–36. https://doi.org/10.1016/j.quascirev.2015.09.018.

Grant, K. M., Rohling, E. J., Bar-Matthews, M., Ayalon, A., Medina-Elizalde, M., Ramsey, C. B., Satow, C., Roberts, A.P., 2012. Rapid coupling between ice volume and polar temperature over the past 150,000 years. Nature 491, 744. https://doi.org/doi:10.1038/nature11593.

Groeneveld, J., Chiessi, C. M., 2011. Mg/Ca of *Globorotalia inflata* as a recorder of permanent thermocline temperatures in the South Atlantic. Paleoceanography 26. https://doi.org/10.1029/2010PA001940.

Grøsfjeld, K., Funder, S., Seidenkrantz, M.-S., Glaister, C., 2006. Last Interglacial marine environments in the White Sea region, northwestern Russia. Boreas 35, 493–520. https://doi.org/10.1080/03009480600781917.

Guihou, A., Pichat, S., Nave, S., Govin, A., Labeyrie, L., Michel, E., Waelbroeck, C., 2010. Late slowdown of the Atlantic Meridional Overturning Circulation during the Last Glacial Inception: New constraints from sedimentary (^{231}Pa/^{230}Th). Earth Planet. Sci. Lett 289, 520–529. https://doi.org/10.1016/j.epsl.2009.11.045.

Häkkinen, S., Rhines, P. B., 2004. Decline of Subpolar North Atlantic Circulation During the 1990s. Science 304, 555. https://doi.org/10.1126/science.1094917.

Håkansson, L., Alexanderson, H., Hjort, C., Möller, P., Briner, J. P., Aldahan, A., Possnert, G., 2009. Late Pleistocene glacial history of Jameson Land, central East Greenland, derived from cosmogenic ^{10}Be and ^{26}Al exposure dating. Boreas 38, 244–260. https://doi.org/10.1111/j.1502-3885.2008.00064.x.

Hald, M., Dokken, T., Mikalsen, G., 2001. Abrupt climatic change during the last interglacial–glacial cycle in the polar North Atlantic. Mar. Geol. 176, 121–137. https://doi.org/10.1016/S0025-3227(01)00158-X.

Hald, M., Andersson, C., Ebbesen, H., Jansen, E., Klitgaard-Kristensen, D., Risebrobakken, B., Salomonsen, G. R., Sarnthein, M., Sejrup, H. P., Telford, R. J., 2007. Variations in temperature and extent of Atlantic Water in the northern North Atlantic during the Holocene. Quat. Sci. Rev. 26, 3423–3440. https://doi.org/10.1016/j.quascirev.2007.10.005.

Hansen, B., Østerhus, S., 2000. North Atlantic–Nordic Seas exchanges. Prog. Oceanogr. 45, 109–208. https://doi.org/10.1016/S0079-6611(99)00052-X.

Hátún, H., Sandø, A. B., Drange, H., Hansen, B., Valdimarsson, H., 2005. Influence of the Atlantic Subpolar Gyre on the Thermohaline Circulation. Science 309, 1841. https://doi.org/10.1126/science.1114777.

Hátún, H., Payne, M.R., Beaugrand, G., Reid, P. C., Sandø, A. B., Drange, H., Hansen, B., Jacobsen, J. A., Bloch, D., 2009. Large bio-geographical shifts in the north-eastern Atlantic Ocean: From the subpolar gyre, via plankton, to blue whiting and pilot whales. Prog. Oceanogr. 80, 149–162. https://doi.org/10.1016/j.pocean.2009.03.001

Haug, G. H., Hughen, K. A., Sigman, D. M., Peterson, L. C., Röhl, U., 2001. Southward Migration of the Intertropical Convergence Zone Through the Holocene. Science 293, 1304. https://doi.org/10.1126/science.1059725.

Hayes, C. T., Martínez-García, A., Hasenfratz, A. P., Jaccard, S. L., Hodell, D. A., Sigman, D. M., Haug, G. H., Anderson, R. F., 2014. A stagnation event in the deep South Atlantic during the last interglacial period. Science 346, 1514–1517. https://doi.org/10.1126/science.1256620.

Hearty, P. J., Neumann, A. C., 2001. Rapid sea level and climate change at the close of the Last Interglaciation (MIS 5e): evidence from the Bahama Islands. Quat. Sci. Rev. 20, 1881–1895. https://doi.org/10.1016/S0277-3791(01)00021-X.

Hearty, P. J., Hollin, J. T., Neumann, A. C., O'Leary, M. J., McCulloch, M., 2007. Global sea-level fluctuations during the Last Interglaciation (MIS 5e). Quat. Sci. Rev. 26, 2090–2112. https://doi.org/10.1016/j.quascirev.2007.06.019.

Hebbeln, D., Wefer, G., 1991. Effects of ice coverage and ice-rafted material on sedimentation in the Fram Strait. Nature 350, 409–411. https://doi.org/10.1038/350409a0.

Hebbeln, D., Wefer, G., 1997. Late Quaternary paleoceanography in the Fram Strait. Paleoceanography 12, 65–78. https://doi.org/10.1029/96PA02753.

Hebbeln, D., Henrich, R., Baumann, K.-H., 1998. Paleoceanography of the Last Interglacial/Glacial cycle in the polar North Atlantic. Quat. Sci. Rev. 17, 125–153. https://doi.org/10.1016/S0277-3791(97)00067-X.

Helmens, K. F., Salonen, J. S., Plikk, A., Engels, S., Väliranta, M., Kylander, M., Brendryen, J., Renssen, H., 2015. Major cooling intersecting peak Eemian Interglacial warmth in northern Europe. Quat. Sci. Rev. 122, 293–299. https://doi.org/10.1016/j.quascirev.2015.05.018.

Helmke, J. P., Bauch, H. A., Röhl, U., Kandiano, E. S., 2008. Uniform climate development between the subtropical and subpolar Northeast Atlantic across marine isotope stage 11. Clim. Past 4, 181–190. https://doi.org/10.5194/cp-4-181-2008.

Hemleben, C., Spindler, M., Anderson, O. R., 1989. Modern planktonic foraminifera. Springer-Verlag New York.

Henderson, G. M., Slowey, N. C., 2000. Evidence from U–Th dating against Northern Hemisphere forcing of the penultimate deglaciation. Nature 404, 61. https://doi.org/doi:10.1038/35003541.

Henderson, G. M., Rendle, R. H., Slowey, N. C., Reijmer, J. J. G., 2000. U-Th dating and diagenesis of Pleistocene highstand sediments from the Bahamas slope. Ocean Drilling Program, Scientific Results 166, pp. 61–76.

Hennekam, R., de Lange, G., 2012. X-ray fluorescence core scanning of wet marine sediments: methods to improve quality and reproducibility of high-resolution paleoenvironmental records. Limnol. Oceanogr. 10, 991–1003. https://doi.org/10.4319/lom.2012.10.991.

Hilbrecht, H., 1996. Extant planktic foraminifera and the physical environment in the Atlantic and Indian Oceans: an atlas based on Climap and Levitus (1982) data. Mitteilungen aus dem Geologischen Institut der Eidgen. Technischen Hochschule und der Universität Zürich, Neue Folge, Zürich, 93 pp.

Hillaire-Marcel, C., de Vernal, A., 2008. Stable isotope clue to episodic sea ice formation in the glacial North Atlantic. Earth Planet. Scie. Lett. 268, 143–150. https://doi.org/10.1016/j.epsl.2008.01.012.

Hillaire-Marcel, C., de Vernal, A., Bilodeau, G., Wu, G., 1994. Isotope stratigraphy, sedimentation rates, deep circulation, and carbonate events in the Labrador Sea during the last ~ 200 ka. Can. J. Earth Sci. 31, 63–89. https://doi.org/10.1139/e94-007.

Hillaire-Marcel, C., de Vernal, A., Bilodeau, G., Weaver, A. J., 2001. Absence of deep-water formation in the Labrador Sea during the last interglacial period. Nature 410, 1073–1077. https://doi.org/10.1038/35074059.

Hodell, D. A., Minth, E. K., Curtis, J. H., McCave, I. N., Hall, I. R., Channell, J. E. T., Xuan, C., 2009. Surface and deep-water hydrography on Gardar Drift (Iceland Basin) during the last interglacial period. Earth Planet. Sci. Lett. 288, 10–19. https://doi.org/10.1016/j.epsl.2009.08.040.

Hoffman, J. S., Clark, P. U., Parnell, A. C., He, F., 2017. Regional and global sea-surface temperatures during the last interglaciation. Science 355, 276. https://doi.org/10.1126/science.aai8464.

Holliday, N. P., Meyer, A., Bacon, S., Alderson, S. G., de Cuevas, B., 2007. Retroflection of part of the east Greenland current at Cape Farewell. Geophys. Res. Lett. 34, L07609. https://doi.org/10.1029/2006GL029085.

Hopkins, T. S., 1991. The GIN Sea—A synthesis of its physical oceanography and literature review 1972–1985. Earth-Sc. Rev. 30, 175–318. https://doi.org/10.1016/0012-8252(91)90001-V.

Huber, R., Meggers, H., Baumann, K.-H., Henrich, R., 2000. Recent and Pleistocene carbonate dissolution in sediments of the Norwegian–Greenland Sea. Mar. Geol. 165, 123–136. https://doi.org/10.1016/S0025-3227(99)00138-3.

Huber, C., Leuenberger, M., Spahni, R., Flückiger, J., Schwander, J., Stocker, T. F., Johnsen, S., Landais, A., Jouzel, J., 2006. Isotope calibrated Greenland temperature record over Marine Isotope Stage 3 and its relation to CH_4. Earth Planet. Sci. Lett. 243, 504–519. https://doi.org/10.1016/j.epsl.2006.01.002.

Husum, K., Hald, M., 2012. Arctic planktic foraminiferal assemblages: Implications for subsurface temperature reconstructions. Mar. Micropal. 96–97, 38–47. https://doi.org/10.1016/j.marmicro.2012.07.001.

Irvali, N., Ninnemann, U. S., Galaasen, E. V., Rosenthal, Y., Kroon, D., Oppo, D. W., Kleiven, H. F., Darling, K. F., Kissel, C., 2012. Rapid switches in subpolar North Atlantic hydrography and climate during the Last Interglacial (MIS 5e). Paleoceanography 27, PA2207. https://doi.org/10.1029/2011PA002244.

Irvali, N., Ninnemann, U. S., Kleiven, H. (Kikki) F., Galaasen, E. V., Morley, A., Rosenthal, Y., 2016. Evidence for regional cooling, frontal advances, and East Greenland Ice Sheet changes during the demise of the last interglacial. Quat. Sci. Rev. 150, 184–199. https://doi.org/10.1016/j.quascirev.2016.08.029.

Jansen, E., Raymo, M. E., Blum, P., 1996. 1. Leg 162: new frontiers on past climates 162, pp. 5–20.

Jansen, J. H.., Van der Gaast, S.., Koster, B., Vaars, A.., 1998. CORTEX, a shipboard XRF-scanner for element analyses in split sediment cores. Mar. Geol. 151, 143–153. https://doi.org/10.1016/S0025-3227(98)00074-7.

Jenkins, R. H., De Vries, B., 1970. Worked examples in X-ray spectrometry. Springer-Verlag.

Jiménez-Amat, P., Zahn, R., 2015. Offset timing of climate oscillations during the last two glacial-interglacial transitions connected with large-scale freshwater perturbation. Paleoceanography 30, 768–788. https://doi.org/10.1002/2014PA002710.

Johannessen, T., Jansen, E., Flatøy, A., Ravelo, A. C., 1994. The Relationship between Surface Water Masses, Oceanographic Fronts and Paleoclimatic Proxies in Surface Sediments of the Greenland, Iceland, Norwegian Seas, in: Zahn, R., Pedersen, T.F., Kaminski, M.A., Labeyrie, L. (Eds.), Carbon Cycling in the Glacial Ocean: Constraints on the Ocean's Role in Global Change: Quantitative Approaches in Paleoceanography. Springer Berlin Heidelberg, Berlin, Heidelberg, pp. 61–85. https://doi.org/10.1007/978-3-642-78737-9_4.

Johns, W. E., Townsend, T. L., Fratantoni, D. M., Wilson, W. D., 2002. On the Atlantic inflow to the Caribbean Sea. Deep Sea Research Part I: Oceanogr. Res. Pap. 49, 211–243. https://doi.org/doi:10.1016/S0967-0637(01)00041-3.

Jonkers, L., Kučera, M., 2015. Global analysis of seasonality in the shell flux of extant planktonic Foraminifera. Biogeosci. 12, 2207–2226. https://doi.org/10.5194/bg-12-2207-2015.

Jonkers, L., Brummer, G.-J. A., Peeters, F. J. C., van Aken, H. M., De Jong, M. F., 2010. Seasonal stratification, shell flux, and oxygen isotope dynamics of left-coiling N. pachyderma and T. quinqueloba in the western subpolar North Atlantic. Paleoceanography 25, PA2204. https://doi.org/10.1029/2009PA001849.

Jonkers, L., van Heuven, S., Zahn, R., Peeters, F. J. C., 2013. Seasonal patterns of shell flux, $\delta^{18}O$ and $\delta^{13}C$ of small and large *N. pachyderma* (s) and *G. bulloides* in the subpolar North Atlantic. Paleoceanography 28, 164–174. https://doi.org/10.1002/palo.20018.

Jungclaus, J. H., Macrander, A., Käse, R. H., 2008. Modelling the Overflows Across the Greenland–Scotland Ridge, in: Dickson, R.R., Meincke, J., Rhines, P. (Eds.), Arctic–Subarctic Ocean Fluxes: Defining the Role of the Northern Seas in Climate. Springer Netherlands, Dordrecht, pp. 527–549. https://doi.org/10.1007/978-1-4020-6774-7_23.

Kandiano, E., Bauch, H. A., 2002. Implications of planktic foraminiferal size fractions for the glacial-interglacial paleoceanography of the polar North Atlantic. J. Foraminiferal Res. 32, 245. https://doi.org/10.2113/32.3.245.

Kandiano, E. S., Bauch, H. A., Fahl, K., Helmke, J. P., Röhl, U., Pérez-Folgado, M., Cacho, I., 2012. The meridional temperature gradient in the eastern North Atlantic during MIS 11 and its link to the ocean–atmosphere system. Palaeogeogr. Palaeoclimatol. Palaeoecol. 333–334, 24–39. https://doi.org/10.1016/j.palaeo.2012.03.005.

Kandiano, E. S., Bauch, H. A., Fahl, K., 2014. Last interglacial surface water structure in the western Mediterranean (Balearic) Sea: Climatic variability and link between low and high latitudes. Glob. Planet. Change 123, 67–76. https://doi.org/10.1016/j.gloplacha.2014.10.004.

Kaufman, D. S., Schneider, D. P., McKay, N. P., Ammann, C. M., Bradley, R. S., Briffa, K. R., Miller, G. H., Otto-Bliesner, B. L., Overpeck, J. T., Vinther, B. M. and Lakes, A., 2009. Recent warming reverses long-term Arctic cooling. Science, 325, 1236-1239. https://doi.org/10.1126/science.1173983.

Knies, J., Vogt, C., 2003. Freshwater pulses in the eastern Arctic Ocean during Saalian and Early Weichselian ice-sheet collapse. Quat. Res. 60, 243–251. https://doi.org/10.1016/j.yqres.2003.07.008.

Knies, J., Vogt, C., Stein, R., 1998. Late Quaternary growth and decay of the Svalbard/Barents Sea ice sheet and paleoceanographic evolution in the adjacent Arctic Ocean. Geo-Mar. Lett. 18, 195–202. https://doi.org/10.1007/s003670050068

Knies, J., Matthiessen, J., Mackensen, A., Stein, R., Vogt, C., Frederichs, T., Nam, S.-I., 2007. Effects of Arctic freshwater forcing on thermohaline circulation during the Pleistocene. Geology 35, 1075–1078. https://doi.org/10.1130/G23966A.1.

Köhler, S.E.I., Spielhagen, R.F., 1990. The Enigma of Oxygen Isotope Stage 5 in the Central Fram Strait, in: Bleil, U., Thiede, J. (Eds.), Geological History of the Polar Oceans: Arctic versus Antarctic. Springer Netherlands, Dordrecht, pp. 489–497. https://doi.org/10.1007/978-94-009-2029-3_28

Kopp, R.E., Simons, F.J., Mitrovica, J.X., Maloof, A.C., Oppenheimer, M., 2009. Probabilistic assessment of sea level during the last interglacial stage. Nature 462, 863–867. https://doi.org/10.1038/nature08686

Kučera, M., 2007. Chapter Six Planktonic Foraminifera as Tracers of Past Oceanic Environments, in: Claude Hillaire–Marcel and Anne De Vernal (Ed.), Developments in Marine Geology. Elsevier, pp. 213–262.

Kuhlbrodt, T., Griesel A., Montoya M., Levermann A., Hofmann M., Rahmstorf S., 2007. On the driving processes of the Atlantic meridional overturning circulation. Rev. Geophys. 45. https://doi.org/10.1029/2004RG000166.

Labeyrie, L. D., Reijmer, J. J. G., 2005. Physical properties of sediment core MD99-2202. https://doi.org/doi.org/10.1594/PANGAEA.253089.

Lantzsch, H., Roth, S., Reijmer, J. J. G., Kinkel, H., 2007. Sea-level related resedimentation processes on the northern slope of Little Bahama Bank (Middle Pleistocene to Holocene). Sedimentology 54, 1307–1322. https://doi.org/10.1111/j.1365-3091.2007.00882.x.

Laskar, J., Robutel, P., Joutel, F., Gastineau, M., Correia, A. C. M., Levrard, B., 2004. A long-term numerical solution for the insolation quantities of the Earth. Astron. Astrophys. 428, 261–285. https://doi.org/10.1051/0004-6361:20041335.

Leduc, G., Schneider, R., Kim, J.-H., Lohmann, G., 2010. Holocene and Eemian sea surface temperature trends as revealed by alkenone and Mg/Ca paleothermometry. Quat. Sci. Rev. 29, 989–1004. https://doi.org/10.1016/j.quascirev.2010.01.004.

Lehman, S. J., Wright, D. G., Stocker, T. F., 1993. Transport of Freshwater into the Deep Ocean by the Conveyor, in: Peltier, W.R. (Ed.), Ice in the Climate System. Springer Berlin Heidelberg, Berlin, Heidelberg, pp. 187–209.

Lehman, S. J., Sachs, J. P., Crotwell, A. M., Keigwin, L. D., Boyle, E. A., 2002. Relation of subtropical Atlantic temperature, high-latitude ice rafting, deep water formation, and European climate 130,000–60,000 years ago. Quat. Sci. Rev. 21, 1917–1924. https://doi.org/10.1016/S0277-3791(02)00078-1.

Levermann, A., Born, A., 2007. Bistability of the Atlantic subpolar gyre in a coarse-resolution climate model. Geophys. Res. Lett. 34, L24605. https://doi.org/10.1029/2007GL031732.

Levitus, S., Antonov, J. I., Baranova, O. K., Boyer, T. P., Coleman, C. L., Garcia, H. E., Grodsky, A. I., Johnson, D. R., Locarnini, R. A., Mishonov, A. V., 2013. The world ocean database. Data Sci. J. 12, WDS229–WDS234.

Lisiecki, L. E., Raymo, M. E., 2009. Diachronous benthic $\delta^{18}O$ responses during late Pleistocene terminations. Paleoceanography 24, PA3210. https://doi.org/10.1029/2009PA001732.

Lisiecki, L. E., Stern, J. V., 2016. Regional and global benthic δ18O stacks for the last glacial cycle. Paleoceanography 31, 1368–1394. https://doi.org/10.1002/2016PA003002.

Lisitzin, A. P., 2012. Sea-ice and iceberg sedimentation in the ocean: recent and past. Springer Science & Business Media.

Liu, W., Xie, S.-P., Liu, Z., Zhu, J., 2017. Overlooked possibility of a collapsed Atlantic Meridional Overturning Circulation in warming climate. Sci. Adv. 3. https://doi.org/10.1126/sciadv.1601666.

Lohmann, G. P., Schweitzer, P. N., 2010. *Globorotalia truncatulinoides'* Growth and chemistry as probes of the past thermocline: 1. Shell size. Paleoceanography 5, 55–75. https://doi.org/10.1029/PA005i001p00055.

Lohmann, K., Drange, H., Bentsen, M., 2009a. Response of the North Atlantic subpolar gyre to persistent North Atlantic oscillation like forcing. Clim. Dyn. 32, 273–285. https://doi.org/10.1007/s00382-008-0467-6.

Lohmann, K., Drange, H., Bentsen, M., 2009b. A possible mechanism for the strong weakening of the North Atlantic subpolar gyre in the mid-1990s. Geophys. Res. Lett. 36, L15602. https://doi.org/10.1029/2009GL039166.

Lototskaya, A., Ganssen, G. M., 1999. The structure of Termination II (penultimate deglaciation and Eemian) in the North Atlantic. Quat. Sci. Rev. 18, 1641–1654. https://doi.org/10.1016/S0277-3791(99)00011-6.

Loulergue, L., Schilt, A., Spahni, R., Masson-Delmotte, V., Blunier, T., Lemieux, B., Barnola, J.-M., Raynaud, D., Stocker, T. F., Chappellaz, J., 2008. Orbital and millennial-scale features of atmospheric CH_4 over the past 800,000 years. Nature 453, 383–386. https://doi.org/10.1038/nature06950.

Luo, H., Castelao, R. M., Rennermalm, A. K., Tedesco, M., Bracco, A., Yager, P. L., Mote, T. L., 2016. Oceanic transport of surface meltwater from the southern Greenland ice sheet. Nature Geosci. 9, 528–532.

Lüthi, D., Le Floch, M., Bereiter, B., Blunier, T., Barnola, J.-M., Siegenthaler, U., Raynaud, D., Jouzel, J., Fischer, H., Kawamura, K., Stocker, T. F., 2008. High-resolution carbon dioxide concentration record 650,000–800,000 years before present. Nature 453, 379. http://dx.doi.org/10.1038/nature06949.

Lutze, G. F., Thiel, H., 1989. Epibenthic foraminifera from elevated microhabitats; *Cibicidoides wuellerstorfi* and *Planulina ariminensis*. J. Foraminiferal Res. 19, 153. https://doi.org/10.2113/gsjfr.19.2.153.

Lysa, A., Landvik, J. Y., 1994. The lower Jyllandselv succession: evidence for three Weichselian glacier advances over coastal Jameson Land, East Greenland. Boreas 23, 432–446. https://doi.org/10.1111/j.1502-3885.1994.tb00611.x.

Mackensen, A., Sejrup, H. P., Jansen, E., 1985. The distribution of living benthic foraminifera on the continental slope and rise off southwest Norway. Mar. Micropal. 9, 275–306. https://doi.org/10.1016/0377-8398(85)90001-5.

Marcott, S. A., Clark, P. U., Padman, L., Klinkhammer, G. P., Springer, S. R., Liu, Z., Otto-Bliesner, B. L., Carlson, A. E., Ungerer, A., Padman, J., He, F., Cheng, J., Schmittner, A., 2011. Ice-shelf collapse from subsurface warming as a trigger for Heinrich events. Proceedings of the National Academy of Sciences 108, 13415–13419. https://doi.org/10.1073/pnas.1104772108.

Marcott, S. A., Shakun, J. D., Clark, P. U., Mix, A. C., 2013. A Reconstruction of Regional and Global Temperature for the Past 11,300 Years. Science 339, 1198. https://doi.org/10.1126/science.1228026.

Marshall, J., Schott, F., 1999. Open-ocean convection: Observations, theory, and models. Rev. Geophys. 37, 1–64. https://doi.org/10.1029/98RG02739.

Martinson, D. G., Pisias, N. G., Hays, J. D., Imbrie, J., Moore, T. C., Shackleton, N. J., 1987. Age dating and the orbital theory of the ice ages: Development of a high-resolution 0 to 300,000-year chronostratigraphy. Quat. Res. 27, 1–29. https://doi.org/10.1016/0033-5894(87)90046-9.

Maslin, M., Sarnthein, M., Knaack, J.-J., Grootes, P., Tzedakis, C., 1998. Intra-interglacial cold events: an Eemian-Holocene comparison. Geol. Soc. London, Spec. Publ. 131, 91–99. https://doi.org/10.1144/GSL.SP.1998.131.01.07.

Masson-Delmotte, V., Buiron, D., Ekaykin, A., Frezzotti, M., Gallée, H., Jouzel, J., Krinner, G., Landais, A., Motoyama, H., Oerter, H., Pol, K., Pollard, D., Ritz, C., Schlosser, E., Sime, L. C., Sodemann, H., Stenni, B., Uemura, R., Vimeux, F.,

2011. A comparison of the present and last interglacial periods in six Antarctic ice cores. Clim. Past 7, 397–423. https://doi.org/10.5194/cp-7-397-2011.

Masson-Delmotte, V., Schulz, M., Abe-Ouchi, A., Beer, J., Ganopolski, A., González Rouco, J. F., Jansen, E., Lambeck, K., Luterbacher, J., Naish, T., 2013. Information from paleoclimate archives, in: Stocker, T.F., Qin, D., Plattner, G.-K., Tignor, M., Allen, S. K., Boschung, J., Nauels, A., Xia, Y., Bex, V., Midgley, P. M. (Eds.), Climate Change 2013: The Physical Science Basis. Contribution of Working Group I to the Fifth Assessment Report of the Intergovernmental Panel on Climate Change, Cambridge: Cambridge University Press, pp. 383–464.

Matthiessen, J., Knies, J., Nowaczyk, N. R., Stein, R., 2001. Late Quaternary dinoflagellate cyst stratigraphy at the Eurasian continental margin, Arctic Ocean: indications for Atlantic water inflow in the past 150,000 years. Glob. Planet. Change 31, 65–86. https://doi.org/10.1016/S0921-8181(01)00113-8.

Mauritzen, C., Rudels, B., Toole, J., 2013. Ocean Circulation and Climate: Chapter 17. The Arctic and Subarctic Oceans/Seas. Elsevier Inc. Chapters.

McManus, J. F., Bond, G. C., Broecker, W. S., Johnsen, S., Labeyrie, L., Higgins, S., 1994. High-resolution climate records from the North Atlantic during the last interglacial. Nature 371, 326–329. https://doi.org/10.1038/371326a0.

McManus, J. F., Oppo, D. W., Keigwin, L. D., Cullen, J. L., Bond, G.C., 2002. Thermohaline Circulation and Prolonged Interglacial Warmth in the North Atlantic. Quat. Res. 58, 17–21. https://doi.org/10.1006/qres.2002.2367.

Mengel, M., Levermann, A., Schleussner, C.-F., Born, A., 2012. Enhanced Atlantic subpolar gyre variability through baroclinic threshold in a coarse resolution model. Earth Syst. Dynam. 3, 189–197. https://doi.org/10.5194/esd-3-189-2012.

Miller, G. H., Brigham-Grette, J., Alley, R. B., Anderson, L., Bauch, H. A., Douglas, M. S. V., Edwards, M. E., Elias, S. A., Finney, B. P., Fitzpatrick, J. J., Funder, S. V., Herbert, T. D., Hinzman, L. D., Kaufman, D. S., MacDonald, G. M., Polyak, L., Robock, A., Serreze, M. C., Smol, J. P., Spielhagen, R., White, J. W. C., Wolfe, A. P., Wolff, E. W., 2010. Temperature and precipitation history of the Arctic. Quat. Sci. Rev. 29, 1679–1715. https://doi.org/10.1016/j.quascirev.2010.03.001.

Mokeddem, Z., McManus, J. F., Oppo, D. W., 2014. Oceanographic dynamics and the end of the last interglacial in the subpolar North Atlantic. Proc. Natl. Acad. Sci. 111, 11263–11268. https://doi.org/doi:10.1073/pnas.1322103111.

Morse, J. W., He, S., 1993. Influences of T, S and PCO_2 on the pseudo-homogeneous precipitation of $CaCO_3$ from seawater: implications for whiting formation. Mar. Chem. 41, 291–297. https://doi.org/10.1016/0304-4203(93)90261-L.

Morse, J. W., MacKenzie, F. T., 1990. Geochemistry of sedimentary carbonates. Elsevier.

Moseley, G. E., Edwards, R. L., Wendt, K. A., Cheng, H., Dublyansky, Y., Lu, Y., Boch, R., Spötl, C., 2016. Reconciliation of the Devils Hole climate record with orbital forcing. Science 351, 165. https://doi.org/10.1126/science.aad4132.

Moseley, H.G.J., 1914. The high-frequency spectra of the elements. Part II. The London, Edinburgh, and Dublin Philosophical Magazine and Journal of Science 27, pp. 703–713. https://doi.org/10.1080/14786440408635141.

Mulitza, S., Dürkoop, A., Hale, W., Wefer, G., Niebler, H. S., 1997. Planktonic foraminifera as recorders of past surface-water stratification. Geology 25(4), 335–338. https://doi.org/doi.org/10.1130/0091-7613(1997)025<0335:PFAROP>2.3.CO;2.

Müller, J., Masse, G., Stein, R., Belt, S. T., 2009. Variability of sea-ice conditions in the Fram Strait over the past 30,000 years. Nature Geosci. 2, 772–776. https://doi.org/10.1038/ngeo665.

Myers, P. G., Kulan, N., Ribergaard, M. H., 2007. Irminger water variability in the West Greenland Current. Geophys. Res. Lett. 34. https://doi.org/10.1029/2007GL030419.

Naafs, B. D. A., Hefter, J., Grützner, J., Stein, R., 2013. Warming of surface waters in the mid-latitude North Atlantic during Heinrich events. Paleoceanography 28, 153–163. https://doi.org/10.1029/2012PA002354.

Nam, S.-I., Stein, R., Grobe, H., Hubberten, H., 1995. Late Quaternary glacial-interglacial changes in sediment composition at the East Greenland continental margin and their paleoceanographic implications. Marine Geology 122, 243–262. https://doi.org/10.1016/0025-3227(94)00070-2.

Nam, S.-I., 1997. Late Quaternary glacial history and paleoceanographic reconstructions along the East Greenland continental margin: evidence from high-resolution records of stable isotopes and ice-rafted debris - Spätquartäre Vereisungsgeschichte und paläozeanographische Rekonstruktionen am ostgrönländischen Kontinentalrand. Berichte zur Polarforschung (Reports on Polar Research) 241.

NEEM community members, 2013. Eemian interglacial reconstructed from a Greenland folded ice core. Nature 493, 489–494. https://doi.org/10.1038/nature11789.

Neumann, A. C., Moore, W.S., 1975. Sea Level Events and Pleistocene Coral Ages in the Northern Bahamas. Quat. Res. 5, 215–224. https://doi.org/10.1016/0033-5894(75)90024-1.

NGRIP community members, 2004. High-resolution record of Northern Hemisphere climate extending into the last interglacial period. Nature 431, 147–151. https://doi.org/10.1038/nature02805.

Nicholl, J. A. L., Hodell, D. A., Naafs, B. D. A., Hillaire-Marcel, C., Channell, J. E. T., Romero, O. E., 2012. A Laurentide outburst flooding event during the last interglacial period. Nature Geosci. 5, 901–904. https://doi.org/10.1038/ngeo1622.

Nørgaard-Pedersen, N., Spielhagen, R. F., Erlenkeuser, H., Grootes, P. M., Heinemeier, J., Knies, J., 2003. Arctic Ocean during the Last Glacial Maximum: Atlantic and polar domains of surface water mass distribution and ice cover. Paleoceanography 18, 1063. https://doi.org/10.1029/2002PA000781

Nørgaard-Pedersen, N., Mikkelsen, N., Kristoffersen, Y., 2007a. Arctic Ocean record of last two glacial-interglacial cycles off North Greenland/Ellesmere Island — Implications for glacial history. Mar. Geol. 244, 93–108. https://doi.org/10.1016/j.margeo.2007.06.008.

Nørgaard-Pedersen, N., Mikkelsen, N., Lassen, S. J., Kristoffersen, Y., Sheldon, E., 2007b. Reduced sea ice concentrations in the Arctic Ocean during the last interglacial period revealed by sediment cores off northern Greenland. Paleoceanography 22, PA1218. https://doi.org/10.1029/2006PA001283.

Obrochta, S. P., Crowley, T. J., Channell, J. E. T., Hodell, D. A., Baker, P. A., Seki, A., Yokoyama, Y., 2014. Climate variability and ice-sheet dynamics during the last three glaciations. Earth Planet. Sci. Lett. 406, 198–212. https://doi.org/10.1016/j.epsl.2014.09.004.

O'Leary, M. J., Hearty, P. J., Thompson, W. G., Raymo, M. E., Mitrovica, J. X., Webster, J. M., 2013. Ice sheet collapse following a prolonged period of stable sea level during the last interglacial. Nature Geosci. 6, 796. https://doi.org/doi:10.1038/ngeo1890.

Oppo, D. W., Horowitz, M., Lehman, S. J., 1997. Marine core evidence for reduced deep water production during Termination II followed by a relatively stable substage 5e (Eemian). Paleoceanography 12, 51–63. https://doi.org/10.1029/96PA03133.

Oppo, D. W., McManus, J. F., Cullen, J. L., 2006. Evolution and demise of the Last Interglacial warmth in the subpolar North Atlantic. Quat. Sci. Rev. 25, 3268–3277. https://doi.org/10.1016/j.quascirev.2006.07.006.

Otto-Bliesner, B. L., Marshall, S. J., Overpeck, J. T., Miller, G. H., Hu, A., 2006. Simulating Arctic Climate Warmth and Icefield Retreat in the Last Interglaciation. Science 311, 1751-1753. https://doi.org/10.1126/science.1120808.

Pados, T., Spielhagen, R. F., 2014. Species distribution and depth habitat of recent planktic foraminifera in Fram Strait, Arctic Ocean. Pol. Res. 33, 22483. https://doi.org/10.3402/polar.v33.22483.

Paillard, D., Labeyrie, L., Yiou, P., 1996. Macintosh Program performs time-series analysis. Eos Trans. AGU 77, 379–379. https://doi.org/10.1029/96EO00259.

Perner, K., Moros, M., Lloyd, J. M., Jansen, E., Stein, R., 2015. Mid to late Holocene strengthening of the East Greenland Current linked to warm subsurface Atlantic water. Quat. Sci. Rev. 129, 296–307. https://doi.org/10.1016/j.quascirev.2015.10.007.

Peterson, L. C., Haug, G. H., 2006. Variability in the mean latitude of the Atlantic Intertropical Convergence Zone as recorded by riverine input of sediments to the Cariaco Basin (Venezuela). Palaeogeogr. Palaeoclimatol. Palaeoecol. 234, 97–113. https://doi.org/10.1016/j.palaeo.2005.10.021.

Peterson, L. C., Haug, G. H., Hughen, K. A., Röhl, U., 2000. Rapid Changes in the Hydrologic Cycle of the Tropical Atlantic During the Last Glacial. Science 290, 1947-1951. https://doi.org/10.1126/science.290.5498.1947.

Pflaumann, U., Duprat, J., Pujol, C., Labeyrie, L. D., 1996. SIMMAX: A modern analog technique to deduce Atlantic sea surface temperatures from planktonic foraminifera in deep-sea sediments. Paleoceanography 11, 15–35. https://doi.org/10.1029/95PA01743.

Pfuhl, H.., Shackleton, N.., 2004. Two proximal, high-resolution records of foraminiferal fragmentation and their implications for changes in dissolution. Deep Sea. Res. Part 1 Oceanogr. Res. Pap. 51, 809–832. https://doi.org/10.1016/j.dsr.2004.02.003.

Plikk, A., Helmens, K. F., Fernández-Fernández, M., Kylander, M., Löwemark, L., Risberg, J., Salonen, J. S., Väliranta, M., Weckström, J., 2016. Development of an Eemian (MIS 5e) Interglacial palaeolake at Sokli (N Finland) inferred using multiple proxies. Palaeogeogr. Palaeoclimatol. Palaeoecol. 463, 11–26. https://doi.org/10.1016/j.palaeo.2016.09.008.

Polyak, L., Alley, R. B., Andrews, J. T., Brigham-Grette, J., Cronin, T. M., Darby, D. A., Dyke, A. S., Fitzpatrick, J. J., Funder, S., Holland, M., Jennings, A. E., Miller, G. H., O'Regan, M., Savelle, J., Serreze, M., St. John, K., White, J. W. C., Wolff, E., 2010. History of sea ice in the Arctic. Quat. Sci. Rev. 29, 1757–1778. https://doi.org/10.1016/j.quascirev.2010.02.010.

Polyakov, I. V., Pnyushkov, A. V., Alkire, M. B., Ashik, I. M., Baumann, T. M., Carmack, E. C., Goszczko, I., Guthrie, J., Ivanov, V. V., Kanzow, T., Krishfield, R., Kwok, R., Sundfjord, A., Morison, J., Rember, R., Yulin, A., 2017. Greater role for Atlantic inflows on sea-ice loss in the Eurasian Basin of the Arctic Ocean. Science 356, 285. https://doi.org/10.1126/science.aai8204.

Poore, R. Z., Dowsett, H. J., Verard, S., Quinn, T. M., 2003. Millennial- to century-scale variability in Gulf of Mexico Holocene climate records. Paleoceanography 18. https://doi.org/10.1029/2002PA000868.

Rahmstorf, S., Box, J. E., Feulner, G., Mann, M. E., Robinson, A., Rutherford, S., Schaffernicht, E. J., 2015. Exceptional twentieth-century slowdown in Atlantic Ocean overturning circulation. Nature Clim. Change 5, 475–480. http://dx.doi.org/10.1038/nclimate2554.

Rasmussen, T. L., Thomsen, E., 2009. Stable isotope signals from brines in the Barents Sea: Implications for brine formation during the last glaciation. Geology 37, 903–906. https://doi.org/10.1130/G25543A.1.

Rasmussen, T. L., Oppo, D. W., Thomsen, E., Lehman, S. J., 2003a. Deep sea records from the southeast Labrador Sea: Ocean circulation changes and ice-rafting events during the last 160,000 years. Paleoceanography 18, 1018. https://doi.org/10.1029/2001PA000736.

Rasmussen, T. L., Thomsen, E., Kuijpers, A., Wastegård, S., 2003b. Late warming and early cooling of the sea surface in the Nordic seas during MIS 5e (Eemian Interglacial). Quat. Sci. Rev. 22, 809–821. https://doi.org/10.1016/S0277-3791(02)00254-8.

Rasmussen, T. L., Thomsen, E., Ślubowska, M. A., Jessen, S., Solheim, A., Koç, N., 2007. Paleoceanographic evolution of the SW Svalbard margin (76°N) since 20,000 ^{14}C yr BP. Quat. Res. 67, 100–114. https://doi.org/10.1016/j.yqres.2006.07.002.

Repschläger, J., Weinelt, M., Kinkel, H., Andersen, N., Garbe-Schönberg, D., Schwab, C., 2015. Response of the subtropical North Atlantic surface hydrography on deglacial and Holocene AMOC changes. Paleoceanography 30, 2014PA002637. https://doi.org/10.1002/2014PA002637.

Repschläger, J., Garbe-Schönberg, D., Weinelt, M., Schneider, R., 2017. Holocene evolution of the North Atlantic subsurface transport. Clim. Past 13, 333–344. https://doi.org/10.5194/cp-13-333-2017.

Richter, T. O., van der Gaast, S., Koster, B., Vaars, A., Gieles, R., de Stigter, H. C., De Haas, H., van Weering, T. C. E., 2006. The Avaatech XRF Core Scanner: technical description and applications to NE Atlantic sediments. Geol. Soc. London, Special Publications 267, 39. https://doi.org/10.1144/GSL.SP.2006.267.01.03.

Rimbu, N., Lohmann, G., Kim, J.-H., Arz, H. W., Schneider, R., 2003. Arctic/North Atlantic Oscillation signature in Holocene sea surface temperature trends as obtained from alkenone data. Geophys. Res. Lett. 30, 1280. https://doi.org/10.1029/2002GL016570.

Risebrobakken, B., Jansen, E., Andersson, C., Mjelde, E., Hevrøy, K., 2003. A high-resolution study of Holocene paleoclimatic and paleoceanographic changes in the Nordic Seas. Paleoceanography 18, https://doi.org/10.1029/2002PA000764.

Risebrobakken, B., Dokken, T., Jansen, E., 2005. Extent and Variability of the Meridional Atlantic Circulation in the Eastern Nordic Seas During Marine Isotope Stage 5 and its Influence on the Inception of the Last Glacial, in: The Nordic Seas: An Integrated Perspective. American Geophysical Union, pp. 323–339. https://doi.org/10.1029/158GM20.

Risebrobakken, B., Balbon, E., Dokken, T., Jansen, E., Kissel, C., Labeyrie, L., Richter, T., Senneset, L., 2006. The penultimate deglaciation: High-resolution paleoceanographic evidence from a north–south transect along the eastern Nordic Seas. Earth Planet. Sci. Lett. 241, 505–516. https://doi.org/10.1016/j.epsl.2005.11.032.

Risebrobakken, B., Dokken, T., Otterå, O. H., Jansen, E., Gao, Y., Drange, H., 2007. Inception of the Northern European ice sheet due to contrasting ocean and insolation forcing. Quat. Res. 67, 128–135. https://doi.org/10.1016/j.yqres.2006.07.007.

Risebrobakken, B., Dokken, T., Smedsrud, L. H., Andersson, C., Jansen, E., Moros, M., Ivanova, E.V., 2011. Early Holocene temperature variability in the Nordic Seas: The role of oceanic heat advection versus changes in orbital forcing. Paleoceanography 26, PA4206. https://doi.org/10.1029/2011PA002117.

Röhl, U., Abrams, L. J., 2000. High resolution, downhole, and nondestructive core measurements from sites 999 and 1001 in the Caribbean Sea: Application to the late Paleocene thermal maximum. In Proceedings of the Ocean Drilling Program, Scientific Results.

Roth, S., Reijmer, J. J. G., 2004. Holocene Atlantic climate variations deduced from carbonate periplatform sediments (leeward margin, Great Bahama Bank). Paleoceanography 19, PA1003. https://doi.org/doi:10.1029/2003PA000885.

Roth, S., Reijmer, J. J. G., 2005. Holocene millennial to centennial carbonate cyclicity recorded in slope sediments of the Great Bahama Bank and its climatic implications. Sedimentology 52, 161–181. https://doi.org/10.1111/j.1365-3091.2004.00684.x.

Rudels, B., 2012. Arctic Ocean circulation and variability-advection and external forcing encounter constraints and local processes. Ocean Sci. 8, 261-286. https://doi.org/10.5194/os-8-261-2012.

Rudels, B., 2015. Arctic Ocean circulation, processes and water masses: A description of observations and ideas with focus on the period prior to the International Polar Year 2007–2009. Progr. Oceanogr. 132, 22–67. https://doi.org/10.1016/j.pocean.2013.11.006.

Rudels, B., Korhonen, M., Budéus, G., Beszczynska-Möller, A., Schauer, U., Nummelin, A., Quadfasel, D., Valdimarsson, H., 2012. The East Greenland Current and its impacts on the Nordic Seas: observed trends in the past decade. ICES J. Mar. Sci.: Journal du Conseil 69, 841–851. https://doi.org/10.1093/icesjms/fss079.

Rühlemann, C., Mulitza, S., Müller, P. J., Wefer, G., Zahn, R., 1999. Warming of the tropical Atlantic Ocean and slowdown of thermohaline circulation during the last deglaciation. Nature 402, 511. https://doi.org/doi:10.1038/990069.

Rühlemann, C., Mulitza, S., Lohmann, G., Paul, A., Prange, M., Wefer, G., 2004. Intermediate depth warming in the tropical Atlantic related to weakened thermohaline circulation: Combining paleoclimate data and modeling results for

the last deglaciation. Paleoceanography 19, PA1025. https://doi.org/10.1029/2003PA000948.

Saloranta, T. M., Svendsen, H., 2001. Across the Arctic front west of Spitsbergen: high-resolution CTD sections from 1998–2000. Pol. Res. 20, 177–184. https://doi.org/10.3402/polar.v20i2.6515.

Salvigsen, O., Forman, S. L., Miller, G. H., 1992. Thermophilous molluscs on Svalbard during the Holocene and their paleoclimatic implications. Pol. Res. 11, 1–10. https://doi.org/10.3402/polar.v11i1.6712.

Sánchez Goñi, M. F., Bakker, P., Desprat, S., Carlson, A. E., Van Meerbeeck, C. J., Peyron, O., Naughton, F., Fletcher, W. J., Eynaud, F., Rossignol, L., Renssen, H., 2012. European climate optimum and enhanced Greenland melt during the Last Interglacial. Geology 40, 627–630. https://doi.org/10.1130/G32908.1.

Sarnthein, M., Van Kreveld, S., Erlenkeuser, H., Grootes, P. M., Kučera, M., Pflaumann, U., Schulz, M., 2003. Centennial-to-millennial-scale periodicities of Holocene climate and sediment injections off the western Barents shelf, 75°N. Boreas 32, 447–461. https://doi.org/10.1111/j.1502-3885.2003.tb01227.x.

Schiebel, R., Hemleben, C., 2017. Planktic Foraminifers in the Modern Ocean. Springer.

Schiebel, R., Spielhagen, R. F., Garnier, J., Hagemann, J., Howa, H., Jentzen, A., Martínez-Garcia, A., Meilland, J., Michel, E., Repschläger, J., Salter, I., Yamasaki, M., Haug, G., 2017. Modern planktic foraminifers in the high-latitude ocean. Mar. Micropal. 136, 1–13. https://doi.org/10.1016/j.marmicro.2017.08.004.

Schlager, W., Reijmer, J. J. G., Droxler, A., 1994. Highstand Shedding of Carbonate Platforms. J. Sedim. Res. 64B, 270–281.

Schlitzer, R., 2016. Ocean data view, edited.

Schmidt, M. W., Vautravers, M. J., Spero, H. J., 2006a. Rapid subtropical North Atlantic salinity oscillations across Dansgaard–Oeschger cycles. Nature 443, 561. https://doi.org/doi:10.1038/nature05121.

Schmidt, M. W., Vautravers, M. J., Spero, H. J., 2006b. Western Caribbean sea surface temperatures during the late Quaternary. Geochem. Geophys. Geosyst. 7. https://doi.org/10.1029/2005GC000957.

Schmitz, W. J., McCartney, M. S., 2010. On the North Atlantic Circulation. Rev. Geophys. 31, 29–49. https://doi.org/10.1029/92RG02583.

Schmitz, W. J., Richardson, P. L., 1991. On the sources of the Florida Current. Deep Sea Res. Part A: Oceanogr. Res. Pap. 38, S379–S409. https://doi.org/10.1016/S0198-0149(12)80018-5.

Schmuker, B., Schiebel, R., 2002. Planktic foraminifers and hydrography of the eastern and northern Caribbean Sea. Mar. Micropal. 46, 387–403. https://doi.org/10.1016/S0377-8398(02)00082-8.

Schott, F. A., Zantopp, R., Stramma, L., Dengler, M., Fischer, J., Wibaux, M., 2004. Circulation and Deep-Water Export at the Western Exit of the Subpolar North Atlantic. J. Phys. Oceanogr. 34, 817–843. https://doi.org/10.1175/1520-0485(2004)034<0817:CADEAT>2.0.CO;2.

Schwab, C., Kinkel, H., Weinelt, M., Repschläger, J., 2013. A coccolithophore based view on paleoenvironmental changes in the open ocean mid-latitude North

Atlantic between 130 and 48 ka BP with special emphasis on MIS 5e. Quat. Sci. Rev. 81, 35–47. https://doi.org/10.1016/j.quascirev.2013.09.021.

Seidenkrantz, M.-S., Kristensen, P., Knudsen, K. L., 1995. Marine evidence for climatic instability during the last interglacial in shelf records from northwest Europe. J. Quat. Sci. 10, 77–82. https://doi.org/10.1002/jqs.3390100108.

Seidenkrantz, M.-S., Bornmalm, L., Johnsen, S. J., Knudsen, K. L., Kuijpers, A., Lauritzen, S.-E., Leroy, S. A. G., Mergeal, I., Schweger, C., Van Vliet-Lanoë, B., 1996. Two-step deglaciation at the oxygen isotope stage 6/5E transition: The Zeifen-Kattegat climate oscillation. Quat. Sci. Rev. 15, 63–75. https://doi.org/10.1016/0277-3791(95)00086-0.

Sejrup, H. P., Haflidason, H., Kristensen, D. K., Johnsen, S. J., 1995. Last interglacial and Holocene climatic development in the Norwegian Sea region: Ocean front movements and ice-core data. J. Quaternary Sci. 10, 385–390. https://doi.org/10.1002/jqs.3390100408.

Sévellec, F., Fedorov, A. V., Liu, W., 2017. Arctic sea-ice decline weakens the Atlantic Meridional Overturning Circulation. Nature Clim. Change 7, 604. https://doi.org/10.1038/nclimate3353.

Shackleton, N. J., 2000. The 100,000-Year Ice-Age Cycle Identified and Found to Lag Temperature, Carbon Dioxide, and Orbital Eccentricity. Science 289, 1897-1902. doi:10.1126/science.289.5486.1897.

Shackleton, N. J., Chapman, M., Sánchez-Goñi, M. F., Pailler, D., Lancelot, Y., 2002. The classic marine isotope substage 5e. Quat. Res. 58, 14–16. https://doi.org/10.1006/qres.2001.2312.

Shackleton, N. J., Sánchez-Goñi, M. F., Pailler, D., Lancelot, Y., 2003. Marine Isotope Substage 5e and the Eemian Interglacial. Glob. Planet. Change 36, 151–155. https://doi.org/10.1016/S0921-8181(02)00181-9.

Shakun, J. D., Clark, P. U., He, F., Marcott, S. A., Mix, A. C., Liu, Z., Otto-Bliesner, B., Schmittner, A., Bard, E., 2012. Global warming preceded by increasing carbon dioxide concentrations during the last deglaciation. Nature 484, 49. https://doi:10.1038/nature1091.

Siccha, M., Kučera, M., 2017. ForCenS, a curated database of planktonic foraminifera census counts in marine surface sediment samples. Sci. Data 4, 170109.

Simstich, J., Sarnthein, M., Erlenkeuser, H., 2003. Paired $\delta^{18}O$ signals of *Neogloboquadrina pachyderma* (s) and *Turborotalita quinqueloba* show thermal stratification structure in Nordic Seas. Mar. Micropal. 48, 107–125. https://doi.org/10.1016/S0377-8398(02)00165-2.

Slowey, N. C., Curry, W. B., 1995. Glacial-interglacial differences in circulation and carbon cycling within the upper western North Atlantic. Paleoceanography 10, 715–732. https://doi.org/10.1029/95PA01166.

Slowey, N. C., Henderson, G. M., Curry, W. B., 1996. Direct U–Th dating of marine sediments from the two most recent interglacial periods. Nature 383, 242. https://doi.org/doi:10.1038/383242a0.

Slowey, N. C., Wilber, R. J., Haddad, G. A., Henderson, G. M., 2002. Glacial-to-Holocene sedimentation on the western slope of Great Bahama Bank. Mar. Geol. 185, 165–176. https://doi.org/10.1016/S0025-3227(01)00295-X.

Smeed, D. A., McCarthy, G., Cunningham, S. A., Frajka-Williams, E., Rayner, D., Johns, W. E., Meinen, C. S., Baringer, M. O., Moat, B. I., Duchez, A., Bryden, H. L., 2013. Observed decline of the Atlantic Meridional Overturning Circulation 2004 to 2012. Ocean Sci. Discuss. 1619–1645. https://doi.org/10.5194/osd-10-1619-2013.

Spielhagen, R. F., Bauch, H. A., 2015. The role of Arctic Ocean freshwater during the past 200 ky. arktos 1, 1–12. https://doi.org/10.1007/s41063-015-0013-9.

Spielhagen, R. F., Erlenkeuser, H., 1994. Stable oxygen and carbon isotopes in planktic foraminifers from Arctic Ocean surface sediments: Reflection of the low salinity surface water layer. Mar. Geol. 119, 227–250. https://doi.org/10.1016/0025-3227(94)90183-X.

Spielhagen, R. F., Werner, K., Sørensen, S. A., Zamelczyk, K., Kandiano, E., Budeus, G., Husum, K., Marchitto, T. M., Hald, M., 2011. Enhanced modern heat transfer to the Arctic by warm Atlantic Water. Science 331, 450. https://doi.org/10.1126/science.1197397.

Spielhagen, R. F., Baumann, K.-H., Erlenkeuser, H., Nowaczyk, N. R., Nørgaard-Pedersen, N., Vogt, C., Weiel, D., 2004. Arctic Ocean deep-sea record of northern Eurasian ice sheet history. Quat. Sci. Rev. 23, 1455–1483. https://doi.org/10.1016/j.quascirev.2003.12.015.

Spratt, R. M., Lisiecki, L. E., 2016. A Late Pleistocene sea level stack. Climate of the Past 12, 1079–1092. https://doi.org/10.5194/cp-12-1079-2016.

Stahr, F. R., Sanford, T. B., 1999. Transport and bottom boundary layerobservations of the North Atlantic Deep Western Boundary Current at the Blake Outer Ridge. Deep Sea Res. Part II: Trop. Stud. Oceanogr. 46, 205–243. https://doi.org/10.1016/S0967-0645(98)00101-5.

Stanford, J. D., Rohling, E. J., Bacon, S., Roberts, A. P., Grousset, F. E., Bolshaw, M., 2011. A new concept for the paleoceanographic evolution of Heinrich event 1 in the North Atlantic. Quat. Sci. Rev. 30, 1047–1066. https://doi.org/10.1016/j.quascirev.2011.02.003.

Stein, R., Nam, S., Grobe, H., Hubberten, H., 1996. Late Quaternary glacial history and short-term ice-rafted debris fluctuations along the East Greenland continental margin. Geological Society, London, Special Publications 111, 135–151. https://doi.org/10.1144/GSL.SP.1996.111.01.09.

Stein, R., Fahl, K., Gierz, P., Niessen, F., Lohmann, G., 2017. Arctic Ocean sea ice cover during the penultimate glacial and the last interglacial. Nat. Commun. 8, 373. https://doi.org/10.1038/s41467-017-00552-1.

Steinsund, P. I., Hald, M., 1994. Recent calcium carbonate dissolution in the Barents Sea: Paleoceanographic applications. Mar. Geol. 117, 303–316. https://doi.org/10.1016/0025-3227(94)90022-1.

Stirling, C., Esat, T., Lambeck, K., McCulloch, M., 1998. Timing and duration of the Last Interglacial: evidence for a restricted interval of widespread coral reef growth. Earth Planet. Sci. Lett 160, 745–762. https://doi.org/10.1016/S0012-821X(98)00125-3

Stommel, H., 1961. Thermohaline convection with two stable regimes of flow. Tellus 13, 224–230.

Stone, E. J., Lunt, D. J., Annan, J. D., Hargreaves, J. C., 2013. Quantification of the Greenland ice sheet contribution to Last Interglacial sea level rise. Clim. Past 9, 621–639. https://doi.org/10.5194/cp-9-621-2013.

Stoner, J. S., Channell, J. E. T., Hillaire-Marcel, C., 1995. Magnetic properties of deep-sea sediments off southwest Greenland: Evidence for major differences between the last two deglaciations. Geology 23, 241–244. https://doi.org/10.1130/0091-7613(1995)023<0241:MPODSS>2.3.CO;2.

Stramma, L., Schott, F., 1999. The mean flow field of the tropical Atlantic Ocean. Deep Sea Res. Part II: Trop. Stud. Oceanogr. 46, 279–303. https://doi.org/10.1016/S0967-0645(98)00109-X.

Struck, U., 1997. Paleoecology of benthic foraminifera in the Norwegian-Greenland Sea during the past 500 ka. Contributions to the Micropaleontology and Paleoceanography of the Northern North Atlantic 5, pp. 51–82.

Swift, J.H., 1986. The arctic waters, in: The Nordic Seas. Springer, pp. 129–154.

Telesiński, M. M., Spielhagen, R. F., Lind, E. M., 2014. A high-resolution Lateglacial and Holocene palaeoceanographic record from the Greenland Sea. Boreas 43, 273–285. https://doi.org/10.1111/bor.12045.

Telesiński, M. M., Bauch, H. A., Spielhagen, R. F., Kandiano, E. S., 2015. Evolution of the central Nordic Seas over the last 20 thousand ye.ars. Quat. Sci. Rev. 121, 98–109. https://doi.org/10.1016/j.quascirev.2015.05.013.

Thiagarajan, N., Subhas, A. V., Southon, J. R., Eiler, J. M., Adkins, J. F., 2014. Abrupt pre-Bolling-Allerod warming and circulation changes in the deep ocean. Nature 511, 75–78. https://doi:10.1038/nature13472.

Thibodeau, B., Bauch, H. A., Pedersen, T. F., 2017. Stratification-induced variations in nutrient utilization in the Polar North Atlantic during past interglacials. Earth Planet. Sci. Lett 457, 127–135. https://doi.org/10.1016/j.epsl.2016.09.060

Thiede, J., Jessen, C., Knutz, P., Kuijpers, A., Mikkelsen, N., Nørgaard-Pedersen, N., Spielhagen, R. F., 2011. Millions of years of Greenland Ice Sheet history recorded in ocean sediments. Polarforschung 80, 141–159.

Thompson, D. W. J., Wallace, J. M., Kennedy, J. J., Jones, P. D., 2010. An abrupt drop in Northern Hemisphere sea surface temperature around 1970. Nature 467, 444. https://doi.org/10.1038/nature09394.

Thornalley, D. J. R., Elderfield, H., McCave, I. N., 2009. Holocene oscillations in temperature and salinity of the surface subpolar North Atlantic. Nature 457, 711–714. https://doi.org/10.1038/nature07717.

Thornalley, D. J. R., Elderfield, H., McCave, I. N., 2010. Intermediate and deep water paleoceanography of the northern North Atlantic over the past 21,000 years. Paleoceanography 25, PA1211. https://doi.org/10.1029/2009PA001833.

Thornalley, D. J. R., Blaschek, M., Davies, F. J., Praetorius, S., Oppo, D. W., McManus, J. F., Hall, I. R., Kleiven, H., Renssen, H., McCave, I. N., 2013. Long-term variations in Iceland–Scotland overflow strength during the Holocene. Clim. Past 9, 2073–2084. https://doi.org/10.5194/cp-9-2073-2013.

Thornalley, D. J. R., Bauch, H. A., Gebbie, G., Guo, W., Ziegler, M., Bernasconi, S. M., Barker, S., Skinner, L. C., Yu, J., 2015. A warm and poorly ventilated deep Arctic Mediterranean during the last glacial period. Science 349, 706. https://doi.org/10.1126/science.aaa9554.

Tjallingii, R., 2006. Application and quality of X-ray fluorescence core scanning in reconstructing late Pleistocene NW African continental margin sedimentation patterns and paleoclimate variations, Doctoral dissertation, Department of Geosciences. University of Bremen.

Tjallingii, R., Röhl, U., Kölling, M., Bickert, T., 2007. Influence of the water content on X-ray fluorescence core-scanning measurements in soft marine sediments. Geochem. Geophys. Geosyst. 8. https://doi.org/10.1029/2006GC001393.

Tjallingii, R., Claussen, M., Stuut, J.-B. W., Fohlmeister, J., Jahn, A., Bickert, T., Lamy, F., Röhl, U., 2008. Coherent high- and low-latitude control of the northwest African hydrological balance. Nature Geosci. 1, 670-675. https://doi:10.1038/ngeo289.

Tucker, M. E., Bathurst, R. G., 2009. Carbonate diagenesis. John Wiley & Sons.

Turney, C. S. M., Jones, R. T., 2010. Does the Agulhas Current amplify global temperatures during super-interglacials? J. Quaternary Sci. 25, 839–843. https://doi.org/10.1002/jqs.1423.

Våge, K., Moore, G. W. K., Jónsson, S., Valdimarsson, H., 2015. Water mass transformation in the Iceland Sea. Deep Sea Res. Part I: Oceanogr. Res. Pap. 101, 98–109. https://doi.org/10.1016/j.dsr.2015.04.001.

Van Nieuwenhove, N., Bauch, H. A., 2008. Last interglacial (MIS 5e) surface water conditions at the Vøring Plateau (Norwegian Sea), based on dinoflagellate cysts. Pol. Res. 27, 175–186. https://doi.org/10.1111/j.1751-8369.2008.00062.x.

Van Nieuwenhove, N., Bauch, H.A., Matthiessen, J., 2008. Last interglacial surface water conditions in the eastern Nordic Seas inferred from dinocyst and foraminiferal assemblages. Mar. Micropal. 66, 247–263. https://doi.org/10.1016/j.marmicro.2007.10.004.

Van Nieuwenhove, N., Bauch, H.A., Eynaud, F., Kandiano, E., Cortijo, E., Turon, J.-L., 2011. Evidence for delayed poleward expansion of North Atlantic surface waters during the last interglacial (MIS 5e). Quat. Sci. Rev. 30, 934–946. https://doi.org/10.1016/j.quascirev.2011.01.013.

Van Nieuwenhove, N., Bauch, H. A., Andruleit, H., 2013. Multiproxy fossil comparison reveals contrasting surface ocean conditions in the western Iceland Sea for the last two interglacials. Palaeogeogr. Palaeoclimatol. Palaeoecol 370, 247–259. https://doi.org/10.1016/j.palaeo.2012.12.018.

Vasskog, K., Langebroek, P.M., Andrews, J.T., Nilsen, J.E.Ø., Nesje, A., 2015. The Greenland Ice Sheet during the last glacial cycle: Current ice loss and contribution to sea-level rise from a palaeoclimatic perspective. Earth-Sci. Rev. 150, 45–67. https://doi.org/10.1016/j.earscirev.2015.07.006.

Vautravers, M.J., Shackleton, N.J., Lopez-Martinez, C., Grimalt, J.O., 2004. Gulf Stream variability during marine isotope stage 3. Paleoceanography 19, PA2011. https://doi.org/10.1029/2003PA000966.

Vautravers, M.J., Bianchil, G., Sackleton, N.J., 2007. 20. Subtropical NW Atlantic surface water variability during the last interglacial, in: Sirocko, F., Claussen, M., Goñi, M.F.S., Litt, T. (Eds.), The Climate of Past Interglacials, Developments in Quaternary Sciences. Elsevier, pp. 289–303. https://doi.org/10.1016/S1571-0866(07)80045-5.

Veres, D., Bazin, L., Landais, A., Toyé Mahamadou Kele, H., Lemieux-Dudon, B., Parrenin, F., Martinerie, P., Blayo, E., Blunier, T., Capron, E., Chappellaz, J., Rasmussen, S. O., Severi, M., Svensson, A., Vinther, B., Wolff, E. W., 2013. The Antarctic ice core chronology (AICC2012): an optimized multi-parameter and multi-site dating approach for the last 120 thousand years. Clim. Past 9, 1733–1748. https://doi.org/10.5194/cp-9-1733-2013.

Voelker, A. H., 1999. Zur Deutung der Dansgaard-Oeschger Ereignisse in ultra-hochauflösenden Sedimentprofilen aus dem Europäischen Nordmeer, Doctoral dissertation, Institut für Geowissenschaften, Christian-Albrechts-Universität.

Voelker, A. H. L., Colman, A., Olack, G., Waniek, J. J., Hodell, D., 2015. Oxygen and hydrogen isotope signatures of Northeast Atlantic water masses. Deep Sea Res. Part II: Trop. Stud. Oceanogr. 116, 89–106. https://doi.org/10.1016/j.dsr2.2014.11.006.

Volkmann, R., 2000. Planktic foraminifers in the outer Laptev Sea and the Fram Strait—modern distribution and ecology. J. Foraminiferal Res. 30, 157. https://doi.org/10.2113/0300157.

Waelbroeck, C., Frank, N., Jouzel, J., Parrenin, F., Masson-Delmotte, V., Genty, D., 2008. Transferring radiometric dating of the last interglacial sea level high stand to marine and ice core records. Earth Planet. Sci. Lett. 265, 183–194. https://doi.org/10.1016/j.epsl.2007.10.006.

Walczowski, W., 2013. Frontal structures in the West Spitsbergen Current margins. Ocean Sci. 9, 957. https://doi.org/10.5194/os-9-957-2013.

Walczowski, W., Piechura, J., 2011. Influence of the West Spitsbergen Current on the local climate. Int. J. Climatol. 31, 1088–1093. https://doi.org/10.1002/joc.2338.

Wang, C., Lee, S., 2007. Atlantic warm pool, Caribbean low-level jet, and their potential impact on Atlantic hurricanes. Geophys. Res. Lett. 34. https://doi.org/10.1029/2006GL028579.

Wang, X., Auler, A. S., Edwards, R. L., Cheng, H., Cristalli, P. S., Smart, P. L., Richards, D. A., Shen, C. C., 2004. Wet periods in northeastern Brazil over the past 210 kyr linked to distant climate anomalies. Nature, 432(7018), 740-743. https://doi:10.1038/nature03067.

Werner, K., Müller, J., Husum, K., Spielhagen, R. F., Kandiano, E. S., Polyak, L., 2016. Holocene sea subsurface and surface water masses in the Fram Strait – Comparisons of temperature and sea-ice reconstructions. Quat. Sci. Rev. 147, 194–209. https://doi.org/10.1016/j.quascirev.2015.09.007.

Wilson, P. A., Roberts, H. H., 1995. Density cascading: off-shelf sediment transport, evidence and implications, Bahama Banks. J. Sedim. Res. 45–56.

Winograd, I. J., Coplen, T. B., Szabo, B. J., Riggs, A. C., 1988. A 250,000-Year Climatic Record from Great Basin Vein Calcite: Implications for Milankovitch Theory. Science 242, 1275. https://doi.org/10.1126/science.242.4883.1275.

Winsor, K., Carlson, A. E., Klinkhammer, G. P., Stoner, J. S., Hatfield, R. G., 2012. Evolution of the northeast Labrador Sea during the last interglaciation. Geochem. Geophys. Geosyst. 13, Q11006. https://doi.org/10.1029/2012GC004263.

Wolff, T. S., Mulitza, S., Rühlemann, C., Wefer, G., 2010. Response of the tropical Atlantic thermocline to late Quaternary Trade Wind changes. Paleoceanography 14, 374–383. https://doi.org/10.1029/1999PA900011.

Wollenburg, J. E., Mackensen, A., 1998. Living benthic foraminifers from the central Arctic Ocean: faunal composition, standing stock and diversity. Mar. Micropal. 34, 153–185. https://doi.org/10.1016/S0377-8398(98)00007-3.

Wollenburg, J. E., Kuhnt, W., Mackensen, A., 2001. Changes in Arctic Ocean paleoproductivity and hydrography during the last 145 kyr: The benthic foraminiferal record. Paleoceanography 16, 65–77. https://doi.org/10.1029/1999PA000454.

Wood, R. A., Keen, A. B., Mitchell, J. F. B., Gregory, J. M., 1999. Changing spatial structure of the thermohaline circulation in response to atmospheric CO_2 forcing in a climate model. Nature 399, 572. https://doi.org/10.1038/21170.

Wu, P., Wood, R., Stott P., 2005. Human influence on increasing Arctic river discharges. Geophys. Res. Let. 32. https://doi.org/10.1029/2004GL021570.

Xiao, W., Wang, R., Polyak, L., Astakhov, A., Cheng, X., 2014. Stable oxygen and carbon isotopes in planktonic foraminifera *Neogloboquadrina pachyderma* in the Arctic Ocean: An overview of published and new surface-sediment data. Mar. Geol. 352, 397–408. https://doi.org/10.1016/j.margeo.2014.03.024.

Yashayaev, L., 2009. Enhanced production of Labrador Sea Water in 2008. Geophys. Res. Lett. 36. https://doi.org/10.1029/2008GL036162.

Young, N. E., Briner, J. P., 2015. Holocene evolution of the western Greenland Ice Sheet: Assessing geophysical ice-sheet models with geological reconstructions of ice-margin change. Quat. Sci Rev. 114, 1–17. https://doi.org/10.1016/j.quascirev.2015.01.018.

Zamelczyk, K., Rasmussen, T. L., Husum, K., Hald, M., 2013. Marine calcium carbonate preservation vs. climate change over the last two millennia in the Fram Strait: Implications for planktic foraminiferal paleostudies. Mar. Micropal. 98, 14–27. https://doi.org/10.1016/j.marmicro.2012.10.001.

Zamelczyk, K., Rasmussen, T. L., Husum, K., Godtliebsen, F., Hald, M., 2014. Surface water conditions and calcium carbonate preservation in the Fram Strait during marine isotope stage 2, 28.8–15.4 kyr. Paleoceanography 29, 1–12. https://doi.org/10.1002/2012PA002448.

Zhang, R., 2007. Anticorrelated multidecadal variations between surface and subsurface tropical North Atlantic. Geophys. Res. Lett. 34. https://doi.org/10.1029/2007GL030225.

Zhuravleva, A., Bauch, H. A., Spielhagen, R. F., 2017a. Atlantic water heat transfer through the Arctic Gateway (Fram Strait) during the Last Interglacial. Glob. Planet. Change 157, 232–243. https://doi.org/10.1016/j.gloplacha.2017.09.005.

Zhuravleva, A., Bauch, H. A., Van Nieuwenhove, N., 2017b. Last Interglacial (MIS5e) hydrographic shifts linked to meltwater discharges from the East Greenland margin. Quat. Sci. Rev. 164, 95–109. https://doi.org/10.1016/j.quascirev.2017.03.026.

Ziegler, M., Nürnberg, D., Karas, C., Tiedemann, R., Lourens, L. J., 2008. Persistent summer expansion of the Atlantic Warm Pool during glacial abrupt cold events. Nature Geosci. 1, 601-605. https://doi.org/doi:10.1038/ngeo277.

Data tables

Chapter 3

Data are also available in the PANGAEA database (https://doi.org/10.1594/PANGAEA.877368).

Abbreviations:

C.w. - *Cibicidoides wuellerstorfi,* N.p. - *Neogloboquadrina pachyderma,* O. u. - *Oridorsalis umbonatus*

Depth[m]	Age[ka BP]	N. p. d18O	N. p. d13C	C. w. d18O	C. w. d13C	O. u. d18O	IRD[#/g]	N pach[%]	T quin[%]	Foram[#/g]	Beella[#/g]
4.615	94.2			4.4	1.182		4229.8	99.82	0.18	17877	
4.625	95.0			4.401	1.135		4762.7	99.88	0.12	15790	
4.635	95.7	3.912	0.841	4.233	1.051		4154.7	100	0	8588	
4.645	96.5	3.577	0.458	4.059	0.992		3450.9	99.9	0	10978	
4.655	97.3	3.846	0.801	4.399	1.151		4526.2	100	0	9888	
4.665	98.1	4.004	0.624	4.55	1.1		3302.2	100	0	6595	
4.675	98.9	3.748	0.631	4.412	1.169		2738.7	100	0	7077	
4.685	99.6	3.863	0.624	4.312	1.008		5479.9	100	0	6354	
4.695	100.4	4.105	0.758	4.237	1.093		2900.1	100	0	13420	
4.705	101.2	3.803	0.714	3.962	1.039		2874.6	99.95	0.05	19294	
4.715	102.0	4.211	0.745	4.106	1.138		1855.7	99.92	0.08	22232	
4.725	102.7	4.113	0.704	4.205	1.107		1812.6	99.8	0.2	19688	
4.735	103.5	4.134	0.690	4.412	1.206		1720.7	100	0	22487	
4.745	104.3	3.787	0.645	4.177	1.109		2047.5	99.78	0.15	26694	
4.755	105.1	3.817	0.719	4.077	1.135		2941.4	99.35	0.65	33859	
4.765	105.8	4.123	0.751	4.294	1.264		3952.6	99.19	0.81	32488	
4.775	106.6	4.104	0.619	4.194	1.269		4160	99.92	0.08	64703	
4.785	107.4	4.148	0.726	4.14	1.099		3801	99.7	0.3	47025	
4.795	108.2	4.136	0.808	4.069	1.205		3095	99.65	0.35	63033	
4.805	108.9	4.146	0.680	4.202	1.282		5572.1	99.58	0.42	79523	
4.815	109.7	4.057	0.709	3.918	1.202		2884.8	99.45	0.55	65486	
4.825	110.5	4.083	0.726	3.891	1.221		4879.5	99.54	0.46	60482	
4.835	111.3	3.946	0.680	3.981	1.19		3067.5	99.67	0.33	73028	
4.845	112.0	4.024	0.707	4.037	1.193		5390.7	100	0	70716	
4.855	112.8	3.922	0.766	4.075	1.258	4.331	6880.2	99.63	0.37	84563	
4.865	113.6	3.690	0.794	4.218	1.363	4.261	6893.7	99.82	0.18	41844	
4.875	114.4	3.746	0.620	3.96	1.309	4.193	6677.1	99.4	0.6	36947	
4.885	115.1	3.726	0.520	3.798	1.184	3.927	10030.4	99.24	0.76	62020	
4.895	115.9	3.664	0.672	3.974	1.175	4.106	9537.5	96.99	3.01	62926	
4.905	116.7	3.618	0.527	3.905	0.934	4.13	6197.8	99.39	0.61	51016	
4.915	117.4	3.572	0.496	3.845	1.105	3.974	3309.7	87.57	12.2	55351	
4.925	118.1	3.157	0.369	3.566	1.107	3.892	3475.4	96.15	3.59	66641	
4.935	118.9	3.535	0.496	3.84	0.986	4.143	4755.5	92.61	7.31	52445	
4.945	119.6	3.580	0.485	3.793	0.898	4.06	5619	95.27	4.63	68038	
4.955	120.3	3.566	0.447	3.783	1.068	4.098	2575.2	88.68	11.11	41247	
4.965	121.0	3.525	0.478	3.783	1.018	4.112	3791.9	96.17	3.73	62453	
4.975	121.8	3.592	0.249	3.894	1.048	4.167	6410	95.99	4.01	49953	
4.985	122.5	3.600	0.359	3.952	1.046	4.029	8447.9	96.63	3.22	48575	
4.995	123.2	3.444	0.253	3.831	1.07	3.84	4645.4	96.2	3.8	38950	0
5.005	123.9	3.280	0.349	3.889	0.946	4.017	7044.7	99.56	0.44	43226	0.6
5.015	124.6	3.518	0.439	3.684	0.924	4.111	8676.6	99.76	0.23	32665	0.4
5.025	125.0	3.371	0.256	3.763	0.74	4.061	8933.2	99.72	0.26	19276	4.31
5.035	125.1	3.583	0.339	3.571	0.753	4.139	9292.5	99.99	0	21327	1.09
5.045	125.2	3.190	0.315	3.814	0.838	4.149	11276.9	99.91	0	17907	3.05
5.055	125.3	3.508	0.363	3.687	0.803	3.871	10759.8	100	0	16527	0.66
5.065	125.4	2.476	0.179	3.99	0.793	4.26	13184.7	99.98	0	13857	2.26
5.075	125.5	2.310	-0.052	3.495	0.588	3.919	11066.1	99.98	0	6420	1.2
5.085	125.6	2.644	0.245	3.908	0.798	4.197	12145.2	99.81	0	9265	1.27
5.095	125.7	1.865	-0.176	3.32	0.376	3.919	13947.3	99.99	0	9704	1.33
5.105	125.8	1.571	-0.148	3.262	0.305	3.853	12280.7	99.99	0	10664	1.29
5.115	125.9	2.712	0.003			4.462	5959.7	99.99	0	5402	0.58
5.125	126.0	2.078	-0.372	3.335	0.354	3.13	6609.3	99.98	0	2369	0.41
5.135	126.1	3.388	0.156			4.434	6385.6	99.98	0	1606	0.29
5.145	126.2	1.866	-0.630			3.066	5029.1	100	0	829	0
5.155	126.3	2.438	-0.231				4232.6	100	0	394	0
5.165	126.4	3.389	0.217				6050.9			207	
5.175	126.5	5.141	-0.134	4.538	0.848		8479.1			130	
5.185	126.5	4.068	0.229			5.065	8905.4			62	
5.195	126.6	2.687	-0.816			2.613	14752.9			59	
5.205	126.7	3.021	-0.898			3.869	13164.5			51	
5.215	126.8	3.695	0.215			3.36	10242.9			42	
5.225	126.9	2.771	-0.260				8516.1			0	
5.235	127.0	3.937	-0.428				13271.8			0	
5.245	127.1	4.030	0.115				13233.1			0	
5.255	127.2	2.536	0.014			3.53	11484.1			95	
5.265	127.3	4.321	-0.034				8550.4			0	
5.275	127.4	2.938	-0.123				4519.4			0	
5.285	127.5	3.962	0.090				7251.7			21	
5.295	127.6	3.653	0.247				6018.7			16	
5.305	127.7	3.895	0.493				3362.7			22	
5.315	127.8	3.982	0.527				2121.8			6	
5.325	127.9						3488.2			0	
5.335	127.9						4138.4			0	
5.345	128.0						5523.3			1	

Depth [m]	Age [ka BP]	N. p. d18O	N. p. d13C	C. w. d18O	C. w. d13C	O. u. d18O	IRD[#/g]	N pach[%]	T quin[%]	Foram[#/g]	Beella[#/g]
5.355	128.1	3.288	0.257				4321.6			20	
5.365	128.2	3.622	-0.160				4299.7			2	
5.375	128.3	3.652	0.401				5076.1			11	
5.385	128.4	2.426	-0.123				4856.8			5	
5.395	128.5	2.383	-0.122				2814.4			7	
5.405	128.6	2.110	-0.165				5457.6			33	
5.415	128.7						2545.7			1	
5.425	128.8	1.826	-1.078				12492.3			5	
5.435	128.9	3.903	0.255				17712.8			84	
5.445	129.0	3.185	-0.574				15754			22	
5.455	129.1	2.260	-0.775				12556			10	
5.465	129.2	3.357	-0.695			3.086	13469.1			52	
5.475	129.3	2.696	-0.826			3.37	8116.8			0	
5.485	129.4	4.174	-0.440			4.639	5328.4			148	
5.495	129.6	3.999	-0.307			4.079	4248.3			106	
5.505	129.9	3.354	-0.641			3.63	3173.1			41	
5.515	130.2	4.170	-0.373			3.614	3527.4			78	
5.525	130.5	2.853	-0.909			3.768	2693.9			6	
5.535	130.8	3.436	-0.112			3.3	2314.4			6	
5.545	131.1	3.678	-0.362			3.905	3236.3			19	
5.555	131.4	3.076	-0.767			4.433	1921.6			25	
5.565	131.7	4.059	0.166			3.575	3004.8			26	
5.575	132.0	2.653	-0.946			2.557	2421.9			13	
5.585	132.4	3.602	-0.498				2199.9			0	
5.595	132.7	3.948	-0.385				1544			7	
5.605	133.0	3.305	-0.398				1447.6			8	
5.615	133.3	4.187	0.012				1128.2			20	
5.625	133.6	3.279	-0.419				1027.8			18	
5.635	133.9	4.571	0.002				1630.7			197	
5.645	134.2	4.576	0.064			3.792	1600.1	100	0	625	
5.655	134.5	4.290	-0.152			4.884	2029.5	100	0	614	
5.665	134.8	4.488	-0.050			4.654	2627.5	100	0	925	
5.675	135.2	4.596	0.031			4.691	2640.5	100	0	641	
5.685	135.5	4.168	-0.153			4.879	3836.8			619	
5.695	135.8	4.507	-0.040			4.741	6778.3			938	
5.705	136.1	4.286	-0.059			4.33	9990.1			876	

Chapter 4

Data are also available in the PANGAEA database (https://doi.org/10.1594/PANGAEA.883805).

Abbreviations:

C.w. - *Cibicidoides wuellerstorfi,* N.p. - *Neogloboquadrina pachyderma*

Depth[m]	Age[ka BP]	N. p. d18O	N. p. d13C	C. w. d18O	C. w. d13C	Depth[m]	Age[ka BP]	Foram[#/g]	IRD[#/g]	Clastic IRD[%]
13.465	92.20	3.988	0.585			13.465	92.20	4213	12109	12
13.495	92.60	3.878	0.712			13.49	92.54	3178	13829	16
13.525	93.00	4.344	0.516			13.495	92.60	3974	39178	69
13.555	93.40	4.571	0.312			13.525	93.00	35	2987	39
13.585	93.80	4.689	0.381			13.555	93.40	84	16340	
13.645	94.59	4.403	0.291			13.57	93.60	47	15918	
13.695	95.26	4.830	0.307			13.585	93.80	67	15787	30
13.745	95.92	4.581	0.187			13.62	94.26	23	12150	
13.795	96.58	4.292	0.189			13.645	94.59	115	21763	21
13.845	97.25	4.926	0.311			13.67	94.92	75	6797	
13.895	97.91	4.109	0.026			13.695	95.26	256	41500	4
13.945	98.57	4.216	0.225			13.72	95.59	216	11762	
13.995	99.24	4.275	0.200			13.745	95.92	195	32288	7
14.035	99.77	4.280	0.368			13.77	96.25	33	4351	
14.065	100.17	4.378	0.353			13.795	96.58	43	11253	31
14.095	100.56	4.390	0.426			13.82	96.92	0	6874	33
14.125	100.96	4.237	0.349			13.845	97.25	20	43600	14
14.155	101.36	4.059	0.354			13.87	97.58	27	9988	
14.185	101.76	4.224	0.286			13.895	97.91	78	18575	13
14.215	102.16	3.936	0.539			13.92	98.24	0	9073	22
14.245	102.55	4.005	0.526			13.945	98.57	79	15536	13
14.275	102.95	4.234	0.485			13.97	98.91	74	9412	
14.305	103.35	3.941	0.502			13.995	99.24	220	20689	17
14.335	103.75	4.434	0.581			14.02	99.57	68	12279	
14.365	104.15	4.213	0.559			14.035	99.77	252	20534	13
14.395	104.55	3.660	0.482			14.065	100.17	182	10808	17
14.425	104.94	3.817	0.385			14.095	100.56	67	11316	15
14.455	105.34	3.843	0.441			14.125	100.96	178	24656	16
14.485	105.74	4.081	0.412			14.155	101.36	1159	23822	18
14.515	106.14	4.160	0.437			14.185	101.76	486	23883	14
14.545	106.54	4.020	0.478			14.215	102.16	1123	35971	11
14.575	106.93	4.692	0.601			14.245	102.55	278	13913	33
14.605	107.33	4.535	0.426			14.275	102.95	221	5123	31
14.635	107.73	4.251	0.564			14.305	103.35	1275	11696	35
14.665	108.13	4.364	0.189			14.335	103.75	209	11527	36
14.685	108.39	4.309	0.268			14.365	104.15	349	11489	24
14.715	108.79	4.225	0.284			14.395	104.55	5333	14804	20
14.745	109.19	3.834	0.284			14.425	104.94	4753	7589	22
14.775	109.59	4.097	0.435			14.455	105.34	6631	7432	32
14.835	110.38	4.397	0.627			14.485	105.74	530	4916	46
14.865	110.78	4.345	0.507			14.515	106.14	549	12404	32
14.895	111.18	4.249	0.424			14.545	106.54	170	5772	28
14.925	111.58	4.459	0.313			14.575	106.93	174	11615	34
14.985	112.37	4.435	0.210			14.605	107.33	302	21550	18
15.015	112.77	4.040	0.234			14.635	107.73	29	16588	15
15.045	113.17	4.381	0.647			14.665	108.13	26	13818	10
15.075	113.57	4.168	0.378			14.685	108.39	33	20146	11
15.135	114.36	4.163	0.149			14.715	108.79	427	13586	22
15.165	114.76	4.207	0.203			14.745	109.19	8185	17922	26
15.195	115.16	4.337	0.189			14.76	109.39	11461	11583	
15.225	115.56	4.489	0.009			14.775	109.59	12990	12431	24
15.285	116.35	4.108	0.381	4.339	0.400	14.81	110.05	9321	11766	
15.315	116.77	3.465	0.279	4.125	0.470	14.835	110.38	12265	14292	8
15.325	116.93	3.605	0.487	4.103	0.583	14.86	110.72	1446	10221	13
15.335	117.10	3.583	0.588	4.579	0.823	14.865	110.78	2337	13388	
15.345	117.26	3.480	0.308			14.895	111.18	498	13579	18
15.355	117.42	3.464	0.417			14.91	111.38	73	14018	
15.365	117.59	3.787	0.520			14.925	111.58	187	14659	22
15.375	117.75	3.828	0.520			14.96	112.04	42	9103	
15.385	117.92	3.731	0.480	4.524	0.742	14.985	112.37	440	11807	24
15.395	118.08	3.436	0.546			15.01	112.71	54	9590	29
15.405	118.25	3.663	0.614			15.015	112.77	262	7456	
15.415	118.41	3.658	0.433			15.045	113.17	3263	13913	10
15.425	118.58	3.918	0.480	5.023	1.144	15.06	113.37	1137	11425	
15.435	118.74	3.703	0.389			15.075	113.57	739	19428	13
15.445	118.91	3.619	0.444			15.11	114.03	37	9860	
15.455	119.07	3.475	0.559			15.135	114.36	305	15487	20
15.465	119.23	3.462	0.543			15.16	114.70	18	9066	
15.475	119.40	3.362	0.478			15.165	114.76	416	9925	17
15.485	119.56	3.379	0.456	4.489	1.240	15.195	115.16	397	14702	9
15.495	119.73	3.448	0.417			15.21	115.36	4	7919	
15.505	119.89	3.199	0.300			15.225	115.56	624	20750	7
15.515	120.06	3.329	0.425			15.26	116.02	1	663	

Depth[m]	Age[ka BP]	N. p. d18O	N. p. d13C	C. w. d18O	C. w. d13C	Depth[m]	Age[ka BP]	Foram[#/g]	IRD[#/g]	Clastic IRD[%]
15.525	120.22	3.201	0.365	3.938	0.707	15.285	116.35	7193	7098	23
15.535	120.39	3.469	0.471			15.31	116.69	3167	2201	
15.545	120.55	3.230	0.346			15.315	116.77	18277	10361	17
15.555	120.72	3.436	0.331			15.325	116.93	8140	5769	17
15.565	120.88	3.405	0.449			15.335	117.10	9208	10473	20
15.575	121.05	3.283	0.544	3.766	0.530	15.345	117.26	5057	9374	18
15.585	121.21	2.334	0.027			15.355	117.42	1966	8437	20
15.595	121.37	3.204	0.341			15.36	117.51	2149	6430	26
15.605	121.54	2.185	-0.144			15.365	117.59	6884	16351	
15.615	121.70	3.550	0.540			15.375	117.75	3922	11535	14
15.625	121.87	3.545	0.477	4.399	0.703	15.385	117.92	4408	13617	18
15.635	122.03	3.236	0.098	4.251	0.559	15.395	118.08	3471	10687	21
15.645	122.20	3.202	0.019			15.405	118.25	2519	5851	29
15.655	122.36	4.086	0.494			15.41	118.33	7362	9012	13
15.665	122.53	2.504	-0.015			15.415	118.41	3495	13876	
15.675	122.69	3.236	0.451	4.452	0.218	15.425	118.58	4433	14314	26
15.685	122.86	-0.025	0.070			15.435	118.74	8474	11940	15
15.695	123.02	3.247	0.281			15.445	118.91	1631	3039	14
15.705	123.19	3.224	0.400			15.455	119.07	11467	12181	19
15.715	123.35	3.337	0.380			15.46	119.15	5442	6331	12
15.725	123.51	3.032	0.201	3.906	0.252	15.465	119.23	19058	15936	
15.735	123.68	3.169	0.357			15.475	119.40	18061	11616	17
15.745	123.84	3.206	0.434			15.485	119.56	17737	5901	18
15.755	124.01	3.079	0.278			15.495	119.73	26425	14491	11
15.765	124.17	3.109	0.404			15.505	119.89	19646	12870	11
15.775	124.34	3.108	0.224	3.586	-0.160	15.51	119.98	35542	8377	
15.785	124.50	3.205	0.359			15.515	120.06	42091	16946	12
15.795	124.67	3.167	0.326	3.924	0.602	15.525	120.22	43206	13066	12
15.805	124.74	3.331	0.278			15.535	120.39	42286	9803	11
15.815	124.79	3.580	0.431			15.545	120.55	42579	9917	13
15.825	124.83	3.841	-0.151	3.840	0.426	15.555	120.72	38546	6533	13
15.835	124.88	4.050	0.289			15.56	120.80	32837	7598	
15.845	124.93	3.303	-0.196			15.565	120.88	42331	7970	8
15.855	124.98	4.283	0.244			15.575	121.05	50084	9522	18
15.865	125.03	3.983	0.121			15.585	121.21	41069	10592	11
15.875	125.08	3.215	-0.366	3.569	-0.524	15.595	121.37	32485	14615	8
15.885	125.12	4.186	0.412			15.605	121.54	19635	16955	11
15.915	125.27	4.357	0.302	4.643	-0.162	15.61	121.62	10628	7462	
15.945	125.41	3.817	-0.169			15.615	121.70	15885	21884	7
15.975	125.56	4.675	0.313	5.160	0.126	15.625	121.87	10759	37473	6
16.035	125.84	2.776	-0.572			15.635	122.03	3757	19109	13
16.065	125.99	4.406	0.284	4.667	-0.021	15.645	122.20	1872	15546	11
16.095	126.13	4.561	0.277			15.655	122.36	2637	17475	13
16.125	126.28	5.018	0.542	5.280	0.362	15.66	122.44	7221	11064	
16.185	126.57	4.062	0.365			15.665	122.53	9748	20463	13
16.225	126.76	4.232	-0.168			15.675	122.69	21421	16597	10
16.255	126.90	3.522	-0.430			15.685	122.86	24615	19200	16
16.285	127.05	3.600	-0.637			15.695	123.02	15660	6801	17
16.315	127.19	3.822	-0.452			15.705	123.19	35829	8898	17
16.345	127.34	3.018	-0.358	3.817	-0.364	15.71	123.27	24646	12363	
16.375	127.48	3.023	-0.409			15.715	123.35	40509	11321	11
16.405	127.62	2.929	-0.280			15.725	123.51	30470	10365	15
16.435	127.77	2.937	-0.621			15.735	123.68	38652	9729	16
16.465	127.91	3.134	-0.372			15.745	123.84	43316	4352	19
16.495	128.06	3.216	-0.566			15.755	124.01	44603	6976	3
16.525	128.20	3.211	-0.350			15.76	124.09	28852	4012	
16.555	128.35	3.048	-0.581			15.765	124.17	46825	4902	19
16.585	128.49	2.673	-0.295			15.775	124.34	57798	7109	17
16.615	128.63	2.468	-0.229	3.678	-0.189	15.785	124.50	45476	6363	20
16.645	128.78	2.856	-0.183			15.795	124.67	49121	10221	13
16.675	128.92	2.857	-0.337			15.805	124.74	18207	18759	15
16.705	129.07	2.926	-0.299			15.81	124.76	1050	11995	
16.735	129.21	2.841	-0.498			15.815	124.79	9318	29731	11
16.765	129.36	3.352	-0.157			15.825	124.83	3157	21552	12
16.795	129.50	4.237	-0.115			15.835	124.88	1860	16951	17
16.825	129.65	4.202	-0.056			15.845	124.93	2436	22153	18
16.855	129.81	3.902	-0.094			15.855	124.98	2167	14043	16
16.885	129.96	4.308	-0.065			15.86	125.00	1223	10468	
16.915	130.11	3.798	-0.048			15.865	125.03	2613	17713	16
16.945	130.26	3.735	-0.242			15.875	125.08	1422	18818	10
16.975	130.42	4.072	-0.029			15.885	125.12	1613	18905	11
17.025	130.67	3.886	-0.131			15.91	125.24	881	13665	
17.065	130.88	4.615	-0.068			15.915	125.27	1726	23747	19
17.095	131.03	4.590	-0.089			15.945	125.41	1765	21688	17
17.145	131.28	4.594	0.098			15.96	125.48	1579	13965	
17.195	131.54	4.531	0.045			15.975	125.56	2162	17004	12
17.245	131.79	4.899	0.152			16.01	125.72	568	11637	
17.295	132.05	4.787	0.105			16.035	125.84	559	17437	36
17.345	132.30	4.720	-0.069			16.06	125.96	51	16014	
17.395	132.56	4.793	0.003			16.065	125.99	192	11188	48
17.445	132.81	4.857	-0.124			16.095	126.13	332	15469	35
17.495	133.07	4.385	-0.004			16.11	126.21	0	9651	
17.545	133.32	4.955	-0.013			16.125	126.28	187	14661	30
17.565	133.42	4.697	-0.113			16.14	126.35	0	5766	
17.595	133.58	4.544	0.048			16.185	126.57	0	5565	54
17.675	133.99	4.780	-0.216			16.195	126.61	0	16935	39
17.695	134.09	4.743	-0.341			16.225	126.76	313	17696	17
17.725	134.24	4.655	-0.273			16.255	126.90	67	13063	13
17.755	134.39	4.819	-0.239			16.285	127.05	0	14692	15

Depth[m]	Age[ka BP]	N. p. d18O	N. p. d13C	C. w. d18O	C. w. d13C	Depth[m]	Age[ka BP]	Foram[#/g]	IRD[#/g]	Clastic IRD[%]
17.785	134.55	4.724	-0.309			16.315	127.19	0	19041	9
17.845	134.85	4.732	-0.321			16.345	127.34	5	17291	10
17.875	135.01	4.967	-0.150			16.375	127.48	8	15154	12
17.905	135.29	4.746	-0.223			16.405	127.62	5	19590	7
17.935	135.58	4.789	-0.132			16.435	127.77	15	12643	6
17.995	136.14	4.701	-0.125			16.465	127.91	17	15063	6
18.025	136.43	4.671	-0.265			16.495	128.06	92	16474	8
18.055	136.71	4.822	-0.325			16.525	128.20	14	4175	11
18.085	136.99	4.672	-0.281			16.555	128.35	58	13224	16
18.115	137.28	4.583	-0.345			16.585	128.49	1260	13816	25
18.145	137.56	4.685	-0.156			16.615	128.63	4308	12767	32
18.175	137.84	4.815	-0.166			16.645	128.78	6206	22061	17
18.205	138.13	4.995	-0.173			16.675	128.92	178	16678	14
18.235	138.41	4.673	-0.258			16.705	129.07	90	13033	63
18.265	138.69	4.620	-0.279			16.735	129.21	0	3775	45
18.295	138.98	4.482	-0.444			16.765	129.36	13959	10662	15
18.325	139.26	4.519	-0.343			16.795	129.50	15154	15479	20
18.355	139.54	4.509	-0.170			16.825	129.65	6010	20766	28
18.385	139.83	4.638	-0.353			16.855	129.81	8783	13174	9
18.415	140.11	4.579	-0.328			16.885	129.96	1274	10280	4
18.445	140.40	4.331	-0.428			16.915	130.11	0	27114	0
18.475	140.68	4.459	-0.701			16.945	130.26	0	18505	1
18.505	140.96	4.156	-0.424			16.975	130.42	0	21266	1
18.535	141.25	4.186	-0.361			17.005	130.57	0	22878	1
18.565	141.53	4.188	-0.498			17.035	130.72	0	17420	1
18.595	141.81	3.827	-0.376			17.065	130.88	0	18641	1
18.625	142.10	4.194	-0.225			17.095	131.03	20868	15177	7
18.655	142.38	4.643	-0.060			17.12	131.16	17795	5428	
18.685	142.66	4.696	-0.485			17.145	131.28	15866	11533	9
18.715	142.95	4.978	-0.182			17.17	131.41	2069	12607	
18.745	143.23	4.651	-0.316			17.195	131.54	19730	15568	6
18.775	143.51	3.777	-0.298			17.22	131.67	4392	11001	
18.805	143.80	4.406	-0.381			17.245	131.79	16039	15909	13
18.835	144.08	4.037	-0.540			17.27	131.92	2651	10624	
18.865	144.36	4.212	-0.393			17.295	132.05	12483	16506	10
18.955	145.21	4.514	-0.336			17.32	132.18	789	9879	
18.985	145.50	4.417	-0.453			17.345	132.30	1327	16245	8
19.015	145.78	4.815	-0.157			17.37	132.43	3274	11625	
19.045	146.06	4.801	-0.193			17.395	132.56	7237	15097	4
19.075	146.35	4.436	-0.535			17.42	132.69	3024	9393	
19.105	146.63	4.444	-0.246			17.445	132.81	17853	13616	2
19.135	146.91	4.293	-0.478			17.47	132.94	11219	12100	
						17.495	133.07	23300	6617	31
						17.52	133.20	13491	9204	
						17.545	133.32	2469	12162	47
						17.57	133.45	6132	14545	
						17.595	133.58	3499	19796	44
						17.62	133.71	2844	8593	
						17.65	133.86	4356	20455	
						17.675	133.99	8180	15925	2
						17.695	134.09	5116	11037	4
						17.72	134.22	2050	22733	1
						17.725	134.24	5245	9872	
						17.755	134.39	9447	17787	5
						17.77	134.47	2419	7907	
						17.785	134.55	427	14468	2
						17.82	134.72	6551	7832	
						17.845	134.85	4337	15726	12
						17.87	134.98	291	13945	
						17.875	135.01	18	13197	48
						17.905	135.29	3490	13640	28
						17.92	135.43	17037	7964	
						17.935	135.58	16323	10681	6
						17.97	135.91	6792	8183	
						17.995	136.14	6573	15249	1
						18.02	136.38	8289	6623	
						18.025	136.43	25209	11941	1
						18.055	136.71	17285	10574	1
						18.085	136.99	20181	8580	3
						18.115	137.28	25905	8674	3
						18.145	137.56	40519	9634	1
						18.17	137.80	16909	8754	
						18.175	137.84	19297	14255	5
						18.205	138.13	10635	14614	5
						18.235	138.41	12088	11668	8
						18.265	138.69	9747	6975	4
						18.295	138.98	5816	8377	15
						18.325	139.26	4166	9037	16
						18.355	139.54	4353	11382	59
						18.385	139.83	5140	11921	53
						18.415	140.11	13893	8308	36
						18.445	140.40	30411	6419	11
						18.475	140.68	20576	6343	13
						18.505	140.96	14862	7252	19
						18.535	141.25	22007	8671	1
						18.565	141.53	12089	19962	4
						18.595	141.81	9940	9120	14
						18.625	142.10	9351	18074	16
						18.655	142.38	5199	14657	26
						18.685	142.66	101	25645	3
						18.715	142.95	69	13872	8
						18.745	143.23	5315	22154	14
						18.775	143.51	9464	17301	6
						18.805	143.80	5641	11795	30
						18.835	144.08	3007	15594	9
						18.865	144.36	3212	32117	13
						18.955	145.21	114	25434	3
						18.985	145.50	30	13996	3
						19.015	145.78	46	8604	37
						19.045	146.06	724	6051	23
						19.075	146.35	1578	20884	25
						19.105	146.63	2400	27429	25
						19.135	146.91	94	23255	20

Depth[m]	Age[ka BP]	Wt%>63 µm	Depth[m]	Age[ka BP]	Coal[%]	Depth[m]	Age[ka BP]	Wt%>63 µm	Depth[m]	Age[ka BP]	Coal[%]
15.755	124.01	2.9	15.875	125.08	0.00	17.095	131.03	4.8	17.695	134.09	0.00
15.765	124.17	3.2	15.885	125.12	0.46	17.145	131.28	2.2	17.725	134.24	0.00
15.775	124.34	2.6	15.915	125.27	0.63	17.195	131.54	1.3	17.755	134.39	0.00
15.785	124.50	2.6	15.945	125.41	0.00	17.245	131.79	0.5	17.785	134.55	0.00
15.795	124.67	3.7	15.975	125.56	0.94	17.295	132.05	1.8	17.845	134.85	0.36
15.805	124.74	1.4	16.035	125.84	0.00	17.345	132.30	24.6	17.875	135.01	0.39
15.815	124.79	1.0	16.065	125.99	0.93	17.395	132.56	7.2	17.905	135.29	1.10
15.825	124.83	0.7	16.095	126.13	1.86	17.445	132.81	1.6	17.935	135.58	0.00
15.835	124.88	1.0	16.125	126.28	0.70	17.495	133.07	2.0	17.995	136.14	1.10
15.845	124.93	0.9	16.185	126.57	0.00	17.545	133.32	1.8	18.025	136.43	0.36
15.855	124.98	1.4	16.195	126.61	0.56	17.595	133.58	1.3	18.055	136.71	1.14
15.865	125.03	0.9	16.225	126.76	3.63	17.675	133.99	0.5	18.085	136.99	0.75
15.875	125.08	1.5	16.255	126.90	0.50	17.695	134.09	1.1	18.115	137.28	1.02
15.885	125.12	0.9	16.285	127.05	0.29	17.725	134.24	0.5	18.145	137.56	0.00
15.915	125.27	0.8	16.315	127.19	0.33	17.755	134.39	0.2	18.175	137.84	0.00
15.945	125.41	1.0	16.345	127.34	0.26	17.785	134.55	3.3	18.205	138.13	0.00
15.975	125.56	0.8	16.375	127.48	0.68	17.845	134.85	5.7	18.235	138.41	0.24
16.035	125.84	2.3	16.405	127.62	0.70	17.875	135.01	14.2	18.265	138.69	0.00
16.065	125.99	7.9	16.435	127.77	0.86	17.905	135.29	15.8	18.295	138.98	0.00
16.095	126.13	3.8	16.465	127.91	0.49	17.935	135.58	4.7	18.325	139.26	0.00
16.125	126.28	6.0	16.495	128.06	0.41	17.995	136.14	3.2			
16.185	126.57	5.8	16.525	128.20	0.33	18.025	136.43	2.2			
16.195	126.61	2.3	16.555	128.35	0.49	18.055	136.71	3.9			
16.225	126.76	9.0	16.585	128.49	0.00	18.085	136.99	2.8			
16.255	126.90	8.5	16.615	128.63	1.00	18.115	137.28	2.3			
16.285	127.05	7.6	16.645	128.78	0.55	18.145	137.56	1.3			
16.315	127.19	5.8	16.675	128.92	0.72	18.175	137.84	2.7			
16.345	127.34	6.6	16.705	129.07	0.00	18.205	138.13	0.5			
16.375	127.48	8.2	16.735	129.21	0.00	18.235	138.41	3.1			
16.405	127.62	7.4	16.765	129.36	0.70	18.265	138.69	4.9			
16.435	127.77	7.9	16.795	129.50	0.00	18.295	138.98	4.8			
16.465	127.91	7.3	16.825	129.65	0.47	18.325	139.26	7.9			
16.495	128.06	5.4	16.855	129.81	0.34	18.355	139.54	7.5			
16.525	128.20	13.4	16.885	129.96	0.00	18.385	139.83	11.0			
16.555	128.35	7.2	16.915	130.11	2.72	18.415	140.11	7.6			
16.585	128.49	6.2	16.945	130.26	2.69	18.445	140.40	2.3			
16.615	128.63	9.4	16.975	130.42	5.37	18.475	140.68	4.9			
16.645	128.78	1.3	17.005	130.57	5.76	18.505	140.96	6.1			
16.675	128.92	0.8	17.035	130.72	3.54	18.535	141.25	3.8			
16.705	129.07	0.3	17.065	130.88	6.13	18.565	141.53	5.7			
16.735	129.21	0.2	17.095	131.03	1.50	18.595	141.81	9.2			
16.765	129.36	6.4	17.145	131.28	0.40	18.625	142.10	6.3			
16.795	129.50	4.8	17.195	131.54	0.00	18.805	143.80	0.0			
16.825	129.65	6.1	17.245	131.79	1.70	18.835	144.08	0.2			
16.855	129.81	9.5	17.295	132.05	0.53	18.865	144.36	0.1			
16.885	129.96	21.0	17.345	132.30	0.49	18.955	145.21	26.6			
16.915	130.11	20.2	17.395	132.56	0.86	18.985	145.50	4.1			
16.945	130.26	20.6	17.445	132.81	1.11	19.015	145.78	13.4			
16.975	130.42	32.9	17.495	133.07	0.31	19.045	146.06	4.0			
17.005	130.57	34.3	17.545	133.32	0.28	19.075	146.35	5.1			
17.035	130.72	32.8	17.595	133.58	0.00	19.105	146.63	1.3			
17.065	130.88	27.3	17.675	133.99	0.62	19.135	146.91	20.4			

Depth[m]	Age[ka BP]	C. w.[#/g]	Depth[m]	Age[ka BP]	Fragment[%]	Depth[m]	Age[ka BP]	N. pach.[%]	T. quinq[%]	Globig.[%]
1528.5	116.35	94.5	15.045	113.17	239	14.665	108.13	99.0	1.0	0.0
1531.5	116.77	136.3	15.075	113.57	261	14.715	108.79	99.3	0.7	0.0
1532.5	116.93	59.5	15.135	114.36	81	14.745	109.19	99.9	0.1	0.0
1533.5	117.10	28.1	15.165	114.76	93	14.775	109.59	99.8	0.2	0.0
1534.5	117.26	6.1	15.195	115.16	130	14.835	110.38	100.0	0.0	0.0
1535.5	117.42	12.8	15.225	115.56	121	14.865	110.78	100.0	0.0	0.0
1537.5	117.75	3.2	15.285	116.35	66	14.895	111.18	100.0	0.0	0.0
1539.5	118.08	10.2	15.315	116.77	29	14.985	112.37	99.7	0.3	0.0
1541.5	118.41	10.5	15.325	116.93	50	15.015	112.77	100.0	0.0	0.0
1543.5	118.74	31.6	15.335	117.10	114	15.045	113.17	100.0	0.0	0.0
1545.5	119.07	35.7	15.345	117.26	172	15.075	113.57	100.0	0.0	0.0
1546.5	119.23	24.1	15.355	117.42	160	15.135	114.36	100.0	0.0	0.0
1547.5	119.40	25.0	15.365	117.59	137	15.165	114.76	100.0	0.0	0.0
1549.5	119.73	5.3	15.375	117.75	142	15.195	115.16	100.0	0.0	0.0
1551.5	120.06	82.0	15.385	117.92	150	15.225	115.56	100.0	0.0	0.0
1553.5	120.39	61.7	15.395	118.08	139	15.285	116.35	98.8	1.2	0.0
1555.5	120.72	16.3	15.405	118.25	153	15.315	116.77	94.4	5.1	0.5
1557.5	121.05	32.8	15.415	118.41	143	15.325	116.93	96.1	3.8	0.1
1559.5	121.37	0.0	15.425	118.58	153	15.335	117.1	99.2	0.7	0.1
1561.5	121.70	0.0	15.435	118.74	113	15.345	117.26	99.8	0.0	0.2
1563.5	122.03	24.3	15.445	118.91	152	15.355	117.42	99.8	0.2	0.0
1565.6	122.38	22.3	15.455	119.07	112	15.365	117.59	99.5	0.4	0.1
1567.5	122.69	7.2	15.465	119.23	113	15.375	117.75	99.9	0.1	0.0
1569.5	123.02	14.0	15.475	119.40	103	15.385	117.92	100.0	0.0	0.0
1571.5	123.35	11.1	15.485	119.56	115	15.395	118.08	99.9	0.1	0.0
1573.5	123.68	86.3	15.495	119.73	111	15.405	118.25	99.9	0.1	0.0
1575.5	124.01	67.9	15.505	119.89	102	15.415	118.41	99.9	0.0	0.1
1577.5	124.34	141.7	15.515	120.06	75	15.425	118.58	99.7	0.3	0.1
1579.5	124.67	31.0	15.525	120.22	76	15.435	118.74	99.4	0.3	0.2
1581.5	124.79	18.0	15.535	120.39	92	15.445	118.91	99.5	0.4	0.1
1583.5	124.88	9.6	15.545	120.55	112	15.455	119.07	99.9	0.1	0.1
1585.5	124.98	31.7	15.555	120.72	113	15.465	119.23	99.9	0.1	0.0
1587.5	125.08	17.1	15.565	120.88	138	15.475	119.4	100.0	0.0	0.0
1588.5	125.12	30.4	15.575	121.05	159	15.485	119.56	99.9	0.0	0.1
1591.5	125.27	21.1	15.585	121.21	194	15.495	119.73	99.9	0.1	0.0
1597.5	125.56	21.1	15.595	121.37	181	15.505	119.89	99.9	0.0	0.1
1603.5	125.84	32.7	15.605	121.54	216	15.515	120.06	99.6	0.4	0.0
1606.5	125.99	8.2	15.615	121.70	205	15.525	120.22	99.5	0.3	0.2
1609.5	126.13	0.0	15.625	121.87	246	15.535	120.39	99.7	0.2	0.1
1612.5	126.28	5.3	15.635	122.03	249	15.545	120.55	99.3	0.4	0.4
1661.5	128.63	13.1	15.645	122.20	255	15.555	120.72	99.8	0.2	0.1
			15.655	122.36	252	15.565	120.88	99.8	0.2	0.0
			15.665	122.53	253	15.575	121.05	99.9	0.0	0.1
			15.675	122.69	215	15.585	121.21	99.9	0.1	0.0
			15.685	122.86	251	15.595	121.37	100.0	0.0	0.0
			15.695	123.02	218	15.605	121.54	100.0	0.0	0.0
			15.705	123.19	200	15.615	121.7	100.0	0.0	0.0
			15.715	123.35	212	15.625	121.87	100.0	0.0	0.0
			15.725	123.51	213	15.635	122.03	100.0	0.0	0.0
			15.735	123.68	216	15.645	122.2	100.0	0.0	0.0
			15.745	123.84	169	15.655	122.36	100.0	0.0	0.0
			15.755	124.01	197	15.665	122.53	100.0	0.0	0.0
			15.765	124.17	194	15.675	122.69	100.0	0.0	0.0
			15.775	124.34	208	15.685	122.86	100.0	0.0	0.0
			15.785	124.50	214	15.695	123.02	100.0	0.0	0.0
			15.795	124.67	190	15.705	123.19	100.0	0.0	0.0
			15.805	124.74	234	15.715	123.35	99.4	0.4	0.3
			15.815	124.79	228	15.725	123.51	97.7	1.5	0.8
			15.835	124.88	140	15.735	123.68	98.3	1.3	0.4
			15.855	124.98	115	15.745	123.84	96.0	2.5	1.4
						15.755	124.01	97.4	1.8	0.8
						15.765	124.17	99.4	0.3	0.4
						15.775	124.34	99.6	0.3	0.1
						15.785	124.5	100.0	0.0	0.0
						15.795	124.67	99.8	0.2	0.0
						15.805	124.74	100.0	0.0	0.0
						15.815	124.79	100.0	0.0	0.0
						15.835	124.88	100.0	0.0	0.0
						15.855	124.98	100.0	0.0	0.0

Chapter 5

All data will also be made available in the online database PANGAEA (www.pangaea.de).

Depth [cm]	Age[ka]	G.trun d18O	G.inf. d18O	Depth [cm]	Age[ka]	G.trun d18O	G.inf. d18O
244.5	100.9	0.984		378.5	121.9	0.315	
246.5	101.7	0.873		380.5	122.1	0.182	
248.5	102.4	0.94		382.5	122.3	0.222	
250.5	103.1	0.983		384.5	122.5	0.24	
252.5	103.6	1.067		386.5	122.7	0.796	
254.5	104.0	0.954		388.5	122.8	0.203	
256.5	104.5	0.779		390.5	123.0	0.338	
258.5	105.0	0.949		392.5	123.2	0.176	
260.5	105.4	0.854		394.5	123.4	0.587	
262.5	105.9	0.996		396.5	123.6	0.377	
264.5	106.3	0.813		398.5	123.7	0.065	
266.5	106.8	0.81		400.5	123.9	0.62	
268.5	107.3	0.842		402.5	124.1	0.134	
270.5	107.7	0.517		404.5	124.3	0.336	
272.5	108.2	0.955		406.5	124.5	0.251	
274.5	108.7	0.947		408.5	124.7	0.241	
276.5	109.1	0.759		410.5	124.8	0.259	
278.5	109.6	1.137		412.5	125.0	0.362	
280.5	110.0	0.907		414.5	125.2	0.187	
282.5	110.5	0.843		416.5	125.4	0.263	
284.5	111.0	0.606		418.5	125.6	0.503	1.699
286.5	111.4	0.786		420.5	125.7	0.145	0.341
288.5	111.9	0.675		422.5	125.9	0.167	0.707
290.5	112.3	0.455		424.5	126.1	0.157	0.164
292.5	112.8	0.74		426.5	126.3	0.022	-0.038
294.5	113.3	0.672		428.5	126.5	-0.012	0.136
296.5	113.7	0.778		430.5	126.6	-0.022	0.359
298.5	114.2	0.651		432.5	126.8	-0.061	0.304
300.5	114.7	0.729		434.5	127.0	0.874	1.069
302.5	115.0	0.956		436.5	127.2	-0.109	1.344
304.5	115.2	0.667		438.5	127.4	-0.115	0.334
306.5	115.4	0.535		440.5	127.6	0.156	0.824
308.5	115.6	0.612		442.5	127.7	0.171	0.718
310.5	115.8	0.51		444.5	127.9	-0.121	0.319
312.5	116.0	0.819		446.5	128.1	0.135	0.719
314.5	116.1	0.747		448.5	128.3	0.287	1.027
316.5	116.3	0.628		450.5	128.5	0.307	0.256
318.5	116.5	0.501		452.5	128.6	0.612	1.523
320.5	116.7	0.712		454.5	128.8	0.545	0.77
322.5	116.9	0.614		456.5	129.0	0.991	0.805
324.5	117.0	0.538		458.5	129.3	0.258	1.211
326.5	117.2	0.405		460.5	129.7	0.676	0.848
328.5	117.4	0.488		462.5	130.0	1.292	0.827
330.5	117.6	0.468		464.5	130.4	0.621	0.979
332.5	117.8	0.692		466.5	130.7	0.869	0.775
334.5	117.9	0.671		468.5	131.2	1.196	1.201
336.5	118.1	1.138		470.5	131.8	0.618	0.993
338.5	118.3	0.217		472.5	132.4	0.692	1.462
340.5	118.5	0.002		474.5	133.0	1.282	1.3
342.5	118.7	0.441		476.5	133.6	0.968	1.511
344.5	118.9	0.289		478.5	134.2	1.165	1.712
346.5	119.0	0.234		480.5	134.8	2.048	1.362
348.5	119.2	0.243		482.5	135.4	1.093	1.811
350.5	119.4	0.353		484.5	136.0	1.725	1.675
352.5	119.6	0.518		486.5	136.6	1.793	1.741
354.5	119.8	-0.047		488.5	137.2	1.984	1.532
356.5	119.9	0.184		490.5	137.8	1.83	1.697
358.5	120.1	0.208		492.5	138.4	1.803	1.615
360.5	120.3	0.303		494.5	139.0	1.9	1.841
362.5	120.5	0.307		496.5	139.6	1.14	1.41
364.5	120.7	0.444		498.5	140.2	1.499	1.688
366.5	120.8	0.268		500.5	140.8	1.947	1.567
368.5	121.0	0.704		502.5	141.4	1.455	1.737
370.5	121.2	0.181		504.5	142.0	1.627	1.503
372.5	121.4	0.32		506.5	142.6	1.64	1.472
374.5	121.6	0.355		508.5	143.2	1.48	1.374
376.5	121.8	0.217					

Depth [cm]	Age[ka]	G. truncatuli	G. truncatuli	G. conglobat	G. ruber p	G. ruber w	G. trilobus	G. sacculifer	G. inflata	G. falconensis
150.5	33.7	2.8	1.1	0.3	1.9	29.3	7.3	0.7	1.9	0.5
160.5	42.2	3.9	1.6	0.4	3.1	29.6	6.9	1.5	1	1.2
170.5	50.7	2.7	0	0.1	1.9	29.9	5.9	1.3	3.1	1.7
180.5	59.2	1.1	1.5	0.9	1.6	33.6	4.5	0.8	2.5	0.2
190.5	67.7	1.6	0.9	0.5	1.5	32.4	5.4	0.4	1.7	0.3
200.5	76.2	1.7	1.1	0.4	1.9	34.8	4.4	0	2.5	1.1
210.5	84.7	0.2	0.7	3.9	4.2	30.5	6	0.7	1.8	1.6
220.5	90.5	1.6	1.3	1.1	1.3	22.4	3.2	0.7	0.9	0.3
230.5	95.6	1.8	0.6	1	1.4	27.7	5.3	0.6	0	0.8
240.5	99.4	1.7	0.6	0.8	1.8	36.7	8.4	0.1	0.2	3.5
244.5	100.9	1.3	1.6	0.5	2.1	29.2	5.8	1.7	0	3.9
246.5	101.7	1.8	0.8	0.5	2.2	31.5	10.9	0.6	0	1.8
248.5	102.4	2.1	0.7	1	3.4	30.2	7.1	0.3	0	1.8
250.5	103.1	2.4	0	1.1	2.1	27.8	6.5	0.1	0.3	4.4
252.5	103.6	0.8	0.5	0.3	2.6	23.6	4.6	0	0	3.8
254.5	104.0	1.3	0.8	0.6	1.3	27.7	2	1	0	4.4
256.5	104.5	0.3	0.8	0	2.1	23.9	5.8	0.8	0	3.5
258.5	105.0	1.5	0.6	0.3	1.7	18.3	5.7	0.6	0	3.4
260.5	105.4	1.3	0	0.3	2.5	15.1	3.8	0	0	3.3
262.5	105.9	1.5	0.9	0.6	1.4	17.4	8.3	0.4	0	3.7
264.5	106.3	1.5	0.3	0.8	2.9	13.2	6	0	0	4.6
266.5	106.8	1.4	0.5	0.3	2.3	16.3	7.3	0.7	0	4.8
268.5	107.3	0.7	1.2	1.1	3.6	14.8	4.8	1.5	0.3	3.9
270.5	107.7	1.6	0.6	1.4	3.5	15.2	5.1	0.4	0	5.4
272.5	108.2	0.9	0.2	0.7	4.1	14.8	8.1	0.5	0.2	7
274.5	108.7	0.4	0.4	1	4	18.1	7.2	0.4	0	4.4
276.5	109.1	0.6	0.2	1.4	4.1	18	5.5	0.4	0.2	3.6
278.5	109.6	1.4	0	0.8	3	17.4	8.6	0.9	0	3.9
280.5	110.0	0.1	0	0.3	3.5	15.4	8.6	0.5	0	2.6
282.5	110.5	0.3	0.2	0.4	3.4	17	9	1.4	0	3.2
284.5	111.0	0.5	0.7	0.3	2.4	15.1	4.1	1.1	0	1.3
286.5	111.4	0.4	0.2	1.6	2.3	23.6	8.7	1.9	0	1.2
288.5	111.9	1	0.1	0.9	3.9	17.8	10	0.8	0	2.2
290.5	112.3	0.1	1	1.1	4.7	18	9.4	2.1	0	0.9
292.5	112.8	1.4	1.3	1.7	3	15.5	8.7	0.4	0	0.8
294.5	113.3	0.5	0.3	0.7	4.5	13.6	4.7	1.4	0	0.4
296.5	113.7	1.2	0	1.3	1.8	19.8	8.3	1.2	0	1.2
298.5	114.2	0.6	0.3	1.8	3.7	21.8	6.2	1.5	0.8	0
300.5	114.7	0	0.9	1.4	1.9	19.7	11.4	1.6	0	0.8
302.5	115.0	0.4	1.1	1.1	2.4	24	9.4	1.3	0.9	0.9
304.5	115.2	0	0.3	2.4	2.1	19.6	5.6	1.9	0.2	0.9
306.5	115.4	0	1.8	1.3	1.3	20.6	12.5	0.6	0	0.8
308.5	115.6	0.8	0.5	1.1	2.2	21.7	14	1.3	0.2	0.4
310.5	115.8	0.3	1	0.7	1.9	27.1	8.9	0	0	1.2
312.5	116.0	1.3	0.8	1.2	3.3	26.5	7.3	0.8	0.4	1.5
314.5	116.1	0	0.6	0.4	1.6	23.4	8.7	3.6	0.6	0.6
316.5	116.3	0	1	0.6	2.2	21.2	12.3	2.9	0	0.9
318.5	116.5	0.6	1.7	0.7	5.6	22	7.2	2.3	0	0.6
320.5	116.7	0.9	1.4	1.8	3.7	25.3	7	2.1	0.9	0
322.5	116.9	0	0.6	0.5	4.3	27.9	5.6	1.4	0.3	0.5
324.5	117.0	0.2	0.6	0.2	5.3	20.7	9.6	1.7	1	1.8
326.5	117.2	0.2	0.4	0.5	5.1	21.9	6.4	1.2	0	1.8
328.5	117.4	0.2	0.4	0.2	6.2	24.3	9	0.8	0.4	1.8
330.5	117.6	0.2	0.4	0.2	4.3	24.9	7.6	2.9	0.4	0.4
332.5	117.8	0	0.3	0.3	7.5	27.1	9.2	2.1	0	1.2
334.5	117.9	0.2	0.4	1.1	5	31.1	9.9	3.4	0	0
336.5	118.1	0	0.3	0.7	4.9	27.2	9.5	1.8	0.3	0.3
338.5	118.3	0.4	0.4	0.6	4.5	27.3	9	2	0	0.4
340.5	118.5	0.2	0.2	0.4	2.6	30	10.2	3.2	0.2	0
342.5	118.7	0.3	0.3	1	4.4	28.5	9.9	2.8	0.2	0.2
344.5	118.9	0	0.2	0.5	6.7	27.1	9.5	2.1	0.2	0
346.5	119.0	0	0.7	0.1	7.3	29.7	6.7	2.3	0	0.2
348.5	119.2	0.3	0.3	1.5	5.3	26.1	5.3	2.1	0.3	0
350.5	119.4	0.3	1.2	0.8	5.1	29.7	8.9	2.2	0.5	0.7
352.5	119.6	0.2	0.2	0.6	3.3	37.4	5.1	3	0	0.8
354.5	119.8	0	0.5	0.6	3.3	28.3	6.9	2.1	0	0.3
356.5	119.9	0	0.2	0.4	5.4	32.8	11.2	1.1	0	0.6
358.5	120.1	0	0.2	0	4.9	32.6	5.6	2.5	0	0.7
360.5	120.3	0.3	0.6	0.6	3.5	31.2	12.1	4.7	0	1.5
362.5	120.5	0	0	0.3	3.8	33.8	13.1	5	0	1.1
364.5	120.6	0	0	0.6	4.2	27.5	11.4	4.4	0	0.8
366.5	120.7	0	0.5	0	5.1	27	14.7	2.6	0	0.7
368.5	120.8	0.3	0.3	1.9	5	30	13.2	3	0	0
370.5	121.0	0	0.2	0.2	5.2	25.2	15.6	3.9	0.2	0.2

Depth [cm]	Age[ka]	G. truncatuli	G. truncatuli	G. conglobat	G. ruber p	G. ruber w	G. trilobus	G. sacculifer	G. inflata	G. falconensis
372.5	121.2	0.3	0.3	0.8	5.8	28.6	10	3.1	0	1
374.5	121.4	0.3	0	1	5.8	30.8	10.5	2.9	0.3	0.3
376.5	121.6	0.2	0.2	0.8	7.6	30.2	9.8	3	0.2	0
378.5	121.8	0	0	0.8	6.4	27.7	13	2.5	0.2	0.6
380.5	121.9	0	0	1.2	6.3	32.8	8.8	2.9	0	0.3
382.5	122.1	0.2	0.2	1.2	8.6	26.4	10.9	2.2	0	0.7
384.5	122.3	0	0	1.3	9.6	31.8	9.4	2.1	0	0.9
386.5	122.5	0.3	0.3	0.9	7.1	30.4	10.1	2.6	0.3	1.1
363.5	122.7	0.8	0.3	1.9	10.8	26.2	12.4	2.2	0	0.5
390.5	123.0	0.5	0.3	0.5	6.8	30.1	7.8	0.6	0	0.5
392.5	123.2	0	0.3	1.6	10.7	24.3	13	1.6	0.2	0.2
394.5	123.4	0.3	0.3	1.3	9.3	27.8	11.8	2.4	0	0
396.5	123.6	0.4	0.5	0.3	6.3	29.8	7.8	1.9	0	0.2
398.5	123.7	0.2	1	1.5	9.7	32.4	8.8	2.5	0.2	0.2
400.5	123.9	0	0.9	1.2	11.1	29.6	16.2	2.4	0.6	0.3
402.5	124.1	0	1.7	3.1	13.4	23	11.5	2.4	0.7	0.5
404.5	124.3	0.3	1	0.8	10	24.1	13.8	1.5	0	0.3
406.5	124.5	0.2	0.9	1.9	12.3	20.7	12.9	4.8	0	0.5
408.5	124.7	0.3	0.3	0.7	9.4	25.6	13.7	2	0.3	0.6
410.5	124.8	0.2	0.6	2	9.5	25.7	12.3	2.1	0	0.3
412.5	125.0	0.6	0.6	1.5	12.6	19.7	15.4	2.2	0	1.1
414.5	125.2	0.7	0.5	1.1	8.9	22.1	11.5	5	0	0.2
416.5	125.4	0.7	1	3.3	16.1	19	12.6	2.1	0.3	1.3
418.5	125.6	1.3	0.3	2.3	17.5	15.4	14.5	2.3	0	0.3
420.5	125.7	0.4	0.4	1.2	11.3	23	9.7	5.1	0.2	0.8
422.5	125.9	0.8	0.4	1.9	11.1	18.9	13.2	2.3	0	1.1
424.5	126.1	1.8	0.6	1.1	12.7	22.9	9.7	1.8	0	0.8
426.5	126.3	0	0.5	2.1	15.3	17	9.6	0.9	0	0.4
428.5	126.5	2.3	0.2	2.2	10.7	24.1	7.9	2.1	0	1.3
430.5	126.6	1.8	0.4	1.2	9.9	24.1	9.2	2	0.3	1
432.5	126.8	1.6	0.3	1.3	13	20.2	7.7	3.7	0	0.8
434.5	127.0	2.1	0	0.5	7	24.5	8.4	3.8	0.9	2.1
436.5	127.2	2	0.2	0.9	12.8	23	11.7	4.2	0.4	1.1
438.5	127.4	2.4	0	1.6	11.2	26.5	12.2	4.6	0	0.8
440.5	127.6	0.9	0.2	2.7	14	19.8	13.8	4.5	0.2	0.8
442.5	127.7	1.2	0	1.1	15.2	20	10.3	3.2	0.2	0.2
444.5	127.9	1.8	0.2	1.1	15.1	20.8	10.7	2.1	0.2	0.2
446.5	128.1	0.9	0	0.8	11.2	24.4	7.5	1.1	0	2.4
448.5	128.3	1.4	0	2	13.5	21.7	12.2	1.9	0.4	0.9
450.5	128.5	2.5	0	2.1	13.3	22	8.2	1	1.3	1.3
452.5	128.6	3	0	0.4	7.7	25.9	6.5	2.1	0.9	1.2
454.5	128.8	0.2	0	1.1	10.6	29	3.2	1.9	0.2	0.9
456.5	129.0	1.7	0	1	12	19.6	8.3	1.1	1.7	2
458.5	129.3	1.3	0.2	0.5	7.5	25.8	7.3	0.7	1.7	1.5
460.5	129.7	1.3	0.2	0.3	9.2	22.1	7.3	2.3	2.4	1.2
462.5	130.0	1.1	0.3	0.3	3.8	26.1	3.3	0.5	6.1	1.5
464.5	130.4	2.8	0	0.9	2	20.9	7.2	0.8	2.8	2
466.5	130.7	3.5	0.5	0.5	2	22.8	5.2	1.6	5.9	0.2
468.5	131.2	2.7	0.6	0.4	3	23.4	5.8	0.9	5.2	0.4
470.5	131.8	2.3	0.6	0.8	3.9	25.4	8.5	2.8	3	1
472.5	132.4	2	0.5	0.4	3	26.9	8.1	1.3	3	1.1
474.5	133.0	3.8	0.6	0.3	0.3	31	7.6	1.6	6	0.3
476.5	133.6	2	0.4	0.5	1.8	26	6.9	1	5.6	0.9
478.5	134.2	3.2	0.2	0.2	3.7	27.8	5.3	1.2	6.9	0.8
480.5	134.8	2.3	0.3	0.4	1.7	22.5	9.2	2.7	7.8	1.2
482.5	135.4	2.5	0.3	0.6	1.3	23.2	10.1	0.8	6.1	0.3
484.5	136.0	1.7	0	0.3	0.3	24.8	7.2	1.1	11.3	1.1
486.5	136.6	1.4	0.2	0.3	0	20.8	8.2	1.4	7.1	0.7
488.5	137.2	2.8	0.2	0.2	1.4	21.5	9.2	1.3	6.1	0.7
490.5	137.8	1.7	0.2	1.2	1.1	20.1	8.4	1.2	6.5	0.2
492.5	138.4	1.9	0	1.2	1.9	23.2	7.6	0.4	4.5	0.3
494.5	139.0	2.7	0.6	0.4	0.3	21.3	6.1	1.3	6.4	0
496.5	139.6	0.9	0.3	0.1	1.3	19.5	8.7	1.1	6.3	0.5
498.5	140.2	2.4	0.7	0.1	2.7	22	8.4	2.4	4.5	0.2
500.5	140.8	0.9	0.2	0.3	3.8	21.1	8.7	2	4.7	1.3
502.5	141.4	1.1	0.3	0.6	0.8	20.4	7.6	2.7	4.7	0.3
504.5	142.0	1.4	1.2	0.1	3.3	21.1	9.8	2.3	6.3	1.6
506.5	142.6	1.4	1.4	0.1	1.8	25	7.1	1.7	5.1	0.2
508.5	143.2	0	1.1	0.4	4.7	22.6	7.2	1.7	4.2	1.1

Depth, cm	Age(ka)	G. menardii(%)	Globiger.(%)	G. men. flex	G. menardii(#)	Depth, cm	Age(ka)	G. menardii(	Globiger.(%)	G. men. flex	G. menardii(#
150.5	33.7	0.1	39.6	0.1	12	368.5	120.8	2.6	53	0.1	321
160.5	42.2	0	41.5	0	16	370.5	121.0	0.9	50.1	0.2	137
170.5	50.7	0	39	0	0	372.5	121.2	1.3	48.3	0.2	85
180.5	59.2	0.2	41.5	0	36	374.5	121.4	1.5	51	0.1	186
190.5	67.7	0	40.2	0	8	376.5	121.6	1.2	51.4	0	314
200.5	76.2	0.1	41.5	0	40	378.5	121.8	2.2	50.4	0.1	218
210.5	84.7	1.2	45.3	0.1	704	380.5	121.9	0.9	52.1	0.1	100
220.5	90.5	3.5	28.7	0.1	1400	382.5	122.1	2.3	49.3	0.1	312
230.5	95.6	4.6	35.9	0.5	1504	384.5	122.3	2.7	54.2	0	394
240.5	99.4	4.5	47.8	0.3	1580	386.5	122.5	3	51.1	0.1	351
244.5	100.9	4.5	39.1	0.6	1413	363.5	122.7	1.5	53.6	0	181
246.5	101.7	2.6	45.6	0.4	918	390.5	123.0	0.7	45.8	0	101
248.5	102.4	4.2	42	0.3	1182	392.5	123.2	1.6	51.3	0.1	165
250.5	103.1	3.5	37.4	0.7	1536	394.5	123.4	1.8	52.6	0	225
252.5	103.6	5.4	31.1	0.7	2684	396.5	123.6	1.2	46.1	0	170
254.5	104.0	5.5	32.6	1.1	2750	398.5	123.7	1.6	54.9	0	217
256.5	104.5	3.4	32.8	0.4	1636	400.5	123.9	1	60.4	0	107
258.5	105.0	4.8	26.7	0.9	2126	402.5	124.1	3.8	53.4	0.3	504
260.5	105.4	4.9	21.7	0.4	2512	404.5	124.3	1.7	50.3	0	219
262.5	105.9	4.9	28	0.8	1772	406.5	124.5	2.1	52.6	0.1	199
264.5	106.3	3.3	22.9	0.6	1764	408.5	124.7	2	51.5	0	206
266.5	106.8	6.2	26.9	0.4	3492	410.5	124.8	2.7	51.6	0	256
268.5	107.3	6.9	25.9	0.8	2908	412.5	125.0	3	51.5	0	269
270.5	107.7	4.8	25.6	0.5	1928	414.5	125.2	1.9	48.5	0	259
272.5	108.2	5.3	28.1	0.9	2316	416.5	125.4	3.7	53.1	0	371
274.5	108.7	6.4	30.7	1.4	2328	418.5	125.6	2.8	52	0	297
276.5	109.1	4.5	29.4	0.6	1606	420.5	125.7	2.1	50.2	0.1	166
278.5	109.6	4.9	30.6	0.9	1460	422.5	125.9	4.4	47.4	0	432
280.5	110.0	4.9	28.2	1.4	1416	424.5	126.1	2.8	48.2	0.2	239
282.5	110.5	5.5	31.2	1.2	914	426.5	126.3	4.5	44.9	0	342
284.5	111.0	3.6	22.9	0.3	1076	428.5	126.5	6.1	47	0	436
286.5	111.4	4.9	38.2	0.8	932	430.5	126.6	4.3	46.4	0	391
288.5	111.9	4.2	33.3	1.3	1100	432.5	126.8	4.2	45.9	0	260
290.5	112.3	4.9	35.3	1.8	1068	434.5	127.0	3.8	44.2	0.3	526
292.5	112.8	6.2	29.3	0.7	1048	436.5	127.2	5.1	52.6	0	451
294.5	113.3	3.5	24.9	0.6	502	438.5	127.4	4.4	56.1	0	418
296.5	113.7	4.1	32.4	0.4	876	440.5	127.6	5	54.8	0	378
298.5	114.2	4	34.9	1	450	442.5	127.7	5.4	49.8	0	724
300.5	114.7	2.8	36	0.4	336	444.5	127.9	5.3	49.8	0	440
302.5	115.0	2.8	38.2	0.9	423	446.5	128.1	4.3	45	0	488
304.5	115.2	4.2	31.6	0.4	572	448.5	128.3	5.3	51.3	0	454
306.5	115.4	5.7	36.3	1.3	722	450.5	128.5	4.6	46.7	0	554
308.5	115.6	5.2	40.3	1.1	413	452.5	128.6	4.8	42.5	0	525
310.5	115.8	6.6	38.7	1.6	435	454.5	128.8	4.1	45.8	0	574
312.5	116.0	4.9	39.1	1.3	864	456.5	129.0	5.1	42.1	0	1050
314.5	116.1	3.7	37.8	1.7	370	458.5	129.3	3.8	41.9	0	1130
316.5	116.3	3.5	39.3	0.3	354	460.5	129.7	4.8	41.3	0	1272
318.5	116.5	2.4	37.9	1.3	248	462.5	130.0	2.4	34.1	0	614
320.5	116.7	6	39.8	1.1	682	464.5	130.4	1.8	31.9	0	424
322.5	116.9	4.1	39.7	0.3	495	466.5	130.7	0.7	32.1	0	98
324.5	117.0	3.6	37.6	1	289	468.5	131.2	0.1	33.5	0	17
326.5	117.2	3.4	35	0.7	344	470.5	131.8	1.6	41.4	0	262
328.5	117.4	2.4	40.5	0.7	211	472.5	132.4	1.4	39.7	0	253
330.5	117.6	3	39.9	0.6	244	474.5	133.0	0.7	40.8	0	138
332.5	117.8	2.4	46.3	0.3	261	476.5	133.6	0.4	36.1	0	73
334.5	117.9	2.2	50.4	0.4	160	478.5	134.2	0	38.4	0	2
336.5	118.1	1.9	44.2	0.2	214	480.5	134.8	0.2	36.5	0	32
338.5	118.3	4.6	43.5	1.6	404	482.5	135.4	0.5	35.9	0	66
340.5	118.5	2.6	46.2	0.6	241	484.5	136.0	0.3	33.7	0	64
342.5	118.7	3.9	46.6	0.6	261	486.5	136.6	0.2	30.6	0	65
344.5	118.9	2.8	46	0.6	191	488.5	137.2	0.3	33.6	0	64
346.5	119.0	4.6	46	0.6	346	490.5	137.8	0.2	32.1	0	32
348.5	119.2	4.3	40.3	0.3	232	492.5	138.4	1.2	34.2	0	286
350.5	119.4	2.9	46.6	0.4	198	494.5	139.0	1.2	29.4	0	264
352.5	119.6	3.3	49.5	0.5	267	496.5	139.6	0.3	30.6	0	80
354.5	119.8	3.2	41.1	0.4	185	498.5	140.2	0	35.7	0	10
356.5	119.9	1.1	50.9	0.1	84	500.5	140.8	0	35.8	0	4
358.5	120.1	1.3	45.5	0.3	169	502.5	141.4	0	32.1	0	0
360.5	120.3	1.6	52.1	0.3	178	504.5	142.0	0.3	36.6	0	38
362.5	120.5	1.5	56	0.2	182	506.5	142.6	0	35.8	0	4
364.5	120.6	2.5	48	0.3	291	508.5	143.2	0	36.7	0	2
366.5	120.7	2.7	49.4	0.4	258						

Depth [cm]	Age[ka]	lnSr (norm)	Ca (norm)	Cl (norm)	Sr/Ca	Fe(norm)	Depth [cm]	Age[ka]	lnSr (norm)	Ca (norm)	Cl (norm)	Sr/Ca	Fe(norm)
150	33.3	0.0545	0.9241	0.0469	0.0993	0.0514	178.7	57.7	0.1827	0.9478	0.0360	0.0696	0.0480
150.3	33.6	0.3826	0.9495	0.0339	0.0798	0.0627	179	58.0	0.2333	0.9450	0.0364	0.0705	0.0505
150.6	33.8	0.3661	0.9514	0.0337	0.0673	0.0584	179.3	58.2	0.2944	0.9439	0.0384	0.0746	0.0543
150.9	34.1	0.2988	0.9528	0.0317	0.0665	0.0538	179.6	58.5	0.2556	0.9421	0.0398	0.0712	0.0506
151.2	34.3	0.3238	0.9547	0.0296	0.0736	0.0580	179.9	58.7	0.2384	0.9471	0.0377	0.0667	0.0466
151.5	34.6	0.4512	0.9572	0.0287	0.0701	0.0583	180.2	59.0	0.2059	0.9425	0.0393	0.0642	0.0474
151.8	34.8	0.5028	0.9576	0.0292	0.0776	0.0580	180.5	59.2	0.1781	0.9487	0.0358	0.0625	0.0466
152.1	35.1	0.4742	0.9564	0.0293	0.0751	0.0620	180.8	59.5	0.2205	0.9497	0.0342	0.0661	0.0503
152.4	35.3	0.4357	0.9561	0.0295	0.0713	0.0632	181.1	59.7	0.1926	0.9476	0.0331	0.0711	0.0508
152.7	35.6	0.4411	0.9561	0.0316	0.0708	0.0617	181.4	60.0	0.1662	0.9506	0.0329	0.0609	0.0601
153	35.9	0.4148	0.9540	0.0323	0.0641	0.0584	181.7	60.2	0.2226	0.9454	0.0350	0.0615	0.0616
153.3	36.1	0.3822	0.9537	0.0328	0.0622	0.0598	182	60.5	0.2485	0.9410	0.0389	0.0631	0.0718
153.6	36.4	0.4258	0.9549	0.0316	0.0680	0.0599	182.3	60.8	0.1846	0.9463	0.0329	0.0614	0.0645
153.9	36.6	0.4588	0.9565	0.0298	0.0724	0.0552	182.6	61.0	0.1752	0.9502	0.0301	0.0649	0.0727
154.2	36.9	0.4786	0.9551	0.0313	0.0666	0.0566	182.9	61.3	0.2935	0.9438	0.0363	0.0755	0.0632
154.5	37.1	0.4430	0.9592	0.0277	0.0686	0.0523	183.2	61.5	0.3119	0.9477	0.0341	0.0823	0.0526
154.8	37.4	0.4128	0.9584	0.0287	0.0660	0.0560	183.5	61.8	0.2457	0.9441	0.0361	0.0839	0.0496
155.1	37.6	0.3471	0.9557	0.0305	0.0716	0.0510	183.8	62.0	0.3257	0.9473	0.0357	0.0838	0.0534
155.4	37.9	0.3650	0.9523	0.0322	0.0709	0.0520	184.1	62.3	0.3537	0.9447	0.0361	0.0773	0.0537
155.7	38.1	0.3360	0.9530	0.0310	0.0751	0.0541	184.4	62.5	0.2302	0.9426	0.0348	0.0751	0.0612
156	38.4	0.3198	0.9564	0.0292	0.0789	0.0559	184.7	62.8	0.2141	0.9443	0.0356	0.0779	0.0624
156.3	38.7	0.3857	0.9478	0.0351	0.0755	0.0501	185	63.1	0.2911	0.9490	0.0316	0.0804	0.0586
156.6	38.9	0.4087	0.9555	0.0311	0.0691	0.0557	185.3	63.3	0.3628	0.9498	0.0308	0.0790	0.0653
156.9	39.2	0.4295	0.9573	0.0299	0.0665	0.0548	193	69.9	0.7744	0.9447	0.0375	0.1294	0.0409
157.2	39.4	0.4734	0.9582	0.0289	0.0694	0.0499	193.2	70.1	0.7710	0.9472	0.0368	0.1259	0.0409
157.5	39.7	0.4793	0.9595	0.0292	0.0653	0.0547	193.5	70.4	0.7058	0.9506	0.0353	0.1033	0.0449
157.8	39.9	0.5020	0.9576	0.0294	0.0643	0.0566	193.8	70.6	0.6373	0.9520	0.0333	0.0892	0.0503
158.1	40.2	0.4991	0.9548	0.0322	0.0670	0.0516	194.1	70.9	0.5350	0.9474	0.0352	0.0752	0.0597
158.4	40.4	0.5337	0.9555	0.0313	0.0646	0.0543	194.4	71.1	0.4834	0.9430	0.0395	0.0731	0.0643
158.7	40.7	0.5435	0.9574	0.0314	0.0658	0.0542	194.7	71.4	0.5274	0.9411	0.0411	0.0770	0.0698
159	41.0	0.4877	0.9592	0.0292	0.0657	0.0530	195	71.6	0.6594	0.9379	0.0445	0.0727	0.0289
159.3	41.2	0.4925	0.9571	0.0295	0.0654	0.0546	195.3	71.8	0.5963	0.9472	0.0380	0.0692	0.0331
159.6	41.5	0.5154	0.9560	0.0299	0.0694	0.0564	195.6	72.1	0.5499	0.9492	0.0357	0.0715	0.0288
159.9	41.7	0.4804	0.9572	0.0295	0.0663	0.0526	195.9	72.3	0.6125	0.9507	0.0362	0.0712	0.0303
160.2	42.0	0.4686	0.9582	0.0285	0.0639	0.0491	196.2	72.6	0.4166	0.9476	0.0406	0.0513	0.0317
160.5	42.2	0.4834	0.9561	0.0305	0.0625	0.0532	196.5	72.8	0.2603	0.9489	0.0381	0.0437	0.0320
160.8	42.5	0.4980	0.9556	0.0302	0.0608	0.0597	196.8	73.1	0.0242	0.9434	0.0415	0.0339	0.0327
161.1	42.7	0.4810	0.9528	0.0331	0.0623	0.0579	197.1	73.3	-0.0549	0.9468	0.0392	0.0349	0.0276
161.4	43.0	0.4661	0.9543	0.0325	0.0643	0.0518	197.4	73.6	-0.0104	0.9403	0.0452	0.0379	0.0287
161.7	43.2	0.4498	0.9507	0.0356	0.0646	0.0539	197.7	73.8	0.3271	0.9427	0.0432	0.0491	0.0290
162	43.5	0.4714	0.9517	0.0358	0.0644	0.0565	198	74.1	0.6374	0.9396	0.0474	0.0718	0.0267
162.3	43.8	0.4545	0.9563	0.0306	0.0649	0.0550	198.3	74.4	0.6910	0.9411	0.0467	0.0777	0.0307
162.6	44.0	0.4480	0.9531	0.0325	0.0637	0.0542	198.6	74.6	0.8015	0.9438	0.0415	0.0895	0.0308
162.9	44.3	0.4146	0.9550	0.0327	0.0620	0.0456	198.9	74.9	0.8401	0.9450	0.0429	0.0965	0.0279
163.2	44.5	0.4426	0.9525	0.0342	0.0632	0.0499	199.2	75.1	0.9003	0.9385	0.0479	0.1154	0.0264
163.5	44.8	0.4485	0.9534	0.0339	0.0648	0.0467	199.5	75.4	0.9415	0.9388	0.0490	0.1350	0.0280
163.8	45.0	0.4717	0.9511	0.0370	0.0634	0.0510	199.8	75.6	0.9896	0.9393	0.0483	0.1372	0.0271
164.1	45.3	0.4808	0.9508	0.0345	0.0648	0.0462	200.1	75.9	0.9733	0.9412	0.0469	0.1375	0.0279
164.4	45.5	0.4378	0.9498	0.0360	0.0633	0.0500	200.4	76.1	0.9376	0.9347	0.0513	0.1388	0.0295
164.7	45.8	0.4557	0.9502	0.0374	0.0624	0.0507	200.7	76.4	0.8864	0.9336	0.0518	0.1374	0.0325
165	46.1	0.4602	0.9506	0.0364	0.0635	0.0467	201	76.7	0.9501	0.9369	0.0494	0.1395	0.0303
165.3	46.3	0.4962	0.9467	0.0396	0.0662	0.0475	201.3	76.9	0.8920	0.9362	0.0499	0.1336	0.0358
165.6	46.6	0.5088	0.9466	0.0399	0.0678	0.0445	201.6	77.2	0.8562	0.9330	0.0515	0.1312	0.0338
165.9	46.8	0.4372	0.9504	0.0369	0.0638	0.0422	201.9	77.4	0.8784	0.9374	0.0494	0.1386	0.0336
166.2	47.1	0.3842	0.9513	0.0353	0.0610	0.0441	202.2	77.7	0.8875	0.9341	0.0511	0.1371	0.0341
166.5	47.3	0.3770	0.9522	0.0346	0.0632	0.0420	202.5	77.9	0.8652	0.9347	0.0511	0.1327	0.0333
166.8	47.6	0.2944	0.9529	0.0321	0.0662	0.0392	202.8	78.2	0.8694	0.9350	0.0526	0.1368	0.0333
167.1	47.8	0.3086	0.9510	0.0346	0.0650	0.0408	203.1	78.4	0.8067	0.9260	0.0594	0.1378	0.0295
167.4	48.1	0.3029	0.9547	0.0312	0.0612	0.0443	203.4	78.7	0.7381	0.9242	0.0597	0.1369	0.0327
167.7	48.3	0.3142	0.9536	0.0327	0.0574	0.0447	203.7	78.9	0.7185	0.9265	0.0580	0.1329	0.0347
168	48.6	0.3269	0.9473	0.0389	0.0591	0.0470	204	79.2	0.6542	0.9234	0.0611	0.1260	0.0302
176	55.4	-0.5915	0.9140	0.0526	0.0709	0.0389	204.3	79.5	0.6684	0.9272	0.0573	0.1300	0.0346
176.3	55.7	-0.3667	0.9272	0.0416	0.0671	0.0453	204.6	79.7	0.6818	0.9298	0.0538	0.1355	0.0342
176.6	55.9	-0.0909	0.9429	0.0378	0.0654	0.0431	204.9	80.0	0.6930	0.9249	0.0593	0.1439	0.0300
176.9	56.2	0.0222	0.9484	0.0343	0.0727	0.0448	205.2	80.2	0.7164	0.9375	0.0490	0.1324	0.0325
177.2	56.4	0.0614	0.9455	0.0353	0.0714	0.0425	205.5	80.5	0.7129	0.9347	0.0496	0.1279	0.0303
177.5	56.7	0.1178	0.9479	0.0345	0.0744	0.0458	205.8	80.7	0.7230	0.9410	0.0438	0.1249	0.0352
177.8	56.9	0.0984	0.9489	0.0334	0.0720	0.0407	206.1	81.0	0.6158	0.9349	0.0490	0.1148	0.0336
178.1	57.2	0.1003	0.9495	0.0331	0.0683	0.0430	206.4	81.2	0.5690	0.9394	0.0448	0.1089	0.0337
178.4	57.4	0.0961	0.9419	0.0369	0.0668	0.0464	206.7	81.5	0.6055	0.9336	0.0515	0.1220	0.0327